Measurements of Greenhouse Gases from Near-Infrared Solar Absorption Spectra

by

Sébastien Roche

A thesis submitted in conformity with the requirements
for the degree of Doctor of Philosophy

Department of Physics
University of Toronto

Measurements of Greenhouse Gases from Near-Infrared Solar Absorption Spectra

Sébastien Roche

Doctor of Philosophy

Graduate Department of Physics
University of Toronto

2021

Abstract

This thesis presents improvements to retrievals of greenhouse gas concentrations, with a focus on CO_2 and the Arctic.

Near-infrared solar absorption spectra were collected at the Polar Environment Research Laboratory (PEARL) in Eureka, Nunavut as part of the Total Carbon Column Observing Network (TCCON), extending the data record to July 2020. Data processing was improved by the application of solar zenith angle corrections to account for pointing offsets of the solar tracker. Issues related to surface pressure records were resolved. TCCON measurements were used to validate simulations of CO_2 and CH_4 by GEM-MACH-GHG, a model in development at Environment and Climate Change Canada.

Vertical profile retrievals of CO_2 from TCCON spectra were evaluated, using improved spectroscopy and line shapes. CO_2 profiles were obtained from sequential retrievals in five spectral windows using synthetic and real spectra. A sensitivity study showed that the leading source of uncertainty in the retrieved CO_2 profiles is errors in the a priori temperature profile as small as 2°C between 600-850 hPa. To distinguish the effect of errors in the instrument alignment and spectroscopic parameters from other error sources, CO_2 profiles were retrieved using an a priori profile built from coincident in-situ measurements. With real spectra, the deviations in retrieved CO_2 profiles were larger than typical vertical variations of CO_2. Remaining errors in the forward model limit the accuracy of the retrieved profiles. Implementing a temperature retrieval or correction is critical to improve CO_2 profile retrievals.

A study was conducted in support of the proposed Canadian satellite mission AIM-North. The ReFRACtor algorithm was adapted to generate synthetic spectra for a Fourier transform spectrometer and a grating spectrometer. Retrievals were performed on these synthetic spectra to estimate the precision and accuracy of retrieved XCH_4, XCO, and XCO_2, in different conditions. Over a standard scene corresponding to a boreal forest, the retrieval precision for the given instrument characteristics was ~0.6% for XCH_4, ~8% for XCO, and ~0.4% for XCO_2. These results can be used by the AIM-North team to decide whether the instrument design should be adapted to meet the mission's precision and accuracy goals and thresholds over specific scenes.

Acknowledgments

I would like to acknowledge and thank the many individuals and institutions that made the work presented in this thesis possible.

The work presented in this thesis was primarily funded by the Natural Sciences and Engineering Research Council of Canada and the Canadian Space Agency.

I am grateful for the opportunities to participate in the Canadian Arctic ACE/OSIRIS Validation Campaigns in Eureka and thank everyone who worked to make this possible: especially Kaley Walker, Pierre Fogal, Paul Loewen, Mike Maurice, Peter McGovern, and John Gallagher.

I thank Dan Weaver for mentoring me on my first trip to Eureka, and Joseph Mendonca from whom I learnt how to take care of the Eureka NIR data and for working with me on AIM-North retrievals. I wish to thank fellow PhD students and postdoctoral fellows with whom I went to Eureka: Xiaoyi Zhao, Erik Lutsch, Tyler Wizenberg, Kristof Bognar. Ellen Eckert, Ghazal Farhani, Sham Gamage, Paul Jeffery, Ali Jalali, Sophie Tran, Zahra Vaziri, Gurpreet Singh, and Emily McCullough. I also wish to thank the staff of the Eureka Weather Station for welcoming us.

I thank Jonathan Franklin for his support with operating the Eureka suntracker and for sharing his codes to derive and apply solar zenith angle corrections to Eureka data.

I thank Orfeo Colebatch for his invaluable support in my six-month lab internship before starting my PhD, and for his help in the following years with setting up the alignment kit for the PEARL spectrometer and with operating the University of Toronto Atmospheric Observatory.

I thank Saroja Polavarapu and Michael Niesh at Environment and Climate Change Canada (ECCC) for letting me contribute to the GEM-MACH-GHG project. I also thank Ray Nassar (ECCC) for the chance to participate in the early phases of the AIM-North mission.

I thank Louis Moreau from ABB Inc. for his help with defining the instrument models for the AIM-North grating spectrometer and FTS and for answering questions on the instruments.

I thank Dylan Jones, as his teaching of the Data Assimilation and Retrieval Theory course gave me the confidence I needed to work towards improving GFIT2.

I thank Brian J. Connor for helping me to get started with GFIT2 and for his feedback.

I thank the NDACC and TCCON communities; their annual meeting was one of the highlights of each year. I thank Frank Hase for his support with running LINEFIT, Joshua Laughner for all his work on GGG2020 and from whom I learnt to write better codes, and Geoffrey C. Toon for his help with understanding GGG and his guidance throughout the CO_2 profile retrieval study.

I also wish to thank co-authors who included me in their projects: David Long, Oliver Schneising, Susan Kulawik, Saroja Polavarapu, Ray Nassar, Maximilian Reuter, Jacob Hedelius, Shoma Yamanouchi, and Mahesh K. Sha. I thank Sébastien Biraud, Bianca Baier, and Colm Sweeney for providing data I needed for the CO_2 profile retrieval work and for their feedback on the paper.

I thank my PhD supervisory committee for their guidance: Debra Wunch, Kimberly Strong, and Dylan Jones.

I thank my co-supervisor Debra Wunch for her support and guidance, I feel lucky that she took a faculty position at the University of Toronto as I started working on GFIT2. Her knowledge of Carbon Cycle Science, and of TCCON and its retrieval algorithm, was invaluable for my research.

I thank my supervisor Kimberly Strong for her support and guidance, and for her infinite patience and kindness. I am thankful for the opportunities she gave me to collaborate and meet with other scientists in Canada and abroad, for trusting me with handling the Eureka NIR data and aligning the instrument, and for giving me the chance to write a part of a textbook chapter. I look up to her as a role model for both her achievements and character.

Finally, I thank my parents François and Michelle Roche and my sister Agnès who have always believed in me. I feel privileged to have been raised by parents who gave me freedom to choose my own path and supported me along the way.

Table of Contents

List of Tables

List of Figures

List of Abbreviations

ACOS	Atmospheric CO_2 Observations from Space
AIRS	Atmospheric Infrared Sounder
AOD	Aerosol Optical Depth
CANDAC	CAnadian Network for the Detection of Atmospheric Change
CC	Continuum curvature
CL	Continuum Level
COP	Conference of the Parties
CT	Continuum Tilt
CSA	Canadian Space Agency
CST	Community Solar Tracker
DOFS	Degrees of Freedom for Signal
EC-CAS	Environment Canada Carbon Assimilation System
ECCC	Environment and Climate Change Canada
EOF	Empirical Orthogonal Function
ESA	European Space Agency
ESRL	Earth System Research Laboratory
FFT	Fast Fourier Transform
FTIR	Fourier Transform Infrared
FTS	Fourier Transform Spectrometer
FWHM	Full Width at Half Maximum
GCOS	Global Climate Observing System
GEM	Global Environment Multiscale
GEO	GEOstationary

GEOS	Goddard Earth Observing System
GEOS5-FP-IT	Goddard Earth Observing System Version 5 Forward Processing for Instrument Teams
GFIT	Gas Fit
GFIT/2	GFIT and GFIT2
GMAO	Global Modeling Assimilation Office
GOSAT	Greenhouse Gases Observing Satellite
GUI	Graphical User Interface
HEO	Highly Elliptical Orbit
HITRAN	High-resolution Transmission Molecular Absorption Database
HWHM	Half Width at Half Maximum
I2S	Interferograms to Spectra
ILS	Instrument Line Shape
IPCC	Intergovernmental Panel on Climate Change
IRWG	InfraRed Working Group
JPL	Jet Propulsion Laboratory
LEO	Low Earth Orbit
LM	Line Mixing
ME	Modulation Efficiency
MOPITT	Measurement Of Pollution In The Troposphere
NASA	National Aeronautics and Space Administration (USA)
NDACC	Network for the Detection of Atmospheric Composition Change
NESR	Noise Equivalent Spectral Radiance
NIWA	National Institute of Water and Atmospheric Research (New Zealand)
NOAA	National Oceanic and Atmospheric Administration (USA)
OCO	Orbiting Carbon Observatory

OEM	Optimal Estimation Method
PE	Phase Error
PEARL	Polar Environment Atmospheric Research Laboratory
ppb	parts per billion
ppm	parts per million
ppt	parts per trillion
qSDV	quadratic Speed-Dependent Voigt
qSDV+LM	quadratic Speed-Dependent Voigt with Line Mixing
RF	Radiative Forcing
RCP	Representative Concentration Pathway
S5P	Sentinel-5 Precursor
SCIAMACHY	Scanning Imaging Absorption Spectrometer for Atmospheric Cartography
SDV	Speed-Dependent Voigt
SG	Solar-Gas stretch
SNR	Signal-to-Noise Ratio
SWIR	Short-Wave Infrared
SZA	Solar Zenith Angle
TCCON	Total Carbon Column Observing Network
TES	Tropospheric Emission Spectrometer
TROPOMI	TROPOspheric Monitoring Instrument
UNFCCC	United Nations Framework Convention on Climate Change
UofT	University of Toronto
VP	Voigt Profile
VZA	Viewing Zenith Angle
WMO	World Meteorological Organization

ZLO	Zero-Level Offset
ZPD	Zero Path Difference

Chapter 1
Introduction and Motivation

1.1 Greenhouse Gases

Without its atmosphere, Earth's surface temperature would be close to -18°C, but instead the global mean surface temperature is approximately +15°C (e.g., Wallace and Hobbs, 2006). This difference is caused by gases that absorb and re-emit thermal radiation, thereby warming the atmosphere; this process is called the greenhouse effect. Solar radiation is composed of a wide range of wavelengths from gamma rays to radio waves, but their distribution peaks at around 500 nm in the visible spectrum (390-700 nm). Earth's atmosphere is transparent for visible light and most of the visible solar radiation can reach the surface. Greenhouse gases absorb and re-emit long-wave radiation in the infrared (IR). Of the incoming solar radiation at the top of the atmosphere, ~47% is absorbed by Earth's surface and ~29% is reflected back to space by clouds and the planet's surface, while the rest is absorbed by the atmosphere. The short-wave radiation absorbed at the surface is re-emitted as infrared radiation. The atmosphere is much less transparent to the emitted terrestrial radiation than it is to the incoming solar radiation. Of the long-wave radiation emitted by Earth's surface, ~86% remains in the troposphere because of the abundance of greenhouse gases and clouds (Hartmann et al., 2013).

To quantify the contribution of the different atmospheric species to the Earth's radiative balance and the greenhouse effect, the Intergovernmental Panel on Climate Change (IPCC) defines the Radiative Forcing (RF) concept. RF is expressed in Watts per square meter ($W.m^{-2}$) and can be used to quantify the energy imbalance caused by a perturbation in atmospheric composition (e.g., a change in atmospheric CO_2 concentration). It is the change in the net difference of downward and upward radiative flux due to the perturbation. The values are generally given with respect to changes since pre-industrial times. RF is directly linked to global mean surface temperature changes through the relation:

$$RF = \lambda \Delta T \tag{1.1}$$

where ΔT is the temperature change associated with a given RF and λ is the climate sensitivity parameter. Each perturbation will have a specific λ, but a positive radiative forcing results in warming while a negative radiative forcing results in cooling. There are natural sources of RF variations such as changes in solar irradiance, or aerosols and greenhouse gas emissions from volcanoes, but those only represent a small fraction of the anthropogenic forcing during the industrial era. The IPCC states "Total radiative forcing is positive, and has led to an uptake of energy by the climate system. The largest contribution to total radiative forcing is caused by the increase in atmospheric concentration of CO_2 since 1750." (IPCC, 2013).

1.1.1 Water Vapour

Water vapour is the largest contributor to the natural greenhouse effect, with a RF two to three times larger than that of CO_2. Unlike other trace gases, water is abundant in all phases on Earth. It is also an essential constituent of the biosphere and is responsible for weather events such as clouds and storms. It is not well-mixed, with most of the water vapour present in the lower troposphere. As it precipitates and condenses, the amount of water vapour in a column of air is variable. It depends on atmospheric temperatures; the atmosphere can hold 7% more water vapour for a 1°C increase in air temperature. The air is drier at the poles than in the tropics. There are direct anthropogenic emissions of water vapour, but they are only a small fraction of emissions from the natural water cycle and should not play a significant role in the greenhouse effect. However, since the water vapour amount depends on temperature, and increasing concentrations of greenhouse gases warm the atmosphere, water vapour is an important climate feedback which amplifies any RF from other agents. In the stratosphere, water vapour amounts have increased due to anthropogenic emissions of CH_4. CH_4 gets oxidized and releases water that does have a RF in the stratosphere, although it is smaller than the RF for CH_4 and CO_2 (Myhre et al., 2013).

1.1.2 Carbon Dioxide

CO_2 has the highest anthropogenic RF for the industrial era ($1.82\ W.m^{-2}$) and is the main driver of the global mean warming. It is a long-lived trace gas and any emissions that are not absorbed by the land and ocean reservoirs remain in the atmosphere for 5 to 200 years. Global mean temperatures are estimated to increase by 0.8-2.5°C for each 1000 Gt C emitted to the atmosphere. Between 445 and 585 Gt C were emitted between 1750 and 2011 (Collins et al., 2013). This corresponds to a CO_2 attributable warming of 0.3-1.5 °C in 2011 relative to the preindustrial era (Gillett et al., 2013). Section 1.2 describes the role of CO_2 in the carbon cycle.

1.1.3 Methane

Although CH_4 is about 200 times less abundant than CO_2 in the atmosphere, its contribution to Earth's radiative forcing is one-quarter of that of CO_2 (Myhre et al., 2013). It is also more chemically reactive than CO_2 and has a shorter life time of ~9 years in the troposphere where is it is removed by reaction with OH (Prather et al., 2012). This lifetime is affected by the concentration of other atmospheric constituents such as reactive nitrogen compounds, OH and CO. Emissions of CH_4 also lead to the production of ozone, water vapour, and CO_2, which bring the total radiative forcing contribution of CH_4 to +0.97 $W.m^{-2}$ (Myhre et al., 2013). Due to its relatively short lifetime and strong global warming potential, mitigating CH_4 emissions can have an impact on global warming trends within a human's lifetime. Atmospheric CH_4 presents seasonal variations driven by the concentrations of OH in the troposphere, which lead to minimum CH_4 concentrations in July-August. The timing in emissions from wetlands and biomass burning, and atmospheric transport, also affect the seasonal cycle (Dlugokencky et al., 2011). Global surface concentrations of CH_4 more than doubled between 1750 and 2016, with a 257% increase from 771 to 1853 ppb (WMO, 2018). The growth rate slowed between 1999-2006, but averaged 6.7 $ppb.yr^{-1}$ for 2007-2015 (WMO, 2017). There still is not one widely accepted explanation for these variations. Suggestions have included increased biogenic emissions from wetlands and agriculture in tropical regions (Nisbet et al., 2016), anthropogenic emissions from oil and gas (Hausmann et al., 2016), and changes in OH concentrations (Prather et al., 2012; Rigby et al., 2017; Turner et al., 2017).

1.1.4 Other Greenhouse Gases

N_2O is a strong greenhouse gas, with the third largest anthropogenic radiative forcing (0.17 $W.m^{-2}$) and a long lifetime of 116±9 years. It is produced naturally by microbial activity in soils and in a similar amount by anthropogenic sources, mainly agriculture. Atmospheric concentrations increased by 20%, from 270 ppb to 331 ppb, between 1750 and 2018 due to fossil fuel combustion and more importantly due to the growth of agriculture (~80% of the increase). N_2O is deposited in soil sediments or leaks to the ocean, through rivers or atmospheric deposition, before being emitted to the atmosphere. N_2O is removed by photochemical processes in the stratosphere producing reactive nitrogen (NO_x) that contributes to ozone depletion (Ravishankara et al., 2009; Ciais et al., 2013; Tian et al., 2020).

Halocarbons are made of carbon atoms and halogen atoms (fluorine, chlorine, bromine, iodine). They can be further divided into different groups, for example chlorofluorocarbons (CFCs), hydrofluorocarbons (HFCs), and hydrochlorofluorocarbons (HCFCs), amongst others. Their atmospheric concentrations are very small, ranging between 2 and 530 parts per trillion, but they are very effective radiative forcing agents with a combined RF value of 0.36 $W.m^{-2}$, and they are also contributing to ozone depletion. Dichlorofluoromethane (CFC-12) used to be the third largest contributor to the anthropogenic RF, but under measures from the Montreal Protocol (and its amendments) to reduce emissions of CFCs, it was overtaken by N_2O in 2011. N_2O has also taken the place of halocarbons as the most important ozone-depleting substance (Ravishankara et al., 2009). However, concentrations of HFCs, HCFCs and other halogens has continued to rise and the forcing due to halocarbons is still increasing (Myhre et al., 2013). It has also recently been found that concentrations of trichlorofluoromethane (CFC-11) started increasing again between 2012 and 2018, inconsistent with reported production since 2006 and with past production, thus failing an objective of the Montreal Protocol to eliminate CFCs emissions by 2010 (Montzka et al., 2018). More recent measurements showed that emissions from unreported CFC-11 production are decreasing again since 2018 (Montzka et al., 2021). This highlights the importance of atmospheric measurements to monitor the concentration of ozone-depleting substances, or greenhouse gases, independently from production reports.

The components of radiative forcing are presented in Figure 1.1, including the contributions of greenhouse gases and aerosols.

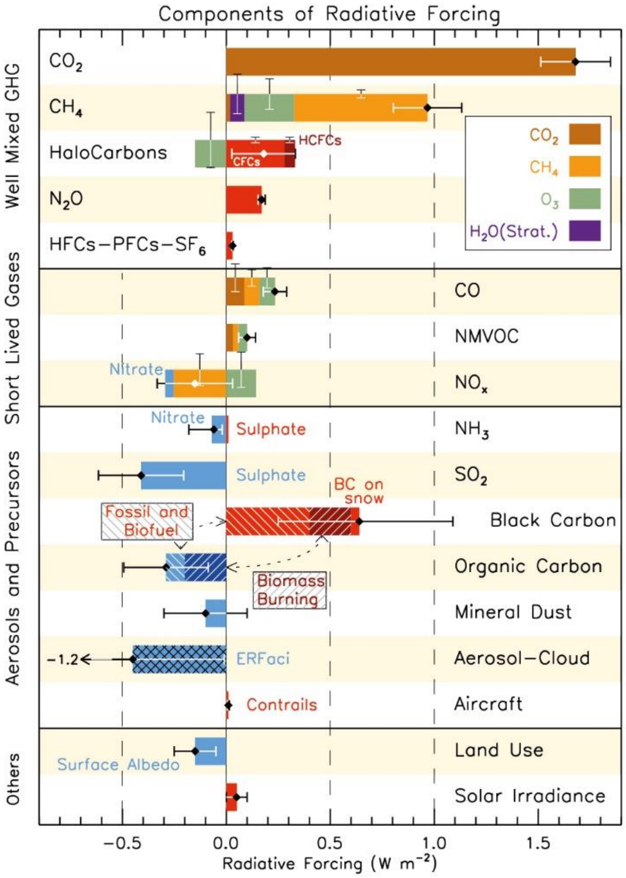

Figure 1.1: Components of radiative forcing for the period 1750-2011. Red and blue indicate positive and negative RF, respectively. Other colours correspond to the indirect RF contributions of affected compounds. A diamond symbol indicates the net impact of all contributions for a given compound. Figure from Myhre et al. (2013).

1.2 The Carbon Cycle

Most of Earth's carbon is stored in rocks, but exchanges between the environment and this reservoir are slow, of the order of 0.01-0.1 Gt C / y. The rest is distributed between the atmosphere, land, and oceans. The exchange of carbon between these reservoirs is called the Carbon Cycle (Ciais et al., 2013). When one reservoir loses carbon, it is added to another. The carbon accumulating in the atmosphere, primarily in the form of CO_2, increases surface temperature (IPCC, 2013). Atmospheric CO_2 is the main influence on the global carbon cycle, and comprises 828 Gt C. Other trace gases and aerosols have a smaller impact, including CH_4 (3.7 Gt C), carbon monoxide (CO, 0.2 Gt C), hydrocarbons, black carbon, and organic aerosols (Ciais et al., 2013).

1.2.1 The Slow Carbon Cycle

The slow carbon cycle, which transfers carbon from the environment to rocks, operates according to several mechanisms. The slow carbon cycle is balanced over periods of several hundred thousand years. Carbon is transferred from the atmosphere to rocks through rain; this is called chemical weathering (Colbourn et al., 2015). Carbonic acid (H_2CO_3) forms in the water and dissolves rocks, producing ions which are carried to the ocean by rivers. In the ocean, calcium ions react with carbonate ions to form calcium carbonate ($CaCO_3$). $CaCO_3$ is used by various organisms to build their shells and by plankton. After their death, shells fall and accumulate on the seafloor where they turn into carbon-storing rocks by lithification. The bodies of dead organisms also contribute to carbon storage in sedimentary rocks like shale. When they accumulate too quickly to be assimilated, the organic carbon turns into oil, coal or gas instead. To close the slow carbon cycle, the rocks are transported in the crust when the sea floor sinks under continental plates. Carbon dioxide is released by volcanic activity above regions where high pressure and temperature melt the rocks. Volcanic emissions are of the order of 0.13-0.44 Gt C / y (Gerlach, 2011).

Direct exchanges of carbon between the atmosphere and the ocean also occur on faster time scales. Carbon dioxide dissolves in water at the ocean surface; it can then react with water to form carbonic acid. The acid dissociates into acidifying hydrogen ions and bicarbonate ions (HCO_3^-), which themselves dissociate into more hydrogen ions and carbonate ions (CO_3^{2-}). This doesn’t result in more stored carbon through the process previously described because the carbonate ions tend to recombine with hydrogen ions. The net effect is a lowering of the pH level and a change in the balance between carbonate and bicarbonate ions. Ocean pH is already 0.1 lower than in pre-industrial times and is predicted to be diminished by another 0.3-0.4 if atmospheric concentrations of CO_2 reach 800 ppm (Doney et al., 2009). Over the next century, this will be a concern for shell-building organisms and corals because they rely on the production of calcium carbonate skeletons. Increases in atmospheric CO_2 concentrations result in increased dissolved CO_2 concentrations in oceans. This is followed by reduced concentrations of carbonate ions, which hampers the ability of marine organisms to produce calcium carbonate (Doney et al., 2009). The decrease in carbonate ion concentrations diminishes the ocean’s ability to absorb CO_2 from the atmosphere (Sabine, 2004).

1.2.2 The Fast Carbon Cycle

The fast carbon cycle occurs on periods of a few years for the atmosphere, to decades to millennia for land and ocean reservoirs. It accounts for fluxes of CO_2 and CH_4 between the atmosphere and living organisms in the biosphere. It also includes anthropogenic activities which consume carbon that usually belong to the slow carbon cycle by burning fossil fuels. Carbon is an essential element in biology as organic molecules are made of long carbon chains. Living organisms use those as fuel by breaking the bonds between carbon atoms. Plants and plankton remove CO_2 from the atmosphere when they combine solar energy, $CO_{2,}$ and water to produce sugar and oxygen; this process is called photosynthesis. The opposite process, respiration, returns CO_2 to the atmosphere, as sugar is consumed with oxygen, which releases CO_2, water and heat (Whitmarsh and Govindjee, 1999). This process is the same whether the plant itself consumes the sugar, burns in a fire, or is eaten and excreted by animals.

The influence of the biosphere on the carbon cycle is evident during the growing season, especially in the Northern Hemisphere because of the large extent of the boreal forest, as it creates an annual minimum in atmospheric CO_2 concentrations. In the Northern Hemisphere winter, plant photosynthesis is weaker (and not necessarily shut down: Sevanto et al., 2006) and atmospheric CO_2 concentrations rise due to respiration and anthropogenic emissions until the next growing season, when increasing photosynthesis removes CO_2 from the atmosphere. This cycle is illustrated in Figure 1.2 using results from the CarbonTracker model (Peters et al., 2007), and in Figure 1.3 surface CO_2 measurements at Mauna Loa (Hawaii) from the Scripps Institute of Oceanography.

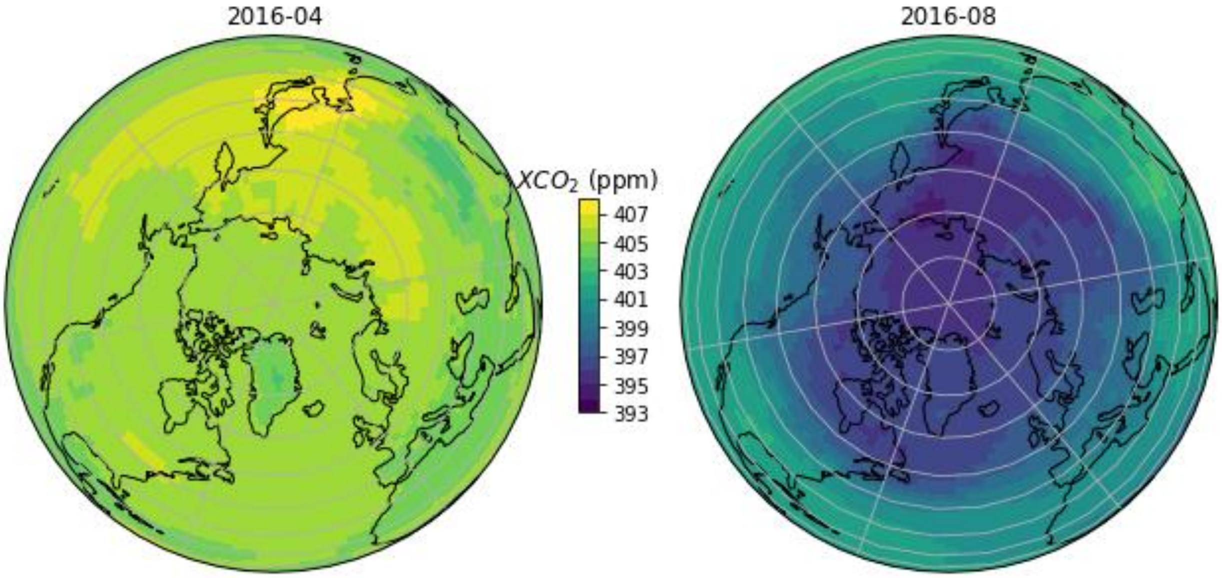

Figure 1.2: Monthly average of the column-average dry-air mole fraction of CO_2 (XCO_2) distribution over the Northern Hemisphere from CarbonTracker CT2017 data, before (left) and at the end of (right) the growing season in 2016. CarbonTracker CT2017 results were provided by the US National Oceanic and Atmospheric Administration (NOAA) Earth System Research Laboratory (ESRL), Boulder, Colorado, USA from the website at http://carbontracker.noaa.gov, last accessed on August 28th 2018.

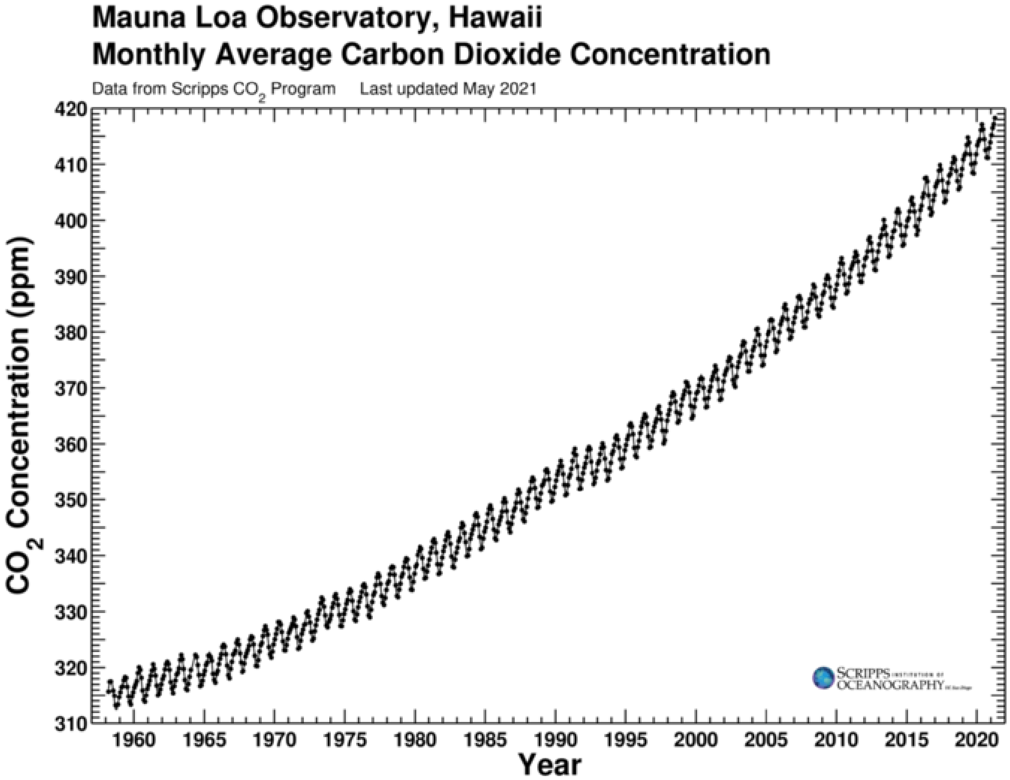

Figure 1.3: Monthly average CO_2 concentration since 1958 using surface measurements by Keeling et al. (2001) at the Mauna Loa Observatory (Hawaii), from https://scrippsco2.ucsd.edu/data/atmospheric_co2/primary_mlo_co2_record.html, last accessed on May 19th 2021.

In addition to the sawtooth seasonal cycle in atmospheric CO_2, there is diurnal variability due to the alternation of solar radiation between days and nights. While photosynthesis requires sunlight, respiration is uninterrupted, and CO_2 thus builds up at night. Photosynthesis and respiration each have global fluxes of ~120 Gt C / y, while exchanges between the atmosphere and ocean are ~80 Gt C / y (Ciais et al., 2013). In Figure 1.3, the sawtooth pattern is superimposed on an increasing trend driven by anthropogenic emissions of CO_2.

1.2.3 Changes in the Carbon Cycle

Information about the composition of the atmosphere at a given time can be trapped in ice cores for thousands of years. This offers the opportunity to investigate time series of CO_2 and temperature up to 800,000 years ago (Lüthi et al., 2008). As illustrated in Figure 1.4, there is a strong correlation (r^2=0.82) between CO_2 concentrations and temperature over the period from 800 ky to present. The Earth is regularly oscillating between ice ages and warmer periods due to shifts in its orbit that affect the amount of energy the surface receives from sunlight; this is called orbital forcing (Masson-Delmotte et al., 2013).

In more recent times, changes in the carbon cycle are due to anthropogenic emissions of greenhouse gases through land use (1.5±0.4 Gt C / y), and more importantly fossil fuel burning (9.5±0.5 Gt C / y, Friedlingstein et al., 2019). The anthropogenic emissions dwarf the natural emissions of the slow carbon cycle, as the global burning of waste gases alone is emitting CO_2 in comparable quantities to volcanoes (0.2 Gt C / y, Gerlach, 2011). Fossil fuels have taken over land use as the dominant source of emission since 1920. The longest record of atmospheric CO_2 concentrations comes from Mauna Loa (Hawaii, USA) and shows an increase of surface CO_2 from 277 to 417 ppm between 1750 and 2020. Since 2001, the globally averaged surface CO_2 has increased at a rate of ~2 ppm / y (varying from ~1.5 to ~3 ppm / y); fossil fuel combustion is the primary source of those increases (Hartmann et al., 2013).

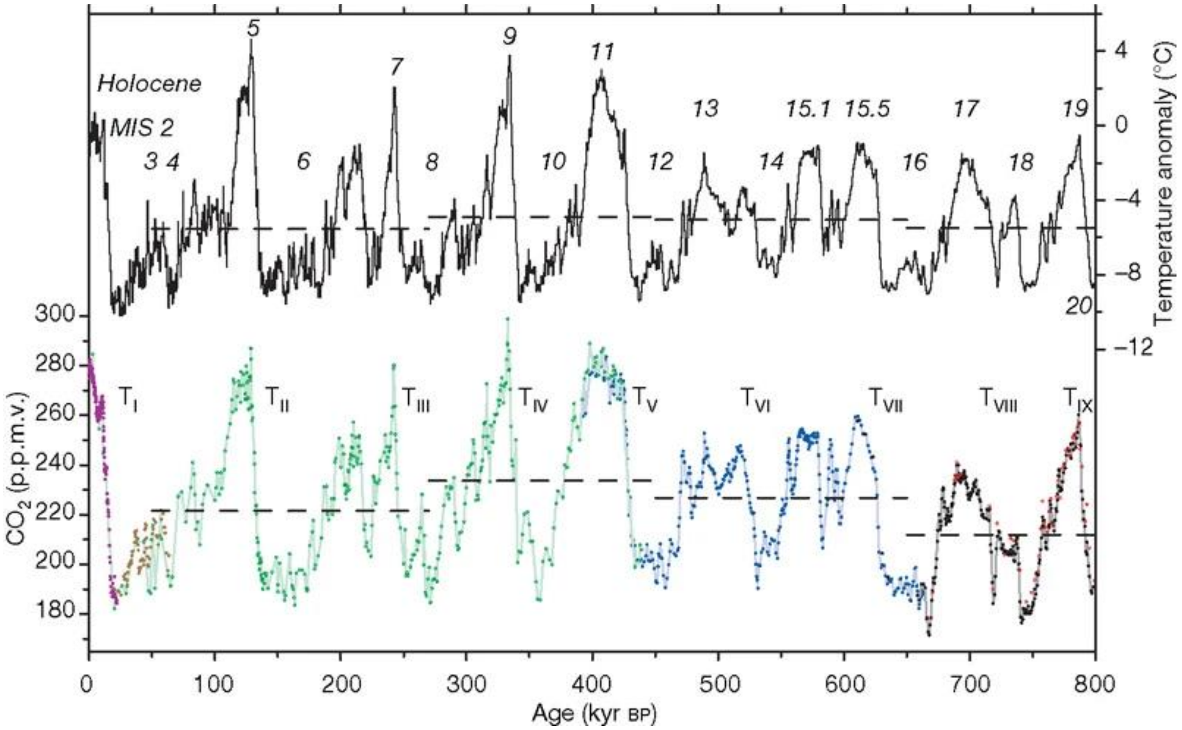

Figure 1.4: CO_2 records and EPICA Dome C (Antarctica) temperature anomaly (relative to the mean temperature of the last millennium) over the past 800 ky before present (BP), from Lüthi et al. (2008). Arabic numbers indicate marine isotope stages and letters T with Roman numbers mark glacial terminations. Horizontal lines indicate the mean values of temperature and CO_2. Colours represent different sample sites and analyses.

Glaciation periods do not only depend on orbital forcing; they are also linked to CO_2 concentrations. If concentrations remain above 300 ppm, models do not predict a glaciation period for the next 50,000 years (Masson-Delmotte et al., 2013). Figure 1.5 shows the impact of anthropogenic emissions of CO_2 on carbon exchanges between land, atmosphere and ocean. Both the land and ocean sinks have grown together with atmospheric concentrations of CO_2; they removed 55% of the total anthropogenic emissions each year between 1958 and 2011 (Ciais et al., 2013). Increasing atmospheric CO_2 concentrations means increasing CO_2 partial pressure which leads to a net flux of CO_2 from the air to the ocean. In 2019, the ocean carbon sink was 2.5±0.6 Gt C / y (Friedlingstein et al., 2019). Meanwhile on land, increasing CO_2 concentrations have a fertilizing effect on vegetation. The response of leaf photosynthesis and respiration to CO_2 and temperature changes is still an active area of research (Dusenge et al., 2019). Plant growth is enhanced if there are no limitations on other sources of nutrients like nitrogen, phosphorous and water. The land carbon sink is also sensitive to climate variability, variations in temperature, precipitation, and exposure to solar radiation.

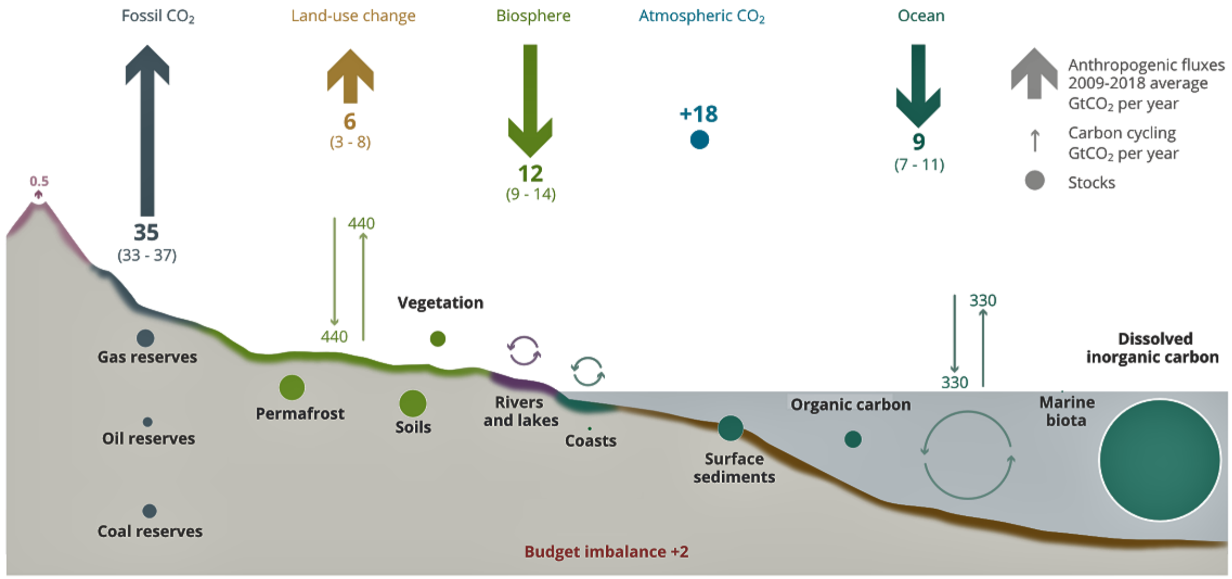

©ⓘGlobal Carbon Project

Figure 1.5: Representation of the impact of anthropogenic activities on the global carbon cycle, averaged globally for 2009-2018, from Friedlingstein et al. (2019).

The Arctic represents up to 25% of the global land carbon sink as the tundra and boreal forests sequester CO_2 (McGuire et al., 2012). In 2014, the Arctic Ocean accounted for 10-12% of the global ocean CO_2 sink even though it only represents 3% of the surface area of all oceans (MacGilchrist et al., 2014). The Arctic thus has a strong influence on the carbon cycle and it is a region that responds strongly to climate change. Mean surface temperatures have increased twice as fast in the Arctic as in the rest of the world, due to Arctic amplification, whereby positive feedbacks enhance any temperature increases in the Arctic (Cohen et al., 2014). As global temperatures rise from anthropogenic emissions of greenhouse gases, sea ice and snow cover are reduced. This unveils darker ocean or land surfaces that absorb more solar radiation, resulting in more warming (Pistone et al., 2014). The warming also causes the atmosphere to become wetter, leading to more warming as water vapour is a strong greenhouse gas (Myhre et al., 2013). Although the ocean carbon sink has increased together with increases in CO_2 emissions since 1970, with increasing surface temperatures the ocean surface tends to stratify (the downward-increasing gradient of density is strengthened) and thus becomes more stagnant. If surface waters continue to warm and the ocean continues to stratify this will reduce the ability of the ocean to take CO_2 out of the atmosphere as the weaker circulation will limit the replenishment of surface waters with carbon-depleted water (Bindoff et al., 2019).

The Arctic is also a region that contains large reservoirs of carbon that do not currently contribute significantly to the carbon cycle but are susceptible to change under a warming climate. The most vulnerable of these reservoirs is permafrost, soil that remains at temperatures below freezing for at least two consecutive years. The permafrost reservoir holds 1400-1850 Gt C (Schuur et al., 2008, 2015; McGuire et al., 2009; Tarnocai et al., 2009; Hugelius et al., 2014). Both CO_2 and CH_4 can be released from warming soil and thawing permafrost. Decomposition of organic matter in dry aerobic soils lead to emissions of CO_2, while both CO_2 and CH_4 are emitted in wet anaerobic soils. In a permafrost carbon feedback, thawing permafrost would stimulate decomposition and ecosystem respiration, releasing greenhouse gases and contributing to further warming (Grosse et al., 2011; Belshe et al., 2013; Schuur et al., 2015; Schoolmeester et al., 2019).

1.3 Measurement Techniques

To mitigate global warming and climate change, the 2015 UNFCCC Conference of the Parties (COP-21), in Paris, set a target goal of limiting the global mean temperature rise to well below 2°C, and preferably below 1.5°C above pre-industrial levels (UNFCCC, 2015). To achieve this goal, countries need to commit to policies to monitor and reduce their emissions of greenhouse gases. Even then, the goal of 1.5°C is so challenging that few models even consider it (Victor et al., 2014). Even if all emissions stopped, the carbon already in the atmosphere could lead to a temperature rise of up to 1.5°C. This policy target is rather optimistic with respect to the different Representative Concentrations Pathways (RCPs). The most optimistic scenario (RCP3) involves significant emission reductions by 2020, while current emissions are already above the most pessimistic one (RCP8.5), which leads to global mean temperature increases of 4.2-5°C by 2100 (Peters et al., 2013). Liu and Raftery (2021) assessed the probability of staying below 2°C by 2100 to only 5% with current engagement in emission reductions. In any case, reduction plans require a capacity to estimate sources and sinks of greenhouse gases and to better understand the carbon cycle to make predictions regarding future climate change. Measurements of greenhouse gases are critical to further our understanding of the global carbon cycle, inform policies and monitor their effectiveness.

Global and regional emission budgets are built using two approaches. The bottom-up approach relies on extrapolating samples of measured emissions (natural sources and sinks) and inventory-based data (anthropogenic sources) to regional and global scales. The top-down approach combines measurements of atmospheric concentrations with transport and chemistry models to infer sources and sinks (inversions). It is difficult to partition separate sources with the top-down approach, but it provides constraints on regional scales and can help determine if emission estimates from the bottom-up approach are over or underestimated (Kirschke et al., 2013). Greenhouse gases such as CH_4 and CO_2 are monitored through several networks using various instruments. However, the Arctic is poorly sampled, and the lack of observation coverage introduces biases that make the estimates of carbon sources and sinks in this region uncertain (Ciais et al., 2014; Schimel et al., 2015).

1.3.1 In-situ Measurements of CO_2

Local surface fluxes of CO_2 are derived from trace gas concentration and wind measurements on flux towers, using the eddy covariance method (Foken et al., 2012). FLUXNET is a major global network of such measurements with more than 500 sites, but especially concentrated in Europe and North America. The FLUXNET 2016 dataset includes 20 sites north of 60°N (FLUXNET, 2016).

Air is sampled either continuously with in-situ measurements or with discrete glass flask samples to be analyzed in laboratories. There are several possible sampling platforms, including towers on land, and ships over oceans for surface air sampling. The vertical range of in-situ measurements can be extended several kilometers when air is sampled on aircraft flights. The NOAA Earth System Research Laboratory (ESRL) Global Monitoring Division collects carbon cycle-relevant gases from a global network of 169 observation sites, including 13 Arctic sites, two of which are Canadian sites run by Environment and Climate Change Canada (ECCC): Alert and Eureka. ECCC also contributes measurements from a network of 11 sites to the World Data Centre for Greenhouse Gases. These observations are used to build data products such as GLOBALVIEW, to enhance their spatial and temporal distributions (Cooperative Global Atmospheric Data Integration Project, 2019, 2020), or the CarbonTracker model to keep track of sources and sinks of carbon (Peters et al., 2007). Although very precise, the spatial and temporal coverage of in-situ measurements is limited. Spatial coverage is limited over deserts, tropical regions, oceans and the Arctic (Peylin et al., 2013). The temporal coverage is also limited for aircraft and ship campaigns.

AirCore measurements are a recent alternative to aircraft profiles. AirCore is a sampling system that consists of a long, coiled stainless-steel tube initially filled with a dry calibrated gas (Karion et al., 2010). As a balloon carries it aloft, the fill gas evacuates. When the AirCore descends from the stratosphere, ambient air enters the tube through the open end. The tube typically closes a few hundred meters above the surface, and after landing it is retrieved for later analysis in a laboratory. The sample is then pumped out of the tube and passed through a continuous gas analyzer. The first gases to come out were the last to enter, and vice versa, allowing the preserved atmospheric trace gas concentration profiles to be derived. This method has a precision and accuracy within 0.07 ppm for CO_2 concentrations in laboratory tests, and standard deviations of differences of 0.3 ppm when compared to flask samples from aircraft flights (Karion et al., 2010). The balloons reach about 25 km altitude, and therefore sample 98% of the mass of the atmosphere.

1.3.2 Remote Sensing Measurements of CO_2

Greenhouse gases have been, and continue to be, observed from space by several satellites. This section presents a short summary of the primary nadir-viewing satellites that measure CO_2 columns. Measurements were made by the Scanning Imaging Absorption Spectrometer for Atmospheric Cartography (SCIAMACHY, Bovensmann et al., 1999; Buchwitz et al., 2005a, 2005b; Schneising et al., 2011; Heymann et al., 2015) from 2002 to 2012, and by the Tropospheric Emission Spectrometer (TES, Beer, 2006; Kulawik et al., 2010, 2013) from 2004 to 2018. Currently in orbit are the Atmospheric Infrared Sounder (AIRS, Aumann et al., 2003; Chevallier et al., 2005; Maddy et al., 2008; Boisvert and Stroeve, 2015), the Greenhouse Gases Observing Satellite (GOSAT, Kuze et al., 2009, 2016; Lindqvist et al., 2015), the Orbiting Carbon Observatory-2 (OCO-2, Crisp, 2008, 2015), TanSat (Liu et al., 2013; Yang et al., 2018), and the more recently launched GOSAT-2 (Nakajima et al., 2012; Suto et al., 2021), and OCO-3 (Eldering et al., 2019; Taylor et al., 2020; Kiel et al., 2021). AIRS and TES operate in the thermal infrared (3-15 µm) while the other satellite instruments mentioned operate in the near-infrared/short-wave infrared (0.75-3 µm). AIRS and TES measure emission spectra while the other instruments measure absorption spectra. All of these missions operate in Low Earth Orbit (LEO) at altitudes less than 2000 km and synchronized with the sun, such that they can measure continuously. These sun-synchronous orbits result in observations sampled along tracks and take days or weeks to accomplish global coverage. Satellite observations have the potential to provide global spatial coverage but in reality, LEO missions provide global sampling as it takes them several days to revisit a given location. The European Space Agency (ESA) is considering using a constellation of at least three LEO satellites for the CO2 Monitoring Mission (CO2M) that would accomplish global land coverage within 5 days (Sierk et al., 2019).

Geostationary (GEO) satellites, like the Geostationary Carbon Cycle Observatory (GeoCarb, O'Brien et al., 2016; Moore III et al., 2018) planned for launch in 2022 over North America, can provide high spatial and temporal sampling of a given region. Such measurements can be used to help partition natural and anthropogenic emissions of CO_2 and CH_4. GeoCarb will be the first GEO satellite dedicated to measure both CO_2 and CH_4. The instrument will scan in the East-West direction with a North-South ground track of ~25° in latitude, spanning for example from Mexico to southern Canada (Moore III et al., 2018). A GEO orbit must be close to the equator, it is not possible to put a satellite in GEO orbit above the poles. Because of high viewing angles, GEO satellites cannot observe high latitudes; GeoCarb will be able to observe regions between 50°S and 50°N, from the southern tip of South America to the south of Hudson Bay.

Retrievals of trace gas concentrations over high albedo surfaces, like the snow- and ice-covered regions of the Arctic, can prove challenging (Merrelli et al., 2015). Satellite observations are validated by ground-based networks such as the Total Carbon Column Observing Network TCCON (Wunch et al., 2011, 2017) or the Infrared Working Group of the Network for the Detection of Atmospheric Composition Change (NDACC-IRWG). The accuracy and precision of observations from surface networks must keep improving in parallel with those of satellite observations (Basu et al., 2011, 2018).

1.3.3 Inversions of Surface Fluxes from Atmospheric Measurements

Total column measurements are representative of large-scale (continental to hemispheric) regions (Keppel-Aleks et al., 2011) because the sensitivity of the total column measurements is largest in the free troposphere. This is because air can move along latitudinal bands, and from the surface to the free troposphere in weeks. The timescales of horizontal and vertical transport are illustrated in Figure 1.6. Panel (a) shows the timescales of horizontal transport; air moves faster from West to East than it does from low to high latitudes. Panel (b) shows the timescales of vertical transport; it takes 1-2 days for surface air to reach the free troposphere, a week to reach the free troposphere, a month to reach the tropopause, and years to reach the stratosphere, while air in the stratosphere descends to the troposphere in mid-latitudes and at the poles after 1-2 years (Jacob, 1999). Thus, total column measurements, generally more sensitive to the free troposphere, are influenced by air which traveled for about a month and could originate from anywhere in the same hemisphere. To capture surface fluxes from total column measurements, inversions must be performed on a global domain (Keppel-Aleks et al., 2011). Obtaining vertical information in different layers, such as the planetary boundary layer (PBL), from the surface to 1-3 km, and the free troposphere would provide more information on regional surface fluxes.

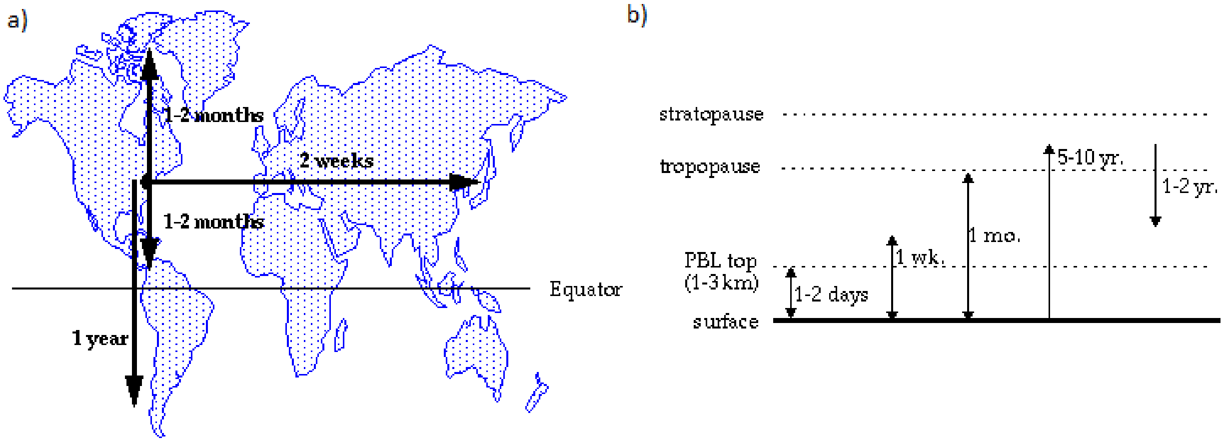

Figure 1.6: Timescales of (a) horizontal transport, and (b) vertical transport. Figures taken from Jacob (1999).

A yearly global carbon budget has been produced by the Global Carbon Project since 2012 (Le Quéré et al., 2013, 2014, 2015a, b, 2016, 2018a, b; Friedlingstein et al., 2019). It presents current knowledge of CO_2 and CH_4 emissions to inform greenhouse gas reduction policies. The project uses ensembles of models and inventories, as well as CO_2 surface measurements, to estimate different components of the global emissions of CO_2. It also uses CO_2 fluxes inverted from various networks of surface measurements as a semi-independent validation tool for these estimates. And since 2014, it makes mention of the potential of inversions using space-based measurements of total column CO_2 to provide additional constraints on source and sinks of CO_2. However, greenhouse gases measured by remote sensing are still not used in these estimates of surface fluxes.

CO_2 fluxes obtained from inversions assimilating OCO-2 observations over land are now becoming as reliable as those obtained from inversions using surface air sampling networks (Chevallier et al., 2019; Crowell et al., 2019). Measurements of the column-averaged dry-air mole fraction of CO_2 (XCO_2) by satellites can be made with spatial coverage that cannot be practically achieved using ground-based instrumentation. Inversions using CO_2 total columns over land are less sensitive to transport errors than inversions using surface CO_2 (Rayner and O'Brien, 2001; Basu et al., 2018), which requires accurate modeling of the planetary boundary layer height and vertical mixing, which are a major source of uncertainty in inversions (Parazoo et al., 2012). However, even small (< 1 ppm) spatially coherent biases in column measurements can have a large impact on inversions assimilating XCO_2 (Chevallier et al., 2007), and efforts must be made to characterize and minimize such biases (O'Dell et al., 2018; Kiel et al., 2019).

1.4 Motivation and Objectives

TCCON is a ground-based network of high-resolution (0.02 cm^{-1}) ground-based Fourier transform Infrared (FTIR) spectrometers that record Near Infrared (NIR, 0.75-3 μm) solar absorption spectra. A map of TCCON sites is shown in Figure 1.7. GGG is the software used by TCCON to transform measured interferograms into spectra, and to retrieve trace gas concentrations from those spectra. Central to this process is the Gas Fit (GFIT) program, a non-linear least-squares spectral fitting algorithm. A forward model computes an atmospheric transmittance spectrum using a priori knowledge of atmospheric conditions. An inverse method then compares the measured spectrum with the resulting calculation and adjusts the retrieved parameters to obtain the best fit. In GFIT, these parameters include volume mixing ratio scaling factors (VSF) for the different fitted gases. GFIT performs profile scaling retrievals: for each retrieved trace gas, a single VSF scales the a priori concentration profile at all altitude levels simultaneously and therefore the retrieved profile shape is unchanged from the a priori profile shape. Scaling retrievals do not require strong constraints on a priori concentration uncertainties. In GFIT, the a priori uncertainty on the VSF of the main target gas in a spectral window is 10^8 %, and XCO_2 can be retrieved with a 1-sigma precision of 0.4 ppm (Wunch et al., 2010). GFIT minimizes the spectral fit residuals: the difference between the measured and calculated spectra. The measurement uncertainty is not required to be accurately known; all retrievals from TCCON CO_2 windows use an assumed signal-to-noise ratio (SNR) of ~200. It has only a small effect on the result because for CO_2, the absorption line depths far exceed the measurement noise.

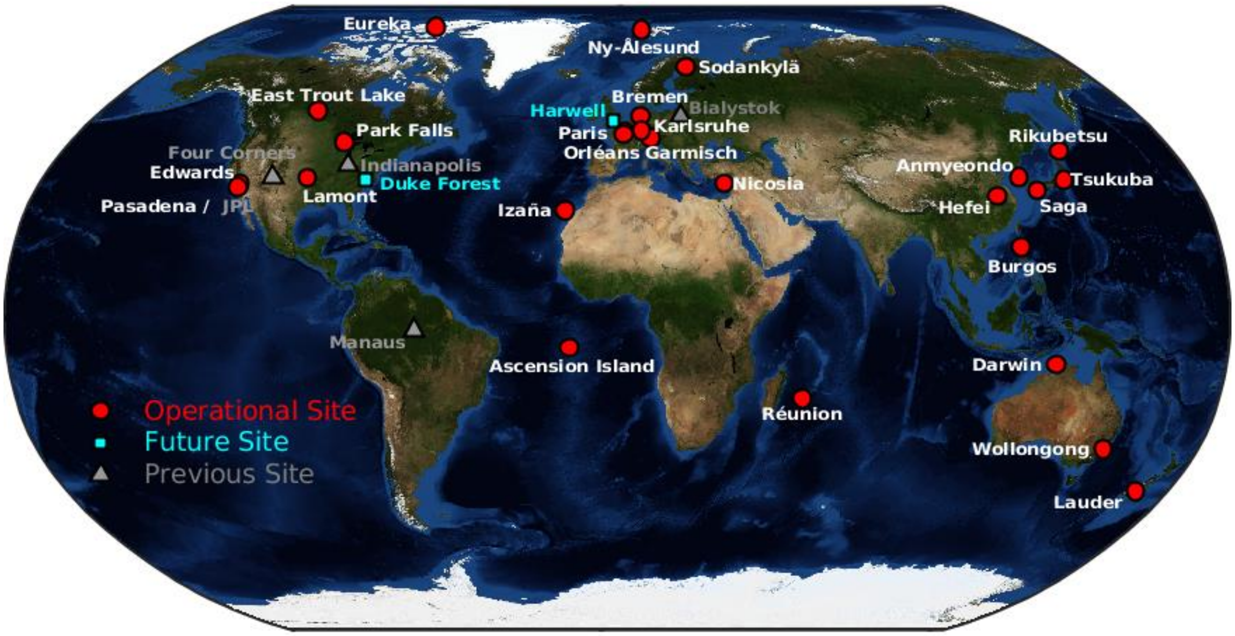

Figure 1.7: Map of TCCON sites, from https://tccondata.org/ on January 28th 2021.

Even though TCCON XCO_2 observations are precise, they lack information about the vertical distribution of CO_2 in the atmosphere, which is of interest for the validation of satellite measurements and model simulations, and could improve the ability of flux inversions to resolve regional scales (Keppel-Aleks et al., 2011). The most precise and accurate source of information on CO_2 profiles comes from measurements that can directly sample air at different altitudes such as from balloons or aircraft, but these measurements are sparse in space and time. Aircraft profiles are used as validation tools for inversion studies (Stephens et al., 2007), which requires them to remain independent from the inversion systems (Chevallier et al., 2019). Obtaining reliable CO_2 profile information from ground-based direct sun measurements could add a new source of data for verification and to assimilate in inversions. Vertical information derived from ground-based absorption spectra cannot be as accurate as aircraft profiles, and would also be spatially sparse, but it would have a high temporal sampling.

Eureka is the northernmost TCCON site at 80.05°N on Ellesmere Island (Nunavut, Canada). A Bruker 125HR spectrometer was installed at the Polar Environment Atmospheric Research Laboratory (PEARL) in 2006 when it started collecting solar absorption spectra in the Mid-Infrared (MIR) for the Network for the Detection of Atmospheric Composition Change (NDACC) (Batchelor et al., 2009). Since 2010, the spectrometer also measures in the NIR for TCCON.

PEARL is one of only a few Arctic sites equipped to collect data for satellite validation. Ground-based measurements in often snow-covered regions like the Arctic are particularly important for satellite validation programs since retrievals from space-based instruments over snow-covered surfaces are challenging while ground-based observations are not affected by surface properties.

To address the lack of coverage of space-based measurements over the Arctic regions and to further our understanding of the Arctic carbon cycle, Environment and Climate Change Canada (ECCC) and the Canadian Space Agency (CSA) are proposing the Atmospheric Imaging Mission for Northern Regions (AIM-North, Nassar et al., 2019). The mission plans to use a pair of satellites in a Highly Elliptical Orbit (HEO) to obtain a high density of measurements between ~40°N and 80°N. This thesis includes a study contributing to the "Phase 0" of the AIM-North mission by demonstrating an algorithm that could be used to retrieve XCO_2, XCH_4, and XCO from the satellite's observations and by conducting sensitivity studies with simulated observations to assess how well these quantities could be retrieved with given instrument characteristics.

The scientific goal of this thesis is to improve CO_2 retrievals from ground-based NIR solar absorption spectra and improve greenhouse gas measurements in the Arctic with these specific objectives:

1. Maintain and improve the record of NIR measurements at Eureka.
2. Develop and assess CO_2 profile retrievals from ground-based NIR solar absorption spectra.
3. Contribute to the AIM-North mission with simulations of CO_2, CH_4, and CO retrievals to inform future instrument design, and to meet the mission precision and accuracy requirements.

1.5 Outline and Contributions

Chapter 1 of this thesis presented an introduction to greenhouse gases and the carbon cycle and provided a motivation for improving remote sensing measurements of CO_2 and measurements in the Arctic region specifically. Some of this background material was included in (Strong et al., 2020a).

In Chapter 2, the PEARL Bruker 125HR will be described, along with the principles of Fourier Transform Spectroscopy. Between 2015 and 2020, I was responsible for acquiring NIR solar absorption spectra with the PEARL 125HR, on site during the Canadian Arctic ACE/OSIRIS

Validation Campaigns of 2015-2019, and remotely when on-site personnel were not available to operate the instrument. During these campaigns, I also performed routine maintenance on the instrument together with fellow PhD students Dan Weaver (2015), Erik Lutsch (2016-2017), and Tyler Wizenberg (2018-2019) who were each responsible for the acquisition of MIR spectra for NDACC. Since the 2016 campaign, we have re-aligned the instrument ourselves with the help of PEARL Site Manager Pierre Fogal. In summer 2015, I accompanied TCCON partner Dietrich Feist and Pierre Fogal to assist in replacing the metrology laser of the PEARL 125HR. Outside of field campaigns, the spectrometer is in the care of operators from the Canadian Network for the Detection of Atmospheric Change (CANDAC). Remote access to the spectrometer and suntracker computers was made possible by Dan Weaver and PhD student Joseph Mendonca in 2014. Jonathan Franklin (Dalhousie University, now Harvard University) developed the control software for the suntracker we use for the PEARL 125HR and continues to help us with any new tracking issues. I implemented in the Eureka processing code a methodology Dr. Franklin developed to correct for tracker mis-pointing by applying corrections to solar zenith angles. The alignment procedure applied during the 2016 and 2019 field campaigns is also described in Chapter 2, following instructions developed by John Robinson from the New Zealand National Institute of Water and Atmospheric Research (NIWA). Orfeo Colebatch (UofT) assembled the alignment kit that we used successfully on site.

Chapter 3 describes how atmospheric trace gases are retrieved from solar absorption spectra and how to properly compare trace gas measurements from different instruments.

Chapter 4 presents the NIR measurements collected at Eureka during this PhD project, and a study using TCCON data to validate simulations of CO_2 from a coupled meteorological and transport model developed at ECCC. Operation of the PEARL 125HR was performed by Joseph Mendonca, Dan Weaver, Erik Lutsch, Tyler Wizenberg, and me. I performed the retrievals on the NIR measurements for TCCON and developed software to generate the necessary auxiliary data files needed for the data processing. Since 2015, several issues were identified with the retrieval setup or the surface pressure measurements, which led to new TCCON data revisions for Eureka: R1 (Strong et al., 2016), R2 (Strong et al., 2017), and R3 (Strong et al., 2019). These issues and how they were addressed are presented in this chapter. I also developed software to automate several steps of the Eureka NIR data processing for TCCON. For the validation study of the ECCC model simulations with TCCON data, Saroja Polavarpu and Michael Neish (ECCC) provided data from the model and the study was included in Polavarapu et al. (2016).

In Chapter 5, work to improve CO_2 profile retrievals from ground-based NIR spectra is presented. This follows on a study started by Connor et al. (2016) which implemented GFIT2, a profile retrieval algorithm, into GGG. I adapted the algorithm to work with the latest version of GGG (GGG2020), which includes work from Joseph Mendonca that improved the line shapes, reducing the spectral residuals in several NIR spectral windows. I tested GFIT2 with the improved algorithm and developed a sensitivity study with synthetic spectra to assess the largest sources of uncertainties in CO_2 profile retrievals. I used AirCore profiles as “truth” to assess how well CO_2 profile retrievals from real spectra compare to true profiles. Brian Connor (B.C. Consulting Ltd.) provided guidance on the use of GFIT2 and on which avenues were worth exploring for its improvement. Geoffrey Toon (Jet Propulsion Laboratory, JPL) is the author of GGG and provided feedback and answers to questions on the retrieval algorithm. Josh Laughner (California Institute of Technology, Caltech) developed the software that generates the new a priori trace gas profiles in GGG2020 and provided feedback. I developed the software that generates the new a priori auxiliary profiles in GGG2020, with contributions from Josh Laughner. Colm Sweeney and Bianca Baier (NOAA) provided AirCore data and feedback. Sébastien Biraud (Lawrence Berkley National Laboratory) provided surface measurements at the Lamont TCCON site. Coleen Roehl and Paul Wennberg (Caltech) provided NIR spectra from the Lamont TCCON site processed with GGG2020. The work in Chapter 5 is described in Roche et al. (2021).

In Chapter 6, a contribution to “Phase 0” of the AIM-North mission is presented. The objective of this work was to demonstrate a retrieval algorithm that could be used to retrieve XCO_2, XCH_4, and XCO with given instrument characteristics. The ReFRACtor (https://github.com/ReFRACtor) algorithm used to retrieve trace gases from OCO-2 observations was adapted by Joseph Mendonca and me to perform simulations using the AIM-North greenhouse gas instrument designs. I developed software to run ensembles of retrievals on simulated observations and used it to assess the impact of specific perturbations on the retrieval precision and accuracy. Instrument characteristics were provided by engineers from ABB and Airbus. This work was included in a report to CSA (Strong et al., 2020b). Finally, Chapter 7 presents a summary of the conclusions of this thesis and outlines suggestions for future work.

Chapter 2
Instrumentation

This chapter explains how solar spectra are obtained from Fourier Transform Spectrometers (FTSs). Section 2.1 describes the instrument and the theory of Fourier transform spectroscopy. Section 2.2 presents results from the monitoring of the instrument alignment at Eureka. Section 2.3 presents the steps of the alignment procedure that were applied during the 2018 Canadian Arctic ACE/OSIRIS Validation Campaign. Section 2.4 presents the suntracker system used to record solar spectra. Finally, Sect. 2.5 describes ancillary instruments.

Chapter 3 describes how atmospheric trace gas concentrations can be retrieved from the spectra collected by the FTS, including details of the TCCON retrieval algorithm and of the theory on which it relies. Then, Chapter 4 describes the spectra collected at PEARL during this PhD, how to handle auxiliary measurements required for their processing, and a method to address issues with the pointing accuracy of the solar tracker.

2.1 The PEARL Bruker 125HR and Fourier Transform Spectroscopy

To meet the observational requirements of TCCON as presented in Table 2.1, the primary instrument used by the network is the Bruker Optics GmbH 125HR FTS, illustrated in Figure 2.1.

Table 2.1: TCCON requirements.

Parameter	Value
Wavenumber range	4000-9000 cm^{-1}
Maximum optical path difference	45 cm
Suntracker pointing accuracy	1 mrad
Surface pressure accuracy	0.3 hPa
Surface temperature accuracy	1 K
Timing of the zero-path-difference crossing time for the interferogram	1 s
Laser sampling error	0.00024 of the sample step
Routine monitoring of instrument line shape	monthly
Modulation efficiency	0.95-1.05 with precision of 0.02

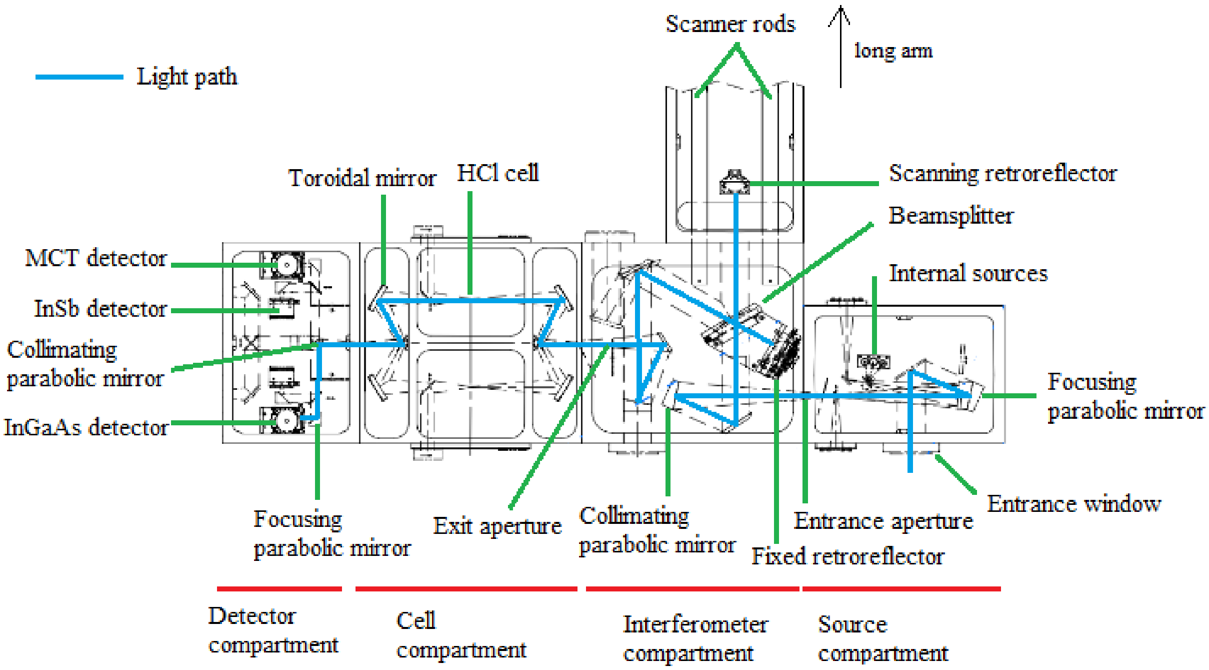

Figure 2.1: Schematic of the PEARL 125HR spectrometer adapted from the Bruker 125HR manual to show the light path through the spectrometer for NIR measurements (blue lines), and with the main components labelled (green lines). The different compartments of the instrument are labelled below the red lines that show the extent of each compartment.

The instrument is a Michelson interferometer (Michelson and Morley, 1887) with a mobile mirror. It uses a beamsplitter to split an input light beam in two and then measures the intensity of the recombined beams as the mobile mirror moves in the long arm of the interferometer. When recombined, the two light beams interfere because of the path length difference introduced by the mobile mirror. A 633 nm HeNe laser is split in the same way; and as it is a nearly monochromatic source, a detector measuring its recombined beam will measure alternating maximum and minimum of intensity due to constructive and destructive interference. When the instrument detects a zero-crossing in the laser interference pattern it samples and records the infrared light. This mechanism allows precise sampling at equal distance intervals as the mobile mirror moves and provides the instrument with a free spectral range of 15798 cm^{-1}. The intensity as a function of position of the mobile mirror is called an interferogram. A spectrum, with intensity as a function of wavenumber, can be obtained from the inverse Fourier transform of the interferogram. The following discussion will assume a perfectly symmetric interferogram. In practice, interferograms are not perfectly symmetric and thus their Fourier transform has a non-zero imaginary part. A method to address this issue is presented in Davis et al. (2001b).

The interferogram intensity dI measured at an optical path difference (OPD) x can be expressed as a function of the spectrum intensity B over the spectral interval $d\sigma$ and at wavenumber σ (Davis et al., 2001d):

$$dI(x) = B(\sigma)d\sigma\cos(2\pi\sigma x)\,. \tag{2.1}$$

The integral over all wavenumbers yields the interferogram intensity at the path difference x:

$$I(x) = \int_0^\infty B(\sigma)\cos(2\pi\sigma x)d\sigma\,. \tag{2.2}$$

And the spectrum can be obtained as the inverse Fourier transform of the interferogram:

$$B(\sigma) = \int_0^\infty I(x)\cos(2\pi\sigma x)dx\,. \tag{2.3}$$

In the case of monochromatic radiation with unit amplitude at a given wavenumber σ_o, the recording of the interferogram would be perfect if we could measure it continuously up to an infinite OPD. The ideal (continuous and infinite) interferogram would be $I_{ideal}(x) = \cos(2\pi\sigma_o x)$, with the monochromatic spectrum represented by a δ-function $B(\sigma) = \delta(\sigma - \sigma_o)$.

However, the ideal interferogram cannot be measured. It is instead sampled at discrete equal distance intervals, and it can only be measured up to a finite maximum OPD. The act of sampling at fixed intervals Δx is equivalent to multiplying the interferogram with a Dirac comb function $III\left(\frac{x}{\Delta x}\right)$ (equal to 1 where x is an integer multiple of Δx, and 0 elsewhere), or convolving the spectrum with a Dirac comb with frequency $\Delta\sigma = \frac{1}{\Delta x}$. For the spectrum, this results in multiple copies repeated every $\Delta\sigma$. If the spectrum is not sampled with a frequency at least twice the highest frequency to be observed, these replicas can overlap and cause artifacts in the spectrum. This is a sampling theorem that requires sampling a cosine wave at least twice per wavelength to be able to accurately measure its frequency, and the minimal sampling frequency is called the Nyquist frequency. The interferogram is sampled exactly twice per laser wavelength with the sampling triggered on each (rising and descending) zero-crossing of the laser interference pattern.

The act of measuring up to a finite maximum path difference L is equivalent to multiplying the infinite interferogram with a rectangular function (Davis et al., 2001b):

$$I_{measured}(x) = I_{ideal}(x) \times rect\left(\frac{x}{2L}\right) \tag{2.4}$$

or to convolving the spectrum with a sine cardinal (sinc) function:

$$B_{measured}(\sigma) = B_{ideal}(\sigma) * 2Lsinc(2L\sigma) \tag{2.5}$$

with $sinc$ the normalized sine cardinal function such that $sinc(x) = \frac{\sin(\pi x)}{\pi x}$.

Thus, the physical limitation of making the measurement up to a finite maximum path length would turn a purely monochromatic absorption line into a broad sine cardinal shaped line with unphysical negative intensities in the side lobes. The presence of these side lobes is called “ringing”. The function that convolves the spectrum is called the instrument function:

$$O(\sigma) = 2Lsinc(2L\sigma). \tag{2.6}$$

The instrument function is shown in Figure 2.2. Only the main central peak corresponds to a real spectral line. The side lobes are unphysical and can become problematic when they overlap with a separate, weaker spectral line. To minimize this problem, the interferogram can be multiplied by a function decreasing with OPD and reaching zero at maximum OPD, instead of a rectangular function. However, doing so will change the instrument function. For example, multiplying the interferogram by a triangular function is equivalent to convolving the spectrum with a squared cardinal sine function, which has a weaker and broader central peak and smaller side lobes without negative frequencies. The act of multiplying the interferogram by such a function is called apodization. Apodization reduces the amplitude of side lobes at the cost of a weaker and wider central peak. Different functions that address this tradeoff are presented in Naylor and Tahic (2007).

The criterion that defines two lines as resolved is the Rayleigh criterion, originally defined to characterize two lines with sinc-squared shapes as distinct. Two lines are distinct when the first zero of a line coincides with the center of the other line. For the rectangular apodization, this corresponds to a separation of $\frac{1}{2L}$ as in Figure 2.2, and of $\frac{0.9}{L}$ for the triangular apodization as shown in Figure 2.3. When taking measurements with the Bruker 125HR via its interface software OPUS, the definition used when specifying the resolution is $\frac{0.9}{L}$. The NIR spectra recorded by TCCON use a maximum OPD of 45 cm. Thus, the resolution given to OPUS for the instrument to measure up to $L = 45\ cm$ is 0.02 cm^{-1}. However, TCCON interferograms are not apodized with a triangular function and the resolution of its spectra is $\frac{1}{2L} = \frac{1}{90} = 0.0111 \ldots cm^{-1}$. The resolution of $\frac{1}{2L}$ is often presented as an intrinsic characteristic of the instrument, but it comes from an arbitrary definition for two lines to be separated. For example, the resolution of TCCON spectra if often stated to be 0.02 cm^{-1}, which corresponds to a criterion for two lines to be completely separated: the first zero of a line coincides with the first zero of the other line. The most unambiguous information to report is the maximum OPD, together with information on which apodization function is applied, if any.

The number of points N in an interferogram measured up to L will be:

$$N = 2L\sigma_{max}. \tag{2.7}$$

When sampling is based on a 633 nm HeNe laser, $\sigma_{max} = 15798\ cm^{-1}$ and $L = 45\ cm$, so $N = 1421820$ points. In practice, trailing zeros are added to the measured interferogram until the number of points is equal to the nearest power of 2 ($N = 2^m$) in order to transform it using the Fast Fourier Transform (FFT) algorithm of Cooley and Tukey (1965): this is called zero-filling. In our case $N = 2^{21}$ and the point spacing in the spectrum obtained after the FFT is $\frac{\sigma_{max}}{2^{21}} \approx 0.007533\ cm^{-1}$. This spectral point spacing being smaller than the resolution does not mean that zero-filling adds more information to the measurement. Zero-filling the interferogram is equivalent to applying a sinc-interpolation to the spectrum. The resolution of the spectrum remains $\frac{1}{2L}$ after zero-filling.

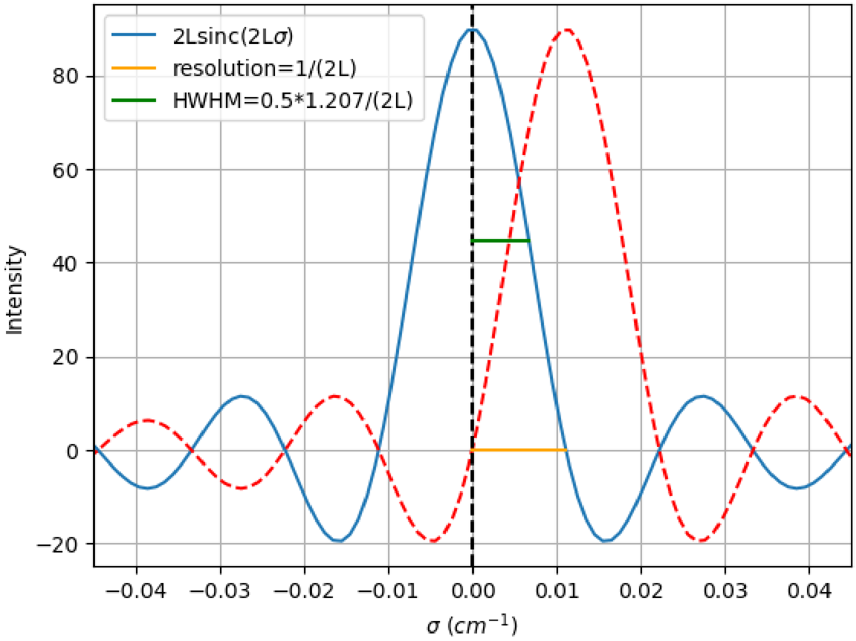

Figure 2.2: Instrument function (blue) for a maximum OPD (L) of 45 cm. The resolution (orange) and half width at half maximum (green) are also shown. The red dashed line shows the instrument function shifted by one resolution element.

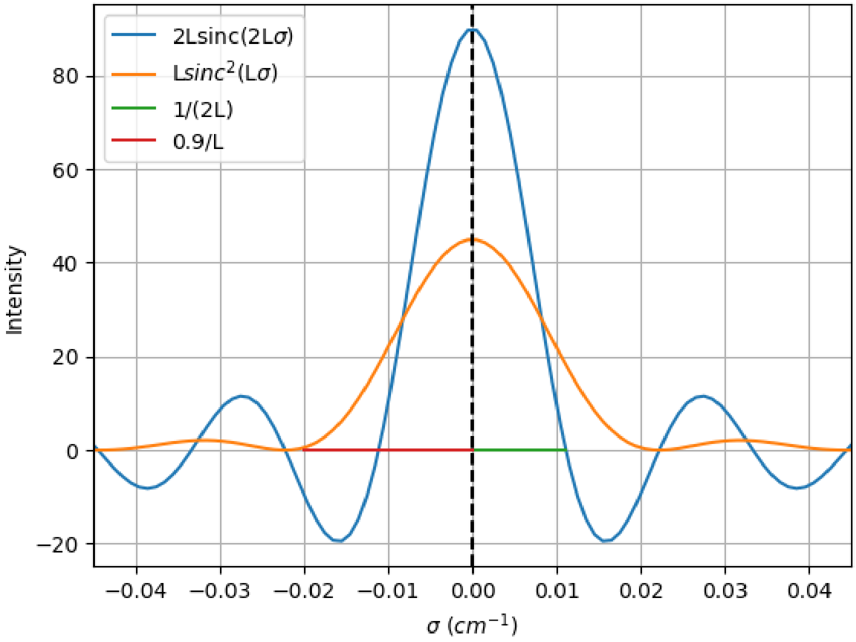

Figure 2.3: Instrument function for an interferogram multiplied by a rectangular function (blue) or by a triangular function (orange) with their distance from the line center to the first zero (green and red, respectively). Here the maximum OPD (L) is 45 cm.

A further instrument limitation that affects the instrument function is the finite size of the entrance field stop, the aperture located at the focal point of the instrument and that determines its internal field of view. Since the PEARL FTS does not use an aperture stop (that simply reduces the number of incoming photons) before the field stop, the "entrance aperture" is the entrance field stop in our case. In an ideal case, the input light is on-axis and travels only through the focal point of the collimating mirror (see the "Collimating parabolic mirror" in the interferometer compartment in Figure 2.1) such that the recombined beam would consist of two plane waves propagating in the same direction. However, the size of the aperture is finite and may need to be large to obtain enough signal for the measurement. This leads the input light to enter with a range of off-axis angles and travel through the arms of the interferometer with a range of different optical path differences. For an off-axis angle α and an optical path difference x, the fringe intensity of the interference pattern is (Davis et al., 2001b):

$$dI = \cos(2\pi\sigma x \cos(\alpha))d\Omega \tag{2.8}$$

with $d\Omega$ a small solid angle increment at the angle α. For simplicity, we have considered the case of monochromatic radiation (as intensity per steradian) at wavenumber σ with unit amplitude such that the right-hand sides of Equations 2.8-2.11 have units of intensity. With the small angle approximation for α, the expression becomes:

$$dI = \cos\left(2\pi\sigma x\left(1 - \frac{\alpha^2}{2}\right)\right) d\Omega. \tag{2.9}$$

For a circular aperture, the solid angle is $\Omega = \pi\alpha^2$. The intensity for a given path difference x is obtained by integrating up to the maximum solid angle Ω_m:

$$I(x) = \int_0^{\Omega_m} dI(x) = \int_0^{\Omega_m} \cos\left(2\pi\sigma x\left(1 - \frac{\Omega}{2\pi}\right)\right) d\Omega \tag{2.10}$$

$$I(x) = \Omega_m sinc\left(\frac{\sigma x \Omega_m}{2\pi}\right)\cos\left(2\pi\sigma x\left(1 - \frac{\Omega_m}{2\pi}\right)\right). \tag{2.11}$$

One of the effects of the finite size of the entrance aperture is to scale the optical path difference and wavenumber by $1-\frac{\Omega_{\mathrm{m}}}{2\pi}$, so a given wavenumber σ will appear as a range of wavenumbers from σ to $\sigma\left(1-\frac{\Omega_m}{2\pi}\right)$. The other effect is to multiply the interferogram by a sine cardinal function. To avoid reducing the signal and amplifying the noise, the choice of the entrance aperture size should be made such that the sinc function is positive up to at least the maximum OPD. The sinc function becomes negative when:

$$\frac{\sigma x \Omega_m}{2\pi} > 1. \tag{2.12}$$

This depends on σ, so it is not possible to have an optimal aperture at all wavenumbers simultaneously. A criterion to decide on the optimal aperture size is to get the maximum fringe amplitude at maximum OPD (L) for the largest wavenumber of interest σ_m. Following Equation 2.11 at $x = L$ and $\sigma = \sigma_m$, the fringe amplitude is proportional to:

$$\Omega_m sinc\left(\frac{\sigma_m L \Omega_m}{2\pi}\right) = \frac{2\sin\left(\frac{\sigma_m L \Omega_m}{2}\right)}{\sigma_m L} \ . \tag{2.13}$$

The criterion is met when the argument of the sin function is equal to $\frac{\pi}{2}$:

$$\frac{\sigma_m L \Omega_m}{2} = \frac{\pi}{2};\ \Omega_m = \frac{\pi}{\sigma_m L} \ . \tag{2.14}$$

The solid angle can also be expressed as a function of the entrance aperture radius *r* and the focal length of the parabolic collimating mirror *f* for the maximum incident angle α_m:

$$\Omega_{\mathrm{m}} = \pi\alpha_m^2 = \frac{\pi r^2}{f^2} \tag{2.15}$$

using the small angle approximation for $r = f\sin(\alpha) \approx f\alpha$. Combining Equations 2.15 and 2.14 leads to the equation for the optimum aperture radius:

$$\Omega_m = \frac{\pi}{\sigma_m L} = \frac{\pi r^2}{f^2};\ \ r = \frac{f}{\sqrt{\sigma_m L}} \ . \tag{2.16}$$

The PEARL Bruker 125HR has a parabolic collimating mirror with a focal length of 418 mm. The optimum aperture size for wavenumbers up to the maximum of the FTS spectral range ($\sigma_m = 15798\ cm^{-1}$) with $L = 45\ cm$ is $r = \frac{418}{\sqrt{15798 \times 45}} \approx 0.5\ mm$. This is the aperture size used to measure NIR spectra for TCCON at PEARL (note the aperture sizes listed by OPUS correspond to their diameter). However, for TCCON observations the largest wavenumber of interest is typically from the dioxygen spectral window centered at 7885 cm^{-1} and 240 cm^{-1} wide. Thus, the aperture could be opened to $r = \frac{418}{\sqrt{8005 \times 45}} \approx 0.7\ mm$ to increase the signal while still meeting the criterion. However, the aperture radius at Eureka was limited to 0.5 mm as the detector could saturate with larger sizes, perhaps due to less water absorption in the dry conditions of the Arctic. Some TCCON sites like Park Falls (WI, USA), Lamont (OK, USA), and Darwin (Australia), use an entrance aperture stop with a diameter of 25-35 mm after the instrument entrance window, and a field stop diameter of 1 mm. Contrary to adjusting the field stop, adjusting the entrance aperture stop changes the signal intensity without affecting the instrument function. With an entrance aperture stop, the light beam uses a smaller section of the optics, this can lead to improved modulation efficiency if the flatness of the corner cube mirrors is imperfect.

With the effect of the finite size of the field stop, Equations 2.4 and 2.5 become (Davis et al., 2001b):

$$I_{measured}(x) = I_{ideal}(x) \times \Omega_m sinc\left(\frac{\sigma_o x \Omega_m}{2\pi}\right) \times rect\left(\frac{x}{2L}\right) \tag{2.17}$$

$$B_{measured}(\sigma) = B_{ideal}(\sigma) * \left[\left(\frac{2\pi}{\sigma_o} \times rect\left(\frac{2\pi\sigma}{\sigma_o \Omega_m}\right)\right) * 2Lsinc(2L\sigma)\right] \tag{2.18}$$

where the instrument line shape function is:

$$ILS(\sigma) = \left(\frac{2\pi}{\sigma_o} \times rect\left(\frac{2\pi\sigma}{\sigma_o \Omega_m}\right)\right) * 2Lsinc(2L\sigma). \tag{2.19}$$

2.2 Monitoring the Instrument Line Shape

To verify that the instrument is properly aligned with an acceptable line shape, a measurement is made through a gas cell containing a known quantity of a gas at a known pressure. This measurement is made with the light from an internal source. To verify the instrument line shape in the NIR, a heated tungsten filament is used as the light source and a HCl gas cell is placed in the optical path (see cell compartment in Figure 2.1). In addition to TCCON measurements in the NIR and with a maximum OPD of 45 cm, the instrument is also used to measure in the mid-infrared for NDACC with a maximum OPD of 257 cm. NIR spectra are collected using a CaF_2 beamsplitter while MIR spectra are collected using a KBr beamsplitter. The line shape in both spectral regions is also monitored with different cells, the HCl cell for the NIR measurements, and either a HBr or N_2O cell for MIR measurements. In this section, only the ILS results from the HCl cell will be shown.

The line shape retrieval software LINEFIT (Hase et al., 1999) is used to fit measured spectra of the source with HCl absorption lines to retrieve the modulation efficiency (ME) and phase error (PE). A loss in ME will widen the ILS, while PE will introduce asymmetry. As errors in ILS most strongly affect the core of absorption lines, which have more information on trace gas concentrations at higher altitudes, errors in the instrument line shape can be an important source of error (5-10%) in the retrieved stratospheric column of species like HCl, HF, O_3, NO, and NO_2 (Hase et al., 1999).

Typical misalignments that affect the line shape include an angular misalignment, when the metrology laser beam and the beam of radiation to measure are not perfectly coaxial, and shear misalignment, when there is an offset between the two corner cube retroreflectors. A typical shear misalignment in a 125HR occurs because of wear of the teflon pads of the scanning mirror plate, which causes it to be lower than the fixed mirror.

The LINEFIT 14.7 results for the Eureka cell measurements since 2015 are shown in Figure 2.4. The low outlier near ~0.75 ME in early 2019 (which also corresponds to the outlier in PE) was obtained after the instrument entrance window and aperture wheels were replaced and before the alignment that followed. In the bottom panel, the time series of ME at MOPD shows that the ILS had been degrading over time up to 2017. The TCCON quality requirement for ME at MOPD is

1±0.05 and the Eureka ME decreased below 0.95 during 2016. This requirement may become more stringent at 1±0.02, which can be achieved with careful alignment. Before 2018, each cell measurement consisted of 50 co-added scans, however due to a new requirement for spectra to have a SNR>3000 for LINEFIT 14.7, 100 scans have been co-added since 2018. The instrument was re-aligned (for the first time not by a Bruker engineer) by fellow PhD student Erik Lutsch and I, and with the PEARL Site Manager Pierre Fogal, in spring 2017. Ideally the instrument alignment should be checked each year and the instrument re-aligned when the ME at MOPD is no longer within 1±0.02. The alignment process will be described in Sect. 2.4. After the alignment, the ME at MOPD was close to 1.01, compared to ~0.93 before the alignment, and the maximum amplitude of the phase error was reduced from ~0.01 rad to ~0.005 rad. There can be variability in ME at MOPD of ~0.01 between consecutive cell measurements, this variability is not well understood, and more frequent cell measurement would be needed for LINEFIT results to be a more robust diagnostic of the ILS. Some TCCON sites like East Trout Lake automate their cell measurements and do them weekly at night so as to not disrupt solar measurements. The HCl cell measurements at Eureka are not yet automated and thus sparser and irregular in time. Figure 2.5 shows the ILS and ME at MOPD before the first alignment in November 2016 and after the last alignment in February 2020, it shows the ME at MOPD improved from less than ~0.95 to ~1.01 and the phase error improved from ~0.01 to less than 0.005 rad. The reduced phase error led to a visible reduction in the asymmetry of the ILS.

The characteristics of the HCl cells used at Eureka are shown in Table 2.2. Before 2014, the cell “Eureka NP #1” was used but it had been leaking over time and was replaced by Joseph Mendonca during the 2014 Canadian Arctic ACE-OSIRIS Validation Campaign with the new “Cell #28”. The cell column and pressure of HCl are required to run LINEFIT, but also when processing measured solar spectra for TCCON. One of the inputs of the 2020 release of GGG (GGG2020), the TCCON retrieval algorithm (discussed in Sect. 3.4), is a file containing the HCl cell information. It includes the time period for each cell with corresponding HCl column amount and pressure at the beginning and end of the time period. The algorithm will then assume a linear decrease of the column amount between the first and last date to account for cells known to be leaking over time. The HCl column scaling factors retrieved with the 2014 release of GGG (GGG2014) showed the decrease of the HCl column amount over time with the “Eureka NP #1” cell, and this decrease was not linear as shown in Figure 2.6. Thus, the information for the "Eureka NP#1" cell is split between two periods for which the decrease is roughly linear. The last known measurements with this cell were done by Frank Hase (KIT) in December 2013 (Column 2 and Pressure 2 in Table 2.2).

Table 2.2: Characteristics of the HCl cells used at Eureka. This information must be provided to GGG2020 via the eu_cell_status_info.dat input file. Numbers "1" and "2" indicate values at the start and end of the time period, respectively.

Cell name	**Dates (yyyy-mm-dd)**	**Length (cm)**	**$H^{35}Cl$ Column 1 (1E22 molecules.m^{-2})**	**$H^{35}Cl$ Column 2 (1E22 molecules.m^{-2})**	**$H^{35}Cl$ Pressure 1 (hPa)**	**$H^{35}Cl$ Pressure 2 (hPa)**
Eureka NP #1	2010-07-01 to 2012-01-01	10	1.0192	0.7194	4.539	3.204
	2012-01-01 to 2013-12-31	10	0.7194	0.5578	3.204	2.483
Cell #28	2014-02-01 to present	10	1.2909	1.2909	4.78	4.78

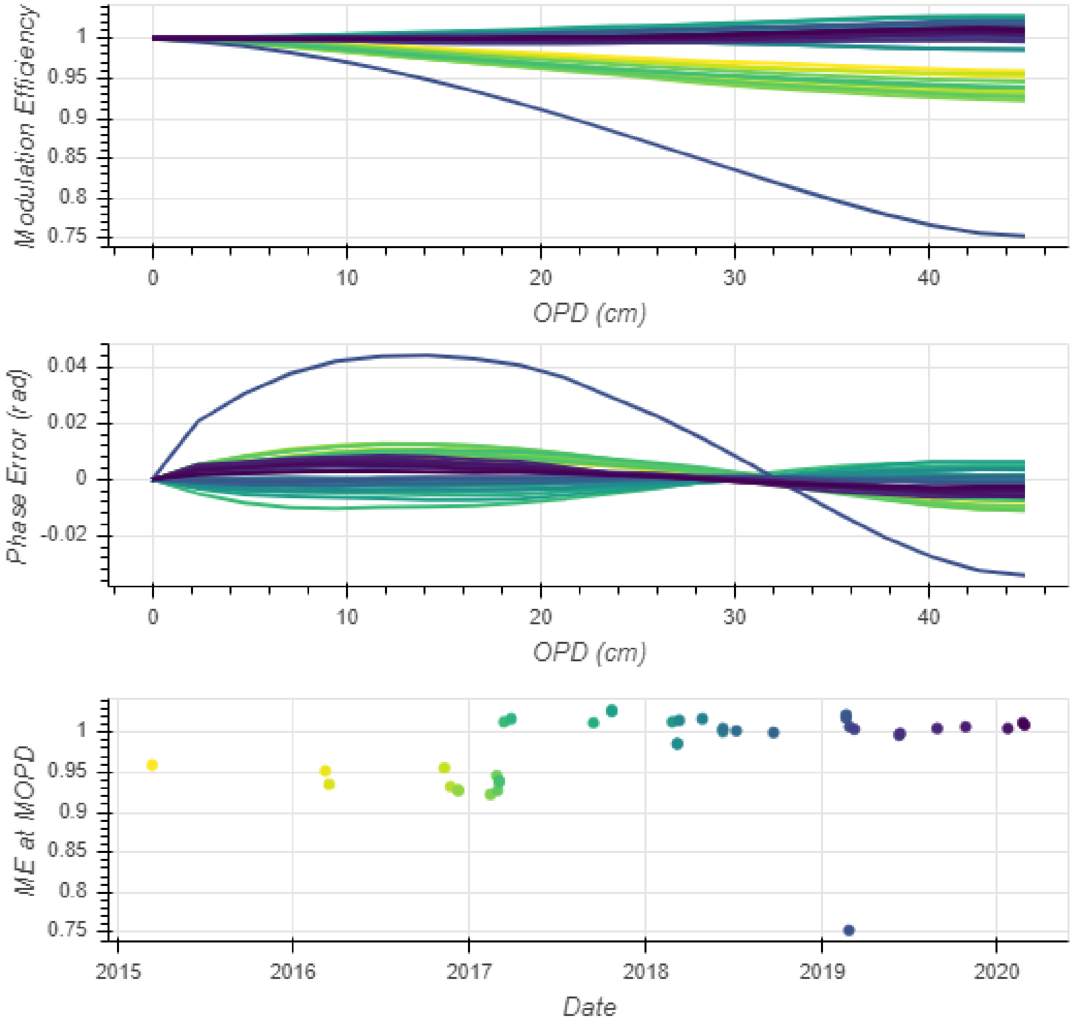

Figure 2.4: Modulation efficiency (top), and phase error (center) as functions of optical path difference, and time series of the modulation efficiency at maximum OPD (45 cm, bottom), for all HCl cell #28 measurements at Eureka since 2015. The instrument was realigned in spring 2017, 2018 (minor adjustment), and 2019. The colours change with time as indicated by the bottom panel.

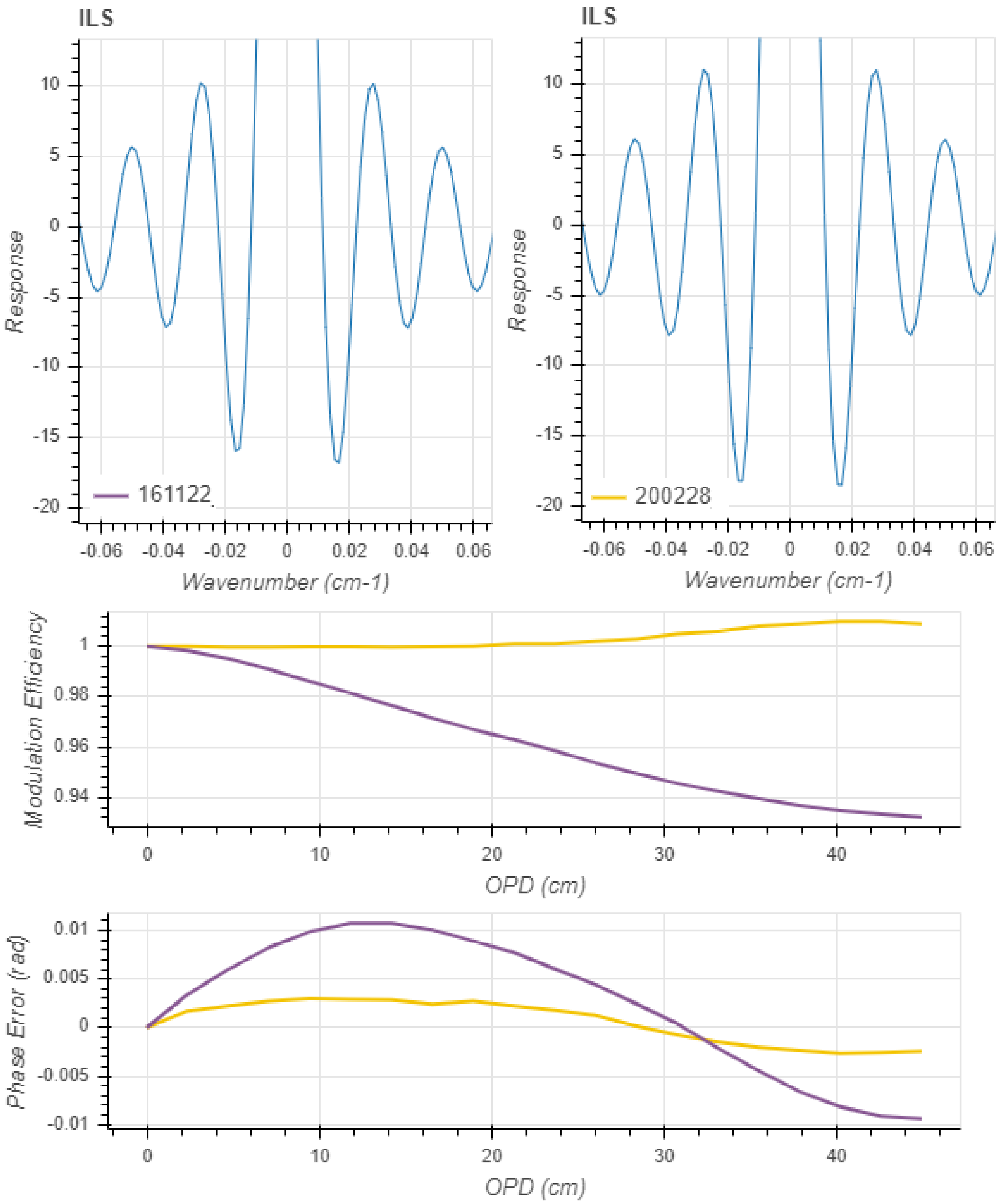

Figure 2.5: ILS retrieved with LINEFIT 14.7 using HCl cell #28 at Eureka on 22 November 2016 (top left), when the ME at MOPD was below 0.95, and on 28 February 2020 (top right) when it was at ~1.01. The ILS is visibly more asymmetric between the first negative lobes on 22 November 2016, a feature attributable to the larger phase error. However, despite a ~6% difference in ME at MOPD, it is difficult to notice a difference in ILS width, but the full width between the first zero crossings is ~0.0004 cm^{-1} wider on 22 November 2016. Panels also show ME and PE for these two cases.

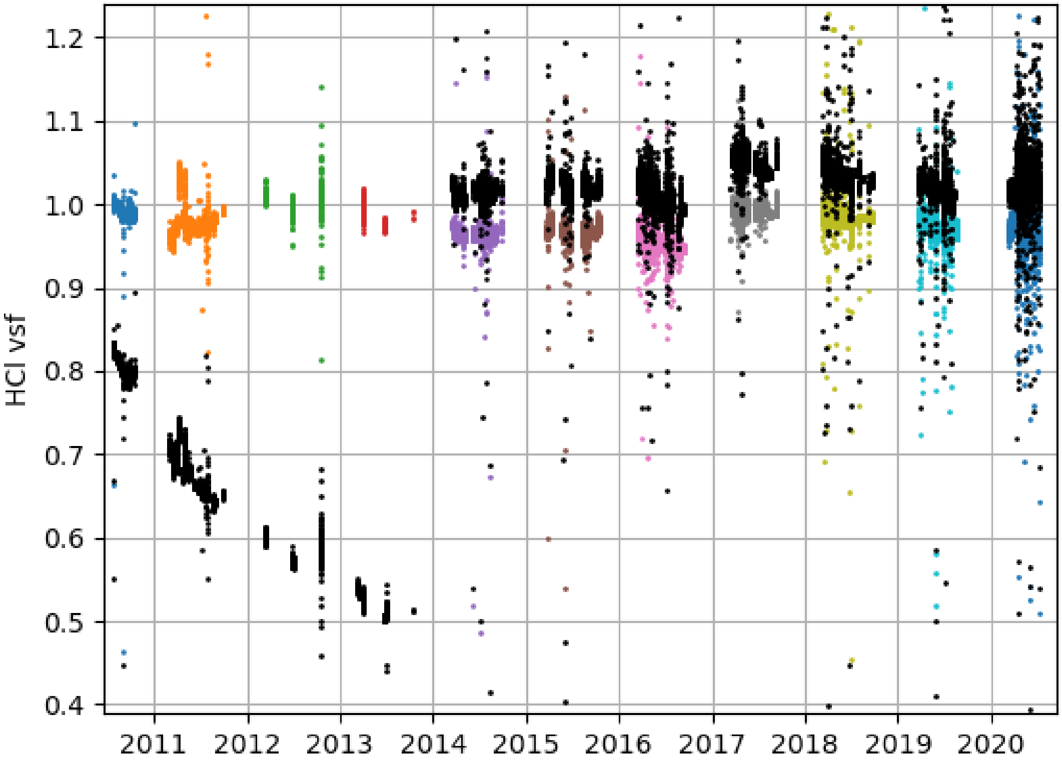

Figure 2.6: 2010-2020 HCl scaling factor (VSF) time series retrieved with GGG2014 (black) and with GGG2020 (colours). Because the a priori HCl column and pressure in the cell is adjusted over time based on a new input file in GGG2020 that can account for leaking cells, the HCl VSF retrieved with GGG2020 remains close to 1 between 2010-2014.

2.3 Alignment of the 125HR

This section describes the procedure used to align the 125HR spectrometer at Eureka. This has been successfully used during the Canadian Arctic ACE-OSIRIS Validation Campaigns since 2017. The procedure assumes no misplacement of the scanner rods on which the mobile mirror platform is sliding. The instrument was re-aligned in March 2017 following a drop in ME at MOPD below 0.95. In 2018, we made a minor adjustment to the flat mirror before the exit aperture to fine tune its alignment with an entrance aperture with a diameter of 1 mm (as used for TCCON NIR measurements and with some filters for NDACC MIR measurements). In 2019, PhD student Tyler Wizenberg and I re-aligned the instrument after the installation of a new entrance window as the old one had degraded due to a dust patch baked onto its surface by the solar beam, reducing the signal intensity. New aperture wheels were also installed as the previous ones had a defect that made it impossible to co-align the entrance and exit aperture for different aperture settings, as the position of center of an aperture of a given size would not coincide with the position of the center of an aperture with a different size. Thus, the alignments in 2017 and 2018 were tuned for an aperture with a diameter of 1 mm as used by TCCON, but were not optimized for NDACC MIR measurements that used different aperture sizes. With the new aperture wheels, the instrument could be well aligned for all aperture sizes in 2019. The alignment steps presented here follow instructions developed by John Robinson (National Institute of Water and Atmospheric Research, New Zealand).

2.3.1 Step 1: Check the Focus on the Entrance Field Stop

The entrance field stop (which can also be called entrance aperture at Eureka) is located between the source compartment and the interferometer compartment (see Figure 2.1). It defines the instrument's field of view and the solid angle subtended at the first collimating mirror in the interferometer compartment. As discussed in Sect. 2.1, the aperture shape and size are important to define the ILS and the first step of the alignment procedure is to ensure that the aperture is at the focal point of the first collimating mirror in the interferometer compartment. This can be checked by placing a telescope, focused on infinity, in the long arm of the interferometer as shown in Figure 2.7. To focus the telescope on "infinity" it was taken outside and focused on mountain peaks on the horizon. If the entrance aperture does not appear sharp, then adjustments must be made to the first parabolic (collimating) mirror in the interferometer compartment. Such an adjustment was not needed, even after replacing the aperture wheels, as the smallest aperture appeared in focus.

Figure 2.7: Photo of the alignment telescope installed in the long arm of the 125HR to check if the apertures are in focus.

2.3.2 Step 2: Define the Interferometer Axis

Once the entrance aperture is at the focal point of the first collimating mirror, the next step makes use of an external HeNe laser as a source to define the interferometer axis, which is the path the input light follows in the instrument. This axis is constrained by the position of the scanner rods in the long arm of the interferometer. The goal of this step is to center the entrance aperture on the observed interference pattern generated by the laser. Thus, the recombined laser beam must be picked off before it reaches the exit aperture to be observed during this step. The laser was mounted outside the instrument with a pick-off mirror to direct the light into the instrument as shown in Figure 2.8. For the input light to appear homogenous and uniformly illuminate the entrance aperture, a 1500 grit diffuser was placed in front of the aperture inside the source compartment and a speckle reducer was used to obtain a clearer image of the interference pattern. The placement of the diffuser and speckle reducer is shown in Figure 2.9.

Figure 2.8: Photo of the HeNe laser, with an attached beam expander, used to align the 125HR.

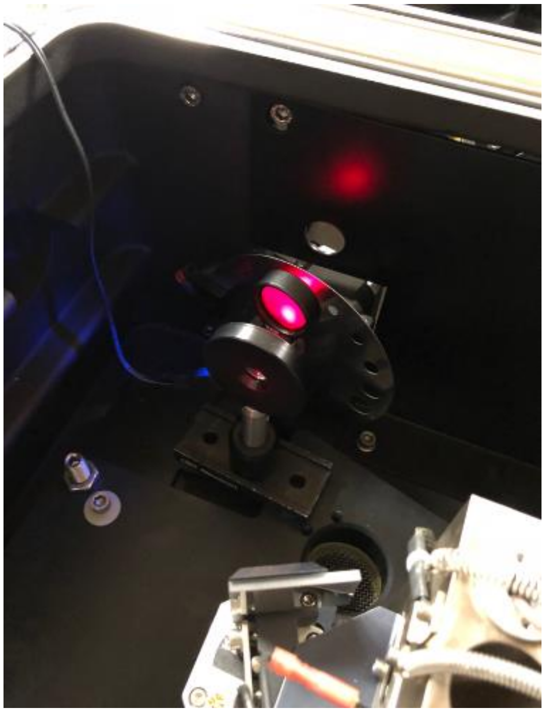

Figure 2.9: Photo of the speckle reducer (with the cable attached) and the 1500 grit diffuser (closer to the aperture wheel) placed in front of the entrance aperture inside the source compartment.

A periscope was made from two flat mirrors placed in the interferometer compartment to pick off the recombined beam as shown in Figure 2.10. Mirror 6 is placed in between mirrors 2 and 3 to reflect the collimated recombined beam upwards towards mirror 7. Mirror 7 then directs the light beam into the same telescope used in Sect. 2.3.1, but now placed outside the spectrometer as shown in Figure 2.11. For this alignment step, it is important to minimize any source of vibration to observe the HeNe interference pattern, and the scanning mirror, which is normally free to oscillate back and forth, must be locked in place. To do so, an Allen key can rest on the magnet at the back of the scanner to keep this mirror in a fixed vertical position, and a jumper can be placed on the board to enable a diode to light up when the mirror is in the correct position to be locked in, as shown in Figure 2.12.

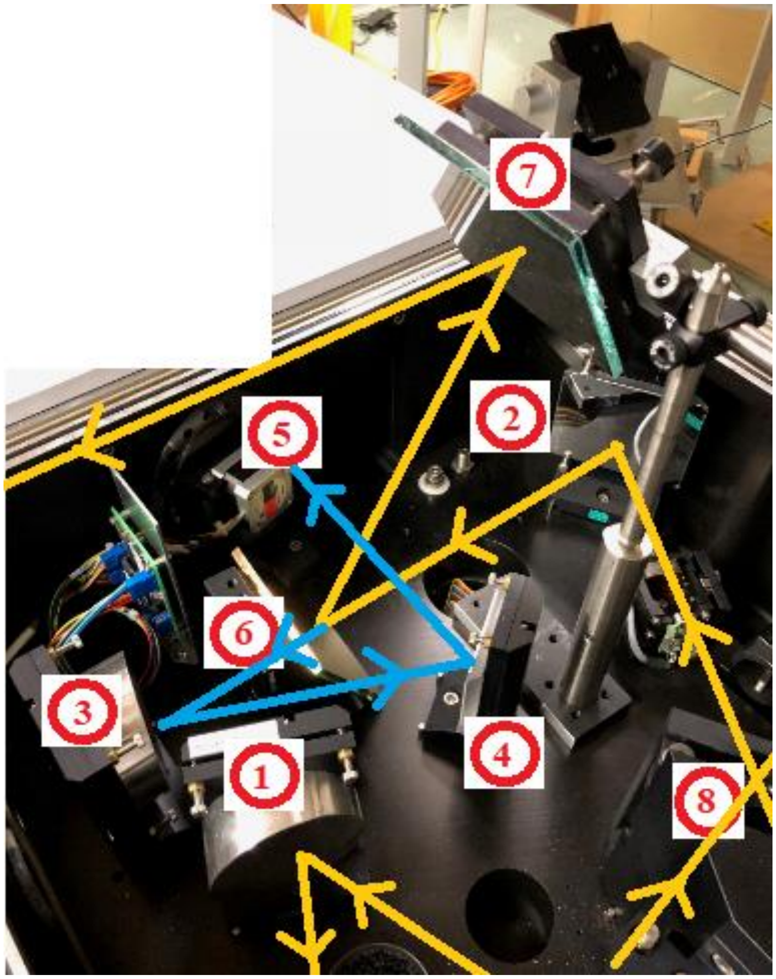

Figure 2.10: Photo of the setup used to bring the light beam out of the interferometer compartment and direct it into the telescope for the centering of the HeNe interference pattern on the entrance aperture. 1: first parabolic (collimating) mirror; 2: flat mirror; 3: collimating (focusing) mirror; 4: flat mirror; 5: exit aperture; 6 and 7: flat mirrors making the periscope to pick off the collimated recombined beam coming from mirror 2; 8: beamsplitter. The yellow arrows indicate the light path, a flat mirror not included in the photo directs the light coming from Mirror 1 towards the beamsplitter. The blue arrows indicate the path light would take without Mirror 6.

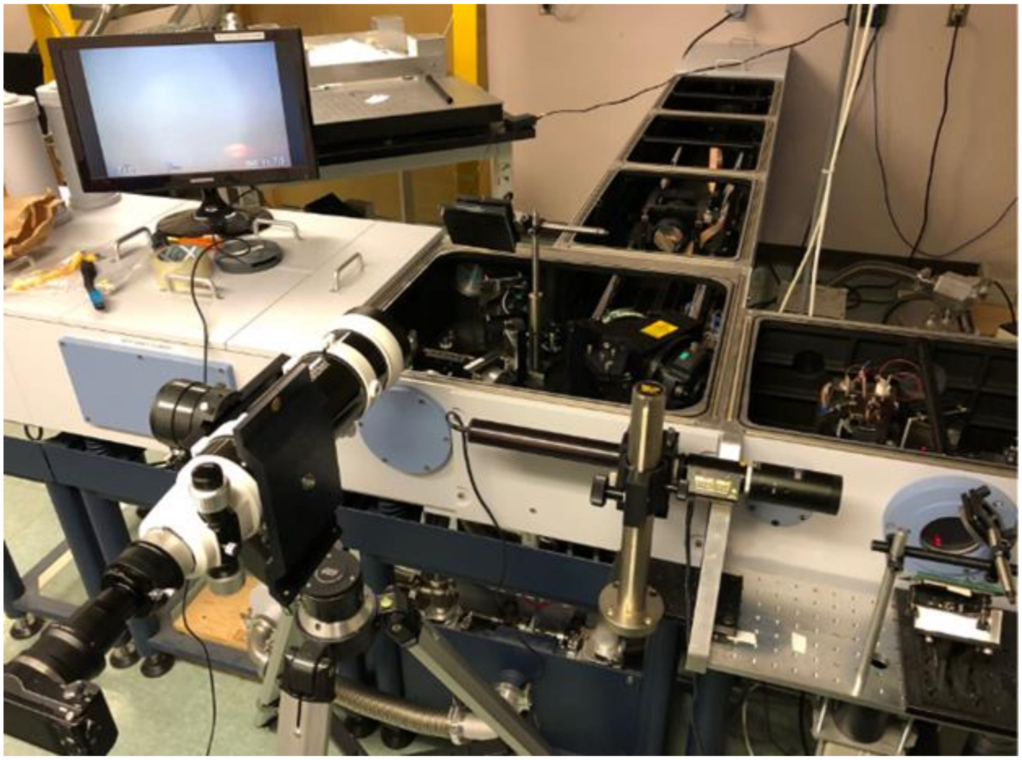

Figure 2.11: Setup of the telescope to view the HeNe fringe pattern through the entrance aperture. A camera looks through the telescope and is controlled from a computer and connected to a screen to view the fringes.

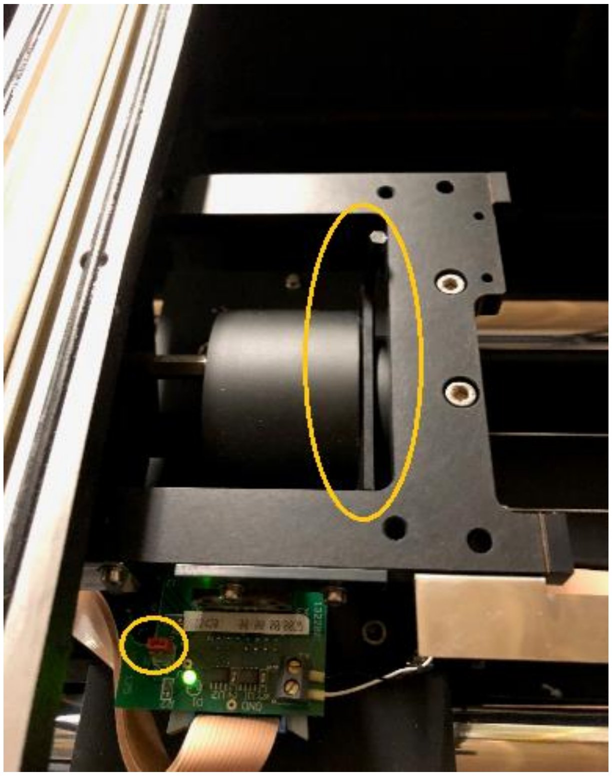

Figure 2.12: Photo of the locking of the scanning mirror mechanism by resting an Allen key on the magnet. A jumper (red circled element on the electronics board) enables the diode to light up when the mirror is in the correct position.

During this step, the first flat mirror in the interferometer compartment, the mirror that directs the input light towards the beamsplitter (not shown in Figure 2.10), was adjusted until the HeNe interference pattern appeared centered in the entrance aperture. This process is illustrated in Figure 2.13 with pictures of the fringes taken during the alignment done in 2019 after installing the new entrance window and new aperture wheels. If there is a shear misalignment, which will manifest itself as an apparent jump of the fringes when crossing the zero-path difference (ZPD), it cannot and should not be fixed by adjusting the flat mirror. This "jump" is apparent in the first two images of each row in Figure 2.13. In Figure 2.13(a) a shear misalignment was clearly present when looking at the position of the mirror at the minimum distance from the beamsplitter (minPD) and at the front of the first compartment of the long arm. These two positions are roughly the same distance from the ZPD position. The center of the fringes is also clearly off the center of the aperture as seen at different positions of the scanning mirror in the long arm with a 4 mm diameter aperture. The compartments of the long arm are numbered starting with the compartment closest to the beamsplitter. The "front" of a compartment is the side closer to the beamsplitter, and the "back" is the opposite side. In Figure 2.13 (b) the same set of pictures was taken after a first adjustment to the flat mirror to center the fringes away from ZPD. Then the adjustments were fine tuned with smaller aperture sizes, once with the 2 mm in Figure 2.13 (c) and with the 1 mm aperture in Figure 2.13 (d).

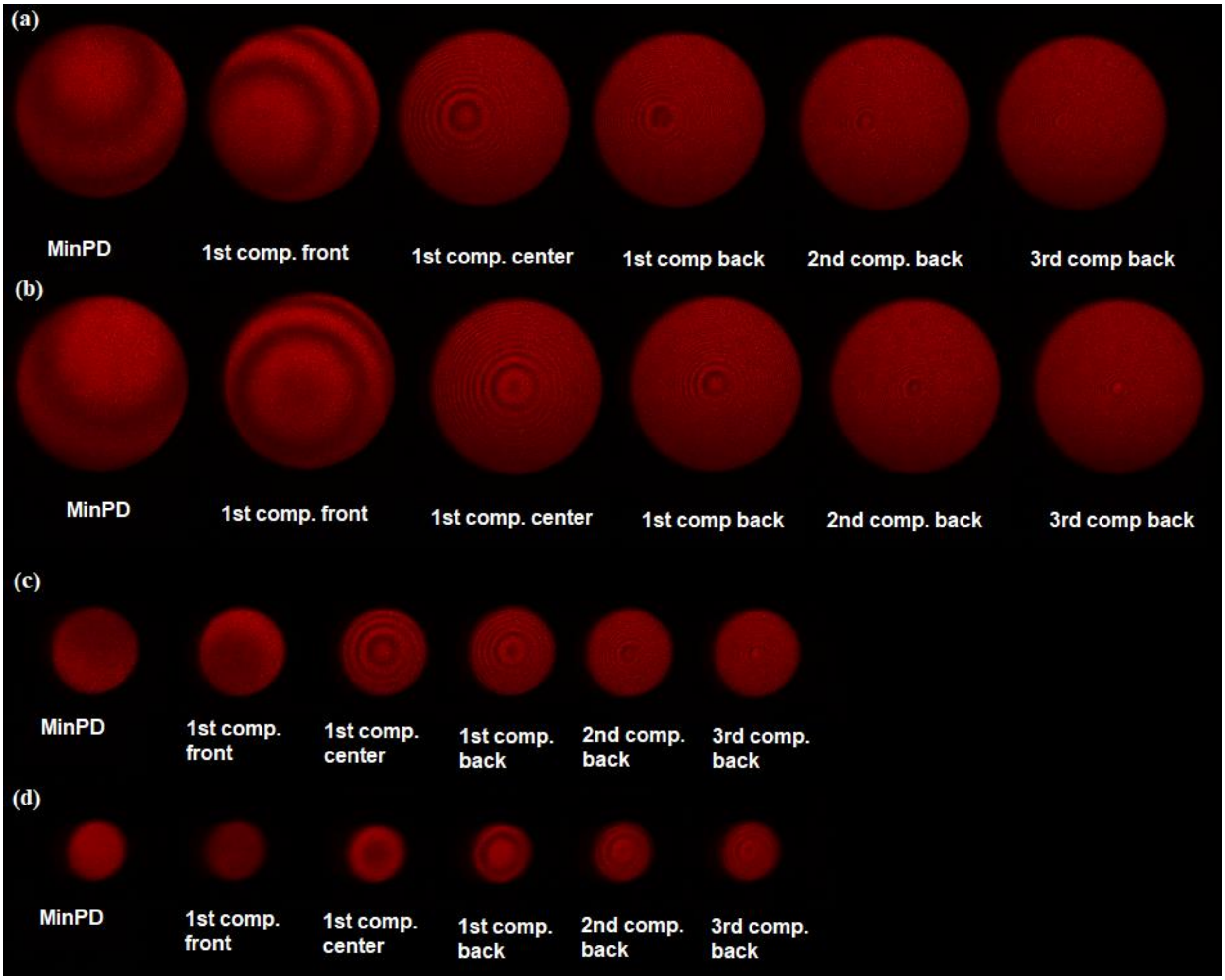

Figure 2.13: The HeNe interference pattern as observed through the telescope for different positions of the scanner mirror in the long arm of the interferometer during the 2019 alignment. The long arm is divided into three compartments ("comp.") and the minimum path difference (minPD) is the position of the scanning mirror when closest to the beamsplitter: (a) with a 4 mm aperture after installing the new entrance window and aperture wheels but before the alignment; (b) with a 4 mm aperture after a first adjustment to the first flat mirror in the interferometer compartment; (c) with a 2 mm aperture after the second adjustment; (d) with a 1 mm aperture after a third adjustment.

2.3.3 Step 3: Adjust the Fixed Corner Cube

After the fringe pattern appears centered away from ZPD, the apparent shift of the fringes when scanning through ZPD can be addressed. This is corrected by adjusting the fixed corner cube, typically only vertically, until the fringes appear unchanged through ZPD. It is best to use the largest aperture for this adjustment. Once there is no apparent shift, the centering of the fringes at longer path differences should be revisited and Steps 2 and 3 may require a few iterations.

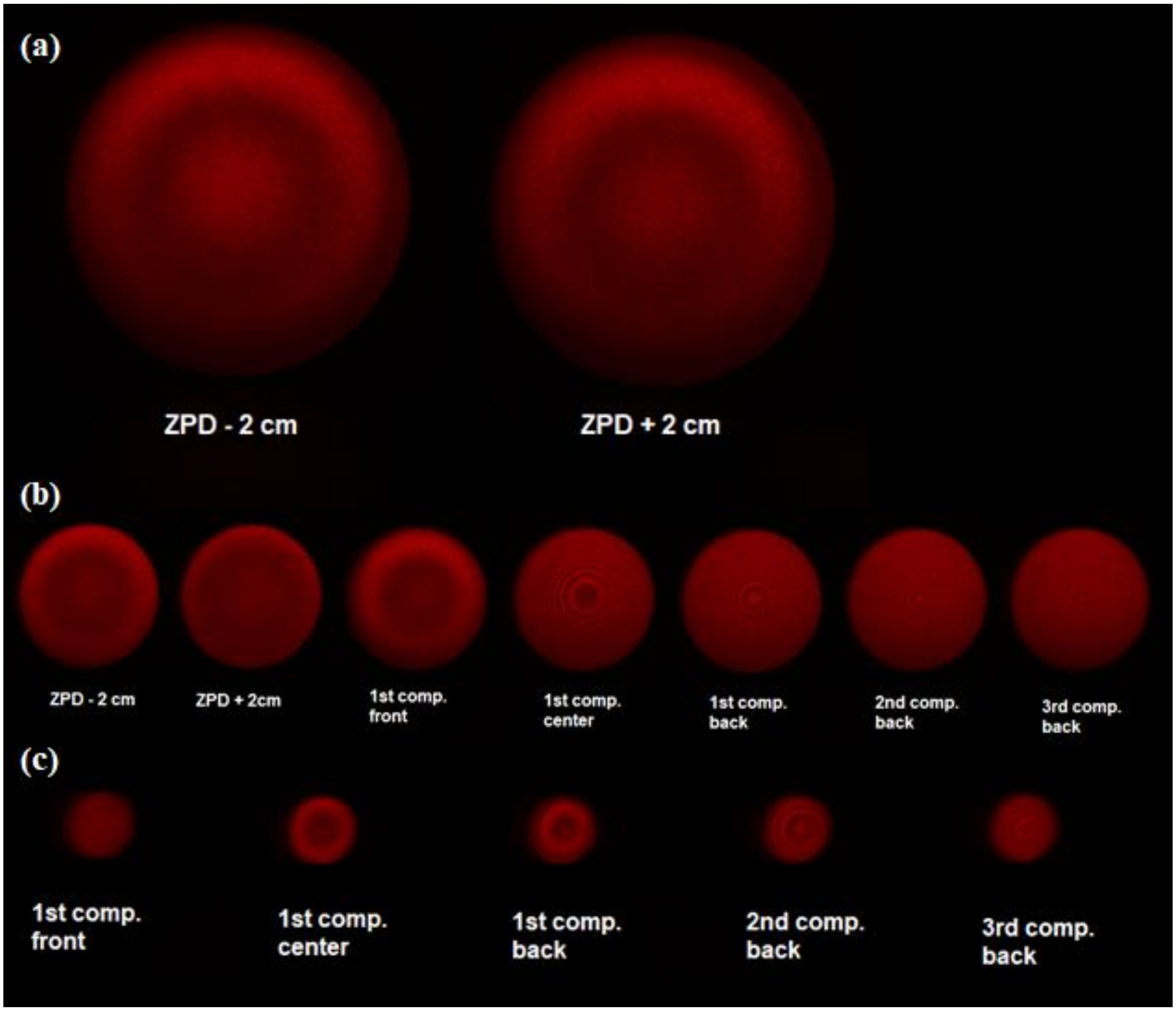

Figure 2.14: The HeNe interference pattern as observed through the telescope for different positions of the scanner mirror in the long arm of the interferometer: (a) with a 6.3 mm aperture at 2 cm on both sides of ZPD after an adjustment to the fixed corner cube; (b) with a 4 mm aperture at 2 cm on both sides of ZPD and along the long arm after a fourth adjustment of the flat mirror; (c) with a 1 mm aperture after the fifth adjustment to the flat mirror.

In Figure 2.14(a), the HeNe laser fringes are shown 2 cm on both sides of ZPD after adjusting the fixed corner cube until there was no apparent shift of the fringes through ZPD. ZPD can be located by noting the position of the mirror where the apparent shift occurs. In 2019, the fixed corner cube only had to be adjusted once, then the centering of the fringes was fine adjusted with a 4 mm aperture as shown in Figure 2.14 (b) and finally with a 1 mm aperture as shown in Figure 2.14 (c). When the instrument is aligned, only the center of the fringes is visible until the mirror is at the back of the first compartment, roughly 50 cm from ZPD (equivalent to 100 cm path difference since the light beam travels both ways).

2.3.4 Step 4: Focus the Exit Aperture and Co-align with the Entrance Aperture

Once the fringes are centered on the entrance aperture and there is no apparent shift through ZPD, the telescope is installed back in the long arm of the interferometer, this time to view the exit aperture. If it does not appear in focus, the flat mirror that directs the light towards the exit aperture (Mirror 4 in Figure 2.10) can be moved forward or backward by turning its three screws the same amount. This was needed in 2019 and the result is shown in Figure 2.15. Once the exit aperture appeared in focus it was co-aligned with the entrance aperture. Both apertures were observed at the same time through the telescope.

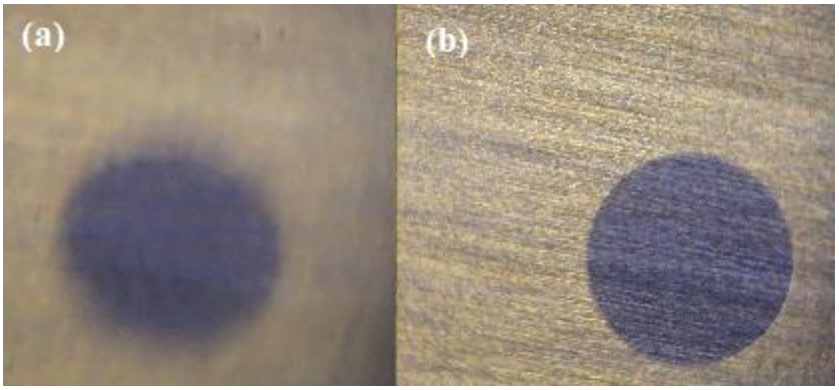

Figure 2.15: Photos of the exit aperture as seen through the telescope placed in the long arm of the interferometer: (a) out of focus; (b) in focus after adjusting the flat mirror that directs light towards the exit aperture.

During solar measurements, the exit aperture is typically one size larger than the entrance aperture and its role is to block radiation coming from the heated entrance aperture wheel. Thus, the fine co-alignment of the exit with the entrance aperture is not critical, but it should not cut off the light beam. Photos of the co-aligned apertures are shown in Figure 2.16 after adjustments to the exit flat mirror.

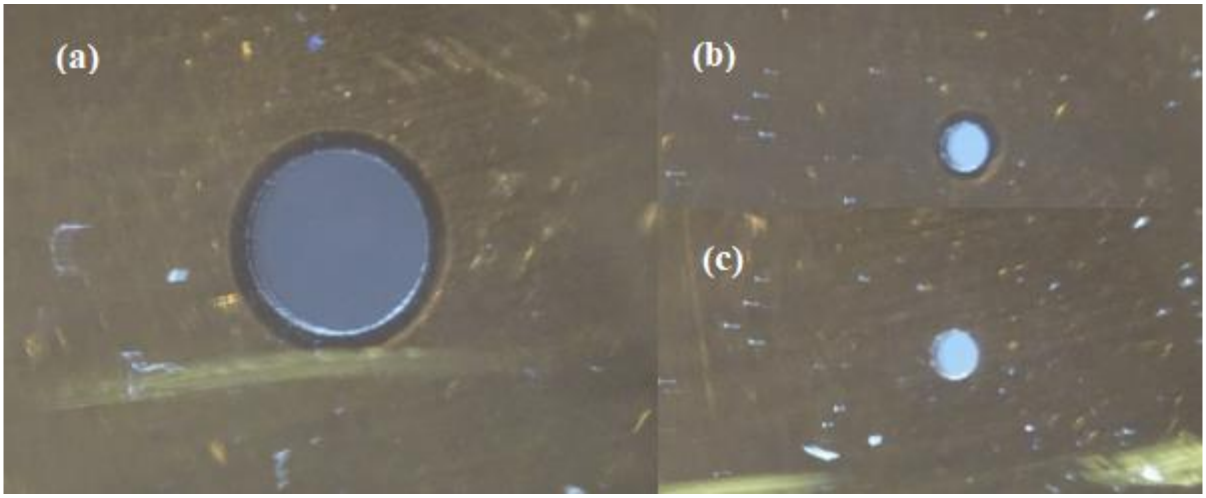

Figure 2.16: Photos of the entrance and exit apertures as seen through the telescope placed in the long arm of the interferometer: (a) with a 2 mm entrance and 2.5 mm exit apertures; (b) with a 0.5 mm entrance and a 0.7 mm exit apertures; (c) with a 0.5 mm entrance and exit apertures.

2.3.5 Step 5: Co-align the Metrology Laser with the Interferometer Axis

Steps 1 to 3 defined the interferometer axis, the path that the input light takes through the instrument. The metrology laser, the internal spectrometer HeNe laser that is used to trigger sampling of the interferogram at equal distance intervals as described in Sect. 2.1, needs to travel parallel to the input light beam. The metrology laser beam comes vertically from under the instrument and is directed through the beamsplitter with a prism. This prism can be adjusted to optimize the modulation efficiency of the laser signals, which can be measured with an oscilloscope. The laser signals are measured by two detectors, LASA and LASB, on both sides of the beamsplitter. When the laser is well aligned, both detectors should observe the same signal. The ME should not vary by more than 15% between the ZPD and maximum path difference (MPD) positions of the scanning mirror. The laser signals are measured, and the ME at a given position of the scanning mirror is computed as:

$$ME = \frac{V_{max} - V_{min}}{V_{max} + V_{min} - 2V_{zero}} \tag{2.20}$$

where V_{max} is the maximum of the signal in Volts, V_{min} is the minimum, and V_{zero} is the zero offset of the signal. The laser modulation efficiency is independent from the modulation efficiency derived with the internal source as described in Sect. 2.2. This is because the laser beam and the solar/source beam are directed into the long arm of the interferometer by two different mirrors. The laser signals and ME at ZPD and MPD obtained after the alignment in 2019 are shown in Table 2.3 for both beamsplitters used by the instrument, the CaF_2 for NIR and the KBr for MIR measurements.

Table 2.3: Laser signals and modulation efficiency for the CaF_2 and KBr beam splitters after the 125HR alignment in March 2019.

CaF2	**Zero (V)**	**Max (V)**		**Min (V)**		**ME**	
		ZPD	**MPD**	**ZPD**	**MPD**	**MPD**	**ZPD**
LASA	-9.250	-2.400	-2.900	-9.000	-8.700	0.841	0.930
LASB	-9.250	-3.700	-4.200	-9.200	-9.000	0.906	0.982
KBr	**Zero (V)**	**Max (V)**		**Min (V)**		**ME**	
		ZPD	**MPD**	**ZPD**	**MPD**	**MPD**	**ZPD**
LASA	-9.230	2.1	1.6	-7	-7.3	0.697	0.671
LASB	-9.240	-1.7	-2.1	-8.15	-7.9	0.684	0.747

To check the alignment of the metrology laser, its two detectors can be lowered, then the laser beam should pass through the smallest entrance and exit apertures with two small laser spots clipping the edge of the aperture, and the main beam passing through the center. The small spots are the results of the multiple reflections through the interferometer.

2.3.6 Step 6: Center and Focus Internal Source Image on the Entrance Aperture

The last step of the alignment is to center and focus the internal sources of the instrument on the entrance aperture. This is done by adjusting the sliding mirror in the source compartment of the interferometer. When in focus, the image of the MIR source appears as a coil, and the entrance aperture should be at the center of one of the coils as shown in Figure 2.17(a). For the NIR source, the image of the tungsten filament should have fine stripes when in focus as shown in Figure 2.17 (b). At this point, cell measurements can be recorded and analyzed with LINEFIT to verify if the modulation efficiency and phase errors are acceptable. Finally, before starting solar measurements, the signal of the solar beam on the instrument detectors should be maximized by adjusting the sliding focusing mirror in the source compartment.

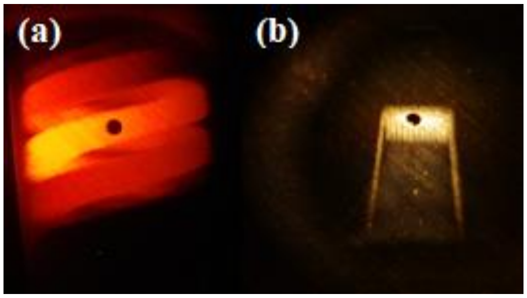

Figure 2.17: Photos of the images of (a) the MIR source, and (b) the NIR source on the aperture wheel. The black circle is the aperture. The image of the NIR source should present fine dark and bright stripes, which do not clearly stand out here because of the quality of the picture.

2.4 Solar Tracker

The original suntracker installed by ECCC in the early 1990s on the Bomem DA8 FTIR (the predecessor of the 125HR at Eureka) could track the sun passively using solar ephemeris calculations, or actively with a portion of the solar beam directed towards a photomultiplier tube working like a quadrant-diode system (Farahani et al., 2007; Fast et al., 2011). A quadrant-diode system traps the solar beam between four diodes by sending commands to the suntracker mirror to move the solar beam away from the diode that detects the highest brightness. This system was coupled to the Bruker 125HR in 2006 and was replaced in 2013 with a new Community Solar Tracker (CST) system. The suntracker development began at the University of Toronto as part of the Middle Atmosphere TRend Assessment (Strong et al., 2005) and PEARL projects (Adams, 2012). The CST development was continued at Dalhousie University by Jonathan Franklin during his PhD (Franklin, 2015) who refined the active tracking method using a camera. At Eureka, the suntracker mirror is installed inside a RoboDome (https://robodome.com/) on the roof of PEARL. The RoboDome is a telescope dome with a shutter, it protects the suntracker mirrors from bad weather. For solar measurements with the new system, a gold-coated elevation mirror is mounted on a platform that rotates in azimuth (see the elevation and azimuth rotational stages in Figure 2.18) and is controlled by the CST Python program. The elevation mirror directs light towards a second, static, gold-coated mirror that directs the light down towards the 125HR inside the laboratory. Part of the solar beam is captured by a camera that the CST program uses to actively track the sun. The program fits an ellipse to the image of the sun and sends instructions to the mirror, platform, and dome motors to follow the sun and keep the center of the ellipse at a given position as viewed by the camera. The tracker setup and tracking method are similar to those presented by Gisi et al. (2011). The CST tracking accuracy is within 20 arcseconds, while the quadrant-diode system had a tracking accuracy of up to hundreds of arcseconds and needed regular operator intervention. The CST can be operated remotely via a graphical user interface (GUI) developed by Jonathan Franklin to control the dome and solar tracker. The CST can actively track the sun using the camera, or passively based on a solar ephemeris calculation when the program fails to fit an ellipse to the sun's image. A schematic of the suntracker platform and mirrors is shown in Figure 2.18.

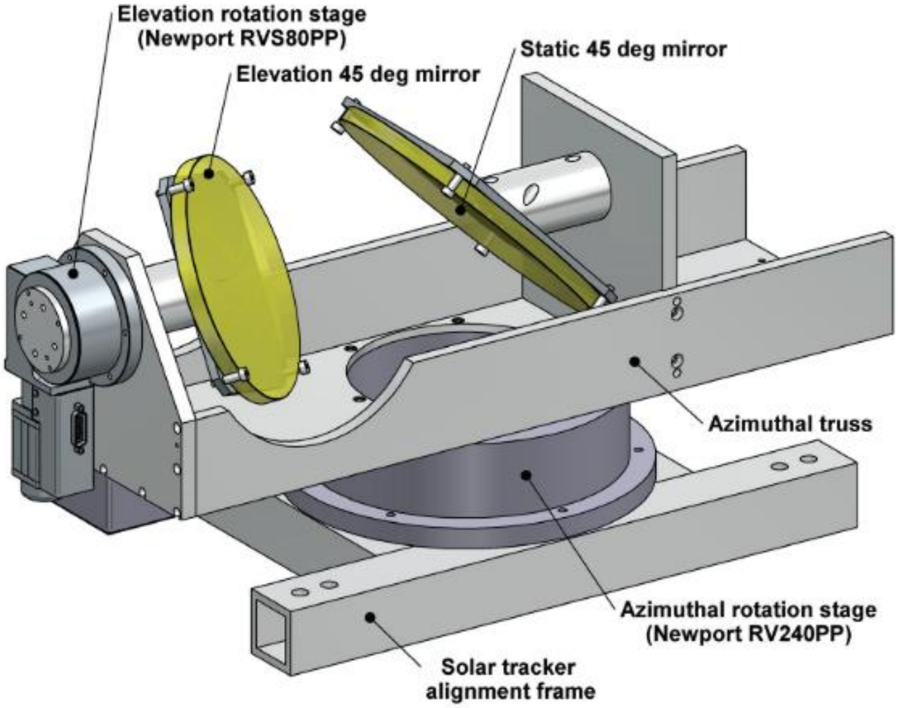

Figure 2.18: Schematic of the CST installed at Eureka in 2013. Figure obtained from Franklin (2015).

2.5 Ancillary Instruments

The 125HR is operated at low pressure (<0.5 hPa) using an Edwards nXDS15i dry scroll pump. To be processed with GGG, each solar spectrum must be associated with coincident auxiliary measurements: surface pressure, temperature, relative humidity, wind speed and direction. The surface pressure is an important input to process spectra with GFIT, while other measurements are used to filter out some interferograms, e.g. at high wind speeds (>30 m.s^{-1}). The surface pressure sensors and their measurements will be described in Sect. 4.5.

Chapter 3
Retrievals

This chapter describes how trace gas concentrations can be obtained from solar spectra. Section 3.1 introduces the principles of rovibrational spectroscopy that describe the structure of solar spectra. Section 3.2 presents the physical processes that give absorption lines their broad shapes, rather than the purely monochromatic transitions described in Sect. 3.1, and also describes the different line shape models.

Section 3.3 describes how ground-based solar spectra can be calculated as a function of the sun position and of the state of the atmosphere (vertical profiles of trace gas concentration, temperature, pressure, and other parameters). This function is called the forward model, and the goal of a retrieval algorithm is to adjust some of these parameters (or adjust factors that scale these parameters) until the calculated spectrum suitably matches a measured spectrum. The meaning of “suitably” can change between retrieval methods.

Section 3.4 describes the GFIT and GFIT2 retrieval algorithms. As introduced in Sect. 1.4, the TCCON retrieval algorithm, GFIT, is used to retrieve column-averaged dry-air mole fractions of atmospheric trace gases from solar absorption spectra. By construction, GFIT scaling retrievals do not contain more vertical information than the total column amount. The GFIT2 profile retrieval algorithm was implemented to experiment with extracting vertical information from solar spectra, and results from such experiments will be the subject of Chapter 5. GFIT scaling retrievals and GFIT2 profile retrievals are both based on the optimal estimation method described by Rodgers (2000) and summarized in Sect. 3.4. The scaling retrieval formulation is a special case of the profile retrieval; as shown in Sect. 3.5, it is possible to constrain the profile retrieval such that it produces the same results as a scaling retrieval. Thus, the more general formulation of the GFIT2 algorithm is presented first in Sect. 3.4.1, followed by the specifics of the GFIT algorithm in Sect. 3.4.2.

Finally, Sect. 3.5 describes the Averaging Kernels obtained from both retrievals. These hold information about the sensitivity and vertical resolution of the retrieval.

3.1 Rovibrational Spectroscopy

This section describes the transitions between rotational and vibrational energy levels that explain the distribution of lines in spectra. This section and the equations it contains follow the work of Hollas (2002, 2007a, 2007b, 2007c).

The wave function ψ that describes the state of a molecule can be divided into separate terms describing the rotational wave function ψ_r, the vibrational wave function ψ_v, and the electronic wave function ψ_e such that:

$$\psi = \psi_r \psi_v \psi_e. \tag{3.1}$$

Following the Born-Oppenheimer approximation, the total energy of the molecule is the sum of each component:

$$E = E_r + E_v + E_e. \tag{3.2}$$

Each of these energy modes is quantized and in general $E_r \ll E_v \ll E_e$.

3.1.1 Vibrational Energy

A molecule with N atoms has 3N degrees of freedom: each atom can move in three dimensions. Of these 3N, three describe a rotation of the whole molecule around each dimension, and a further three describe a translation of the whole molecule along each dimension. The remaining 3N-6 degrees of freedom are vibrational modes. A linear molecule has one less rotational degree of freedom as no energy is required for it to rotate around the inter-nuclear axis. Thus CO_2, which is linear, has $3N - 5 = 4$ vibrational modes. These are illustrated in Figure 3.1 with a symmetrical (ν_1) and asymmetrical (ν_3) stretching modes, and a doubly degenerate bending mode (ν_2) for in-plane and out-of-plane bending. These two bending modes have the same energy but are described by different vibrational wave functions. The bending modes require less energy than the stretching modes.

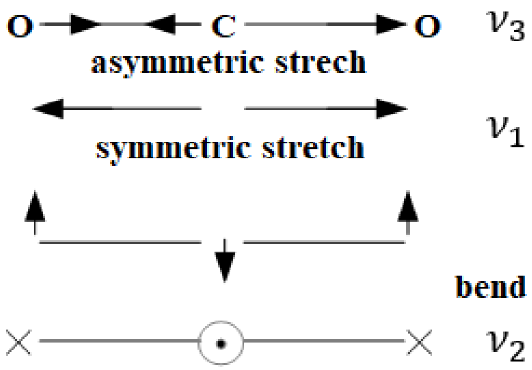

Figure 3.1: Vibrational modes of the CO_2 molecule. The bending mode is doubly degenerate with an in-plane and out-of-plane bending.

The bonds between atoms can be treated as springs, and diatomic molecules can be treated as anharmonic oscillators with quantized energy levels:

$$E_v = hc\sigma\left(v + \frac{1}{2}\right) - \chi\left(v + \frac{1}{2}\right)^2 + \cdots \tag{3.3}$$

where h is the Planck constant, c is the speed of light, σ is the wavenumber of the vibration, the integer v is the vibrational quantum number, and χ is an anharmonic constant. The value of σ depends on the bond strength between two atom and their reduced mass. If the anharmonicity is ignored, the unperturbed harmonic wavenumbers of each vibration mode of CO_2 are (Witteman, 1987):

$$\sigma_1 = 1351.2\ cm^{-1};\ \ \sigma_2 = 672.2\ cm^{-1};\ \ \sigma_3 = 2396.4\ cm^{-1}. \tag{3.4}$$

For a polyatomic molecule, each vibration “i”can be treated as an anharmonic oscillator and the total vibrational energy is:

$$E_v = hc\sum_i \sigma_i\left(v_i + \frac{d_i}{2}\right) + \sum_i\sum_j \chi_{ij}\left(v_i + \frac{d_i}{2}\right)\left(v_j + \frac{d_j}{2}\right) \tag{3.5}$$

where d_i is the degeneracy of the vibration. For CO_2 $d_{1,3} = 1$ and $d_2 = 2$. The energy levels of vibrational modes of polyatomic molecules are complicated by their dependence on other vibrational modes in the anharmonic term (when $i \neq j$).

For anharmonic oscillators, the transition rule between two vibrational energy levels follows:

$$\Delta v = \pm 1, \pm 2, \pm 3, \ldots \ . \tag{3.6}$$

When $\Delta v \geq 2$, the transition is called a vibrational overtone. A molecule has a rotational spectrum in the infrared if it has a non-zero electric dipole moment. CO_2 has no dipole moment during a symmetric stretch, but it has a dipole moment during an asymmetric stretch because of the unequal C=O bonds, and when it is bent.

3.1.2 Rotational Energy

In the rigid rotor approximation, the rotational energy of a diatomic or linear polyatomic molecule can be expressed as:

$$E_r = BJ(J+1) \tag{3.7}$$

where J is the rotational quantum number and B is a rotational constant that depends on the moment of inertia I of the molecule:

$$B = \frac{h^2}{8\pi^2 I};\ I = \mu r^2 \tag{3.8}$$

where r is the bond length between two atoms, and μ is their reduced mass. For a polyatomic molecule with N, atoms the moment of inertia is:

$$I = \sum_{i=1}^{N} m_i r_i^2 \tag{3.9}$$

where m_i is the mass of the ith atom and r_i is its distance from the center of mass of the molecule.

The “constant” B actually depends on the vibrational state:

$$B_v = B_e - \alpha\left(v + \frac{1}{2}\right) \tag{3.10}$$

where α is the vibration-rotation interaction constant, and B_e is the rotational constant for the equilibrium bond length when no vibration is taking place.

The rotation occurs along any axis passing through the center of mass of the molecule. For a linear molecule like CO_2, the axis of rotation is orthogonal to the internuclear axis. If the CO_2 molecule is in a bending vibrational mode it behaves like a non-linear, prolate symmetric top molecule, and its moment of inertia has three components along orthogonal axes a, b, and c passing through the center of mass and $I_a \ll I_b = I_c$. There are then three rotation constants A, B, and C, with B=C. A linear molecule is a special case of a prolate symmetric top with $I_a = 0$:

$$A = \frac{h^2}{8\pi^2 I_a};\ C = B = \frac{h^2}{8\pi^2 I_b}. \tag{3.11}$$

The rotational energy levels are then described with an additional rotational quantum number *K*:

$$E_r = BJ(J+1) + (A-B)K^2. \tag{3.12}$$

Since $I_a < I_b$, the quantity $A - B$ is always positive and the energy for a given J increases with increasing K. The magnitude of the rotational angular momentum along the axis of rotation is $\hbar\sqrt{J(J+1)}$ and its projection on the a-axis is $k\hbar$ with $K = |k| = 0, 1, 2, \dots, J$, and with $\hbar = \frac{h}{2\pi}$. Rotational energy with a given *K* is doubly degenerate; it can have the same value in two opposite directions along the a-axis. Thus, for each rotational quantum number J, there are $2J + 1$ possible values of k. In the linear configuration we indeed have $A = \infty$, but the rotational angular momentum of a linear molecule is always orthogonal to the internuclear axis and $K = 0$.

The rotational energy levels are further affected by centrifugal distortion, where the rotation causes a stretching of the atomic bonds away from the center of mass due to centrifugal force. This slows down the rotation. Additional terms can be added to the expression of rotational energy to account for this effect:

$$E_r = BJ(J+1) + (A-B)K^2 - D_J[J(J+1)]^2 + \cdots \tag{3.13}$$

where D_J is the positive centrifugal distortion constant of the quartic term, and higher-order terms may be added each with their own constant. As suggested by the subscript, there is a specific D_J for each value of the rotational quantum number J.

3.1.3 Rovibrational Transitions

The rovibrational energy of a polyatomic molecule is the sum of its rotational energy and vibrational energy:

$$E_{rv} = hc\left[\sum_i \sigma_i\left(v_i + \frac{d_i}{2}\right) + \sum_i\sum_j \chi_{ij}\left(v_i + \frac{d_i}{2}\right)\left(v_j + \frac{d_j}{2}\right) + \sum_i A_v\varphi_{ii}^2 l_i^2 - A_v\varphi_{ii}l_i k \right.$$
$$\left. + B_v J(J+1) + (A_v - B_v)K^2 - D_J J^2(J+1)^2\right]. \quad (3.14)$$

For degenerate fundamental vibration modes like the two perpendicular v_2 bending modes of CO_2, a mixture of the two modes generates angular momentum that contributes the additional terms:

$$\sum_i A_v\varphi_{ii}^2 l_i^2 - A_v\varphi_{ii}l_i k \quad (3.15)$$

where l is the quantum number describing the projection of the resulting angular momentum on the a-axis, with $|l| = v_2, v_2 - 2, v_2 - 4, \dots, 0\ or\ 1$; ending with 0 or 1 if v_2 is even or odd, respectively. The coefficient φ is a Coriolis coefficient which is always equal to 1 for linear molecules.

A molecule can transition between rovibrational states following transition rules:

$$\Delta v = \pm 1, \pm 2, \pm 3, \dots\ ; \Delta J = 0, \pm 1\ ; \Delta K = 0. \quad (3.16)$$

Due to these rules, rovibrational absorption spectra take the form of bands centered on the wavenumber corresponding to the transition between the upper and lower vibrational state and with two groups of absorption lines above and below that wavenumber that correspond to the possible transitions between rotational levels. When the rotational quantum number of the lower state is lower than that in the upper state we have $\Delta J = +1$ and this forms the R branch of a band with absorption lines at wavenumbers higher than the band center. The P branch is at wavenumbers lower than the band center, corresponding to $\Delta J = -1$. Each line of a branch is typically labelled using the J value of the lower energy level such that $R(J-1)$ and $P(J+1)$ correspond to a transition to (in absorption) or from (in emission) the same upper level J.

In the rigid rotor approximation, the line spacing is constant throughout a rovibrational band of a diatomic molecule and is equal to $2B$. However due to centrifugal distortion the spacing in the R branch decreases away from the band center, with increasing J, while the spacing in the P branch increases away from the band center, also with increasing J. This effect is relatively small for CO_2 because of the strength of C=O bonds. It would be more pronounced for rovibrational bands of molecules with weaker single bonds.

The case with $\Delta J = 0$ is only possible when the change in dipole moment is perpendicular to the the principal axis of symmetry of the molecule and leads to absorption lines close to each other near the band center, with a spacing of $2(A-B)$. If the difference between A and B is small, all the lines appear at the same position and will look like a very intense single line. These transitions form the Q branch. For CO_2, this only occurs for transitions involving the v_2 bending modes when $K \neq 0$. Another rule for these perpendicular bands is $\Delta K = \pm 1$, while $\Delta K = 0$ applies when the change in dipole moment is parallel to the principal axis of symmetry. These selection rules for rovibrational transitions are summarized in Table 3.1.

Table 3.1: Selection rules for rovibrational transitions.

Δv	ΔJ	ΔK	K	Change in dipole moment relative to principal axis of symmetry
$\pm 1,2,3$	± 1	0	0	Parallel
	$0, \pm 1$	0	$\neq 0$	
	$0, \pm 1$	± 1		Perpendicular

CO_2 is a special case, as the wavenumber σ_1 of the symmetric stretch mode is almost equal to twice the wavenumber σ_2 of the bending mode. Thus, a CO_2 molecule can have almost equal energy levels with different combinations of v_1 and v_2 vibrations; this is called Fermi resonance (Amat and Pimbert, 1965). When two vibrational modes are in Fermi resonance, their spacing in energy is increased. One notation describing a vibrational energy level could be made with the vibrational quantum numbers $(v_1 v_2 l_2 v_3)$ including the vibrational angular momentum quantum number l_2, set equal to v_2. But to distinguish levels in Fermi resonance, a fifth number n is added $(v_1 v_2 l_2 v_3 n)$ in the High-resolution Transmission Molecular Absorption Database (HITRAN) spectroscopic parameters (Rothman et al., 2005, 2009, 2013; Gordon et al., 2017). This number is used to differentiate vibrational states in Fermi resonance with $n > 1$ from other vibrational states with $n = 1$. To convert from the five-number notation to the four-numbers notation, for each unit of n above one, v_1 should be reduced by 1 and v_2 should be increased by 2 (Toth et al., 2008). For example, (10002) corresponds to (0220). A sixth number can also be used to differentiate the degenerate v_2 modes; it characterizes the symmetry, or parity, of the molecule. It is equal to 1 for non-degenerate states and is equal to either 1 (alternatively using the letter e), or 2 (alternatively using the letter f) for states with $l_2 \neq 0$ (Brown et al., 1975; Toth et al., 2008).

To derive its public XCO_2 products, TCCON uses two spectral windows centered at 6220 and 6339.5 cm^{-1}. The main $^{12}C^{16}O_2$ bands in these windows correspond to the transition between rovibrational levels $(30013) - (00001)$ and $(30012) - (00001)$, respectively. With the four-number notation, these would be $(1401) - (0000)$ and $(2201) - (0000)$, respectively, both with $l_2 = 0$ and thus without a Q branch. The $(30013) - (00001)$ rovibrational band is shown in Figure 3.2, which also includes weak CO_2 lines from overlapping bands. In this CO_2 band, transitions from odd-J in the lower state do not exist and the line spacing is close to $4B$ instead of $2B$. This constraint comes from additional rules for electric dipole transitions between states based on the change in parity of the total wave function of the molecule. For a more detailed discussion, see di Lauro (2020b, 2020a).

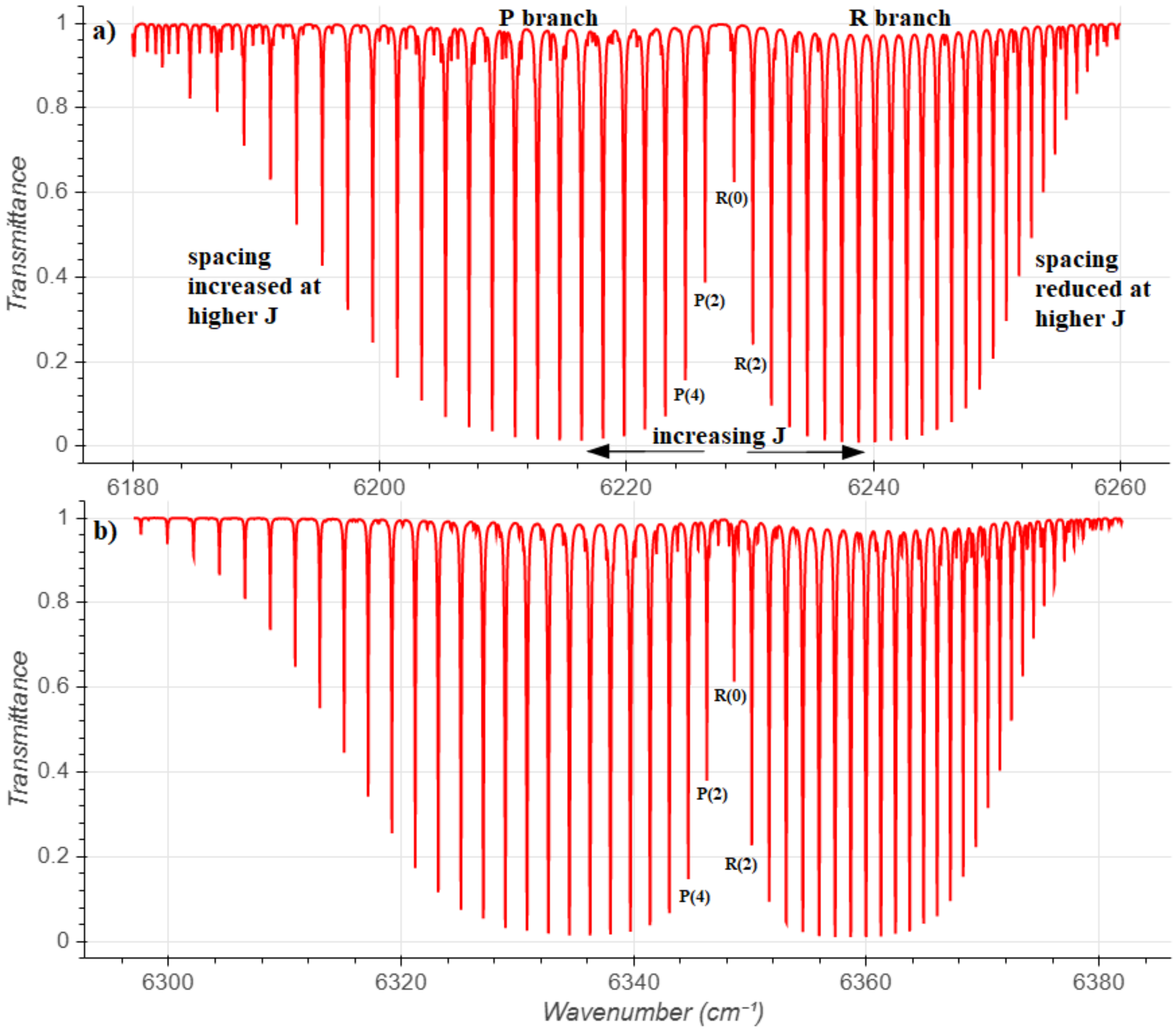

Figure 3.2: Rovibrational transmittance spectrum of CO_2 in the TCCON window centered at (a) 6220 cm^{-1}. The lines correspond mainly to the $(30013) - (00001)$ band. The effect of centrifugal distortion is apparent with an increased spacing at higher *J* in the *P* branch and a reduced spacing in the *R* branch. In (b), the same plot is shown for the window centered at 6339 cm^{-1} with the main lines corresponding to the $(30012) - (00001)$ band. Not all the lines shown in these figures are from the main band, for example the weak lines overlapping the *P* branch in (a) correspond to a different CO_2 band centered at ~6195 cm^{-1}.

As indicated by their fifth label, the (30013) and (30012) levels are two of four levels in Fermi resonance, the $v_1 + 4v_2 + v_3$ and $2v_1 + 2v_2 + v_3$ levels, respectively. The other two levels of the tetrad are the $3v_1 + v_3$ and $6v_2 + v_3$ levels. The two TCCON bands both correspond to transitions from the ground state (00001). Transitions from the ground state to the two other levels form bands centered close to 6076 cm^{-1} and 6503 cm^{-1}, respectively. Another noticeable band in this spectral region is the $(00031) - (00001)$ band, from the ground state to the second overtone

($v_3 = 3$) of the asymmetric stretch mode with a center close to 6972 cm^{-1}. The effect of the Fermi resonance is to cause a splitting of energy levels compared to where they would be expected in the unperturbed anharmonic case. For example, in the unperturbed case, the (30013) level would be close to 6285 cm^{-1}, but because of the resonance with the other levels of the triad, it is found close to 6228 cm^{-1} instead. Similarly the (30011) level is found close to 6503 cm^{-1} instead of the expected 6273 cm^{-1} (Suzuki, 1968).

In Chapter 5, we will use this Fermi tetrad of CO_2 bands as well as a strong band, with intense absorption resulting from $(20013) - (00001)$ transitions, to investigate the feasibility of retrieving vertical profiles of atmospheric CO_2 concentration.

3.2 Absorption Line Profiles

Section 3.1 described the structure of rovibrational bands, where each transition between two rovibrational energy levels is characterized by a unique wavenumber. However physical processes contribute to the broadening of these lines. This section describes the line profiles that characterize the shape of absorption lines. It follows the work of Brown et al. (1992), Lévy et al. (1992), and Hartmann et al. (2008).

One of the parameters the forward model uses to calculate spectra is the absorption coefficient k. It depends on the intensity of the transition S at the wavenumber σ_0 and on the line profile $f(\sigma - \sigma_0)$ that describes the shape of the absorption line about the line center:

$$k(\sigma) = Sf(\sigma - \sigma_0)\,. \tag{3.17}$$

The line intensity S at temperature T is given by (Rothman et al., 1998):

$$S(T) = S(T_{ref})\frac{Q(T_{ref})}{Q(T)}\frac{e^{-\frac{hcE''}{k_BT}}}{e^{-\frac{hcE''}{k_BT_{ref}}}}\frac{\left[1 - e^{-\frac{hc\sigma_0}{k_BT}}\right]}{\left[1 - e^{-\frac{hc\sigma_0}{k_BT_{ref}}}\right]} \tag{3.18}$$

where $S(T_{ref})$ is the line intensity at a reference temperature and is part of the spectroscopic line parameters in the HITRAN databases ($T_{ref} = 296\ K$ in HITRAN linelists), Q is the total internal partition function, h is the Planck constant, c is the speed of light, E'' is the lower state energy, and k_B is the Boltzmann constant.

3.2.1 Pressure Broadening

At lower altitudes, where the pressure is high, spectral line shapes are mainly affected by broadening by collisions and can be described by a Lorentz profile:

$$f_L(\sigma, \sigma_0, T, P) = \frac{1}{\pi} \frac{\gamma_L}{\gamma_L^2 + [\sigma - \sigma_0 - \delta \mathrm{P}]^2} \tag{3.19}$$

where T is the air temperature, P is the pressure, δ is the pressure shift, a displacement of the transition wavenumber that depends on pressure, γ_L is the Lorentzian half-width at half-maximum (HWHM) defined for a given molecule with partial pressure P_{self} as (Predoi-Cross et al., 2009; Devi et al., 2016):

$$\gamma_L(P, T) = \left(\frac{T_{ref}}{T}\right)^{n_{air}} \gamma_{air}(P_{ref}, T_{ref})(P - P_{self}) + \left(\frac{T_{ref}}{T}\right)^{n_{self}} \gamma_{self}(P_{ref}, T_{ref}) P_{self} \,. \tag{3.20}$$

Here $P_{ref} = 1\ atm$ and $T_{ref} = 296\ K$ are the reference pressure and temperature, γ_{air} is the half-width broadening coefficient that characterizes broadening due to collisions between the given molecule and different molecules in air, γ_{self} is the half-width broadening coefficient that characterizes broadening due to collisions between the given molecule with same molecules, and n_{air} and n_{self} are the temperature dependence exponents of the air- and self-broadening coefficients, respectively.

The pressure shift is obtained as (Devi et al., 2016):

$$\delta(\mathrm{P}, \mathrm{T}) = \delta_{\mathrm{air}} \left[1 - \frac{P_{self}}{P}\right] + \delta_{self} \frac{P_{self}}{P} \tag{3.21}$$

where the air- and self- pressure shift parameters are expressed as a function of the shift at T_{ref} and a pressure-induced shift coefficient δ' such that (Devi et al., 2016):

$$\delta_{GAS}(T) = \delta_{GAS}(T_{ref}) + \delta'[T - T_{ref}]. \tag{3.22}$$

In practice, the forward model does not compute spectroscopic parameters such as transition wavenumbers, intensities, and the pressure-broadening coefficients from theoretical equations. GGG uses a “linelist” that compiles these parameters from different versions of the HITRAN database and other spectroscopic literature in order to produce a list with parameters that best fit observations. This compilation is done because newer HITRAN versions do not always improve fits in all spectral regions and for all absorbers. When necessary, the resulting “atm” linelist also includes empirical corrections to the spectroscopic parameters (Toon et al., 2016a). The GFIT/2 (GFIT and GFIT2) forward model uses these parameters to compute the absorption coefficients described by Eq. 3.17. For the CO_2 bands used by TCCON, the line parameters are determined experimentally using a multispectrum nonlinear least squares fitting technique with laboratory spectra (Benner et al., 1995). The technique has been applied in the $(30013) - (00001)$ (Devi et al., 2007, 2016), $(30012) - (00001)$ (Malathy Devi et al., 2007), and $(20013) - (00001)$ (Benner et al., 2016) bands. In these studies, the line position in wavenumber is defined as:

$$\begin{aligned}\sigma = G' - G'' + \{B'J'(J' + 1) - D'[J'(J' + 1)]^2 + H'[J'(J' + 1)]^3\} \\ - \left\{B''J''(J'' + 1) - D''[J''(J'' + 1)]^2 + H''\left[J''(J'' + 1)\right]^3\right\} \quad (3.23)\end{aligned}$$

where J' is the rotational quantum number of the upper state and J'' that of the lower state, and $G' - G''$ is the difference in vibrational wavenumber between the two states. Equation 3.23 is the difference between two levels with energies described by Eq. 3.14, with $k = 0$ and including the sextic term (in J) of the centrifugal distortion effect in addition to the quartic term. The multispectrum fits solve for the constants G, B, D, and H.

3.2.2 Doppler Broadening

Spectral line profiles are also affected by Doppler-broadening that arises because of the motion of molecules relative to the direction of propagation of the radiation. This causes a shift in the transition frequency. The velocity of a molecule along the direction of propagation of the radiation can be described by the Maxwell-Boltzmann distribution. At temperature T, the most probable velocity of a molecule of mass m is $V_p = \sqrt{\frac{2k_BT}{m}}$, where k_B is the Boltzmann constant. Due to Doppler broadening, the frequency ν of a transition becomes $\frac{\nu V_m}{c}$, where V_m is the mean velocity of the distribution. At high altitudes, this broadening is much larger than the pressure broadening, and the line profile is Gaussian and can be described by:

$$f_G(\sigma, \sigma_0, T) = \sqrt{\frac{ln2}{\pi \gamma_D^2}} e^{-\frac{(\sigma-\sigma_0)^2 ln2}{\gamma_D^2}} \tag{3.23}$$

where ln is the natural logarithm and γ_D is the HWHM of the Doppler-broadened line. The HWHM is defined by:

$$\gamma_D = \frac{\sigma_o V_p \sqrt{ln2}}{c} = \frac{\sigma_0}{c} \sqrt{\frac{2N_A kT ln2}{M}} \; . \tag{3.24}$$

Here N_A is the Avogadro constant, M is the molar mass of the molecule in grams, k_B is the Boltzmann constant, c is the speed of light, and T is the temperature. The $\sqrt{ln2}$ term in Eq. 3.23 and Eq. 3.24 arises from using the HWHM rather than the standard deviation (STD) of the normal distribution ($\frac{1}{e}$ half width). As a reminder, the HWHM is related to the STD as $HWHM = 2\sqrt{2ln2}\, STD.$

Since the pressure-broadened HWHM depends on pressure, retrieval algorithms can exploit line shapes to retrieve trace gas concentrations at different altitudes, but this altitude-dependent information becomes more difficult to extract when the HWHM of the Gaussian profile becomes larger than that of the Lorentzian profile. And since the Doppler HWHM increases with increasing wavenumber, this “ceiling” for vertical information moves to lower altitudes at higher wavenumbers (for a given temperature). This is illustrated in Figure 3.3, where γ_L and γ_D were derived for a given temperature, pressure, and CO_2 concentration profile using Eq. 3.20 and Eq. 3.24. The spectroscopic parameters required by Eq. 3.20 ($n_{air}, \gamma_{air}, and\ \gamma_{self}$) were obtained from the GGG2020 linelist (atm.161) (Toon et al., 2016a). Vertical information is more difficult to derive for altitudes higher than at the intersection of the γ_L and γ_D curves. In the strong $(20013) - (00001)$ CO_2 band (near 4852 cm^{-1}) the vertical information is “Doppler limited” to up to ~20-25 km depending on the transition. Because of the wavenumber dependence of γ_D, the limit is at ~18-23 km in the $(30011) - (00001)$ band (near 6500 cm^{-1}). In the mid-infrared (at wavenumbers below ~3333 cm^{-1}), the limit is at higher altitudes, for example in the $(01101)-(00001)$ CO$_2$ band (near 672 cm^{-1}) the Gaussian HWHM curves intersect the Lorentzian curves at ~31-37 km.

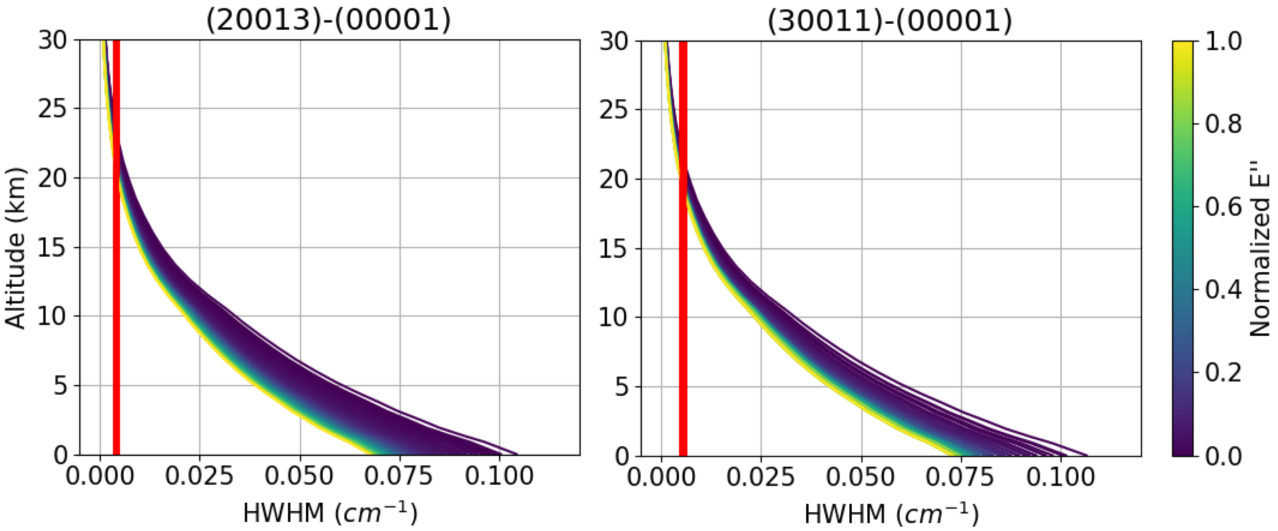

Figure 3.3: Half-width at half maximum of the Gaussian profile (red), and of the Lorentz profile for all transitions of the $(20013)-(00001)$ CO$_2$ band centered at ~4852 cm^{-1} (left), and of the $(30011)-(00001)$ band centered at ~6500 cm^{-1} (right). The Lorentz HWHM lines are coloured by the normalized lower state energy (E'') of the corresponding transition.

The HWHM of the Gaussian profile is affected by the "Dicke narrowing" effect due to the higher probability that the velocity of a molecule decreases rather than increases after a collision. This reduces the mean velocity and leads to a narrower Gaussian profile (Hartmann et al., 2008b).

3.2.3 The Voigt Profile

As the Gaussian shape due to Doppler broadening dominates at low pressure, and the Lorentzian shape due to pressure broadening dominates at high pressure, the convolution of the two profiles is often used to account for both effects. This convolution is called the Voigt Profile. This combined profile can be expressed as (Boone et al., 2011):

$$f_{VP} = \frac{1}{\gamma_D}\sqrt{\frac{ln2}{\pi}}\mathbb{R}\{K(x,y) + iL(x,y)\} \tag{3.25}$$

$$K(x,y) = \frac{y}{\pi}\int_{-\infty}^{+\infty}\frac{e^{-t^2}}{y^2+(x-t)^2}dt \quad ; L(x,y) = \frac{1}{\pi}\int_{-\infty}^{+\infty}\frac{(x-t)e^{-t^2}}{y^2+(x-t)^2}dt \tag{3.26}$$

with $\mathbb{R}\{a\}$ indicating the real part of a, i the imaginary unit such that $i^2 = -1$, and with the dimensionless variables $x = \frac{(\sigma - \sigma_0 - \delta P)\sqrt{ln2}}{\gamma_D}$ and $y = \frac{\gamma_L \sqrt{ln2}}{\gamma_D}$.

The Voigt Profile is the line shape used by GGG versions up to GGG2014, and for most bands in GGG2020. The Voigt Profile is based on several approximations or assumptions:

1. A molecule rovibrational state does not change during collisions (no line mixing, see Sect. 3.5.4).
2. Collisions do not alter the velocity distribution of molecules (no Dicke narrowing).
3. The Lorentz HWHM γ_L and pressure shift δ depend only on the mean velocity of molecules.

With increasing precision standards for trace gas retrievals, the Voigt Profile has become inadequate and is being replaced with more complex line profiles in spectroscopic databases (Tran et al., 2013). Section 3.2.4 describes one of these that addresses the third approximation of the Voigt Profile, and Sect. 3.2.5 describes a further development that addresses the first approximation.

3.2.4 The Speed-Dependent Voigt Profile

The Voigt Profile can be improved by taking into account the speed dependence of the collisional broadening, addressing the third assumption made for the Voigt Profile. The line shape is then the weighted sum of Voigt Profiles for a range of absolute velocities with the weights determined by the Maxwell-Boltzmann distribution of velocities. The speed dependence of the Lorentzian HWHM and pressure shift can be expressed as (Tran et al., 2013):

$$\begin{aligned}\gamma_L(V) + i\delta(V)P &= [\gamma_L(V_m) + i\delta(V_m)P] + [\gamma_L(V_m)S_\gamma + i\delta(V_m)S_\delta P]\left[\left(\frac{V}{V_p}\right)^2 - 1.5\right] \\ &= C_0 + C_2\left[\left(\frac{V}{V_p}\right)^2 - 1.5\right] \qquad (3.27)\end{aligned}$$

where S_γ and S_δ are the speed-dependent parameters of γ_L and δ, respectively. The quadratic Speed-Dependent Voigt Profile (qSDV) can be expressed as (Tran et al., 2013):

$$f_{qSDV} = \frac{1}{\gamma_D}\sqrt{\frac{ln2}{\pi}}\mathbb{R}\{w(iZ_1) - w(iZ_2)\} \tag{3.28}$$

$$Z_1 = \sqrt{X+Y} - \sqrt{Y}\,; \quad Z_2 = \sqrt{X+Y} + \sqrt{Y} \tag{3.29}$$

$$X = \frac{i(\sigma - \sigma_0) + C_0 - 1.5C_2}{C_2}; \; Y = \left(\frac{\gamma_D}{2C_2\sqrt{ln2}}\right)^2 . \tag{3.30}$$

Here, $w(z)$ is the complex probability function defined as:

$$w(z) = \frac{i}{\pi}\int_{-\infty}^{+\infty} \frac{e^{-t^2}}{z-t}dt = e^{-z^2}erfc(-iz) \tag{3.31}$$

with $erfc$ the complementary error function:

$$erfc(z) = 1 - \frac{2}{\sqrt{\pi}}\int_0^z e^{-t^2}dt\,. \tag{3.32}$$

3.2.5 Line Mixing

An assumption of the Voigt Profile is that transitions are collisionally isolated, that is, collisions cannot change the rovibrational state of a molecule. However, collisions can cause transfers of population between energy levels of a molecule. This is illustrated in Figure 3.4 for two transitions, one from lower level l to upper level u, and another from lower level l' to upper level u'. A molecule can go from l to u through two different paths: first by absorbing a photon with wavenumber σ_{lu}; or second, initially in the lower level l but transferred to level l' by collision, then transferred to u' by absorbing a photon with wavenumber $\sigma_{l'u'}$, and finally transferred to u by another collision. This process transfers intensity from a part of the absorption line centered at σ_{ul} to the line centered at $\sigma_{l'u'}$. Similarly, the blue path transfers intensity from a part of the absorption line centered at $\sigma_{l'u'}$ to the line centered at σ_{ul}. This effect is significant when $\gamma_L > |\sigma_{lu-}\sigma_{l'u'}|$ (Hartmann et al., 2008a), at high pressures or between closely spaced lines. The mixing between two lines do not cancel each other, as the transfer of intensity is from regions of weak absorption to regions of strong absorption. Typically, the intensity of the peaks of two coupled lines, and of the trough between them, will increase and the intensity of the wings will decrease.

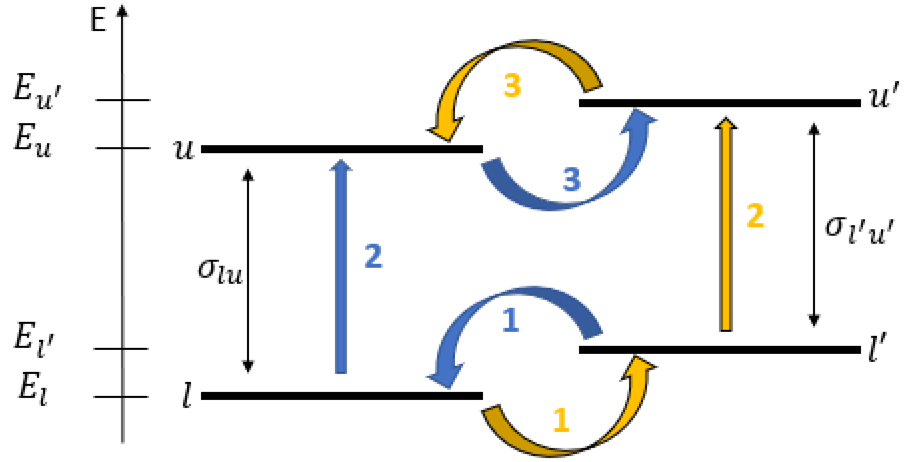

Figure 3.4: Schematic of line mixing between the transition from lower level l to upper level u and the transition from lower level l' to upper level u'. The filled arrows numbered 1 and 3 correspond to collisionally induced transfer of population between l and l' or between u and u'. The filled arrows numbered 2 correspond to transitions due to the absorption of a photon. The yellow path corresponds to a transfer of intensity from the absorption line centered at σ_{ul} cm^{-1} to the one centered at $\sigma_{l'u'}$ cm^{-1}. The blue path corresponds to a transfer of intensity from the absorption line centered at $\sigma_{l'u'}$ cm^{-1} to the one centered at σ_{ul}cm^{-1}. Based on Figure IV.1 in Hartmann et al. (2008a).

When including the effect of line mixing (LM) with the qSDV, the line profile becomes (Ngo et al., 2013):

$$f_{qSDV+LM} = \frac{1}{\gamma_D}\sqrt{\frac{ln2}{\pi}}\left[\mathbb{R}\{w(iZ_1) - w(iZ_2)\} + Y_l \mathbb{I}m\{w(iZ_1) - w(iZ_2)\}\right] \tag{3.33}$$

with X, Y, Z_1 and Z_2 previously defined for Eq. 3.28, and Y_l the Rosenkranz first-order line coupling coefficient (Rosenkranz, 1975; Hartmann et al., 2008a). $\mathbb{I}m\{a\}$ is the imaginary part of a.

The qSDV line shape is a special case of more detailed line shapes that can address the second assumptions for the Voigt Profile listed in Sect. 3.2.3. These profiles are described in Hartmann et al. (2008b) and Tran et al. (2013).

The qSDV+LM line shape was implemented in GGG2020 for the $(30013) - (00001)$, $(30012) - (00001)$, and $(20013) - (00001)$ CO_2 bands (Mendonca et al., 2016), for the CH_4

$2\nu_3$ band centered near 6000 cm^{-1} (Mendonca et al., 2017), and for the O_2 band centered near 7885 cm^{-1} (Mendonca et al., 2019). The *R* branch of the CH_4 $2\nu_3$ band overlaps with the CO_2 $(30011) - (00001)$ band centered near 6073 cm^{-1}, hence reducing the interfering effect of CH_4 lines when retrieving CO_2 in that band. The largest improvement to spectral fits from the Voigt Profile to qSDV+LM is in the strong $(20013) - (00001)$ CO_2 band, which is more strongly affected by LM than the other CO_2 bands of this Fermi tetrad. Figure 3.5 illustrates this improvement with spectral fit residuals using the Voigt Profile or qSDV+LM profile in the $(20013) - (00001)$ CO_2 band using real measured spectra. The RMS of residuals decreased from more than ~2% to less than ~0.9%.

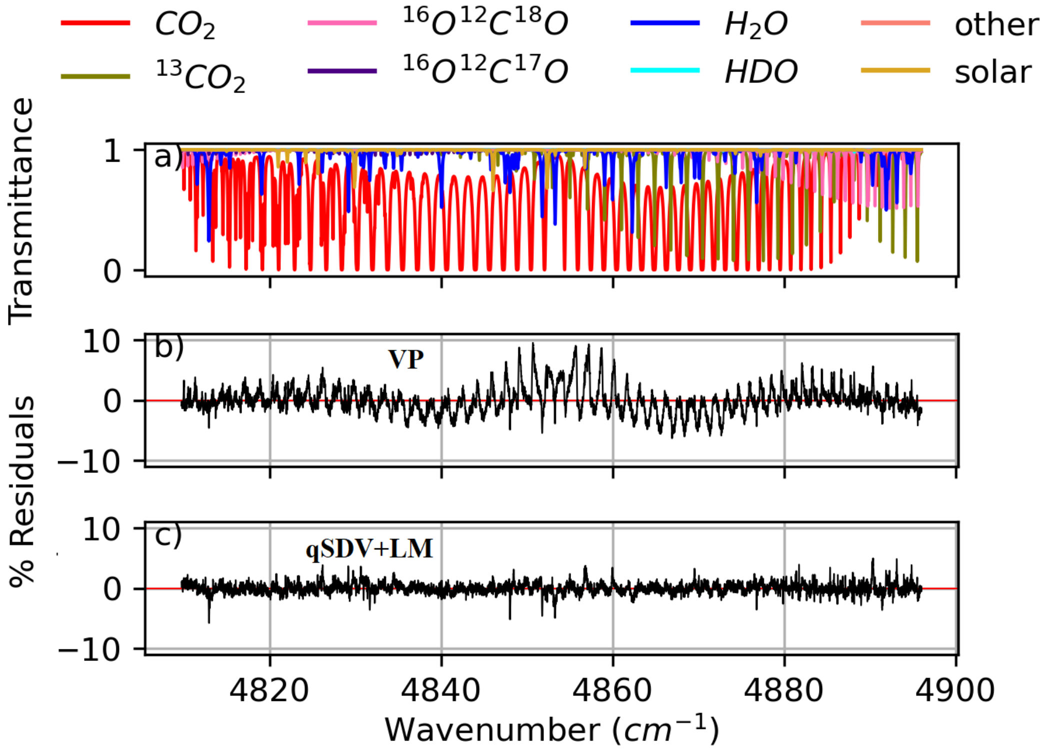

Figure 3.5: Spectral fit residuals in the $(20013) - (00001)$ CO_2 band using (b) the Voigt Profile, and (c) the qSDV+LM profile. The calculated contribution of each absorber to the transmittance spectrum is shown in (a).

Improvements to the line shape model used in the forward model should also improve our ability to retrieve vertical profile information about atmospheric trace gas concentrations. Connor et al. (2016) first tested the GFIT2 profile retrieval algorithm for the $(30013) - (00001)$ CO_2 band centered near 6220 cm^{-1} using GGG2014 with the Voigt Profile. Chapter 5 will present a follow-up evaluation of GFIT2 using the improvements in GGG2020, including the qSDV+LM profile in CO_2 bands. The qSDV+LM allowed for the inclusion of the strong CO_2 window, which contains the $(20013) - (00001)$ band, as its spectral fit residuals are now more comparable to those in the other TCCON CO_2 windows. This is of interest because the pressure-broadened lines of the strong band should contain useful information on the vertical distribution of CO_2 in the lower troposphere.

In Chapter 6, the retrieval algorithm used to simulate observations from the proposed AIM-North satellite mission also includes qSDV+LM profiles and uses the strong $(20013) - (00001)$ and weak $(30013) - (00001)$ CO_2 bands.

3.3 Forward Model

The structure of spectra and absorption lines have been described in Sect. 3.1 and 3.2. Section 3.3 describes how this information is used in the forward model of GFIT/2.

The Beer-Lambert law describes how the intensity I_o of a monochromatic light is affected by its passage through a medium of length L, containing an absorbing species with number density n:

$$I(\sigma, g) = I_o(\sigma) e^{-k(\sigma, \mathrm{f_g}, P, T) n(f_g, P, T) L} \tag{3.34}$$

where k is the absorption coefficient of a species at wavenumber σ as described by Eq. 3.17, f_g is the mole fraction of gas g, and P and T are the pressure and temperature of the medium, respectively. The term knL is called the optical depth of the medium for the wavenumber σ and gas g. The number density $n(f_g, P, T)$ follows the ideal gas law:

$$n(f_g, P, T) = \frac{f_g N_a P}{RT} \tag{3.35}$$

where N_a is the Avogadro constant and R is the gas constant. In GFIT/2, the mole fraction is not the adjusted parameter, but instead a scaling factor is retrieved.

In terms of transmittance Tr:

$$Tr(\sigma, f_g, P, T, L) = e^{-k(\sigma, \mathrm{f_g}, P, T) n(f_g, P, T) L} \tag{3.36}$$

when multiple absorbing species are present the resulting transmittance spectrum is the product of the transmittance spectrum of each species:

$$Tr(\sigma, P, T, L) = e^{-\sum_g k(\mathrm{\sigma}, \mathrm{f_g}, P, T) n(f_g, P, T) L} . \tag{3.37}$$

Finally, in the forward model the atmosphere is divided into a user-specified number of layers. The total transmittance through the atmosphere is the product of the transmittance through each layer:

$$Tr_{tot}(\sigma, P, T) = e^{-\sum_i \sum_g k(\mathrm{\sigma}, \mathrm{f_g}, \mathrm{P}, \mathrm{T})_i n(f_g, P, T)_i L_i} . \tag{3.38}$$

The absorption coefficients are calculated for each atmospheric level i, each associated with a layer width L above it. Here the absorption coefficient is also a function of the atmospheric level because it is a function of the temperature and pressure which will be different at each altitude. In GFIT the retrieved column scale factor would appear outside of the sum over levels (and inside the sum over gases) in Eq. 3.38, while in GFIT2 a scale factor would be retrieved at each level.

A retrieval algorithm functions by comparing a calculated spectrum to a measured spectrum, and then iteratively adjusts retrieval parameters until the calculated spectrum suitably matches the measurement. A new spectrum is calculated at each iteration with the adjusted parameters. The spectrum calculated by the forward model is:

$$S(\sigma) = ILS(\sigma_{center}) * (cont(\sigma) \times [Tr_{tot}(\sigma) \times SPTS(\sigma) + ZLO]) \tag{3.39}$$

where $*$ indicates a convolution operation, and $\times$ a multiplication. The ILS was described mathematically in Eq. 2.19. The ILS is computed using the central wavenumber σ_{center} of the spectral window. The function $cont$ describes the continuum of the spectrum, which is the form the spectrum would have in the absence of absorbers. $SPTS$ is the solar pseudo-transmittance spectrum, the solar spectrum with absorption features caused by gases in the atmosphere of the sun. Finally, ZLO is the zero-level offset; it is typically zero. There is a zero-level offset when the tip of a saturated absorption line does not have a transmission value equal to zero. The ZLO value can be retrieved in spectral windows that contain saturated lines. Zero-level offsets can arise because of detector non-linearity with respect to the incoming photon flux (Abrams et al., 1994;

Corredera et al., 2003; López et al., 2010). Above a given photon flux the electric signal output by a detector is no longer linearly dependent on the photon flux, without a correction this would lead to erroneous signal intensity in the interferogram, especially for the center burst at zero path difference. Although GGG includes a non-linearity correction scheme for the interferograms, these are not perfect and small zero-level offsets can occur in the spectra. This is why the ZLO can be used in the GFIT forward model. It is not always retrieved, it can be set to a fixed value to empirically fix an observed offset. In TCCON retrievals it is not retrieved in windows that contribute to public products and is assumed equal to zero, but the strong CO_2 band (centered near 4852 cm^{-1}) with saturated lines is used to fit ZLO as a diagnostic for potential anomalous non-linearity.

The continuum function is expressed as the instrument spectral response multiplied by the solar Planck function. It describes broad spectral structures, as opposed to *SPTS* and *Tr* which describe high-frequency structures. The broad spectral structure is fitted using Discrete Legendre orthogonal polynomials (Neuman and Schonbach, 1974):

$$P_m(K,N) = \sum_{j=0}^{m} (-1)^j \binom{m}{j} \binom{m+j}{j} \frac{K^{(j)}}{N^{(j)}} \tag{3.40}$$

where *m* is the order of the polynomial, *N* is the number of spectral points, and $K = 1,2,\dots,N$, and $\binom{m}{j}$ is a binomial coefficient defined as:

$$\binom{m}{j} = \frac{m!}{j!\,(m-j)!} \tag{3.41}$$

with *m!* indicating the factorial of *m*. $K^{(m)}$ is the falling factorial of *K* with m factors defined as:

$$K^{(m)} = K(K-1)(K-2)\dots(K-m+1) \tag{3.42}$$

$$cont(\sigma) = CL\left(P_0(K(\sigma),N) + CT \times P_1(K(\sigma),N) + \sum_{i=2}^{m} CC_i \times P_i(K(\sigma),N)\right) \tag{3.43}$$

where $K(\sigma)$ is the index of wavenumber σ in the spectral window with N spectral points. The fitting routine adjusts m parameters to fit the continuum: the continuum level CL, the continuum tilt CT, and $m-2$ continuum curvature (CC) terms.

An important term in the transmittance spectrum described by Eq. 3.38 is the absorption coefficient k, computed for each atmospheric level (with its own pressure, temperature, density, and trace gas concentrations) and each wavenumber. It is a function of absorption line intensities and depends on the spectral line profile considered, the physical model that describes the shape of absorption lines. To retrieve the total column amount of a trace gas, GFIT uses a single scale factor α for the whole profile such that Eq. 3.38 uses $n(\alpha_g f_g, P, T)$ for the number density. GFIT/2 precomputes the absorption coefficients using the a priori mole fraction f_g of each gas g and does not recompute them at each iteration with $\alpha_g f_g$, but the number density of each gas to be retrieved is updated at each step. The complete set of parameters adjusted during GFIT/2 retrievals is presented in Table 3.2. Two of these have not been introduced yet, GFIT/2 retrieves a frequency stretch (frequency offset per spectral point) to correct for possible mismatches between the calculated and measured wavenumber scales. Starting with GGG2020, GFIT/2 also retrieves a second "solar-gas" stretch that accounts for the difference in stretch between the telluric absorption lines of Tr_{tot} and the solar absorption lines of $SPTS$. The mismatch between calculated and measured wavenumber scale can be caused by errors in the pointing of the suntracker as the forward model assumes it is pointing exactly at the center of the sun. Section 4.4 will discuss a method that has been applied to NIR measurements from Eureka to correct for such pointing errors.

Table 3.2: Retrieved parameters in GFIT2 profile retrievals. The same parameters are retrieved in GFIT except for a single scaling factor applied to the mole fraction of the target gas.

State vector parameter	Number of elements
Main target gas (CO_2)	51 (number of atmospheric levels)
Interfering species	3–6 (scaling retrievals)
Continuum basis functions:	N (5 in the Strong window, 3 in the other windows)
Continuum level	1
Continuum tilt	1
Continuum curvature	N-2
Frequency stretch	1
Solar-gas stretch	1
Zero-level offset	0 (1 in the Strong window)

3.4 Retrieval Algorithm

Fourier transform spectrometers measure light intensity as a function of position of the scanning mirror: the interferogram. The interferogram is converted to a spectrum, light intensity as a function of wavenumber, through a FFT algorithm. In the GGG software, this is done through the I2S program (Interferogram to Spectrum). The resulting spectra are then analyzed with the GFIT program, which iteratively adjusts retrieval parameters to produce a calculated spectrum that best fits the measured spectrum. This is done by minimizing the sum of the χ^2 of the difference between the measured spectrum and the calculated spectrum, and of the χ^2 of the difference between the a priori state vector and the state vector (Rodgers, 2000):

$$\chi^2 = \left(\boldsymbol{y} - f(\boldsymbol{x})\right)^T \mathbf{S}_\mathbf{y}^{-\mathbf{1}}\left(\boldsymbol{y} - f(\boldsymbol{x})\right) + (\boldsymbol{x_a} - \boldsymbol{x})^{\boldsymbol{T}}\mathbf{R}(\boldsymbol{x_a} - \boldsymbol{x}) \tag{3.45}$$

where $\boldsymbol{y}$ is the measured spectrum, $f(\boldsymbol{x})$ is the spectrum calculated by applying the forward model, f, to the state vector, $\boldsymbol{x}$, $\mathbf{S_y}$ is the measurement covariance matrix, $\boldsymbol{x_a}$ is the a priori state vector, $\mathbf{R}$ is a regularization matrix that constrains the a priori variability in the state vector elements, and the T superscript indicates the transpose of a vector or matrix. In the optimal estimation method, the regularization matrix is the inverse of the a priori covariance matrix $\mathbf{S_a}$, which represents the statistics of realistic ensembles of the quantities to be retrieved (Rodgers, 2000). The state vectors of GFIT and GFIT2 contain scaling factors that are applied to vertical profiles of a priori mole fractions, and also contain other fitted parameters listed in Table 3.2. The forward model f is also a function of parameters that are not fitted (not part of the state vector) as described in Sect. 3.3.

Equation 3.45 is minimized by iteratively solving for the state update $\boldsymbol{\Delta x}$ in the least squares problem:

$$\left(\mathbf{K_i^T}\mathbf{S_y^{-1}}\,\mathbf{K_i} + \mathbf{S_a^{-1}} + \gamma\mathbf{D}\,\right)\boldsymbol{\Delta}\mathbf{x} = \mathbf{K_i^T}\mathbf{S_y^{-1}}\left(\boldsymbol{y} - f(\boldsymbol{x_i}\,)\right) + \mathbf{S_a^{-1}}(\boldsymbol{x_a} - \boldsymbol{x_i}\,). \tag{3.46}$$

For the ith iteration, where $\mathbf{K}$ is the Jacobian matrix, each column of $\mathbf{K}$ contains the derivative of the spectrum with respect to an element of the state vector, $\mathbf{K} = \frac{\boldsymbol{\delta f}}{\delta x}$. The Levenberg-Marquardt parameter γ is applied to a scaling matrix $\mathbf{D}$, which is taken to be $\mathbf{S_a^{-1}}$. This is a choice, as the scaling matrix does not have to be equal to the regularization matrix. The Levenberg-Marquardt parameter affects the size of the state update such that smaller steps may be taken when the linearization of the forward model is not satisfactory. In the GFIT2 algorithm for profile retrievals, Eq. 3.46 is used as is. In GFIT scaling retrievals, the Levenberg-Marquardt parameter is not used and instead the size of the state update in the first two iterations is empirically limited. Both GFIT and GFIT2 use the optimal estimation method and adjust the state vector to obtain the maximum a posteriori probability. In Sect. 3.4.1, the details of the GFIT2 algorithm are presented and follow the formulations of Rodgers (2000). In Sect. 3.4.2 the specifics of the GFIT algorithm are highlighted.

3.4.1 GFIT2

The expected χ^2 of the maximum a posteriori probability should be:

$$\chi^2(\hat{\boldsymbol{x}}-\boldsymbol{x}) = (\hat{\boldsymbol{x}}-\boldsymbol{x})^T\left(\mathbf{K^T S_y^{-1} K} + \mathbf{S_a^{-1}}\right)(\hat{\boldsymbol{x}}-\boldsymbol{x}) \cong n \tag{3.47}$$

where n is the number of state vector elements. A solution is accepted when the ratio of the squared state update to the estimated variance is a negligible fraction of the expected χ^2.

$$\Delta\boldsymbol{x}\left(\mathbf{K^T S_y^{-1}}\left(\boldsymbol{y} - f(\boldsymbol{x}) + \mathbf{S_a^{-1}}(\boldsymbol{x_a} - \boldsymbol{x})\right)\right) \ll n. \tag{3.48}$$

In an algorithm, “<< n” must use a specific limit, and in GFIT2, “< $n/10$” was used. If the inequality check is made with a parameter that is too large, like “<n”, the algorithm may take fewer iterations to converge, but will take the same steps at each iteration, often leading to a retrieved profile closer to the a priori. The inequality check should be done with a small enough fraction of n that reducing it further does not significantly affect the solution.

If convergence is not reached in the i$^{\text{th}}$ iteration, an algorithm determines if the Levenberg–Marquardt parameter needs to be adjusted for the next iteration (Fletcher, 1971). Three different cost functions are calculated:

$$J_{old} = \left(\boldsymbol{y} - f(\boldsymbol{x}_i)\right)^T \mathbf{S}_y^{-1}\left(\boldsymbol{y} - f(\boldsymbol{x}_i)\right) + (\boldsymbol{x}_a - \boldsymbol{x}_i)^T \mathbf{S}_a^{-1}(\boldsymbol{x}_a - \boldsymbol{x}_i) \tag{3.49}$$

$$J_{new} = \left(\boldsymbol{y} - f(\boldsymbol{x}_i + \Delta\boldsymbol{x})\right)^T \mathbf{S}_y^{-1}\left(\boldsymbol{y} - f(\boldsymbol{x}_i + \Delta\boldsymbol{x})\right) + (\boldsymbol{x}_a - \boldsymbol{x}_i - \boldsymbol{\Delta x})^T \mathbf{S}_a^{-1}(\boldsymbol{x}_a - \boldsymbol{x}_i - \Delta\boldsymbol{x}) \tag{3.50}$$

$$J_{pred} = \left(\boldsymbol{y} - f(\boldsymbol{x}_i) - \mathbf{K}\Delta\boldsymbol{x}\right)^T \mathbf{S}_y^{-1}\left(\boldsymbol{y} - f(\boldsymbol{x}_i) - \mathbf{K}\Delta\boldsymbol{x}\right) + (\boldsymbol{x}_a - \boldsymbol{x}_i - \boldsymbol{\Delta x})^T \mathbf{S}_a^{-1}(\boldsymbol{x}_a - \boldsymbol{x}_i - \Delta\boldsymbol{x}) \quad (3.51)$$

where J_{old} is the cost function using the state vector at the beginning of the ith iteration, J_{new} is the cost function using the updated state vector at the end of the ith iteration, and J_{pred} is the cost function using the state vector update and the linear approximation:

$$f(\boldsymbol{x} + \Delta\boldsymbol{x}) \cong f(\boldsymbol{x}) + \mathbf{K}\Delta\boldsymbol{x}. \quad (3.52)$$

The ratio r is then evaluated:

$$r = \frac{J_{new} - J_{old}}{J_{pred} - J_{old}}. \quad (3.53)$$

This is the relative change in the cost function produced by a state vector update when using the forward model compared to a linear approximation of the forward model. The Levenberg–Marquardt parameter is then adjusted as follows:

- $r > 0.75$: the linearization of the forward model is satisfactory and γ is reduced to allow larger steps (larger state updates $\Delta\boldsymbol{x}$).
  - $\gamma = \frac{\gamma}{2}$
- $r \geq 0.25$: intermediate case, make no change to γ and reset the number of consecutive divergences.
  - $ndiv = 0$
- $r < 0.25$: the linearization of the forward model is not satisfactory, increment the number of consecutive divergences, γ is increased to take smaller steps.
  - $ndiv = ndiv + 1$
  - if $\gamma = 0$ then γ=1
  - if $\gamma > 0$ then $\gamma = 10\gamma$

If $ndiv$ reaches some specified maximum number, there will not be another iteration. When $r < 0.25$, it means that the linearization of the forward model is not good enough. In GFIT2, this was not allowed to happen more than twice in a row. Increasing γ will lead to a smaller step for the state vector update, increasing the chance that the linearization of the forward model at the next step will be better and $r \geq 0.25$.

In GFIT2, $r > 0.75$ in most cases, and if γ is not initially set to 0 it will tend towards 0 until the convergence criterion is met, thus the initial value of γ was set to 0. However, the increase of the parameter is often triggered when fitting noisier spectra and can give the algorithm a chance to converge when it would otherwise need more iterations or fail without γ.

After the last iteration, the goodness of fit of the retrieval is checked by evaluating the reduced χ^2 of the difference between the measured and calculated spectrum:

$$\chi_{red}^2(\boldsymbol{y} - f(\boldsymbol{x})) = \frac{1}{N}\sum_{i=1}^{N}\left(\frac{\boldsymbol{y}_i - f(\boldsymbol{x})_i}{\epsilon_y}\right)^2 \tag{3.54}$$

where ϵ_y is the measurement uncertainty, and N the number of spectral points.

The retrieval covariance matrix is:

$$\widehat{\boldsymbol{S}} = \left(\boldsymbol{K}^T\mathbf{S}_y^{-1}\mathbf{K} + \mathbf{S}_a^{-1}\right)^{-1}. \tag{3.55}$$

The square root of its diagonal elements is used as the uncertainty on the retrieved scaling factors.

3.4.2 GFIT

The GFIT scaling retrieval algorithm implementation differs slightly from that of GFIT2. GFIT only uses one state vector element to scale the entire a priori mole fraction profile of a target gas. The equation it uses to solve for the state update is slightly different from Eq. 3.2, instead two equations are solved simultaneously:

$$\begin{pmatrix} \mathbf{K_s} \\ \dfrac{\epsilon_y}{\boldsymbol{\epsilon_a}} \end{pmatrix} \boldsymbol{\Delta x} = \begin{pmatrix} \boldsymbol{y} - f(\boldsymbol{x}) \\ (\boldsymbol{x_a} - \boldsymbol{x})\dfrac{\epsilon_y}{\boldsymbol{\epsilon_a}} \end{pmatrix} \tag{3.56}$$

where the matrix $\mathbf{K}_{\boldsymbol{s}}$ has dimensions (nmp, nfp). nmp is the number of measured spectral points, and nfp is the number of fitted parameters. The subscript s is to differentiate the Jacobian from the scaling retrievals to that of the profile retrievals used in Sec. 3.4.1. The scalar ϵ_y is the measurement uncertainty, it characterizes the noise of the spectrum, but not systematic instrumental errors. The vector $\boldsymbol{\epsilon_a}$ is the a priori uncertainty of the fitted parameters, with size nfp. The term $\frac{\epsilon_y}{\boldsymbol{\epsilon_a}}$ on the left-hand side is an (nfp, nfp) diagonal matrix. Rather than determining convergence based on Eq. 3.48, GFIT iterates until the root mean square of the residuals falls below a given threshold. GFIT defines residuals in two ways to determine convergence, once when computing residuals as:

$$\boldsymbol{r} = f(\boldsymbol{x}) \log_e \left(\frac{\boldsymbol{y}}{f(\boldsymbol{x})} \right) \tag{3.57}$$

and then once when computing residuals as $\boldsymbol{r} = \boldsymbol{y} - f(\boldsymbol{x})$. The two formulations are equivalent in the limit of small residuals, but Eq. 3.57 allows faster convergence by making the problem more linear for the first iterations. Rather than using the Levenberg-Marquardt parameter to limit the size of the state update, it is empirically limited in the first two iterations. In the first iteration, the state update is reduced by at least 60%, and in the second iteration it is reduced by at least 20%. The state update is multipled by the fraction fr if $fr < 0.4$ in the first iteration, and if $fr < 0.8$ in the second iteration, with fr defined as:

$$fr = \frac{0.2 + 0.5|\boldsymbol{x}|}{|\Delta \boldsymbol{x}|} \ . \tag{3.58}$$

In the first iteration, the initial state vector values are set to the a priori state vector values and the a priori scaling factors on target gases are set to 1. In the first iteration the state update is at most $0.4\Delta x$, and at most $0.8\Delta \boldsymbol{x}$ in the second iteration. In the third and subsequent iterations, the state update is $fr \times \Delta \boldsymbol{x}$.

3.5 Averaging Kernels

The averaging kernel matrix describes a change in the retrieved state $\hat{\boldsymbol{x}}$ for a change in the state vector $\boldsymbol{x}$:

$$(\mathbf{A}_{\mathrm{SF}})_{i,j} = \frac{\delta \hat{\boldsymbol{x}}_i}{\delta \boldsymbol{x}_j}. \tag{3.59}$$

Even though the averaging kernel is dimensionless, its units can be written as e.g., “ppm per ppm” to indicate that it is the change at a given level for a change at a different level. Here the SF subscript indicates that $\mathbf{A_{SF}}$ is a change in the retrieved scaling factors. The averaging kernel matrix is calculated as:

$$\mathbf{A_{SF}} = \left(\mathbf{K^T S_y^{-1} K} + \mathbf{S}_{\boldsymbol{a}}^{\mathbf{-1}}\right)^{-1} \mathbf{K}^{\boldsymbol{T}} \boldsymbol{S}_{\boldsymbol{y}}^{\mathbf{-1}} \mathbf{K}. \tag{3.60}$$

The GFIT averaging kernel matrix can also be computed using Eq. 3.60 and a very strong regularization matrix instead of the a priori covariance matrix $\mathbf{S_a}$. Although the scaling retrievals do not require explicit interlayer constraints, they are equivalent to a profile retrieval with infinitely strong constraint on interlayer correlations. To use Eq. 3.60 for scaling retrievals, one could use the discrete first order derivative operator $\mathbf{L_1}$ (Steck, 2002) to compute a regularization that is used for Tikhonov-type retrievals (Tikhonov, 1963). The $\mathbf{L_1}$ operator is a rectangular matrix with one more column than rows:

$$\mathbf{L_1} = \begin{pmatrix} -1 & 1 & 0 & \dots & 0 \\ 0 & \ddots & \ddots & \ddots & \vdots \\ \vdots & \ddots & \ddots & \ddots & 0 \\ 0 & \dots & 0 & -1 & 1 \end{pmatrix}. \tag{3.61}$$

It can be used to build the regularization matrix $\mathbf{R}$:

$$\mathbf{R} = \alpha \mathbf{L_1^T L_1} \tag{3.62}$$

where $\mathbf{L_1}$ has dimensions $(nlev - 1, nlev)$ and $\mathbf{R}$ has dimensions $(nlev, nlev)$, where $nlev$ is the number of atmospheric levels. Then $\mathbf{R}$ can be extended to include the covariance terms for fitted parameters that are not retrieved as profiles. The adjustable input parameter alpha determines the regularization strength. Eq. 3.60 can be used with $\mathbf{R}$ and $\alpha \rightarrow \infty$ to approximate the averaging kernel matrix of a scaling retrieval.

In practice, GFIT scaling retrieval averaging kernels are derived by solving for $\boldsymbol{a}_{\boldsymbol{sf}}$ in:

$$\mathbf{K}\boldsymbol{a}_{\boldsymbol{sf}} = \mathbf{K_s} \tag{3.63}$$

where $\boldsymbol{a_{sf_j}} = \sum_{i=1}^{nlev} (\mathbf{A_{SF}})_{i,j}$ and $\mathbf{K_s}$ is the column Jacobian introduced in Equation 3.56.

To obtain the averaging kernel in ppm per ppm:

$$(\mathbf{A}_{VMR})_{i,j} = (\mathbf{A}_{SF})_{i,j} \frac{vmr_i}{vmr_j} \tag{3.64}$$

where vmr is the a priori mole fraction at the ith and jth levels. The partial column averaging kernel matrix in molecules.cm^{-2} per molecules.cm^{-2} is:

$$(\mathbf{A}_{\mathrm{col}})_{i,j} = (\mathbf{A}_{\mathrm{SF}})_{i,j} \frac{vmr_i \times d_i \times sp_i}{vmr_j \times d_j \times sp_j} \tag{3.65}$$

where *sp* (slant path) are the widths of the slant layers along the sun ray that correspond to the altitude levels of the prescribed vertical grid. The total column averaging kernel vector can be obtained from the partial column averaging kernel matrix using:

$$\boldsymbol{a_{col}}_j = \sum_{i=1}^{nlev} (\mathbf{A}_{\mathrm{col}})_{i,j}\,. \tag{3.66}$$

It represents the change in the total column (molecules.cm^{-2}) caused by a change in the partial column of the jth layer. It should ideally be equal to 1 at each level, meaning that adding N target molecules anywhere in the atmosphere will lead to N more molecules in the retrieved total column.

In practice, the GFIT scaling retrieval column averaging kernels are derived as:

$$\boldsymbol{a_{col_j}} = \boldsymbol{a_{sf_j}} \frac{\sum_{i=1}^{nlev} vmr_i \times d_i \times sp_i}{vmr_j \times d_j \times sp_j}\,. \tag{3.67}$$

The averaging kernel matrix would ideally be an identity matrix, meaning that adding N molecules in the jth layer would lead to N more molecules retrieved in that layer. However, adding N molecules in the jth layer will lead to an increase in the width of CO_2 absorption lines of a spectrum observed from the ground. Each wavenumber is affected by the CO_2 concentration over a range of altitudes, because the spectrum observed on the ground is the product of all the spectra that would be observed at each altitude. Even if that change in line widths were the only change in the spectrum and could be fitted perfectly, it would be impossible to exactly attribute that change to a specific altitude level. Although the total column averaging kernel could be exactly 1 at each level, the averaging kernel matrix can never be exactly the identity matrix for direct sun measurements from the ground.

The column averaging kernel matrix can be used to degrade higher resolution profiles before comparing them to retrieved profiles (Rodgers and Connor, 2003).

$$\boldsymbol{c}_s = \mathbf{A}_{col}(\boldsymbol{c} - \boldsymbol{c}_a) + \boldsymbol{c}_a \tag{3.68}$$

where $\boldsymbol{c}_s$ is the smoothed partial column profile, $\boldsymbol{c}$ is the partial column profile to be smoothed, and $\boldsymbol{c}_a$ is the a priori partial column profile. Or using the total column averaging kernel:

$$c_s^{tot} = c_a^{tot} + \boldsymbol{a}_{\boldsymbol{col}}^T(\boldsymbol{c} - \boldsymbol{c}_a) \tag{3.69}$$

where $\boldsymbol{a}^T$ is the transpose of $\boldsymbol{a}$, and the “tot” superscript indicates a total column:

$$c_a^{tot} = \sum_{i=1}^{nlev} c_{a_i}\,. \tag{3.70}$$

In Chapter 4, measurements of NIR solar spectra at Eureka and their processing with GFIT scaling retrievals are presented. Section 4.8 presents a comparison of TCCON XCO_2 and XCH_4 with a model developed at ECCC, in these comparisons the model XCO_2 is smoothed with the GFIT column averaging kernel as described by Eq. 3.69.

In Chapter 5, the partial column averaging kernels of GFIT2 are presented to describe the sensitivity of the profile retrieval to CO_2. The GFIT and GFIT2 averaging kernels are also used to smooth XCO_2 derived from AirCore profiles of CO_2.

Chapter 4

TCCON Measurements at Eureka

The PEARL Ridge Lab (80.053°N, 86.42°W) is located on Ellesmere Island (Nunavut, Canada) about 12 km away from the Eureka Weather Station, on a ridge at 600 meters above sea level. After Alert (Ellesmere Island), and Nord (Greenland), the Eureka Weather Station is the third-northernmost permanent research settlement. It is one of the few Arctic sites that collect MIR and NIR solar spectra that can be used to validate models and satellite observations in the region. The importance of the Arctic region due to its high sensitivity to climate change and its potential to become a carbon source in the next century were discussed in Sect. 1.2.3. The atmospheric dynamics are also peculiar in the Arctic and the concentrations of atmospheric constituents in the region are affected by the polar vortex. This strong circulation isolates Arctic air from air at lower latitudes, changing the strength of the horizontal mixing between the Arctic and mid-latitudes and of the vertical mixing inside the vortex (Manney et al., 1994; van den Broek et al., 2003). Thus, ground-based total column measurements can be useful to validate model simulations of vortex conditions. Trace gas retrievals over snow- and ice-covered regions like the Arctic are also difficult with satellite measurements like those from GOSAT and OCO-2 because of the low albedo of these surfaces in the NIR (O'Dell et al., 2018). Direct-sun measurements from ground-based instruments use a simpler forward model that is not affected by surface properties, and because of the high signal, these measurements are also minimally affected by aerosols. Finally, ground-based instruments are accessible for maintenance so they can continue to be used as a ground-truth metric for satellite instruments.

This chapter presents the NIR measurements collected at Eureka for TCCON, explains how they were improved during this thesis leading to new data revisions (Strong et al., 2016, 2017, 2019), and describes how they contributed to validation studies of TROPOspheric Monitoring Instrument (TROPOMI) XCO and XCH_4 (Schneising et al., 2019; Sha et al., 2021), of XCO measurements from the Measurements Of Pollution In The Troposphere (MOPITT) instrument (Hedelius et al., 2019), of OCO-2 XCO_2 (Kulawik et al., 2019), and of XCO_2 and XCH_4 simulations from the GEM-MACH-GHG model (Polavarapu et al., 2016).

4.1 NIR Spectral Measurements at Eureka

The PEARL Bruker 125HR FTS has collected NIR solar spectra since 2010 as part of TCCON. It uses a room temperature Indium Gallium Arsenide (InGaAs) detector (3500-11000 cm^{-1}) and a Calcium Fluoride (CaF_2) beamsplitter (1200-15000 cm^{-1}). Figure 4.1 shows an example of a measured solar spectrum from Eureka obtained on April 21st 2020 with different spectral regions highlighted by their principal absorber. Other TCCON sites also use a room temperature Silicon (Si) detector to extend the measured spectral region to 15500 cm^{-1}, or a liquid-nitrogen-cooled Indium antimonide (InSb) detector to extend it down to 1800 cm^{-1}. Although the instrument at Eureka is equipped with an InSb detector, it is not used for TCCON measurements. Measurements are also collected in the MIR for NDACC using a Potassium Bromide (KBr) beamsplitter (450-4800 cm^{-1}) with InSb and Mercury Cadmium Telluride (MCT, 600-6000 cm^{-1}) detectors.

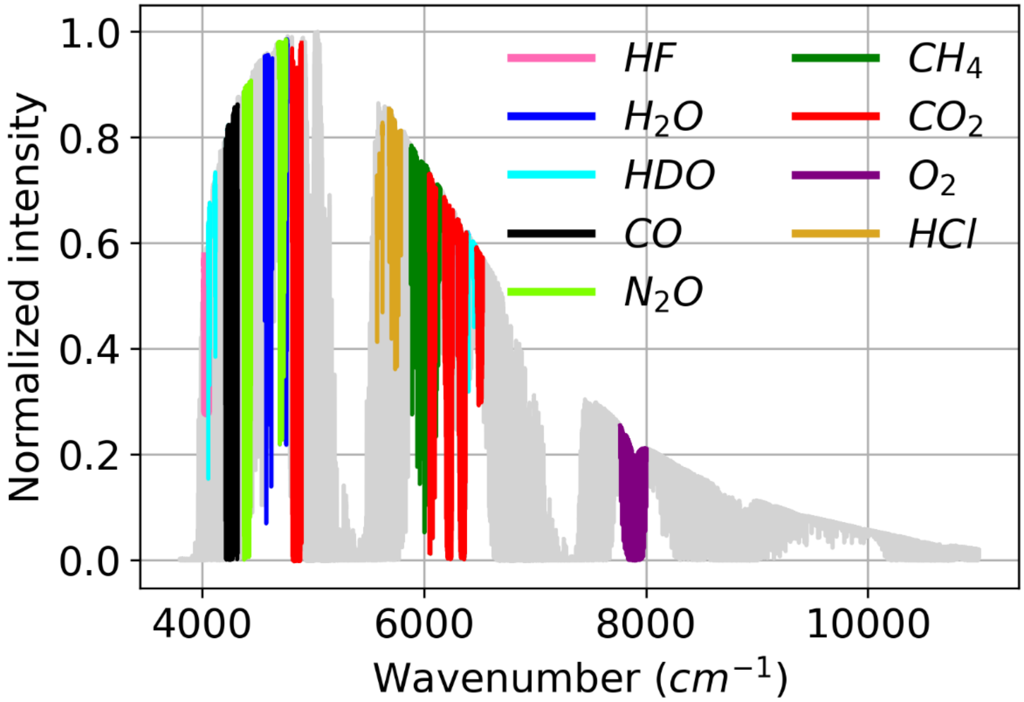

Figure 4.1: Normalized solar absorption spectrum measured by the PEARL FTS on April 21st 2020. The full spectrum is in light grey and spectral windows used by TCCON are highlighted in colours and labeled with the main absorber in that spectral region. HF is retrieved from a single absorption line at 4038.95 cm^{-1}.

The 125HR takes ~1.2 min to record an interferogram with 45 cm maximum optical path difference. It is used to make both TCCON NIR and NDACC MIR measurements. Typically, one full day of NIR measurements is followed by a full day of MIR etc. as there is value in obtaining a record of the variation of trace gas concentration throughout the day. The measurements are not fully automated and require operator intervention to open the dome and start the suntracker, to cool the detectors with liquid nitrogen for MIR measurements, and to swap the NIR (CaF_2) and MIR (KBr) beamsplitters. Because of this, the site does not take full advantage of the permanent daylight from mid-April to late August as the observations are shut down when operators return to the Eureka Weather Station.

The instrument is shut down during polar night from mid-October to late February. Figure 4.2 shows the solar zenith angle at PEARL throughout 2020. When the solar zenith angle is less than 90° at all azimuth angles, it is permanent daylight, and when it is larger than 90° at all azimuth angles it is polar night. There are two transition periods that last ~2 months each from late February to mid-April and from late August to mid-October when the number of daily sunlit hours changes rapidly. The NIR measurements for TCCON get filtered based on various quality criteria before being released publicly. One of these criteria for measurements using GGG2014 is that the solar zenith angle must be smaller than 82° because the retrieved trace gases are affected by an airmass dependence (which increases with solar zenith angle as the sun ray travels a longer distance through the atmosphere). However, future improvements to the TCCON algorithm could reduce the airmass dependence of retrieved gases and potentially allow a looser SZA quality criterion. Thus, even if NIR measurements at $SZA>82°$ are currently not included in the public TCCON products, NIR spectra recorded before mid-March (when the solar noon SZA first drops below 82° SZA) can still be useful.

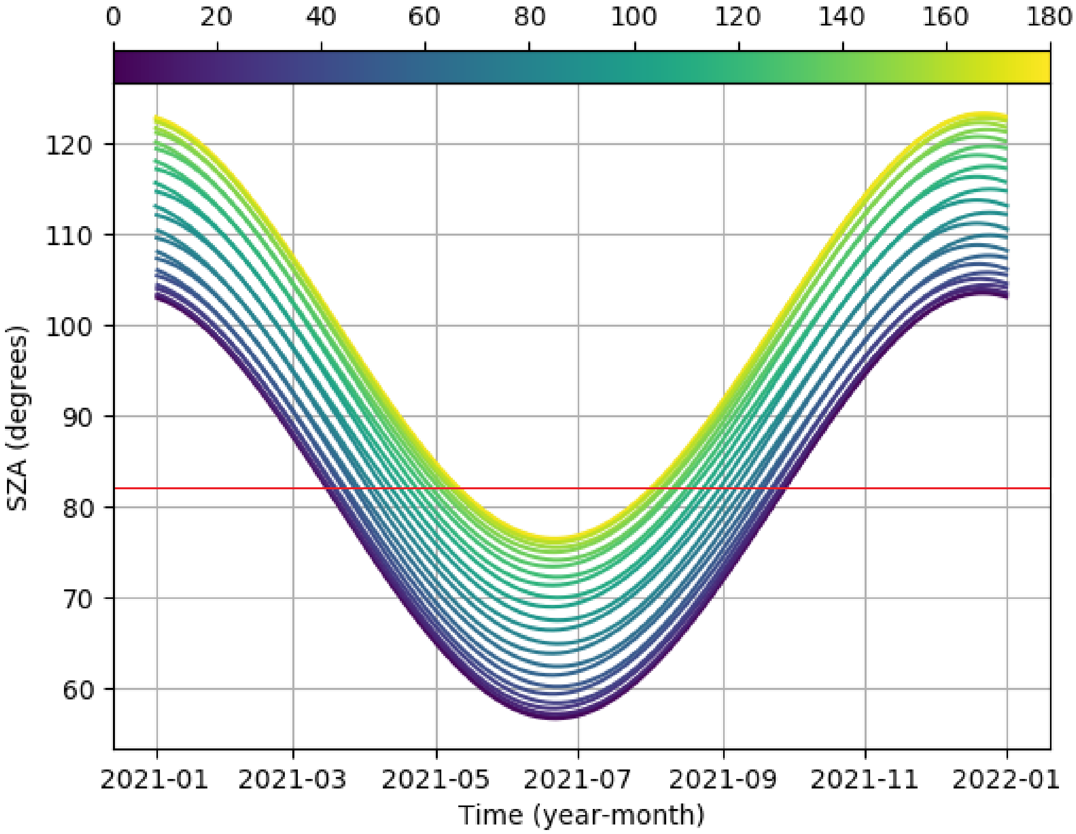

Figure 4.2: Solar zenith angle at the location of the PEARL Ridge Lab throughout 2021. The colour bar indicates the absolute azimuth angle in degrees, 0° corresponds to solar noon. The red line indicates the TCCON quality flag at SZA=82°.

The spectral windows used for TCCON retrievals are presented in Table 4.1. For each target gas, a column scaling factor is retrieved from multiple spectral windows separately, then the results from each of those windows are combined in a post-processing routine to derive the column-averaged dry-air mole fraction of the target gas after removing any window-dependent multiplicative biases. For CO_2, only two of the five windows presented in Table 4.1 are used to derive XCO_2, these include the $(30013) - (00001)$ and $(30012) - (00001)$ bands.

Table 4.1: Spectral windows for the gases retrieved by TCCON. The CO_2 windows highlighted in red do not contribute to deriving XCO_2 reported in the public TCCON data.

Main target gas	Window center (cm^{-1})	Window width (cm^{-1})	Primary interfering species
Dry air	6146.9	1.6	
O_2	7885	240	H_2O, HF, CO_2, HDO
CO_2	6220	80	H_2O, HDO, CH_4
	6073.5	63.4	H_2O, CH_4
	6339.5	85	H_2O, HDO
	6500.4	58	
	4852.2	87.6	$^{13}CO_2$, $OC^{18}O$, $OC^{17}O$, $O^{13}C^{18}O$, H_2O, HDO
CH_4	5938	116	CO_2, H_2O, N_2O
	6002	11.1	CO_2, H_2O, HDO
	6076	138	
N_2O	4719.5	73.1	CH_4, H_2O, CO_2
	4430.1	23.1	
	4395.2	43.4	CH_4, H_2O, HDO
CO	4233.1	48.4	
	4290.5	56.6	
HF	4038.95	0.32	H_2O
H_2O	4565.2	2.5	CO_2, CH_4
	4570.35	3.1	
	4571.75	2.5	
	4576.85	1.9	CH_4
	4598.69	10.78	CH_4, CO_2, N_2O
	4611.05	2.2	
	4622	2.3	CO_2, N_2O
	4631.55	1.4	
	4699.55	4	CO_2, N_2O
	4734.6	7.3	
	4761.15	10.7	CO_2
	6076.9	3.85	HDO, CO_2, CH_4
	6099.35	0.95	CO_2
	6125.85	1.45	HDO, CO_2, CH_4
	6177.51	1.26	
	6255.95	3.6	CO_2, HDO

	6301.35	7.9	
	6392.45	3.1	HDO
	6401.15	1.15	HDO, CO_2
	6469.6	3.5	
HDO	4045.6	3.3	H_2O, CH_4
	4067.6	8.8	
	4116.1	8	
	4212.45	1.9	
	4232.5	11	H_2O, CH_4, CO
	6330.05	45.5	H_2O, CO_2
	6377.4	50.2	
	6458.1	41.4	
HCl	5577.3	0.4	H_2O, CH_4
	5597.8	0.4	
	5625.02	0.29	
	5683.57	0.36	H_2O
	5687.65	1.1	H_2O, CH_4
	5702	0.7	
	5706.2	0.5	
	5719.12	2.26	
	5735.05	0.52	
	5749.8	0.6	
	5754	0.8	
	5763.2	0.68	
	5767.35	1.7	
	5779.5	1	
	5790.45	0.9	

4.2 Column-Averaged Dry-Air Mole Fractions

In GGG2020, the vertical profiles of atmospheric quantities are defined on 51 vertical levels from 0 to 70 km following:

$$z_i = i \times (0.4 + 0.02i) \tag{4.1}$$

where z_i is the altitude in kilometers of the i^{th} level. This results in levels with spacing increasing with altitude such that adjacent layers have a more similar airmass than those with a fixed altitude spacing. The width of the layer above the i^{th} level is the effective vertical path vp_i (in km):

$$vp_i \approx 0.4 + 0.04 \times i. \tag{4.2}$$

The effective vertical path distance of the level directly below a given site surface altitude is truncated, and the effective vertical path of levels below it is 0.

The total column of air in molecules per square meter can be obtained as:

$$column_{air} = \sum_{i=1}^{N} vp_i \times d_i \tag{4.3}$$

where d_i is the air number density of the i^{th} level in molecules per cubic meter, and N is the number of atmospheric levels. The total column of a target gas G is:

$$column_G = \sum_{i=1}^{N} sf_G \times vmr_{G,i} \times d_i \times vp_i \tag{4.4}$$

where sf_G is the retrieved column scale factor for gas G and $vmr_{G,i}$ is its a priori wet mole fraction (molecules of G per molecule of air) at the i^{th} level. In the forward model, the retrieval grid is not vertical but along the slant path from the instrument towards the sun. The scaling factors retrieved for the slant layers are used with the corresponding vertical layers to compute the vertical columns. The a priori profiles used by GFIT are built on the altitude grid directly above the site. This contributes to an unknown error, largest at high solar zenith angles, when the projection of the sun ray on the ground can reach a few hundred kilometers, and the a priori slant profiles of temperature and water vapour could differ significantly from the vertical profiles directly above the instrument.

Because of the high variability of H_2O in the troposphere (see Sect. 1.1.1), the mole fraction of trace gases is often reported in dry air to distinguish their own variability from the variability in the H_2O amount. The column-averaged dry-air mole fraction of gas G (XG) is the ratio of $column_G$

to $column_{dry-air}$. The column of dry air can be expressed as the column of O_2 divided by 0.2095 (Wunch et al., 2011):

$$XG = 0.2095\frac{\overline{column_G}}{column_{O_2}} \tag{4.5}$$

where the O_2 column is retrieved from the spectral window centered at 7885 cm^{-1} (see Table 4.1), and $\overline{column_G}$ is a weighted average of the columns retrieved from all the spectral windows in which gas G is the main target gas.

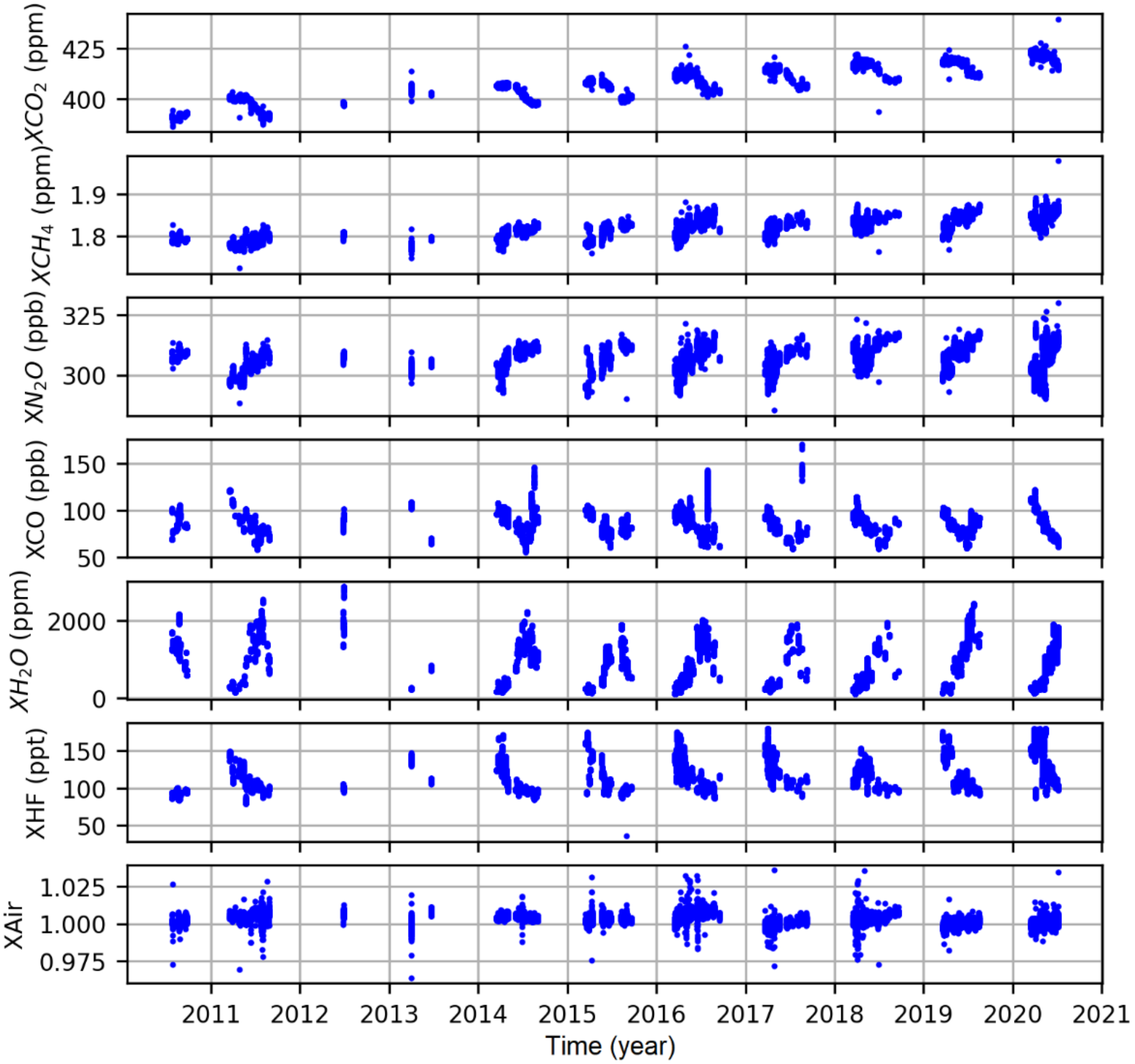

Figure 4.3: Column-averaged dry-air mole fractions retrieved with GGG2020 from NIR spectra measured by the PEARL FTS since 2010.

4.3 XAir

Figure 4.3 shows the Eureka time series of XG for trace gases retrieved with GGG2020. It also includes Xluft (XAir in GGG2014, luft means air in German), which is a diagnostic variable to verify that the ratio of $column_{dry-air}$ to $\frac{column_{O_2}}{0.2095}$ is indeed close to 1. The column of dry air can be expressed as (Wunch et al., 2011):

$$column_{dry-air} = \frac{P_s}{gm_{dry-air}} - column_{H_2O}\frac{m_{H_2O}}{m_{dry-air}} \tag{4.6}$$

where P_s is the surface pressure, g is the column-averaged gravitational acceleration, and m_G is the mean molecular mass of gas G. Anomalies in XAir can be caused by issues with surface pressure measurements (resulting in errors in $column_{dry-air}$), tracking accuracy (resulting in errors in $column_{O_2}$ and $column_{H_2O}$ due to an incorrectly calculated path through the atmosphere), or instrument misalignment (resulting in errors in $column_{H_2O}$ and $column_{O_2}$ due to mismatch between measured and calculated line shapes). Thus, if surface pressure measurements and tracking can be done with sufficient precision, XAir is a diagnostic for instrument misalignments. Surface pressure can be measured in-situ at Eureka with an accuracy of 0.15 hPa using a Vaisala pressure sensor (see Section 4.5). Figure 4.4 highlights the improvement in XAir after the alignment of the PEARL FTS in March 2017 (see Sect. 2.3).

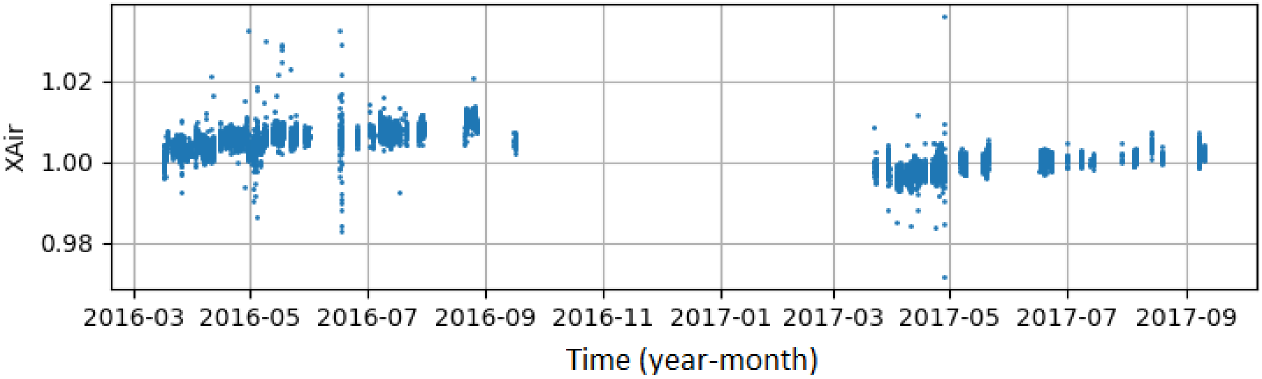

Figure 4.4: GGG2020 XAir at Eureka in 2016 and 2017; the FTS was re-aligned in March 2017.

4.4 Solar Zenith Angle Corrections

GFIT calculates a solar pseudo-transmittance spectrum (SPTS) to obtain the absorption lines due to gases in the atmosphere of the sun (see Sect. 3.3 and Eq. 3.39). This solar spectrum is calculated assuming a pointing at the center of the sun. But if the tracker points at a part of the sun with a velocity component V (from the rotation of the sun) along the direction of propagation of the radiation, the spectral point spacing $\Delta\sigma$ is Doppler stretched to $\Delta\sigma'$ following:

$$\Delta\sigma' = \Delta\sigma\left(1 + \frac{V}{c}\right) \tag{4.7}$$

where c is the speed of light. Calculating the solar spectrum with $V = 0$ leads to a mismatch between the observed and calculated wavenumber scales for solar lines. In GGG2020, this stretch is retrieved and corrected for when fitting measured spectra; the retrieved parameter is the Solar-Gas (SG) stretch in ppm of the spectral point spacing (for TCCON spectra with $\Delta\sigma = 0.007533\ cm^{-1}$, $SG = 1\ ppm$ corresponds to a frequency shift of $0.007533 \times 10^{-6}\ cm^{-1}$ per spectral point).

However, a pointing error not only affects the wavenumber scale, but also leads to errors in the calculated path of radiation through the atmosphere. This path is computed from the SZA, the angle between the vertical and the center of the sun. Pointing off-center at a given Pointing Zenith Angle (PZA) means that the true radiation path through the atmosphere is different from that computed with the SZA. To produce the same absorption spectrum through a shorter (longer) path, the number of absorbing molecules must increase (decrease). Thus, the retrieved total column amount will be larger when $SZA < PZA$ and smaller when $SZA > PZA$.

This will affect total column amounts similarly for different gases and thus the SZA error $\Delta SZA = PZA - SZA$ will have a limited effect on the ratio XG. However, this effect is still significant for XCO_2 as shown in Figure 4.5 with the change in retrieved XCO_2 at Eureka resulting from the SZA corrections. The corrections result in differences of up to ~0.05 ppm, caused by SG shifts of up to 2 ppm. Other TCCON sites may benefit from applying this method if they have periods where tracking issues result in SG shifts larger than 1 ppm.

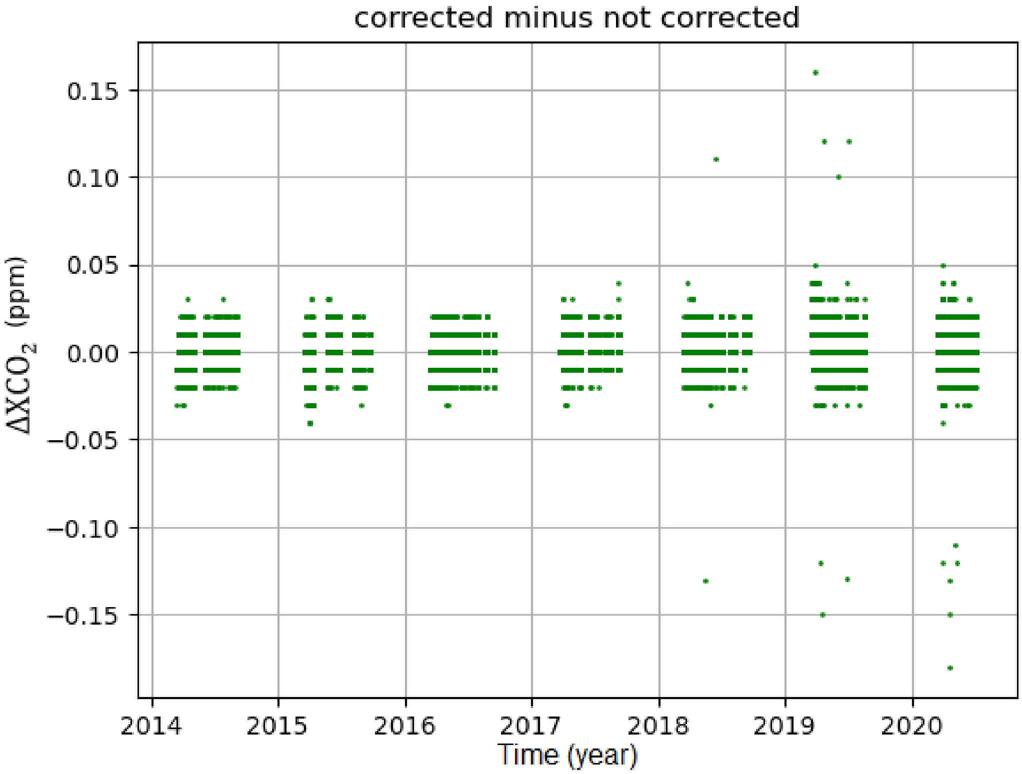

Figure 4.5: Difference in Eureka XCO_2 retrieved with GGG2020, with and without applying solar zenith angle corrections.

There is also a noticeable effect of pointing errors on XAir, which may prevent the use of XAir as a diagnostic for identifying instrument misalignment. Contrary to the Doppler stretch of the wavenumber scale, the SZA error is not systematically corrected in TCCON retrievals. The Eureka TCCON data are processed with a SZA correction starting in 2014-2015 when a noticeable SZA dependence of XAir was discovered and linked to tracking issues. Jonathan Franklin developed an algorithm to derive ΔSZA using the retrieved SG stretch and the rotation angle of the image of the sun on the tracker camera (relative to a reference position) (Franklin, 2015). The processing of the Eureka data with GGG2020 is thus done in two steps, first with the original SZA to obtain the retrieved SG, and second with $SZA = SZA + \Delta SZA$. SG (in ppm of wavenumbers: 1 ppm of 1 cm^{-1} is 10^{-6} cm^{-1}) is converted to an angular shift in arcseconds (as) following:

$$SG_{as} = \frac{SG}{-6.5 \times 10^{-3}} \tag{4.8}$$

using the change in wavenumber per arc minute of mispointing at the solar equator (Gisi et al., 2011): $\frac{\Delta\sigma}{\sigma} \approx 3.9 \times 10^{-7}\ cm^{-1}.arcmin^{-1} = 6.5 \times 10^{-9}\ cm^{-1}.arcsec^{-1} = 6.5 \times 10^{-3}\ ppm.arcsec^{-1}$.

A fit is then performed to derive the amplitude A (in arcseconds) and phase B (in degrees) of SG_{as} as a sinusoidal function of the rotation angle of the sun θ (in degrees):

$$\theta = Az - Alt + C + 9.95 \sin\left(\frac{\pi}{180} Az\right) \tag{4.9}$$

$$SG_{as} = A \cos\left(\frac{\pi}{180}(\theta + B)\right) \tag{4.10}$$

where Alt and Az are the sun altitude ($Alt = 90° - SZA$) and azimuth angles (in degrees) of the sun, respectively. The calibration angle C is set for a given arrangement of the tracker camera and obtained from the CST calibration mode; a new value must be derived any time the camera is moved. The solar zenith angle correction ΔSZA (in degrees) is then obtained as:

$$\Delta SZA = \frac{A}{3600} \sin\left(\frac{\pi}{180}\big(-B - (Az - Alt + C)\big)\right). \tag{4.11}$$

The $\frac{1}{3600}$ factor converts arcseconds to degrees. Figure 4.6 and Figure 4.7 show SG, ΔSZA, and the XAir retrieved with and without applying the SZA correction using Eureka data from 2014 and 2020, respectively. In both cases, the inclusion of ΔSZA of the order of 0.1-0.2 degrees leads to reduced diurnal variability in XAir.

Figure 4.8 illustrates the fit of SG_{as} as a function of θ as described by Eq. 4.9 and 4.10, using Eureka NIR data from 2014. The relationship described by Eq. 4.10 is specific to a given configuration of the tracker camera. If the camera were to be moved, different fits should be made for the periods before and after the change. In May 2015, it was also discovered that changing the neutral density filter in front of the tracker camera could lead to a shift of the solar beam and periods before and after that change needed to be fitted separately. It is thus important to keep a record of each time the tracker camera moves. However, it has been found that different time periods needed to be fitted separately even without known changes to the tracker camera setup.

Another complication for the procedure to derive ΔSZA is the need to filter out data that do not appear to follow a sinusoidal relationship as described by Eq. 4.10, hence the step in which the amplitude A and phase B are determined for different time periods is not easily reproductible by different users. If this process cannot be made more systematic, it might need to be abandoned despite the resulting reduced diurnal variability in XAir.

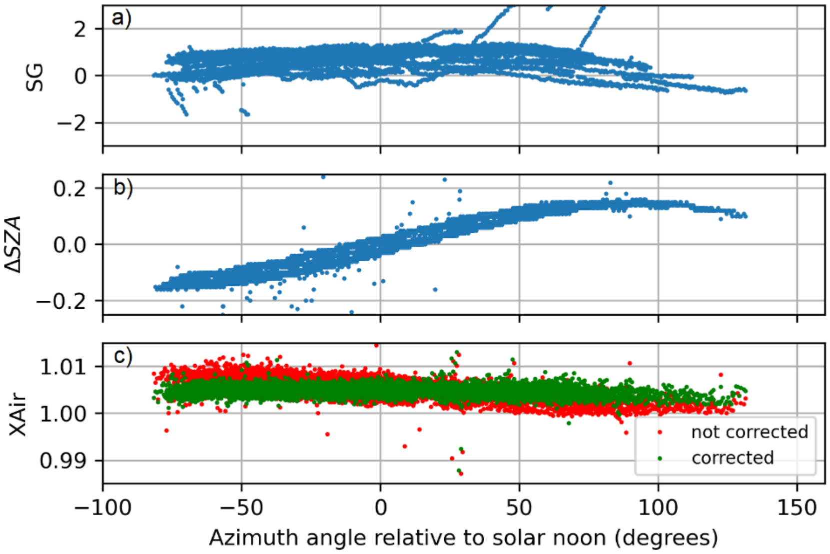

Figure 4.6: Solar zenith angle correction using 2014 Eureka data: (a) solar-gas stretch (in ppm), (b) solar zenith angle correction (ΔSZA in degrees), and (c) XAir retrieved with (green) and without (red) the correction. The horizontal axis shows the azimuth angle of the sun, with solar noon at 0.

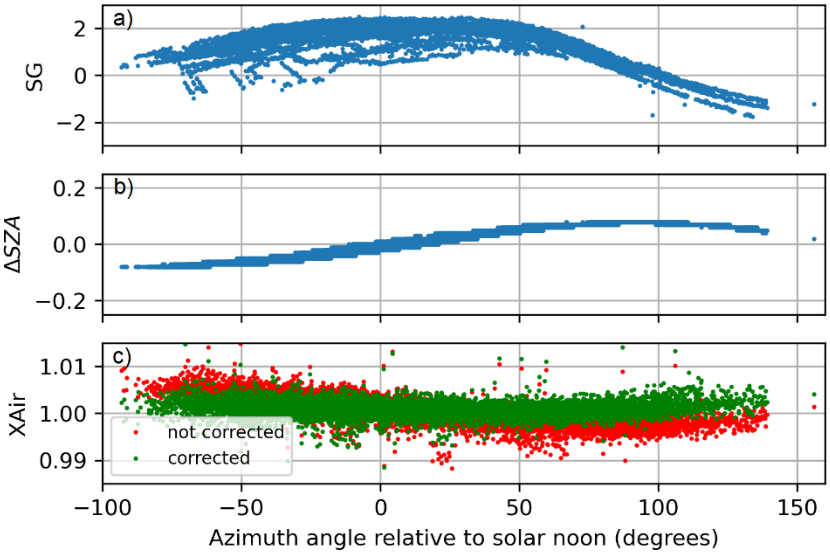

Figure 4.7: Same as Figure 4.6 but for 2020 Eureka data.

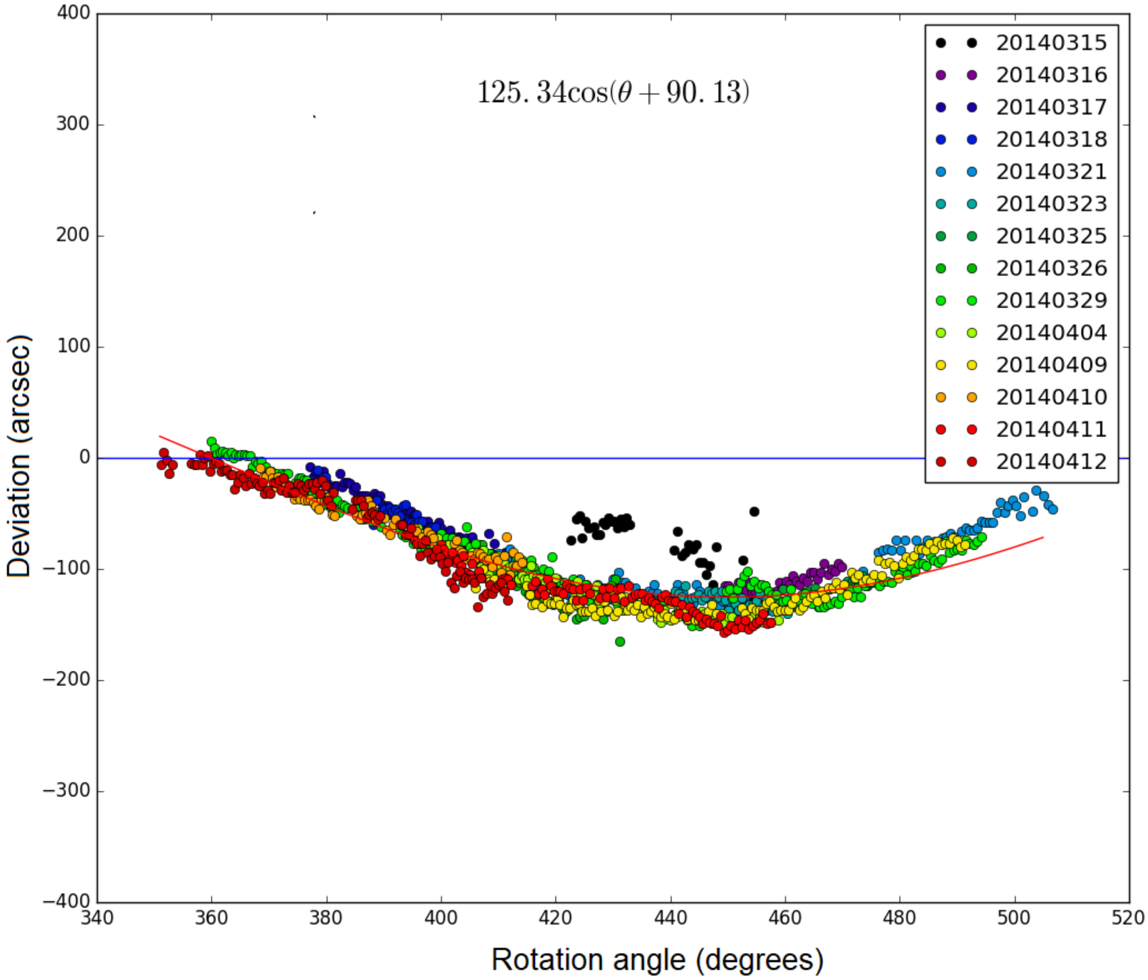

Figure 4.8: Deviation angle (SG_{as}) as a function of the rotation angle of the sun (θ) for Eureka NIR data from 2014 on the dates indicated by the legend (YYYYMMDD).

4.5 Surface Pressure Measurements

Surface pressure measurements are among the auxiliary data used by GGG to process measured solar absorption spectra. These measurements must be made with an accuracy better than 0.3 hPa for TCCON. Since 2010, three different pressure sensors have been used to measure surface pressure at the PEARL Ridge Lab. A Setra Model 270 (M270) since 2010, a Vaisala PTB330 from 2016 to 2019, and a Vaisala PTU300 since March 2020. The Setra Model 270 measurements are included in the outputs of a weather station that also records outside air temperature and humidity, and wind direction and speed. These quantities are measured with a frequency of one minute. Each solar spectrum is paired with a 3-minute average of this auxiliary data.

Another weather station is installed on a safe hut close to the PEARL Ridge Lab, and its measurements of relative humidity are used when there is a gap in the records of the PEARL Ridge Lab weather station.

Biases of a few hPa in surface pressure can result in biases of a few tenths of ppm in XCO_2, it is thus important to monitor the accuracy of the pressure sensors as they can drift in time by as much as 0.1 hPa / y. Table 4.2 presents a summary of the pressure sensors used at PEARL, the last time they were compared to a well-calibrated pressure standard and the resulting correction to be applied. The Setra sensor has been recording since 2010, but since 2016 the more accurate measurements of the Vaisala instruments are used in priority.

Table 4.2: Instruments used to measure surface pressure at the PEARL Ridge Lab. Since 2016, the Setra measurements are only used if there is a gap in the records of the Vaisala sensors.

Sensor	Accuracy (hPa)	Last calibration	Calibration correction (hPa)	Altitude correction	Period
Setra M270	0.3	March 2017	+0.24	Yes	2010-present
Vaisala PTB330	0.15	March 2017	-0.20	Yes	2016-2020
Vaisala PTU300	0.15	March 2020	0.00	No	2020-present

The M270 and PTB330 instruments have been measuring air pressure inside the PEARL Ridge Lab building, in the same room as the FTS. However, GGG needs the pressure at the height of the suntracker mirror, which is located on the roof of the building 4.65 m above. This is because surface pressure is used in the computation of the airmass-dependent path of the sun rays through the atmosphere. Thus, the entire record of surface pressure measurements from the M270 and PTB330 instruments is altitude-corrected using the hydrostatic equilibrium equation:

$$P_{Z_2} = P_{Z_1} e^{-\frac{gM(Z_2 - Z_1)}{RT}} \tag{4.12}$$

where Z_2 is the altitude of the corrected pressure, Z_1 is the altitude at which the pressure is measured, g is the Earth acceleration, M is the molar mass of air, R is the gas constant, and T is the air temperature. The choice of temperature is not critical and taking the inside room temperature or the outside air temperature will have an effect of less than ~0.05 hPa on the pressure correction, even with low Arctic temperatures as illustrated in Figure 4.9.

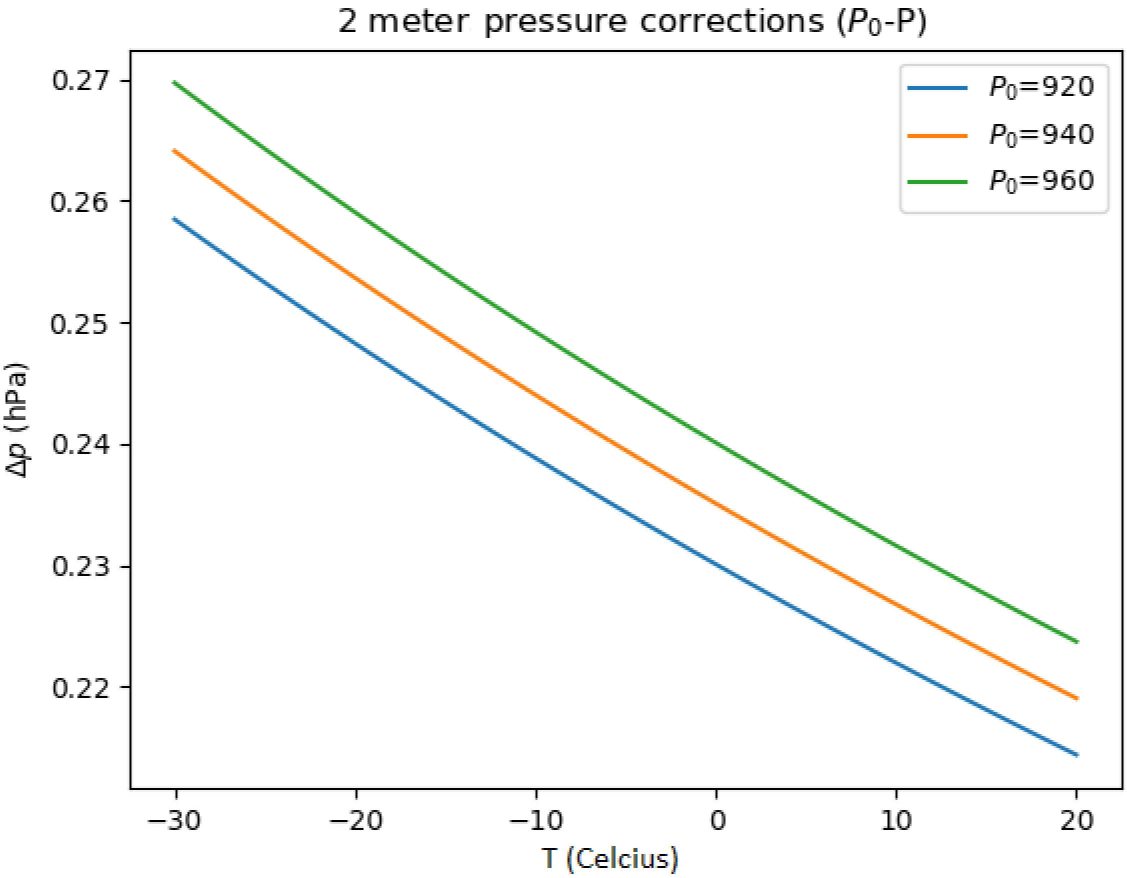

Figure 4.9: Pressure correction (ΔP) for a 2 m altitude difference for a range of air temperatures (T) encountered at Eureka and for three different initial pressures (P_0) as indicated by the legend.

Figure 4.10 shows the raw surface pressure measurements collected by the M270 and PTB330 in 2019. It highlights the need for frequent calibrations of the instruments due to drifts in their accuracy over time. A third calibration sensor is required to determine if the drift comes from only one instrument, or both. For the calibration done in March 2017, the difference between the Digiquartz Paroscientific calibrating sensor and M270 and PTB330 were almost equal in magnitude, but with opposite sign (see Table 4.2). The pressure measurements with altitude and calibration corrections are shown in Figure 4.11.

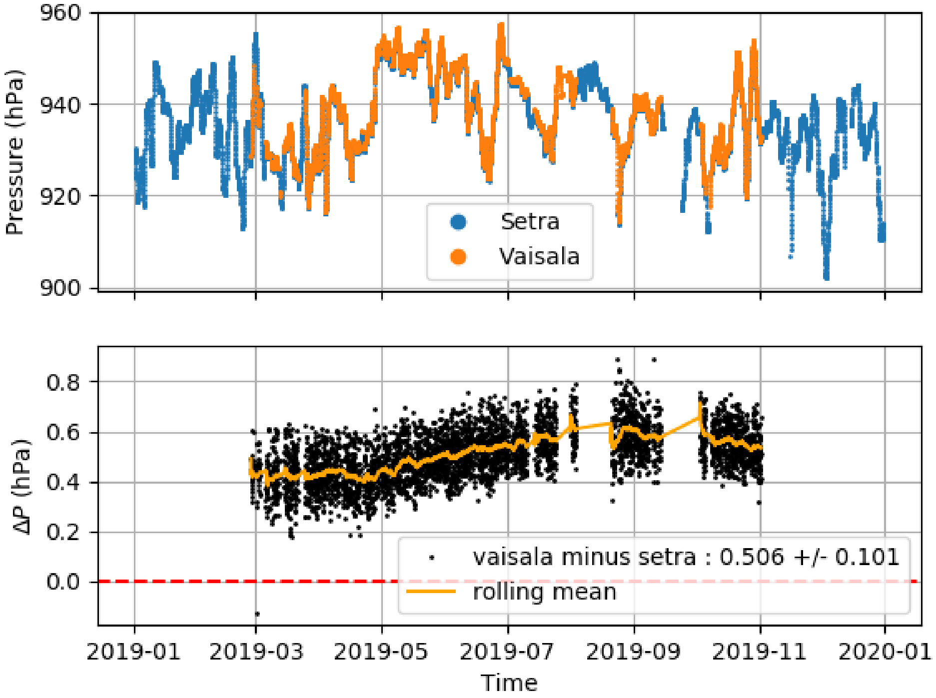

Figure 4.10: Hourly averaged uncorrected surface pressure data for 2019 (upper panel), collected with the M270 (blue) and PTB330 (orange) instruments at the PEARL Ridge Lab. There is a growing offset between the two sensors of ~0.2 hPa from March to August. The long-term stability of these sensors is 0.1 hPa / y. This should motivate yearly calibration of these instruments. The lower panel shows the difference between the two uncorrected pressures measured by the sensors, with the legend indicating the average ± standard deviation of the differences. The red dashed line highlights 0 hPa.

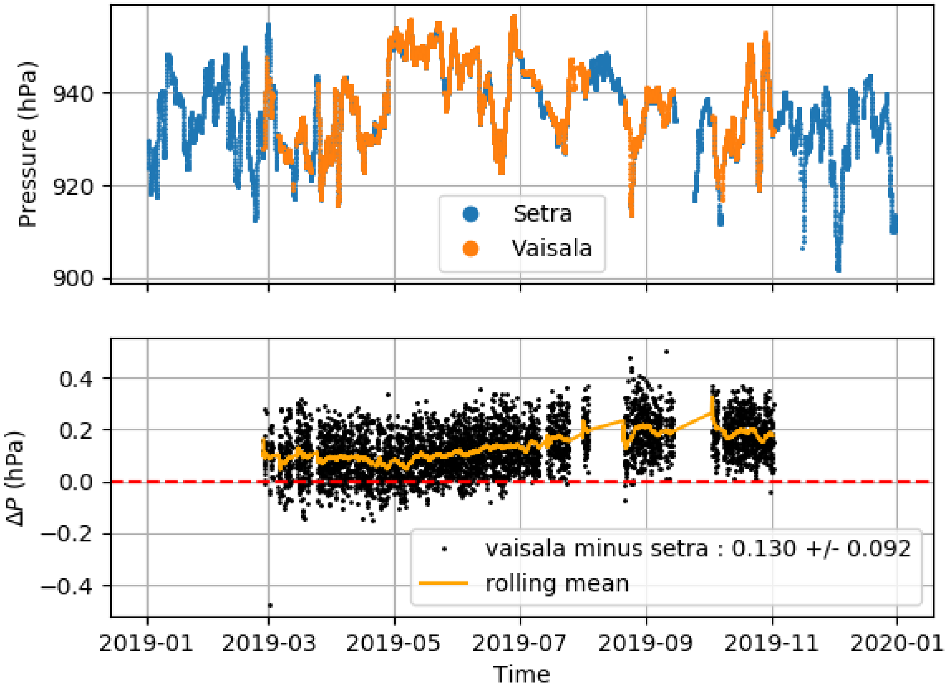

Figure 4.11: Same as Figure 4.10 but including altitude corrections and calibration corrections (based on the calibration done in March 2017).

The PTU300 sensor replaced the PTB330 in March 2020 after the PTB330 stopped working. It was compared to another Vaisala PTB330 pressure sensor from ECCC at the Eureka Weather Station, which was itself last calibrated with a travelling Paroscientific pressure standard in 2018. The differences between the PTU300 and the ECCC instrument were less than 0.05 hPa, so no calibration correction is applied to the surface pressure measurements from the PTU300. The PTU300 is placed on the mezzanine of the PEARL infrared laboratory ~2 m below the suntracker mirror, with an inlet tube attached to sample air at the height of the suntracker mirror. No altitude correction is applied to the measurements of the PTU300. However, it was not verified that the instrument is properly sampling air at the height of the suntracker mirror. This should be verified with a calibrating sensor measuring outside air at the height of the suntracker mirror, once it is possible to return to the Ridge Lab. When this is done, if it is found that the PTU300 is sampling indoor air, it will mean the surface pressure used to process the 2020 Eureka TCCON data was ~0.2-0.3 hPa too high.

4.6 Eureka TCCON Data Revisions

Issues related to surface pressure measurements at PEARL have resulted in three new Eureka TCCON data revisions for spectra processed with GGG2014 in addition to the original R0 (Strong et al., 2014) version: R1 (Strong et al., 2016), R2 (Strong et al., 2017), and R3 (Strong et al., 2019). The changes to and issues with each data revision are summarized below.

R0: 2010 to 2015

- The Airmass Independent Path length (AIPL), between the instrument and the suntracker mirror, was set to 10 m instead of 4.65 m.
- An unnecessary constant surface pressure offset pout_corr=0.7 hPa was mistakenly applied as it was in the original Park Falls input file that should have been modified for Eureka.
- The surface pressure was measured inside the laboratory instead of at the height of the suntracker mirror, without altitude correction.
- Pointing error corrections were only applied for 2014-2015 data.

R1: 2010 to 2016-08

- The correct AIPL (4.65 m) was used.
- The surface pressure offset was set to pout_corr=0 hPa.
- Surface pressure measured in the laboratory was altitude-corrected to the suntracker altitude (4.65 m above) for the whole time series.

- Pointing error corrections were only applied for 2014-2015 data.

R2: 2010 to 2017-09

- The surface pressure was corrected based on comparisons with a well calibrated Paroscientific sensor in March 2017 (before the first NIR measurements of 2017).
- Pointing error corrections were applied for 2014-2018.
- Uncorrected timing offsets of up to 5h were included in the surface pressure measurements.
- An inlet tube was attached to the Vaisala PTB330 pressure sensor on November 5th 2016 to sample air at the height of the suntracker mirror instead of the air inside the laboratory. An altitude correction (of 4.65 m) was mistakenly applied to the data after the installation, instead of before. It was later found the tube was not properly sampling air at the height of the suntracker mirror and the sensor was still measuring indoor air, thus the R2 surface pressure after November 5th 2016 is fortuitously correct. But the surface pressure is ~0.5 hPa too high before November 5th, 2016.

R3: 2010 to 2020

- Timing offsets in surface pressure measurements that affected R2 were fixed. These came from unannounced changes in the time units of the timestamps of the M270 raw measurements, which resulted in shifts up to 5 hours and surface pressure errors of several hPa in R2.
- The inlet tube installed on the Vaisala PTB330 was not properly sampling air at the height of the suntracker mirror, and the measured pressure was still the pressure inside the laboratory (see last bullet for R2). Thus for R3, all measurements from the Vaisala PTB330 sensor are using the altitude correction.
- Because of an issue in the code handling the surface pressure measurements, the R3 2019 data is using pressure from the Setra Model 270 sensor rather than the Vaisala PTB330 sensor. The R3 2019 data are not “wrong”, but this was not intended and the more accurate Vaisala PTB330 measurements should have been used.

The differences in retrieved XCO_2 resulting from the changes between each data revision and earlier revisions are shown in Figure 4.12. The changes in XCO_2 between R1, R2 and R3 are all smaller than differences relative to the original R0 data, which had the largest surface pressure errors, ~1.2 hPa too high because of the cumulative effect of a missing altitude correction (~ +0.5 hPa) and the erroneous +0.7 hPa offset that was applied. Differences between subsequent revisions caused by smaller corrections lead to XCO_2 variability of ~0.1 ppm. These differences are significant because they are of the same order as the 0.4 ppm 1σ precision of TCCON GGG2014 products. With improvements to the retrieval algorithm, these kinds of issues become increasingly important.

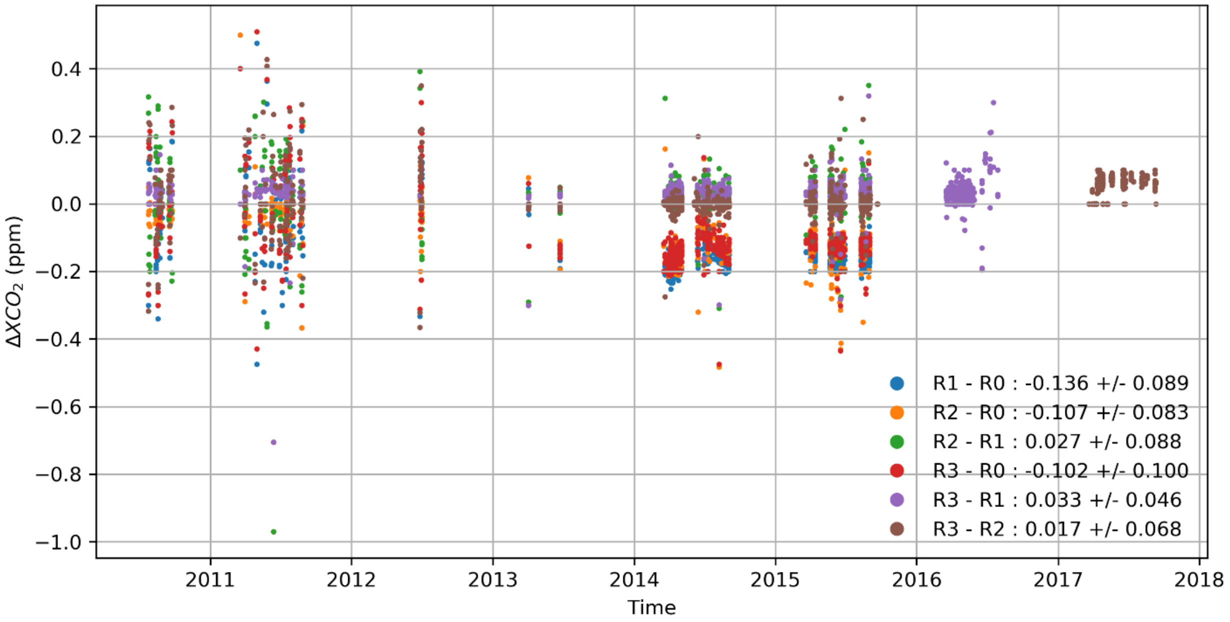

Figure 4.12: Difference in retrieved XCO_2 between each data revision and earlier revisions as indicated by the legend. The legend also shows the mean ± standard deviation of the differences.

4.7 Contributions to Validation Projects

The NIR measurements collected during this thesis contributed to validations studies that rely on TCCON data as the reference. Hedelius et al. (2020) used GGG2014 TCCON data to evaluate Version 7 joint (V7J) XCO products from the MOPITT instrument on the Terra satellite. MOPITT, launched in 1999, was the first instrument dedicated to measure CO from space (Drummond et al., 2010). Results showed MOPITT V7J has a high XCO bias of 6-8% when compared to standard TCCON XCO products as illustrated in Figure 4.13. However, the TCCON XCO products are tied to the World Meteorological Organization (WMO) in-situ scale using comparisons with aircraft measurements; the resulting scaling factor applied to GGG2014 XCO is +7% (Wunch et al., 2010). Without that scaling applied, MOPITT XCO has a bias less than 0.5%. The +7% scaling applied to TCCON XCO is inconsistent with retrieval errors expected from uncertainties in spectroscopic parameters and there is an ongoing effort to determine if the scaling is appropriate for XCO. If the scaling is appropriate, the estimated 1σ accuracy of TCCON XCO is 2 ppb (Wunch et al., 2010).

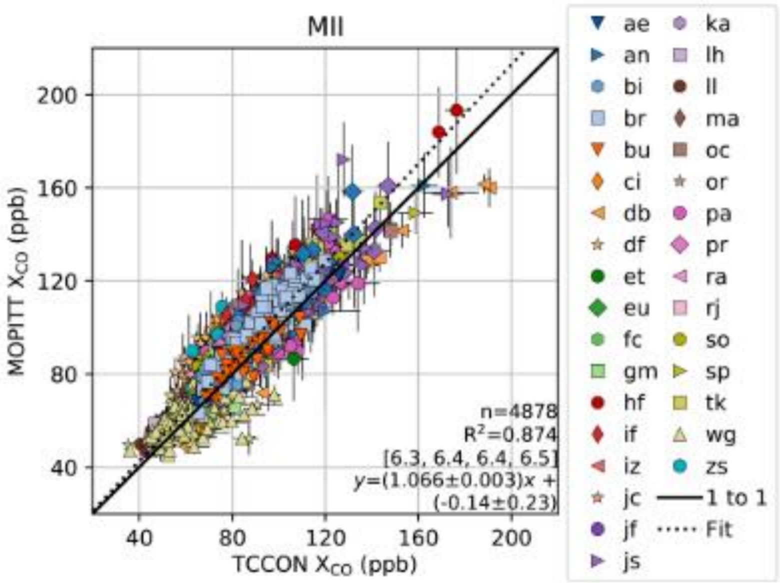

Figure 4.13: Correlation plot comparing MOPITT and TCCON XCO. Figure obtained from Hedelius et al. (2019).

TROPOMI was launched on the Sentinel-5P Precursor (S5P) satellite in 2017 to measure atmospheric trace gases such as ozone, NO_2, SO_2, CO, CH_4, CH_2O (formaldehyde), and aerosol properties (Veefkind et al., 2012). Schneising et al. (2019) used TCCON data to validate XCH_4 and XCO derived from the operational retrieval algorithm of TROPOMI using the first measurements from the mission start until 2018. The target accuracy of TROPOMI is 15% for XCO and 2% for XCH_4 (Veefkind et al., 2012; Fehr, 2016). The TCCON 1σ accuracy for XCH_4 is 3.5 ppb (Wunch et al., 2010). Results showed global offsets of 4.49 ppb for XCO and -1.3 ppb for XCH_4. Figure 4.14 shows the comparisons of TROPOMI with TCCON using daily averages of XCO and XCH_4.

Sha et al. (2021) used both NDACC-IRWG and TCCON data to validate TROPOMI XCO and XCH_4 measurements from November 2017 to September 2020. The study considered both the uncorrected TROPOMI data and bias corrected data. They found the systematic differences between TROPOMI and TCCON XCH_4 was -0.69±0.73% for the uncorrected data and -0.25±0.57% for the bias-corrected data. For XCO they found systematic differences of 9.14±3.33% using standard TCCON XCO, and 2.36±3.22% using TCCON XCO without the +7% in-situ scaling.

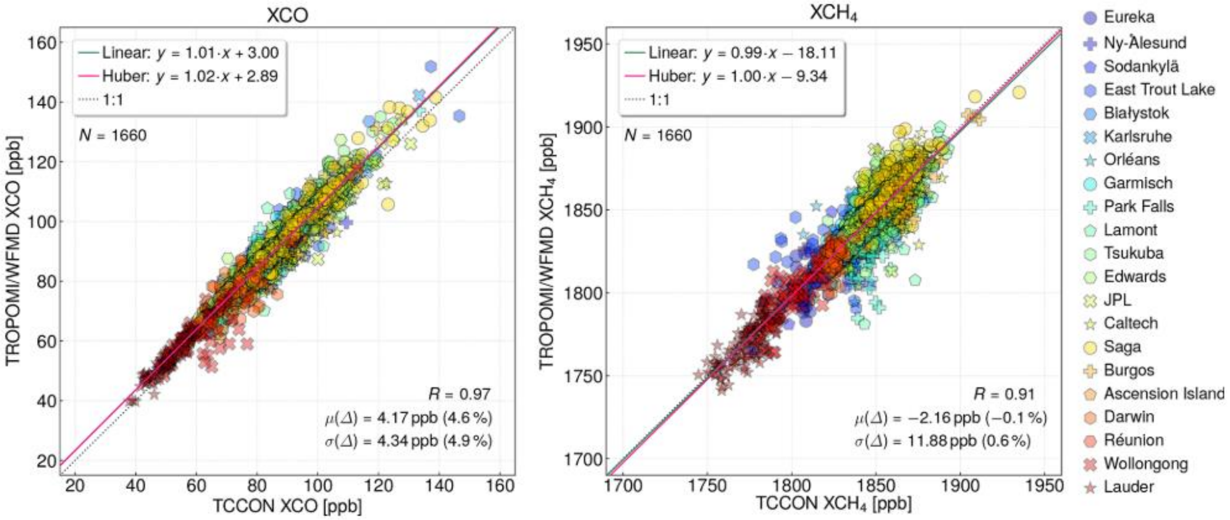

Figure 4.14: Correlation plots of TROPOMI XCO (left) and XCH_4 (right) compared to TCCON based on daily means. The linear regression results are shown as well as the correlation (R), and also the mean (μ) and standard deviation (σ) of the differences. Figure taken from Schneising et al. (2019).

Reuter et al. (2020) used TCCON data to validate a new XCO_2 and XCH_4 data product that aims to produce a consistent long-term data record of these variables. They merged satellite data products from SCIAMACHY, GOSAT, and OCO-2 using the ensemble median algorithm (EMMA) developed by Reuter et al. (2013) to provide a dataset useful for surface flux inversions. The resulting Level 2 (L2) dataset consists of a merged across-track data product in addition to the original data from each satellite. The L2 merged data were used to generate Level 3 (L3) data consisting of gridded 5°x5° global files of monthly XCO_2 and XCH_4. This data product is available on the Copernicus Climate Data Store (CDS: https://cds.climate.copernicus.eu, last accessed April 8th, 2021). The comparison with TCCON was done for both the L2 and L3 datasets; the results for the L2 product showed a global bias of 0.2±1.29 ppm (mean difference ± standard deviation of differences) for XCO_2 and -2.0±17.4 ppb for XCH_4. The results for the L3 product showed a global bias of 0.18±1.18 ppm for XCO_2 and -2.9±8.7 ppb for XCH_4.

Finally, Kulawik et al. (2019) compared OCO-2 and the Atmospheric Observations from Space (ACOS) GOSAT XCO_2 to TCCON and in-situ measurements to characterize the spatiotemporal variability of XCO_2 biases in the OCO-2 Version 8 products and ACOS GOSAT version 7.3 products. They found a systematic error of 0.6±0.1 ppm over land for both satellite products and this error is reduced by 0.5 ppm with bias corrections. They found OCO-2 XCO_2 errors were correlated on spatial scales of 0.3° and 5-10°, and on temporal scales of 60 days. They then assimilated the OCO-2 XCO_2 bias-correction term of +0.7 ppm in a surface flux inversion to estimate the effect of OCO-2 spatiotemporal biases on fluxes in regions defined for the Atmospheric Tracer Transport Model Intercomparison Project phase 3 (TransCom-3). The assimilations of the OCO-2 biases caused patterns of positive and negative flux variation with standard deviations of 0.4 $PgC.y^{-1}$ over land.

4.8 Comparisons of TCCON XCO_2 and XCH_4 with GEM-MACH-GHG Simulations

XCO_2 and XCH_4 retrieved from NIR spectra collected at the PEARL Ridge Lab and other TCCON stations were used to validate simulations of a new model for greenhouse gas transport developed at ECCC: the Global Environmental Multiscale - Modelling Air Quality and CHemistry for GreenHouse Gases (GEM-MACH-GHG). This work was published in Polavarapu et al. (2016). GEM is an integrated forecasting and data assimilation system developed for operational weather forecasts in Canada (Côté et al., 1998; Girard et al., 2014). GEM-MACH (Moran et al., 2010) adds complete tropospheric chemistry in a limited domain over North America. GEM-MACH-GHG replaces the GEM-MACH chemistry model with a simplified model for CO and CH_4 chemistry in the troposphere. It only includes their oxidation reaction with OH (Polavarapu et al., 2016; Kim et al., 2020).

The simulations were run using CarbonTracker (CT2013B; Peters et al., 2007) 3-hourly optimized CO_2 surface fluxes at every time step in the model. The initial conditions are from CT2013B on January 1st, 2009. A 1-year spin-up period is used to reduce the effect of initial and boundary conditions. The CH_4 surface fluxes are from CarbonTracker-CH_4 (provided by NOAA ESRL, Boulder, Colorado, USA, from the website at https://www.esrl.noaa.gov/gmd/ccgg/carbontracker-ch4). The CO surface fluxes were prepared by Sylvie Gravel (Meteorological Service of Canada) from the Hemispheric Transport of Air Pollution project (HTAP; Janssens-Maenhout et al., 2015). The simulated CO_2 and CH_4 for the year 2010 were compared to TCCON measurements. The TCCON sites included in the comparison are presented in Table 4.3.

Table 4.3: TCCON sites used to compare with GEM-MACH-GHG simulations.

Site	Latitude	Longitude	Reference
Eureka	80.05	-86.42	Strong et al. (2019)
Sodankylä	67.37	26.63	Kivi et al. (2014)
Bialystok	53.23	23.02	Deutscher et al. (2019)
Bremen	53.1	8.85	Notholt et al. (2019)
Karlsruhe	49.1	8.44	Hase et al. (2015)
Orléans	47.97	2.11	Warneke et al. (2019)
Garmisch	47.48	11.06	Sussmann and Rettinger (2018)
Park Falls	45.94	-90.27	Wennberg et al. (2017)
Lamont	36.6	-97.49	Wennberg et al. (2016)
Izaña	28.3	-16.48	Blumenstock et al. (2017)
Darwin	-12.43	130.89	Griffith et al. (2014)
Wollongong	-34.41	150.88	Griffith et al. (2014b)
Lauder	-45.05	169.68	Sherlock et al. (2014a, 2014b)

The model outputs vertical profiles of CO_2 and CH_4 dry-air mole fractions at each site's location. To be properly compared to TCCON products, both the model and TCCON total columns are derived in the same way. The vertical column of a gas, gas, is obtained as:

$$VC_{gas} = \sum_{i=1}^{N} \frac{f_{gas,i}}{g_i m_{air}} \Delta p_i \tag{4.13}$$

where $f_{gas,i}$ is the mole fraction of that gas at the ith layer with pressure thickness Δp_i, g_i is Earth's acceleration, and m_{air} is the molecular weight of air. GEM-MACH-GHG produces profiles of dry-air mole fraction $f_{gas}^{dry} = \frac{f_{gas}}{1-f_{H_2O}}$, as well as specific humidity $q = \frac{[kg_{H_2O}]}{[kg_{air}]}$. Considering $\frac{1-f_{H_2O}}{m_{air}} = \frac{1-q}{m_{air}^{dry}}$ we can express Eq. 4.13 as:

$$VC_{gas} = \sum_{i=1}^{N} \frac{(1-q_i) f_{gas,i}^{dry}}{g_i m_{air}^{dry}} \Delta p_i\,. \tag{4.14}$$

The total column amounts derived from the model outputs are then smoothed using:

$$VC_{gas,a} = \sum_{i=1}^{N} \frac{a_i(1-q_i)f_{gas,i}^{dry}}{g_i m_{air}^{dry}} \Delta p_i \tag{4.15}$$

where $\boldsymbol{a}$ is the TCCON column averaging kernel. Finally, the smoothed model column-averaged dry-air mole fraction X_{gas} is obtained as (Rodgers and Connor, 2003):

$$X_{gas}^{model} = X_{gas}^{a\ priori} + \frac{VC_{gas,a}^{model} - VC_{gas,a}^{a\ priori}}{VC_{air}^{dry}} \tag{4.16}$$

where “a priori” refers to the TCCON a priori mole fraction being used in Eq. 4.15. Here the model output is treated like a true profile, and X_{gas}^{model} is the estimate of how the TCCON instrument would measure that profile in the absence of retrieval error. In the absence of retrieval errors, replacing $VC_{gas,a}^{model}$ with the smoothed true atmospheric profile $VC_{gas,a}^{true}$ in Eq. 4.16 would produce the retrieved X_{gas}^{TCCON}.

GEM-MACH-GHG has an output frequency of 15 min. Hourly averages of X_{gas} are considered in the comparisons with TCCON and the following statistics are used, with N the number of pairs (hours) for which there are TCCON measurements. The Bias is the average difference between the model and TCCON:

$$Bias = \frac{1}{N}\sum_{i=1}^{N}\left(X_{gas}^{model} - X_{gas}^{TCCON}\right)_i . \tag{4.17}$$

The root-mean-square of the differences is:

$$RMS = \sqrt{\frac{1}{N}\sum_{i=1}^{N}\left(X_{gas}^{model} - X_{gas}^{TCCON}\right)^2_i} . \tag{4.18}$$

The Scatter is the standard deviation of the differences:

$$Scatter = \sqrt{\frac{1}{N-1}\sum_{i=1}^{N}\left[\left(X_{gas}^{model} - X_{gas}^{TCCON}\right)_i - Bias\right]^2}\,. \quad (4.19)$$

The Pearson's correlation coefficient is defined as:

$$R = \frac{\sum_{i=1}^{N}\left(X_{gas,i}^{model} - {X_{gas}^{model}}_{mean}\right)\left(X_{gas,i}^{TCCON} - {X_{gas}^{TCCON}}_{mean}\right)}{\sqrt{\sum_{i=1}^{N}\left(X_{gas,i}^{model} - {X_{gas}^{model}}_{mean}\right)^2}\sqrt{\sum_{i=1}^{N}\left(X_{gas,i}^{TCCON} - {X_{gas}^{TCCON}}_{mean}\right)^2}}\,. \quad (4.20)$$

The mean bias is:

$$Bias_{mean} = \frac{1}{N_s}\sum_{i=1}^{N_s} Bias_i \quad (4.21)$$

where N_s is the number of TCCON stations. And the standard deviation of the biases provides an estimate of the variability in the Bias from station to station:

$$SD = \sqrt{\frac{1}{N_s - 1}\sum_{i=1}^{N_s}\left(Bias_i - Bias_{mean}\right)^2}\,. \quad (4.22)$$

This last quantity is an estimate of regional-scale accuracy and is only meaningful if the station-to-station Bias of TCCON products with respect to the true state of the atmosphere is negligible compared to the model-TCCON station-to-station bias. The best approximation to the true state of the atmosphere is obtained with in-situ measurements of trace gases from aircraft, which are used to "calibrate" TCCON and improve its accuracy. The resulting 2σ precision and accuracy of the network is ~0.8 ppm for XCO_2 (Wunch et al., 2010).

The statistics for the XCO_2 comparisons are shown in Table 4.4, using all GGG2014 TCCON data in 2010. The Bias is below 1 ppm at every station but Eureka, which only had 56 hours (i.e., N=56) of measurements in 2010, the year that NIR capability was added to the 125HR. All the data are included when computing the Mean, SD, and ALL statistics. At Eureka the -2.4 ppm bias significantly impacts SD, it is 0.83 ppm with Eureka and 0.26 ppm without. And the mean bias increases from 0.23 ppm to 0.45 ppm without Eureka. The large negative bias relative to Eureka stands out from the other station, possibly pointing to issues with transport to this region in the model, or an incompatibility between CT2013B fluxes and the GEM-MACH-GHG transport. The CT2013B fluxes are optimized for CarbonTracker to produce results consistent with observations. Since the GEM-MACH-GHG transport is different from that of CarbonTracker, GEM-MACH-GHG CO_2 and CH_4 concentrations cannot be expected to compare better to observations than CarbonTracker when using CT2013B fluxes (Polavarapu et al., 2016). Except for Eureka and Lauder with the 120HR instrument, the bias is positive with an overall standard deviation of 0.89 ppm and a high correlation of 0.93. The record from the Lauder station is split into two distinct periods using two different instruments: the 120HR spectrometer, which measured until December 2010, and the 125HR that started measuring in February 2010. The XCO_2 obtained from the 120HR shows poorer correlation (0.8 instead of 0.88 ppm) and scatter (0.76 instead of 0.47 ppm).

Table 4.4: Statistics of comparisons between TCCON XCO_2 and GEM-MACH-GHG hourly-averaged smoothed XCO_2. Bias is the mean difference, RMS is the root-mean square of differences, Scatter is the standard deviation of the differences, and R is Pearson's correlation coefficient. The "ALL" field presents statistics using all data from all sites combined. The "Mean" is the average of each parameter and SD is the standard deviation of the station's bias. N is the number of data pairs used in the computation of the statistics. For Mean and SD, N is the number of sites (14).

Site	Latitude	N	Bias (ppm)	RMS (ppm)	Scatter (ppm)	R
Eureka	80.05	56	-2.4	2.64	1.11	0.76
Sodankylä	67.37	757	0.49	1.17	1.06	0.97
Białystok	53.23	586	0.62	1.3	1.14	0.9
Karlsruhe	49.1	274	0.94	1.36	0.98	0.92
Orléans	47.97	571	0.72	0.98	0.66	0.97
Garmisch	47.48	734	0.26	1.1	1.07	0.91
Park Falls	45.94	954	0.15	0.8	0.78	0.95
Lamont	36.6	2239	0.33	0.87	0.8	0.89
Izaña	28.3	140	0.65	1.13	0.92	0.87
Darwin	-12.43	289	0.39	0.62	0.49	0.57
Wollongong	-34.41	856	0.54	0.92	0.75	0.69
Lauder 125	-45.04	826	0.34	0.58	0.47	0.88
Lauder 120	-45.05	384	-0.02	0.76	0.76	0.8
ALL		8666	0.4	0.98	0.89	0.93
Mean			0.23	1.09	0.85	0.85
SD			0.83			

The statistics for the XCH_4 comparisons are shown in Table 4.5. In this case, Eureka does not present an anomalous bias compared to other sites, but shows a poor correlation of 0.34, along with Darwin at 0.53. The Bias is positive except at Izaña, which is the only high-altitude site at 2.3 km above sea level. The Bias is less than 10 ppb except at Lauder and Sodankylä, with an overall scatter of 8.42 ppb. Like CO_2, CH_4 is a well mixed gas in the troposphere and variations are small relative to the background concentrations of ~1800 ppb (in 2010). The precision requirement for satisfactory observations, or simulations, is thus relatively high at ~1% (~18 ppb) and the comparisons shows that the model can simulate XCH_4 to better than 1%.

Table 4.5: Same as Table 4.4 but for XCH_4.

Site	Latitude	N	Bias (ppb)	RMS (ppb)	Scatter (ppb)	R
Eureka	80.05	56	3.78	10.25	9.61	0.34
Sodankylä	67.37	757	12.44	15.73	9.63	0.89
Białystok	53.23	586	4.08	7.89	6.75	0.77
Karlsruhe	49.1	274	7.99	10.66	7.07	0.73
Orléans	47.97	571	5.19	7.56	5.5	0.78
Garmisch	47.48	734	0.1	7.38	7.39	0.72
Park Falls	45.94	954	3.15	6.69	5.91	0.82
Lamont	36.6	2239	1.78	7.55	7.34	0.86
Izaña	28.3	140	-3.13	7.37	6.69	0.68
Darwin	-12.43	289	6.68	8.33	4.99	0.53
Wollongong	-34.41	856	8.86	11.51	7.36	0.79
Lauder 125	-45.04	826	14.66	15.24	4.19	0.93
Lauder 120	-45.05	384	14.4	15.26	5.08	0.91
ALL		8666	5.48	10.05	8.42	0.96
Mean			6.15	10.11	6.73	0.75
SD			5.42			

Chapter 5
Retrieval of CO_2 Vertical Profiles from Ground-Based Near-Infrared Spectra

This chapter presents a study that aims to improve retrievals of CO_2 from ground-based solar spectra as measured by the TCCON instruments. This was done through the use of the GFIT2 algorithm, which performs full profile retrievals rather than the scaling retrievals performed by the TCCON algorithm GFIT. TCCON and GFIT were first introduced in Sect. 1.4, along with the motivation for the development of CO_2 profile retrievals. A methodology was developed to assess the performance of profile retrievals, first using retrievals on synthetic spectra, and then using AirCore profiles (see Sect. 1.3.1) as the a priori in retrievals from real spectra to isolate the effect of a priori errors from those of other errors in the forward model. The work presented in this chapter was published in Roche et al. (2021).

This study assesses the quality of CO_2 profile retrievals with GFIT2 implemented in GGG2020. Section 5.2 describes the retrieval algorithm and our methodology. Section 5.3 presents a sensitivity study using synthetic spectra, followed by retrievals using real measured spectra. Section 5.4 investigates the use of empirical orthogonal functions to empirically correct forward model errors. Finally, Sect. 5.5 presents a summary of the results and conclusions.

5.1 Introduction

CO_2 profile retrievals from ground-based Short-Wave Infrared (SWIR) spectra have been performed in other studies using the band centered at 1.6 µm fitted with a Voigt line shape (Kuai et al., 2012), and in the band centered at 2.06 µm with the PROFFIT optimal estimation software package (Hase et al., 2004) fitted with a Voigt line shape with line mixing (Dohe, 2013). Connor et al. (2016) showed that CO_2 profile retrievals in the CO_2 band centered at 1.6 µm are very sensitive to errors in spectroscopy. In our approach, we use the GFIT2 software package initially described by Connor et al. (2016), which is a profile retrieval algorithm based on the GGG software suite, but modified such that it allows the profile shape to vary during the retrieval process. Instead of retrieving a single VSF value that scales the whole a priori profile, a VSF value is retrieved for each atmospheric level. The algorithm thus has much more freedom to fit the observed spectra but is also more sensitive to uncertainties in the forward model calculations such as errors in the atmospheric temperature profile, spectroscopic errors, and instrument misalignment, for example.

GFIT2 was first developed using the GGG2014 version of the GGG suite (Wunch et al., 2015), which uses a Voigt line shape to compute absorptions coefficients. In this study, we use the GGG2020 version, which will be released in mid 2021. This version of the code implements quadratic speed-dependent Voigt line shapes with line mixing (qSDV+LM) for CO_2 (Mendonca et al., 2016) and CH_4 (Mendonca et al., 2017) bands, and qSDV line shapes for O_2 in the band centered at 1.27 µm (Mendonca et al., 2019). The line mixing coefficients are derived with the first-order Rosenkranz approximation (Rosenkranz, 1975). This leads to significantly better spectral fits, especially in the strong CO_2 band centered at 2.06 µm, as was shown in Figure 3.5, and smaller variations of gas amount with airmass. Other improvements to the forward model include: (1) updates to the spectroscopic linelist (Toon, 2015); (2) a solar-gas stretch fitted to account for Doppler-driven differences between solar and telluric wavenumber scales (see Sect. 4.4), whereas in GGG2014 only the stretch in the telluric wavenumber scale was fitted; and (3) improved a priori profiles as described in Sect. 5.2.

5.2 Methods

In this study, GFIT2 is used to retrieve CO_2 profiles from the two original TCCON retrieval windows and three new windows that possess a large range of opacities, and therefore vertical sensitivities. These windows are presented in Table 5.1 and Figure 5.1. The TCCON1 window (centered at 6220 cm^{-1}) and TCCON2 window (centered at 6339.5 cm^{-1}) are used to derive XCO_2 for the public TCCON data products, because the spectral absorption lines opacities are close to 1 and are therefore equally sensitive at most altitudes. The CO_2 line intensities in the two weak windows are 10 times smaller those in the standard TCCON windows, providing more sensitivity to CO_2 variations aloft. The CO_2 lines in the strong window are 15 times stronger than those in the standard TCCON windows, providing more sensitivity to CO_2 variations near the surface. All windows have an average lower-state energy (E’’) of roughly 240 cm^{-1}, rendering the retrieved total column of CO_2 highly independent of the assumed temperature ($<0.1\%.K^{-1}$). The derivation of XCO_2 as calculated in GGG was described in Sect. 4.2. XCO_2 is the ratio of the CO_2 column to the column of dry air, and the column of dry air is expressed as the retrieved O_2 column (from the window centered at 7885 cm^{-1}, see Table 5.1) divided by 0.2095 (Wunch et al., 2011b). OCO-2/3 and GOSAT/2 use two windows comparable to the Weak1 and Strong windows to retrieve CO_2, and use the O_2 A-band (centered near 13158 cm^{-1}) to obtain the O_2 column.

Table 5.1: CO_2 spectral windows used with GFIT2. Interfering absorbers labeled "solar" are due to absorption by heavy metal ions (e.g., Fe, Si, Ca, Ni) in the solar atmosphere. Also shown are the strength-weighted averages of the lower-state energy (E''), and of the line strengths (S) over all the CO_2 lines in each window. The column of O_2, retrieved with scaling retrievals from the O_2 window, is used to compute XCO_2.

Window name	Center (μm)	Center (cm^{-1})	Width (cm^{-1})	Primary interfering absorbers	E'' (cm^{-1})	S (cm^{-1}/(molecule.cm^{-2})) $\times 10^{-23}$
TCCON1	1.61	6220	80	solar, H_2O	245.3	1.14
TCCON2	1.58	6339.5	85	solar, H_2O	254.6	1.14
Weak1	1.65	6074	70.8	CH_4, solar, H_2O	223.5	0.118
Weak2	1.54	6499.1	69.8	solar, H_2O, HDO	229.3	0.130
Strong	2.06	4852.87	86.26	H_2O, $^{13}CO_2$, solar	243.8	17.8
O_2	1.27	7885	240	solar, H_2O, HF, CO_2	203.4	0.00518

A qualitative representation of the vertical sensitivity due to the range of different line opacities is presented in Figure 5.2, which shows the normalized CO_2 Jacobian for typical absorption lines in the Strong window (centered at 4852.87 cm^{-1}), the Weak1 window (centered at 6074 cm^{-1}), and the TCCON1 window (centered at 6220 cm^{-1}). The strong saturated lines of the Strong window are more sensitive to levels below 5 km than lines in the TCCON1 window, but the Strong window also contains lines of intermediate absorption strength that provide more uniform sensitivity up to ~10 km, and that extend the window's sensitivity to up to 30–40 km. The saturated lines in the Strong window correspond to the 20013–00001 band, while the lines of intermediate strength around 4820 cm^{-1} come from the R-branch of the 21113–01101 band. The TCCON1 window has more uniform sensitivity up to ~10–15 km and includes weak lines that contain information on CO_2 above 15 km. The Weak1 window is less sensitive below 10 km and has more uniform sensitivity between 10–20 km. Figure 5.2 also shows little to no sensitivity to levels above ~30 km in all windows.

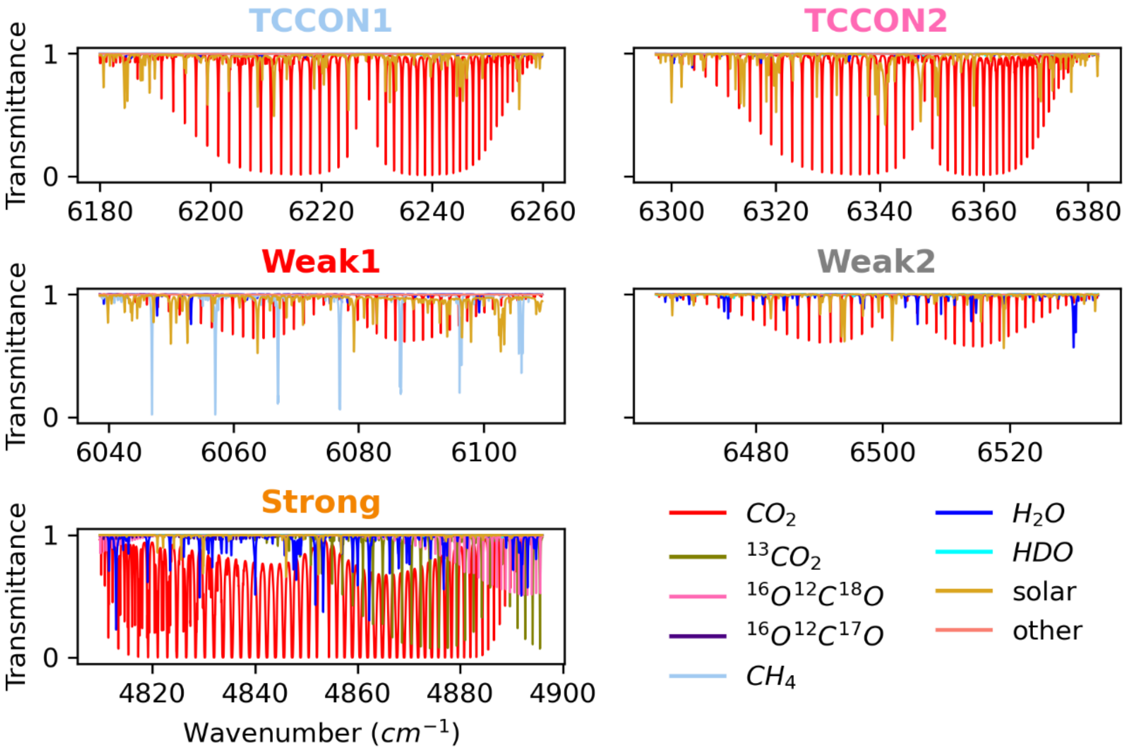

Figure 5.1: Contributions of different absorbing gases to the calculated transmittance spectrum on a dry winter day at Lamont on January 14th, 2012 and at a solar zenith angle of 60.6° for each of the spectral windows used to retrieve CO_2.

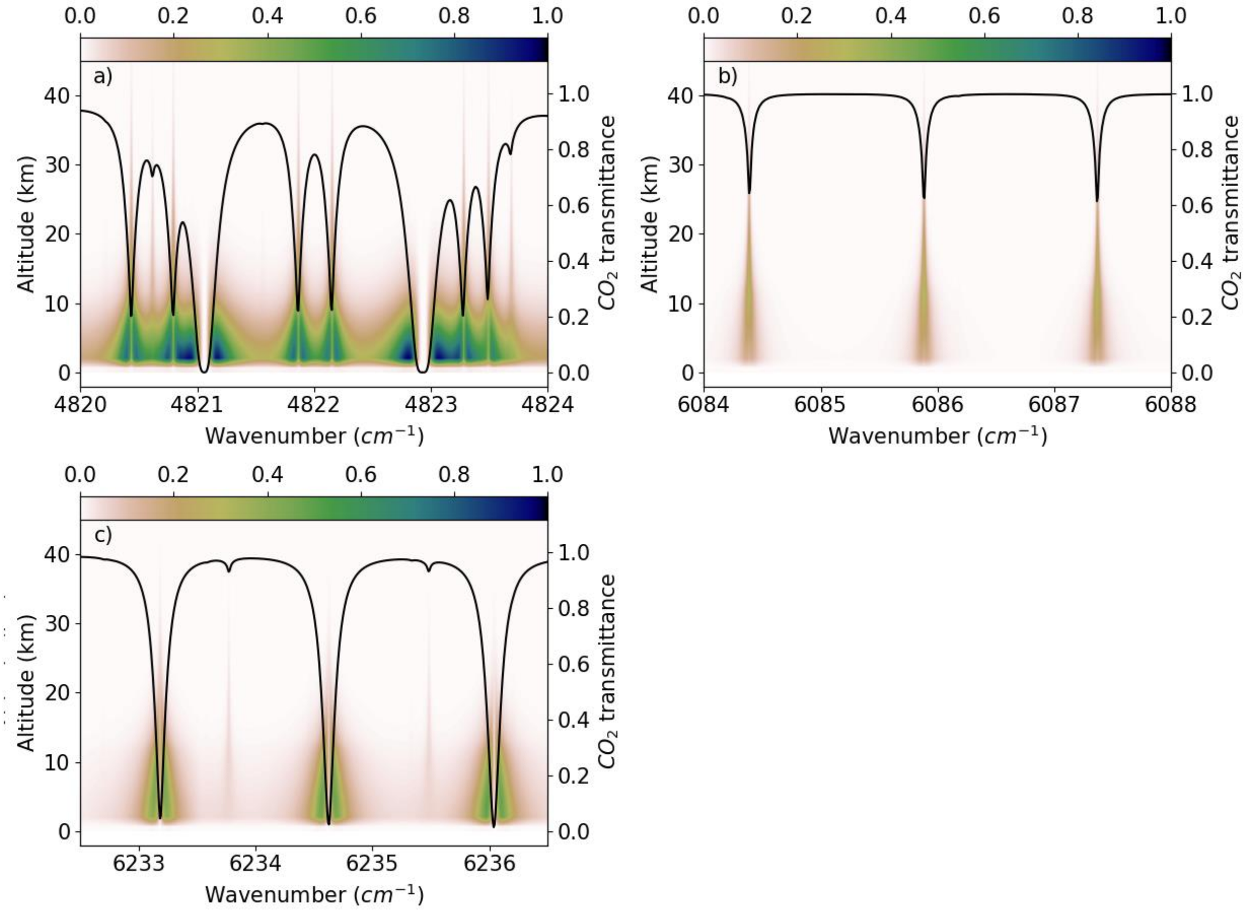

Figure 5.2: CO_2 absorption lines (black line) overlaid on heatmaps of the CO_2 Jacobian for lines of (a) the Strong window; (b) the Weak1 window; and (c) the TCCON1 window. The colour bar represents the normalized Jacobian where 1 corresponds to the maximum amongst all the CO_2 Jacobians from the five CO_2 windows. Lines of the Weak2 and TCCON2 windows are not shown as they look like the Weak1 and TCCON1 windows, respectively.

5.2.1 Retrieval Algorithm

The details of the GFIT and GFIT2 retrieval algorithm were presented in Sect. 3.4, with the complete set of retrieved parameters presented in Table 3.2. In principle, a CO_2 profile retrieval should have less sensitivity to errors in the a priori CO_2 profile compared to scaling retrievals (i.e., differences from the true profile) since it can adjust for differences between measured and calculated spectra caused by erroneous prior profile shapes (Connor et al., 2016). However, the retrieval may also conflate errors due to other sources, such as incorrect spectroscopic parameters, incorrect modeling of the instrument line shape, or errors in the a priori meteorology and profiles of interfering species, with these errors in the a priori CO_2 profile.

5.2.2 Data Sets

The CO_2 and CH_4 a priori profiles were built by combining the balloon-borne AirCore (Karion et al., 2010) profiles with surface in situ measurements, adding the GGG2020 a priori profile above the maximum altitude sampled by AirCore. These composite profiles will be referred as "truth". The CH_4 profile is included because CH_4 is an interfering gas in the Weak1 window. In Sect. 5.3.2, AirCore profiles from the v20181101 dataset were used as "truth" to assess the quality of GFIT2 profile retrievals. We used all AirCore profiles measured over the Lamont TCCON station that had coincident ground-based measurements within ± 1 h of the AirCore landing and within ±1.5 h of the closest a priori time. All figures showing profiles use the average of profiles retrieved from the coincident spectra. The launch dates of the eight AirCore profiles used are presented in Table 5.2. An iMet-1 radiosonde carried by the same balloon as the AirCore provides in situ temperature and relative humidity profiles.

Table 5.2: AirCore launch dates and number of coincident spectra within ±1 h of the AirCore last sampling time and within ±1.5 h of the closest a priori time. The range of solar zenith angles covered by the coincident spectra is also shown.

Launch date	Coincident spectra	Solar zenith angles (degrees)
January 14th, 2012	65	60.6–73.8
January 15th, 2012	48	65.6–77.9
July 23rd, 2013	44	20.8–36.5
February 26th, 2014	61	46.6–59.0
February 27th, 2014	41	46.2–53.3
September 17th, 2014	48	37.9–51.1
October 19th, 2016	31	47.1–50.3
April 11th, 2017	33	31.2–39.2

Instead of the diagonal prior covariance used in Sect. 5.2.1, a more realistic CO_2 prior covariance matrix was built for retrievals with real spectra in Sect. 5.3.2. The difference between GGG2020 a priori CO_2 profiles and aircraft profiles (Biraud et al., 2013) over Lamont from NOAA's ObsPack (Sweeney et al., 2017) between 500 and 5000 m were computed for 382 aircraft profiles and for each month between 2008 and 2016. The mean difference profile plus one standard deviation of the month with the largest differences, August, was used to build the diagonal of the a priori covariance matrix. The a priori CO_2 uncertainty can be expressed as an exponential fit to this data:

$$\boldsymbol{\sigma}_i = 3.99e^{-0.92\boldsymbol{x}_i} + 0.98 \tag{5.1}$$

where $\boldsymbol{x}_i$ is the altitude of the i^{th} atmospheric level in kilometers. The a priori covariance matrix is expressed as:

$$\boldsymbol{z}_{i,j} = \boldsymbol{x}_i \tag{5.2}$$

$$(\boldsymbol{\Delta}\mathbf{z})_{i,j} = \left|\mathbf{z}_{i,j} - \mathbf{z}^T{}_{i,j}\right| \tag{5.3}$$

$$(\boldsymbol{S}_a)_{i,j} = (\boldsymbol{\sigma}^{\mathrm{T}}\boldsymbol{\sigma})_{i,j} \times e^{-\frac{(\boldsymbol{\Delta z})_{i,j}}{h}} \tag{5.4}$$

where z is a matrix with each row containing the altitude profile, $\boldsymbol{\Delta z}$ is the matrix of absolute altitude differences between each level, $\mathbf{S}_{\mathrm{a}}$ is the a priori covariance matrix, and h is the length scale of interlayer correlations. The length scale was set to 2 km based on the width of the rows of correlation matrices built from the ensemble of aircraft vertical profiles.

The vertical grid used in the retrievals presented in this study has 51 levels between 0 and 70 km, and the spacing between levels increases with altitude (see Sect. 4.2). Figure 5.3 shows the a priori uncertainty as a function of pressure for each of the eight a priori states used to process the Lamont spectra presented in Table 5.2.

Since the AirCore profiles do not extend down to the surface or above about 25 km, other sources are used to complete the “true” CO_2 profile. The TCCON spectrometer used in this study is located at the U.S. Department of Energy Atmospheric Radiation Measurement program (ARM) central facility in Lamont, Oklahoma. The facility hosts a suite of instruments for remote and in-situ measurements of the atmosphere. When available within 5 h of the last AirCore sampling time, surface CO_2 and CH_4 measurements from precision gas systems were used (Biraud and Moyes, 2001). When they were not available, measurements from discrete flask samples were used (on 23 July 2013, 27 February 2014, and 17 September 2014) (Biraud et al., 2002). Surface pressure, temperature and relative humidity were obtained from in situ measurements at the Lamont central facility.

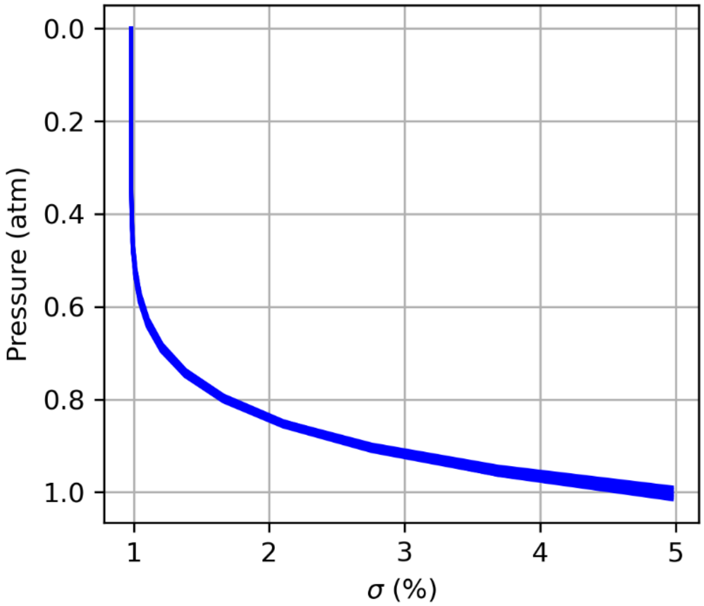

Figure 5.3: A priori uncertainty profiles for each of the ten dates presented in Table 5.2. These are defined by Eq. 5.1. Since σ is defined on an altitude grid, it varies slightly with pressure.

GGG2020 uses 3-hourly a priori profiles of the atmospheric state. For each spectrum in the retrievals, GGG uses the nearest a priori profile in time. The a priori meteorology and H_2O profiles are obtained from analyses of the Global Modeling and Assimilation Office (GMAO) Goddard Earth Observing System Version 5 Forward Processing for Instrument Teams (GEOS5-FPIT) (Lucchesi, 2015). The CO_2 a priori profiles are constructed from the deseasonalized NOAA Mauna Loa and Samoa flask data (Dlugokencky et al., 2019) by determining the transport lag between the measurement site and each level of the a priori (Laughner et al., n.d.). In the troposphere, this is done with an age-of-air formula and an effective latitude that accounts for synoptic motion of air. In the stratosphere, this is obtained from an age climatology derived from a Chemical Lagrangian Model (McKenna, 2002) of the stratosphere using equivalent latitude to account for air motion. The stratospheric priors also account for atmospheric transport with age spectra (Andrews et al., 2001). A seasonal cycle parametrization is then applied and the resulting CO_2 profiles are corrected to match the CO_2 latitudinal gradients observed by the High-Performance Instrumented Airborne Platform for Environmental Research (HIAPER) Pole-to-Pole Observations (HIPPO) (Wofsy, 2011), and by the Atmospheric Tomography (ATom) mission (Wofsy et al., 2018).

The parameters that differ between the “GGG2020 a priori” and the “truth” are the CO_2, CH_4, H_2O, and temperature profiles.

5.2.3 Information Content and Degrees of Freedom

The information content in the profile retrieval can be quantified using the averaging kernel matrix **A** (Rodgers, 2000). The Shannon information content *H* is defined as:

$$H = -\frac{1}{2} ln(|\mathbf{I} - \mathbf{A}|), \tag{5.5}$$

where “ln” is the natural logarithm and $|\mathbf{I} - \mathbf{A}|$ is the determinant of the difference between the identity matrix and the averaging kernel matrix. The degrees of freedom for signal (DOFS) can be expressed as:

$$DOFS = tr(\mathbf{A}). \tag{5.6}$$

The DOFS can be divided into the CO_2 profile DOFS and the DOFS corresponding to the rest of the state vector elements. The profile DOFS can be interpreted as the number of independent pieces of information that improve the retrieved CO_2 profiles compared to the a priori. The DOFS are shown in Figs. 5.4-5.7 and 5.9-5.10.

5.3 Results

In Sect. 5.3.1, we investigate the sensitivity of the profile retrievals to different sources of error using synthetic spectra produced by running the GGG forward model with a given set of atmospheric conditions. The resulting spectra are then used as input to the profile retrieval algorithm using the same set of atmospheric conditions, except for a perturbation in either the CO_2, temperature, or H_2O profiles, or in the spectroscopic parameters of CO_2 lines (air- and self-broadened half-width coefficients, and their temperature dependence). In these retrievals, the SNR of the spectrum to be fitted is set to 1000 and the CO_2 a priori covariance matrix is diagonal with 5% (~20 ppm) uncertainty at all levels. No noise is added to the calculated spectra, but the assumed 1000:1 SNR is used to build the measurement covariance matrix and affects the relative weight of the measurement and the a priori. The weak prior constraint and high SNR serve to highlight the sources of variability in the retrieved profiles.

In Sect. 5.3.2, CO_2 profile retrievals are tested with atmospheric solar absorption spectra measured at the Lamont TCCON site. If the forward model were perfect and the a priori state equal to the true state of the atmosphere, the retrieved scale factor at each level would be equal to 1. However, errors in the forward model (including spectroscopy, a priori meteorological information, radiative transfer, and instrument line shape) cause the retrieved scale factors to deviate from 1. To isolate the effect of instrument misalignment and errors in spectroscopic parameters from errors in a priori meteorology, we build a priori profiles of H_2O, temperature, CO_2 and CH_4 using in situ measurements. In Sect. 5.3.2 we also use an a priori covariance matrix with off-diagonal elements based on comparisons between the a priori profile and aircraft profiles, as described in Sect. 5.2.2.

5.3.1 Synthetic Spectra

In this section, we attempt to identify the main sources of error in the retrieved CO_2 profiles. To do this, we use synthetic spectra that are calculated with GFIT's forward model for a given set of inputs (atmospheric conditions and spectroscopic parameters). Note here that there is no difference in the forward model of GFIT and GFIT2 for generating synthetic spectra; both are using the same atmospheric state on a given altitude grid, and the same linelist to compute spectra. These "perfect" synthetic spectra are then used as measurements to be fitted in retrievals with one perturbed input. Thus, when the perturbed input is not the a priori CO_2 profile itself, the a priori CO_2 profile is the "truth". In Sect. 5.3.1.1, we look at the ability of the retrieval algorithm to retrieve CO_2 when it is the only unknown.

Over the course of a day, the water vapour profile can vary by 40% and the temperature profile can vary by more than 10°C in the lowest troposphere, and therefore 3-hourly a priori meteorological information could differ from the true atmospheric state by several degrees C for temperature and by 10% for water vapour. In Sect. 5.3.1.2, we perturb the a priori H_2O profile, the main interfering absorber.

In Sect. 5.3.1.3, we perturb the temperature profile, as the intensity and width of all absorption lines depend on temperature. In Sect. 5.3.1.4, we perturb spectroscopic line parameters themselves to within their uncertainties. In Sect. 5.3.1.5, we perturb the zero-level offset and the internal field of view of the instrument, the latter leads to a change in the width of the ILS. Finally, in Sect. 5.3.1.6, we present a discussion of the results of Sect. 5.3.1.

The total retrieval random error for the retrievals presented in this section is ~4.5% (~18 ppm) and the contribution of random noise is ~0.8% (~3 ppm). See Sect. 5.3.2.2 for definitions of total and measurement noise errors. When the deviations from the truth are larger than the a priori uncertainty (~20 ppm), it means the perturbation applied has a severe effect on the retrieval. Of course this can be mitigated by using a stronger a priori constraint or a measurement covariance matrix that reflects expected systematic errors, and not just random noise, but always at the cost of reduced sensitivity to CO_2 too. The goal here is to estimate the relative effect of different kinds of expected systematic errors on retrieved profile shapes. Stronger constraints can only reduce the amplitude of the deviations from the truth, but the same structures would remain. When the perturbation to a parameter other than CO_2 results in deviations from the truth much larger than those presented in Sect. 5.3.1.1, it means that errors in that parameter will dominate the variability in the retrieved CO_2 profiles regardless of the retrieval constraints. This discussion applies for the CO_2 profiles, as the total column amount derived from wildly oscillating retrieved profiles may still be a good estimate of the true total column.

5.3.1.1 Perturbed CO_2 Profile

With a perturbed CO_2 prior profile, the algorithm can retrieve the true profile shape very well in all windows, even with an a priori profile vastly different from the truth as shown in Figure 5.4. In Figure 5.4(a), when using the same prior that generated the synthetic spectrum, the retrieved profiles do not align exactly with the prior profile. This is due to small imperfections in the synthetic spectra, but these result in differences of less than 1 ppm at any altitude. In Figure 5.4(c) the standard GGG2020 a priori is used as the a priori, while the “true” CO_2 profile used to generate the synthetic spectrum was built from a composite “true” profile as described in Sect. 5.2.2. In each window, the retrieved profile is within 2 ppm of the truth. In Figure 5.4(e), a constant CO_2 profile with 380 ppm at all levels is used as the a priori. Again, the retrieved profiles are within 2 ppm of the truth except at the bottom and top of the profile where most of the information comes from the a priori. This self-consistency test shows that the GFIT2 algorithm works as expected and can accurately retrieve CO_2 when the a priori CO_2 profile is the only source of uncertainty.

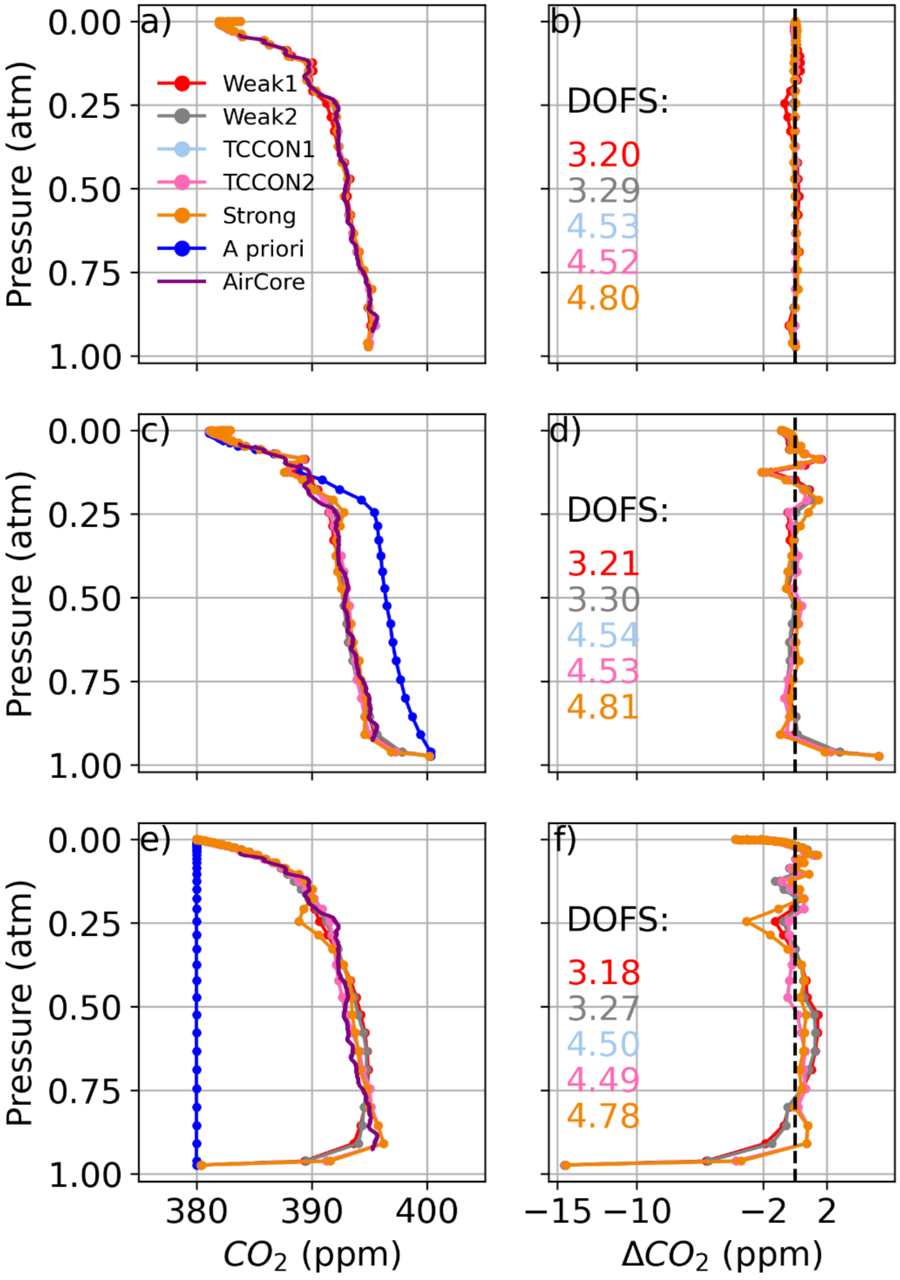

Figure 5.4: The left-hand panels show CO_2 profiles retrieved using synthetic spectra. In (a), we use the AirCore profile, which was used to generate the synthetic spectra, as the a priori. In (c), we use the GGG2020 a priori CO_2 profile as the a priori profile. In (e), we use a constant CO_2 a priori profile. The right-hand panels: (b), (d), and (f) show the difference between the retrieved profiles and AirCore, corresponding to (a), (c), and (e) respectively. Here 5 km corresponds to ~0.55 atm, 8–13 km to ~0.36–0.17 atm, and 15 km to ~0.125 atm.

5.3.1.2 Perturbed H_2O profile

Figure 5.5 shows the effect on CO_2 profile retrievals of a +10% perturbation to the H_2O vapour profile below 5 km for a dry winter day and a wet summer day. It leads to 2 ppm deviations from the CO_2 a priori profile in the Strong window under dry conditions and up to 15 ppm under wet conditions. In both cases, the deviations from the truth in the CO_2 profiles retrieved from the other windows were within 2 ppm.

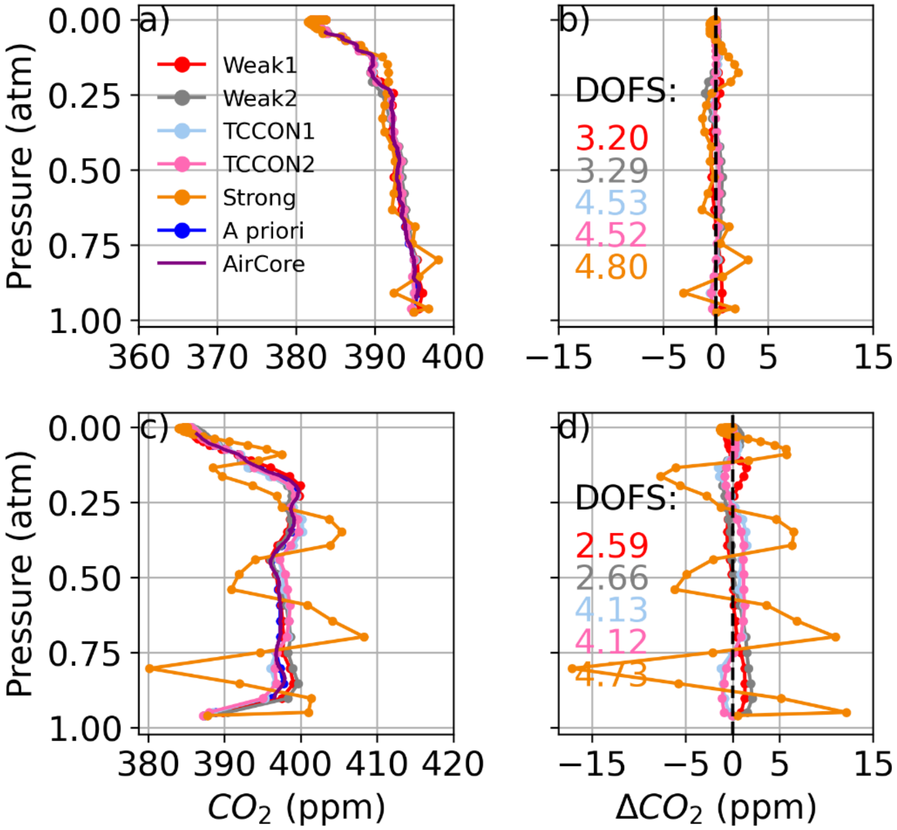

Figure 5.5: The left-hand panels show CO_2 profiles retrieved using synthetic spectra. 10% is added to the H_2O profile below 5 km for (a) dry conditions on January 14th, 2012, and for (c) wet conditions on July 23rd, 2013. The right-hand panels: (b) and (d), show the difference between the retrieved profiles and AirCore, corresponding to (a) and (c) respectively. Here 5 km corresponds to ~0.55 atm, 8–13 km to ~0.36–0.17 atm, and 15 km to ~0.125 atm.

5.3.1.3 Perturbed Temperature Profile

A +5°C perturbation to the temperature profile below 5 km (0.5 atm < P < 1.0 atm), as in Figure 5.6(a), leads to deviations from the truth in the retrieved CO_2 profiles of up to 50 ppm in the Weak and TCCON windows, and up to 100 ppm in the Strong window. In this case, the fit residuals can exceed 1% in the Strong window and 0.5% in the TCCON windows. For the retrievals used to obtain the profiles in Figure 5.6(a), the SNR was set to 100 in the Strong window, 200 in the TCCON windows, and 1000 in the Weak windows. In Figure 5.6(c) and (e), the SNR is set to 1000 in all windows. In Figure 5.6(c), a +2°C perturbation is applied between 8 and 13 km (0.2 atm < P < 0.35 atm). The amplitude of deviations in the TCCON windows and in the Strong window is close to 50 ppm at ~0.9 atm and 100 ppm at ~0.2 atm. In the two Weak windows, the deviation amplitude is ~10 ppm at ~0.9 atm and ~20 ppm at 0.2 atm. In Figure 5.6(e), a +2°C perturbation is applied above 15 km. In the Strong window, the resulting deviation at pressures > 0.6 atm has the smallest amplitude amongst the five windows, within 4 ppm, and the deviation at ~0.2 atm is ~20 ppm. In the TCCON windows, the deviation at pressures > 0.6 atm is reduced to ~10 ppm while the deviation at pressures > 0.6 atm is comparable to that in Figure 6(b). In the two Weak windows, the deviations at ~0.9 atm is unchanged when to compared to Figure 5.6(b) and the deviation at ~0.2 atm is reduced from ~15 ppm to ~10 ppm.

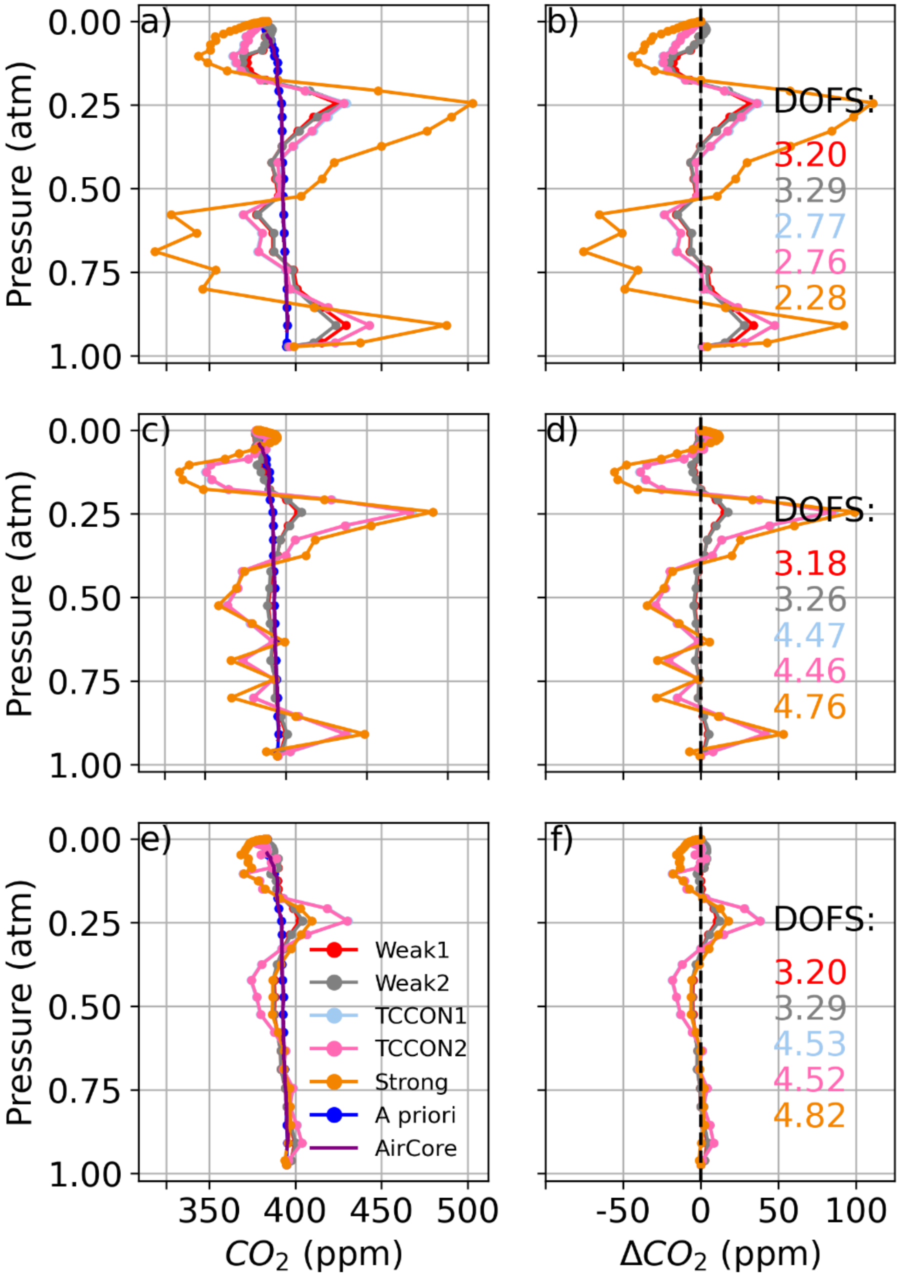

Figure 5.6: The left-hand panels show CO_2 profiles retrieved using synthetic spectra for: (a) +5°C added to the a priori temperature profile below 5 km, (c) +2°C between 8 and 13 km, and (e) +2°C above 15 km. The right-hand panels: (b), (d), and (f) show the difference between the retrieved profiles and AirCore profile, corresponding to (a), (c), and (e) respectively. Note the difference in the horizontal axis range between the panels. Here 5 km corresponds to ~0.55 atm, 8–13 km to ~0.36–0.17 atm, and 15 km to ~0.125 atm.

From the results in Sect. 5.3.1.1 to 5.3.1.3, we observe that CO_2 profile retrievals do not need accurate prior knowledge of the CO_2 profile, but require accurate knowledge of the prior temperature and water vapour profiles. Moreover, these results suggest that errors in the temperature profile are the main source of deviations from the truth in retrieved CO_2 profiles. Retrievals using the two Weak windows are the least affected by biases in the prior temperature and water vapour profiles. The need for accurate a priori water vapour profile could be alleviated by retrieving H_2O profiles simultaneously with CO_2 profiles, but this was not tested with GFIT2 which currently can only retrieve the main target gas in a window with profile retrievals. In addition, H_2O profile retrievals would also be affected by temperature errors.

5.3.1.4 Perturbed Line Parameters

The linelist used by GGG is a compilation of different versions of the HITRAN linelists (Rothman et al., 2005, 2009, 2013; Toon, 2015; Toon et al., 2016a; Gordon et al., 2017). GGG2020 has the option to use either the qSDV+LM line shape or the Voigt line shape for some windows and gases (Mendonca et al., 2016, 2017, 2019). The reference linelists and the uncertainties on air- and self-broadened Lorentz half-width coefficients, and their temperature dependence, are summarized in Table 5.3. The qSDV+LM line shape is only implemented for the CO_2 lines of the two TCCON windows and the Strong window, for the CH_4 lines of the Weak1 window, and for the O_2 lines of the oxygen window centered at 7885 cm^{-1}. The qSDV+LM line shape is not implemented for the CO_2 lines of the Weak1 and Weak2 windows, but these weak lines are minimally affected by line mixing, and they lack laboratory measurements of speed-dependent line parameters.

The effect of errors in the half-width coefficients on the retrieved CO_2 profiles was tested by increasing both the self- and air-broadened Lorentz half-width coefficients by 0.1% for all CO_2 lines as shown in Figure 5.7(a). This perturbation corresponds to the median uncertainty of these parameters in the Strong and TCCON windows as shown in Table 5.3. This caused deviations of up to 10 ppm in the Strong window, 5 ppm in the TCCON windows, and 2 ppm in the Weak windows. Similar deviations are obtained by perturbing the temperature dependence of the half-width coefficients by -1% as shown in Figure 5.7(b). In this case, the deviations appear mirrored about the a priori compared to Figure 5.7(a). The shape of deviations in both cases is similar; it is also similar to the shape obtained in Figure 5.6 from perturbing the temperature profiles. This is because all those perturbations ultimately lead to an altered line width and all cause residual patterns that cannot be distinguished from each other, as illustrated in Figure 5.8. This implies that errors in the a priori temperature profile, water vapour profile, and spectroscopic widths are difficult to disentangle in the current GFIT2 profile retrieval. A simultaneous temperature (hence pressure) and CO_2 profile retrieval would be necessary to overcome these issues.

A factor of 10 increase in the perturbations applied to the width coefficients or their temperature dependence also leads to a factor of 10 increase in the amplitude of deviations in the retrieved CO_2 profiles. Panels (a) and (b) of Figure 5.7 use perturbations corresponding to uncertainties in the line parameters when using qSDV+LM for the TCCON windows and the Strong window. The same perturbations were applied for all five windows. However, in the Weak1 and Weak2 windows, these perturbations are 10 times smaller than realistic uncertainties as reported in Table 5.3 for the Voigt line shape. Therefore, with real spectra and for the Weak windows, we can expect deviations from the truth 10 times larger than in Figure 5.7, within ~10–20 ppm.

Table 5.3: 1σ relative errors of the air- and self-broadened Lorentz half-width coefficients (b) and of their temperature dependence (n). The values from Benner et al. (2016) and Devi et al. (2007a,b) use the median 1σ uncertainty for the whole band, from the Appendix or supplemental files of these studies. The values for the Voigt line shape use the error codes reported in the HITRAN2016 linelist (Gordon et al., 2017).

Line shape	Window (band)	b (air) (%)	n (air) (%)	b (self) (%)	n (self) (%)	Reference
Voigt	TCCON1	>=1 and <2	-	>=1 and <2	-	(Toth et al., 2008)
	TCCON2					
	Weak1		From <10 To <1			(Lamouroux et al., 2015) (Gordon et al., 2017)
	Weak2					
	Strong					
qSDV+LM	TCCON1 (30013–00001)	0.13	-	0.07		(Devi et al., 2007)
	TCCON2 (30012–00001)	0.14		0.07		(Malathy Devi et al., 2007)
	Strong (20013–00001)	0.03	0.12	0.09	0.33	(Benner et al., 2016)
	Strong (21113–01101)	0.25	1.47	0.49	2.27	

In Connor et al. (2016), the authors used a Voigt line shape. Figure 5.7(e) shows the effect of fitting with a Voigt line shape a synthetic spectrum that was generated using qSDV+LM. In that case the fit residuals in the Strong window can exceed 1% and the residuals in the TCCON windows can exceed 0.5%. For these retrievals, the SNR is set to 100 in the Strong window, 200 in the TCCON windows, and 1000 in the Weak windows. The profiles retrieved from the Strong window present deviations from the truth within 60 ppm. In the two TCCON windows, the deviations from the truth are within 30 ppm. In the Weak1 window, the deviations from the truth are within 10 ppm, because qSDV+LM was not used to calculate the CO_2 line absorptions themselves, but only for the relatively strong CH_4 lines in that window. In the Weak2 window, there is no difference between the two linelists or line shape, and thus the retrieved profile does not differ from the a priori profile. Therefore, even if we assume perfect a priori meteorology, the deviations in the CO_2 profiles retrieved from the TCCON1 window observed by Connor et al. (2016), when fitting real spectra could be entirely due to the use of the Voigt line shape.

The effect of the errors in the a priori water vapour and temperature profiles, and in the spectroscopic parameters cannot be mitigated by adjusting the measurement covariance, for example by using a variable SNR. Figure 5.8 shows an example of spectral residuals from fits to synthetic spectra from the Strong window using scaling retrievals, but with different perturbations applied. Showing residuals from scaling retrievals reveals systematic features that the profile retrieval will attempt to suppress. Figure 5.8(b) presents residuals from fitting a synthetic spectrum using the same a priori profile that was used to generate the synthetic spectrum. It shows small (< 0.05 %) residuals, caused by the use of a constant ILS across the window for a faster convolution of the spectrum with the ILS. The corresponding profiles are shown in Figure 5.4(a). In Figure 5.8(c), a 2°C offset is applied to the a priori temperature profile between 8 and 13 km before fitting the synthetic spectrum. In Figure 5.8(d), a constant a priori CO_2 profile is used to fit a synthetic spectrum that was generated with an AirCore CO_2 profile as a priori. In Figure 5.8(e), the air- and self-broadened Lorentz half-width coefficients are increased by 0.1% compared to the parameters used to generate the synthetic spectrum. In Figure 5.8(f), the temperature dependence of the air- and self-broadened Lorentz half-width coefficients is decreased by 1% compared to the parameters used to generate the synthetic spectrum. In Figure 5.8(g), the GGG2020 a priori meteorology and trace gas profiles are used as a priori profiles instead of the a priori constructed with AirCore profiles used to generate the synthetic spectrum.

In all panels of Figure 5.8 except (c) and (g), all the residual features correspond to CO_2 absorption lines. In Figure 5.8(c), with a perturbation to the a priori temperature profile, there is an added contribution of temperature errors on interfering species. Furthermore, the residuals in Figure 5.8(g) result from a combination of errors in the a priori meteorology and trace gas profiles but are dominated by temperature errors. Perturbations in the temperature profile, CO_2 profile, or CO_2 line width coefficients all cause residuals with the same shape because they all affect the width of CO_2 lines. It is not possible to de-weight the effect of any of those errors by adjusting the measurement error without also losing the ability to correct for residuals caused by CO_2 errors. Residuals caused by realistic temperature errors as shown in Figure 5.8(c) are of the same magnitude of those caused by unrealistically high errors in the a priori CO_2 profile shape as shown in Figure 5.8(d).

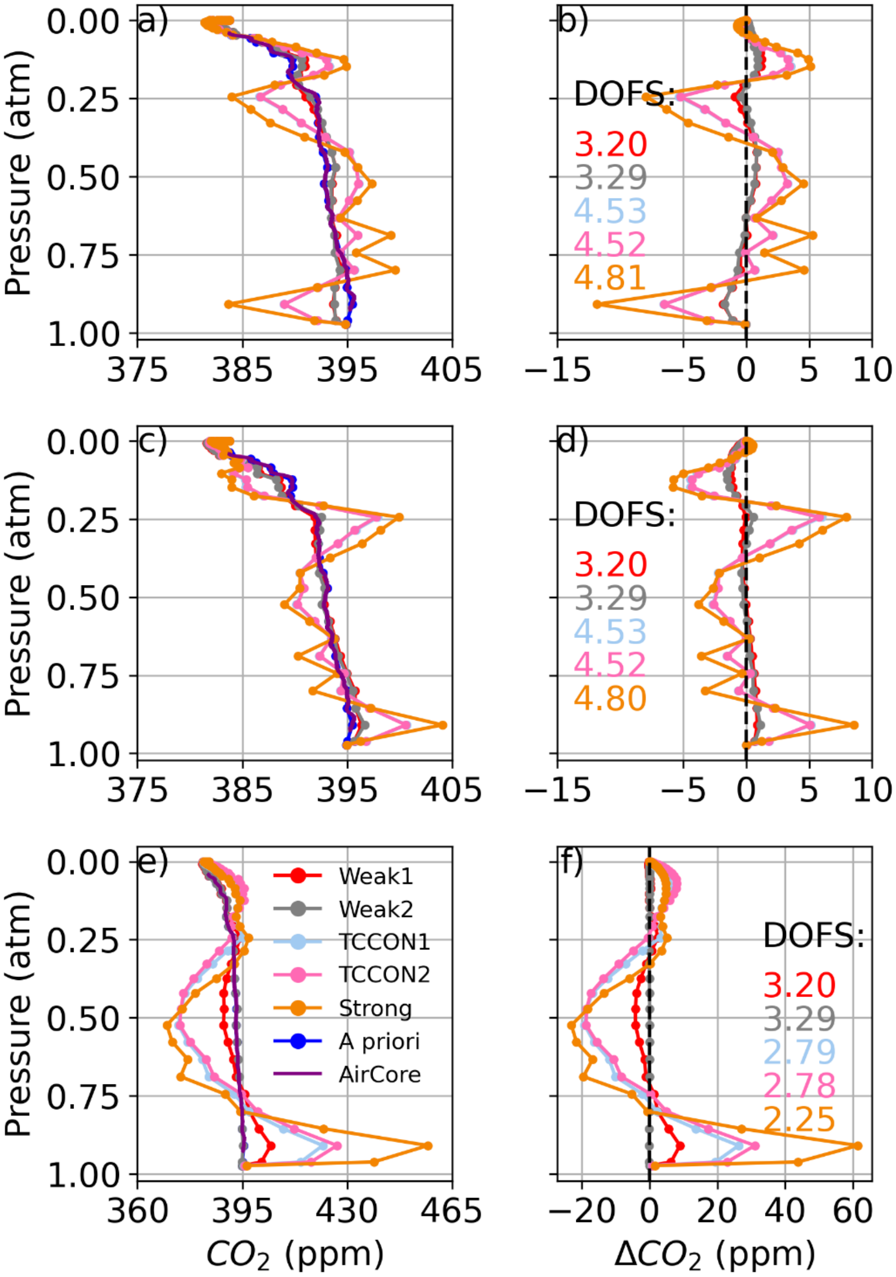

Figure 5.7: The left-hand panels show CO$_2$ profiles retrieved using synthetic spectra. In (a) the air- and self-broadened half-width coefficients of all CO$_2$ lines are increased by 0.1%. In (c) the temperature dependence of these coefficients is decreased by 1%. In (e), the synthetic spectrum used as "measurement" is generated with the speed-dependent Voigt line shape with line mixing, but profiles are retrieved using a Voigt line shape. The right-hand panels: (b), (d), and (f) show the difference between the retrieved profiles and AirCore, corresponding to (a), (c), and (e) respectively. Here 5 km corresponds to ~0.55 atm, 8–13 km to ~0.36–0.17 atm, and 15 km to ~0.125 atm.

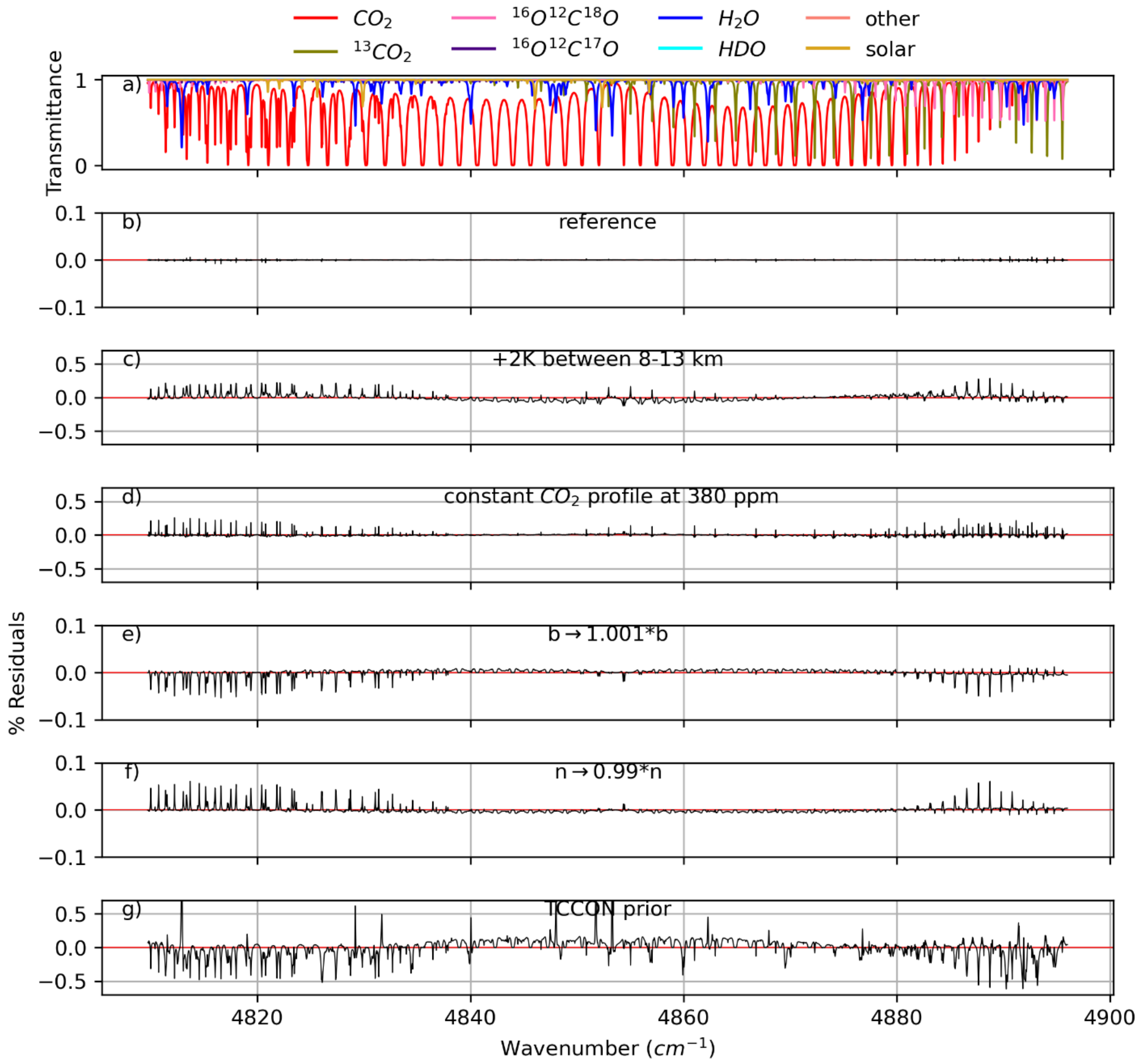

Figure 5.8: Panel (a) shows an example of calculated lines in the Strong CO_2 window. The other panels show residuals from fits to a synthetic spectrum, using the same inputs used to generate the synthetic spectrum except for: (b) no perturbation; (c) +2°C perturbation to the a priori temperature between 8 and 13 km; (d) CO_2 prior profile set to 380 ppm at all levels, corresponding to ~15 ppm offset from the unperturbed prior; (e) air- and self-broadened Lorentz half-width coefficients is increased by 0.1%; (f) temperature dependence of the half-width coefficients decreased by 1%; and (g) using the a priori that would be used by TCCON operational processing, instead of that constructed from in situ measurements, resulting in a combination of different errors in the a priori such as H_2O, temperature, and CO_2. Note the vertical scale of panels (b), (e), and (f) is five times smaller than that of panels (c), (d), and (g).

5.3.1.5 Perturbed Zero-Level Offset and Field of View

The saturated lines of the Strong window allow the fitting of a zero-level offset (see Sect. 3.3). Figure 5.9 shows the zero-level offset retrieved from the Strong window using real spectra for each of the days with Lamont data presented in Table 5.2. The median absolute value is at most 0.001 on July 23rd, 2013. The effect of a zero-level offset on retrieved profiles was tested with synthetic spectra. Figure 5.10(a) and (b) are the same as Figure 5.4(a) and (b) and show profiles retrieved from synthetic spectra in the reference case, when no perturbation is applied. Figure 5.10(e) and (f) show the effect of a +0.002 perturbation to the zero-level offset, without retrieving it in the Strong window. This has a large effect in the profile retrieved from the Strong window, with deviations from the truth within 30 ppm, and a smaller effect in the other bands with deviations up to 10 ppm.

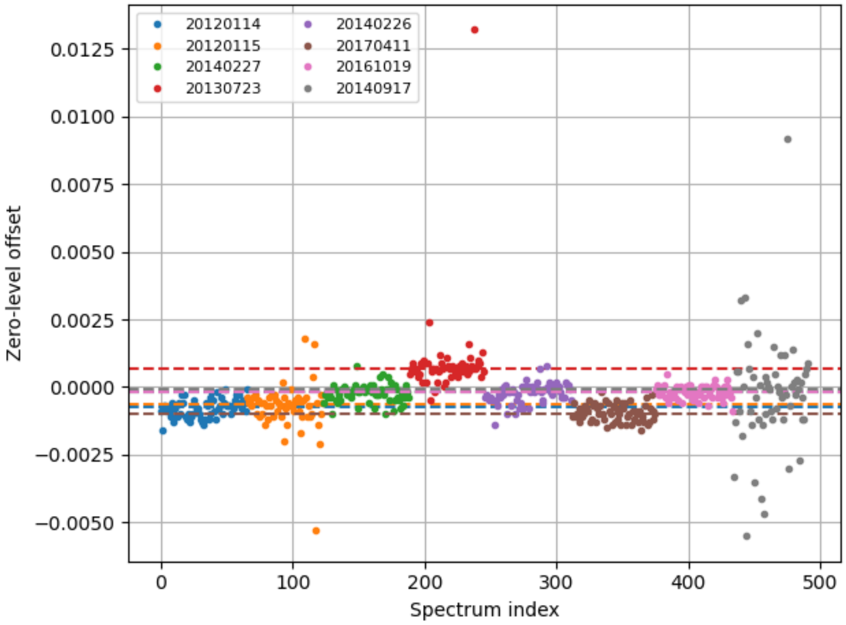

Figure 5.9: Zero-level offset retrieved from the Strong CO_2 window for the Lamont spectra coincident within ±1 hour of the last AirCore sampling time and within ±1.5 hour of the closest a priori time on each of the days indicated by the legend. The dashed lines mark the median value for each date.

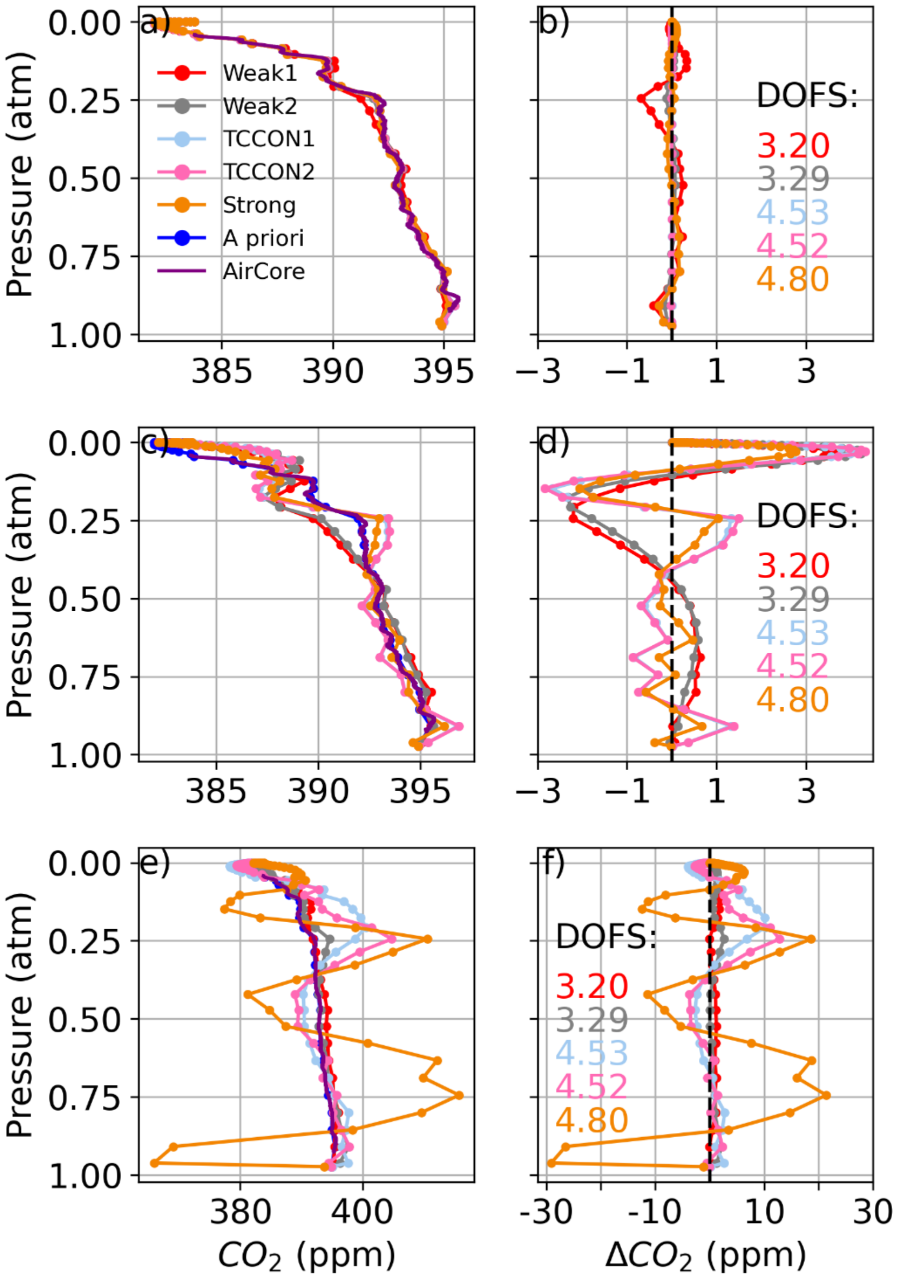

Figure 5.10: The left-hand panels show CO_2 profiles retrieved using synthetic spectra. In (a), we use the AirCore profile, which was used to generate the synthetic spectra, as the a priori. In (c), the internal field of view is perturbed by +7%, increasing the width of the ILS. In (e), the zero-level offset is perturbed by +0.002 and is not retrieved in the Strong window. The right-hand panels: (b), (d), and (f) show the difference between the retrieved profiles and AirCore, corresponding to (a), (c), and (e) respectively. Here 5 km corresponds to ~0.55 atm, 8–13 km to ~0.36–0.17 atm, and 15 km to ~0.125 atm.

In Figure 5.10(c) and (d), we also consider the effect of one type of ILS error by perturbing the internal field of view by +7%: this leads to a widening of the ILS. The unperturbed internal field of view of the spectrometer is 2.4 mrad. The deviations from the truth are within 1 ppm for P > 0.5 atm and within 3 ppm for P < 0.5 atm.

This sensitivity test shows that the effect of zero-level offsets and field of view errors will not be a major source of variability in the retrieved profiles. If the zero-level offset retrieved from the Strong window is added to the TCCON and Weak windows before the retrieval, the change in the retrieved profiles is less than 3 ppm at all altitudes as shown in Figure 5.11 using days with AirCores at Lamont.

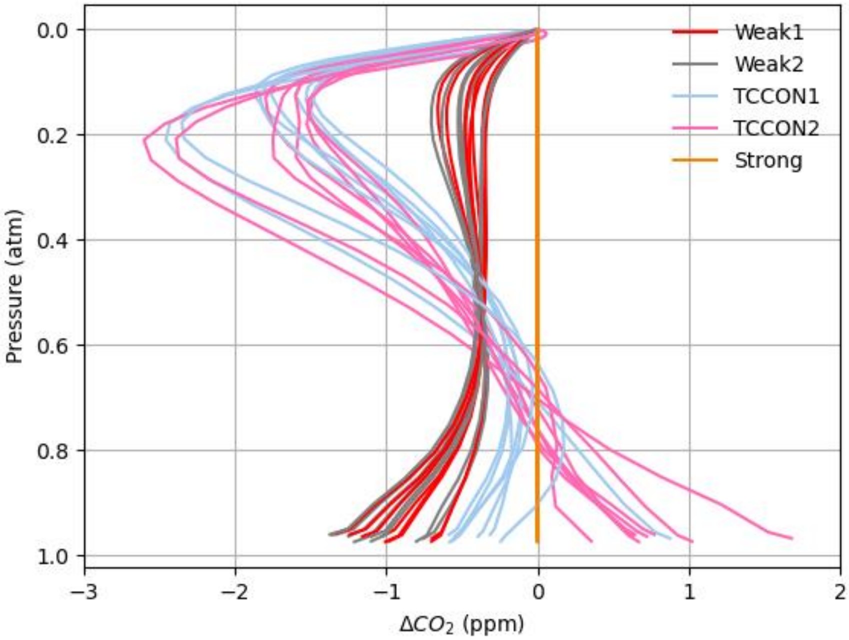

Figure 5.11: Using real Lamont spectra with the AirCore profile as a priori, the zero-level offset was first retrieved from the Strong window and then added in the Weak and TCCON windows. The difference in the retrieved profiles with and without the added offset is shown for each window and for all the days with AirCore profiles over Lamont. In the Strong window, where the offset is retrieved, the differences are less than 0.001 ppm.

5.3.1.6 Synthetic Spectra: Discussion

For retrievals on synthetic spectra, the "measurement" SNR is set to 1000, which is high compared to most solar spectra measured by TCCON. This highlights the sources of variability in the retrieved profiles. For profiles retrieved from real spectra, we can expect a greater influence of the a priori CO_2 profile: the deviations will be smaller, and the degrees of freedom for signal will be lower than those shown in the figures of Sect. 5.3.1. This is not a desirable outcome; the a priori CO_2 covariance is meant to nudge the retrieval such that the solution lies close to realistic ensembles of CO_2 profiles, not to constrain deviations caused by temperature errors. Tuning the a priori or measurement covariances is not the right approach unless profile deviations caused by typical errors in spectroscopy or meteorology are smaller than typical vertical variations in CO_2 profiles. Figure 5.4 shows that the profile retrieval algorithm works well and could be a powerful tool to derive information about the vertical distribution of CO_2, even with ill-defined a priori CO_2 profiles. Panels (a) and (b) of Figure 5.7 show that profile information could still be retrieved to within ~5 ppm given realistic errors in line width parameters. But as shown with Figure 5.6, a temperature retrieval, or correction, is critical to producing reliable CO_2 profile retrievals. This study does not show the effect of typical instrument misalignment errors on the retrieved profiles. GFIT/2 currently has no capacity to fit the instrument line shape (ILS) of a misaligned instrument given specific angular and shear misalignments, and instead always assumes a perfect ILS. This is an area of future development for the GFIT/2 program. However, the effect of an error in the instrument's internal field of view and the effect of a zero-level offset were presented in Sect. 5.3.1.5; both should lead to minor deviations from the truth, within less than 3 ppm with real spectra.

In Sect. 5.3.2, GFIT2 is tested with real spectra using an a priori profile built from in situ measurements. In that case, the deviations from the truth in the retrieved CO_2 profile caused by errors in the a priori meteorology (temperature, pressure, and water vapour profiles) are minimized, and the remaining deviations are caused by errors in the spectroscopic line parameters, in the radiative transfer, in the instrument line shape, or in the pointing of the suntracker.

5.3.2 Real Spectra

Here the algorithm is tested with real spectra measured at Lamont as described in Sect. 5.2.2. A scaling retrieval is performed before each profile retrieval and the root mean square of the residuals from the scaling retrieval is used as measurement uncertainty for the profile retrieval. Since the residuals from the scaling retrieval include systematic features larger than the random noise in the measurement, the root mean square residual is a conservative estimate of the noise. Thus, for a given a priori constraint (the one described by Eq. 5.1-5.4), the deviations of the retrieved profile from the truth presented in this section are underestimated compared to that which would be obtained by using the same measurement uncertainty as for the scaling retrieval. We do not try to adjust the SNR to account for specific systematic features because in operational TCCON retrievals, there is no a priori knowledge of systematic errors and the measurement uncertainty only describes random noise in the spectrum. Thus, scaling retrievals do overweight spectral features caused by systematic errors as they underestimate the measurement uncertainty by only considering random errors. However, because of the inherent restricted freedom of the scaling retrieval to fit a measured spectrum by only adjusting a single scale factor for all levels at once, systematic errors have a more limited effect on scaling retrieval than on profile retrievals. Furthermore, the formulation of the optimal estimation method is based on the assumption that the physical quantities measured and the retrieved parameters follow Gaussian statistics; tuning the a priori or measurement covariance matrices as tools to correct for systematic errors strays away from that assumption.

In Sect. 5.3.2.1, we present CO_2 profiles retrieved from real spectra and we attempt to isolate the effect of errors in instrument line shape, in spectroscopic parameters, and in pointing, from the effect of errors in meteorology. To do this, we take advantage of the availability of AirCore measurements of CO_2, and radiosonde measurements of temperature and H_2O, to build as good an approximation of the true state of the atmosphere as possible. We use that true state as a priori in retrievals to quantify the combined effect of the systematic errors listed above. Although the results of Sect. 5.3.1 with synthetic spectra are applicable to all TCCON sites, the profile deviations observed in Sect. 5.3.2.1 are specific to the Lamont TCCON site.

In Sect. 5.3.2.2, we present an analysis of the information content and altitude sensitivity of the retrieval, as well as the error analysis for the profile retrieval. In Sect. 5.3.2.3, we compare XCO_2 derived from the scaling retrieval to XCO_2 derived from the profile retrieval. Finally, Sect. 5.3.2.4 discusses the results of Sect. 5.3.2.

5.3.2.1 Profiles

Figure 5.12 and 5.13 show CO_2 profiles retrieved from real spectra measured at Lamont, OK, on January 14th, 2012 and April 11th, 2017, respectively. In each figure, panel (a) shows profiles retrieved using in situ profiles as the a priori (the "truth" as described in Sect. 5.2.2). In those cases, we assume that deviations from the truth caused by errors in a priori meteorology (pressure, temperature and water vapour profiles) are minimized, and the remaining deviations can be attributed to the combination of instrument misalignment (ILS), pointing errors, or errors in spectroscopic parameters. Panel (c) shows profiles retrieved using the GGG2020 a priori (see Sect. 5.2.2). A first complication for obtaining a satisfactory CO_2 profile retrieval is that the a priori CO_2 profiles in GGG2020 already compare well with in situ profiles, typically within 5 ppm over Lamont. In Figure 5.12(c) and 5.13(c), the profile that most closely matches the AirCore is the a priori.

Even with ideal prior knowledge of the meteorology and trace gas profiles, the CO_2 deviations from the truth can be as large as 50 ppm as shown in Figure 5.12(a) and 5.13(a). When synthetic spectra were perturbed with realistic errors in line width parameters, profile deviations remained within 5 ppm for profiles retrieved from the Strong window and within 10 ppm for the TCCON windows. This suggests that the main cause of deviations in Figure 5.12(a) and 5.13(a) is not due to errors in spectroscopic parameters. The assumption that there is no contribution from temperature errors in the radiosonde profile is supported by the CO_2 profile deviation being smallest in the Strong window, which is the most sensitive to temperature errors. Although the effect of typical perturbations in the instrument field of view, zero-level offset, and spectroscopic parameters is relatively small compared to the effect of temperature errors, the cumulative effect of these errors could explain the deviations from the truth in Figure 5.12(a) and 5.13(a).

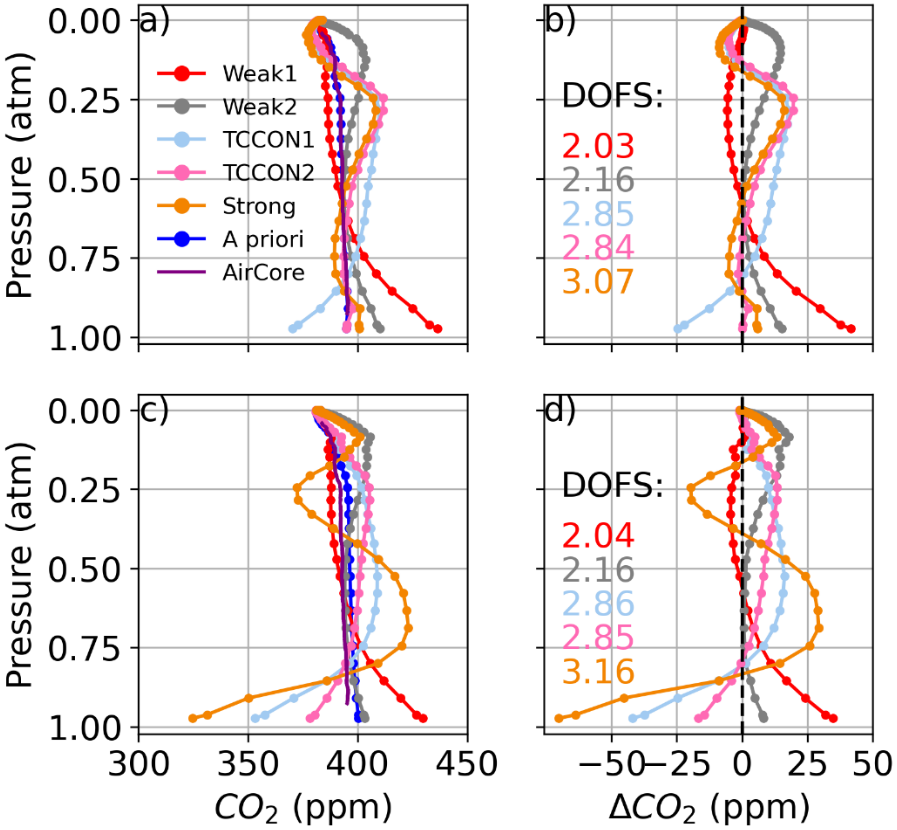

Figure 5.12: CO_2 profiles retrieved from spectra measured at the Lamont TCCON site on January 14th, 2012, at 61–74° solar zenith angle, coincident with AirCore measurements using: (a) the "truth" as a priori and (c) the GGG2020 a priori. In (b) and (d) the difference of the retrieved profiles minus the AirCore profile is shown, corresponding to (a) and (c), respectively. The points represent the 51 levels of the vertical grid. The DOFS for each retrieval window are indicated in (b) and (d).

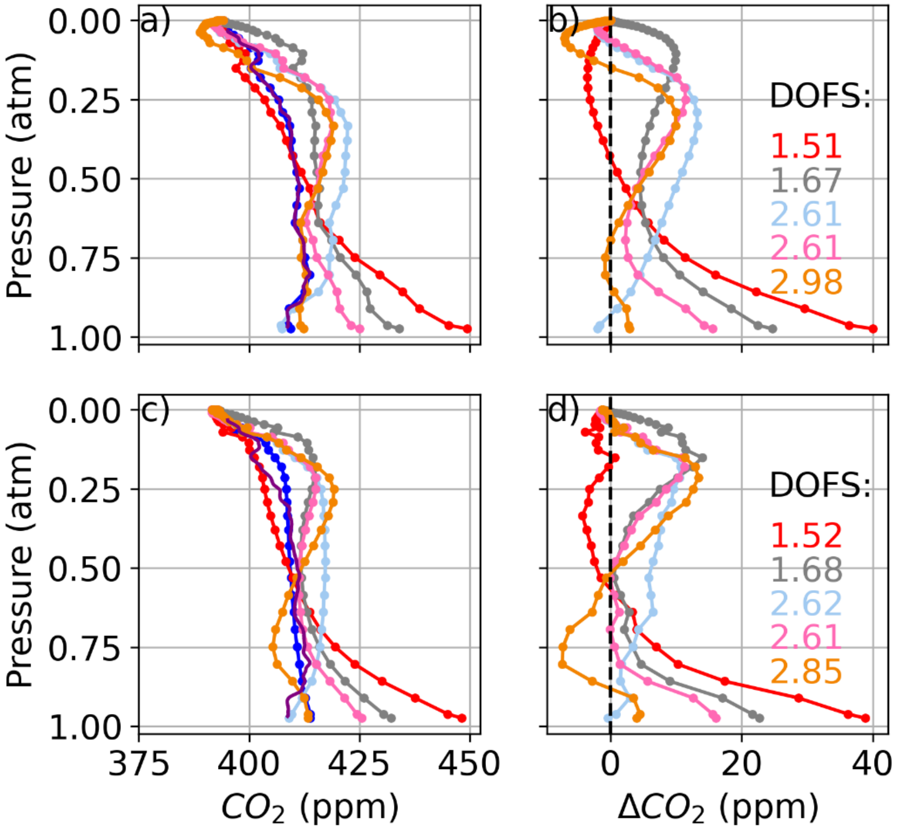

Figure 5.13: Same as Fig. 5.12 but for spectra measured on April 11th, 2017 at 28–39° solar zenith angle.

Figure 5.14 shows the difference between the GGG2020 a priori temperature profile, used in Figure 5.12(c) and 5.13(c), and the radiosonde temperature profile used in Figure 5.12(a) and 5.13(a). In both cases, we replace the a priori surface temperature with the measured surface temperature. On January 14th, 2012, the radiosonde temperature profile is about 1°C higher than the GGG2020 a priori profile at pressures < 0.6 atm. The shape of the Strong window CO_2 profile deviations in Figure 5.12(c) is consistent with the sensitivity tests using synthetic spectra in Sect. 5.3.1.3. In Figure 5.6(a), a +5°C offset below 5 km results in +500 ppm CO_2 error at ~0.9 atm, while in Figure 5.10, a -1°C offset in the lower troposphere leads to a -50 ppm error at ~0.9 atm. The deviations are smoother in Figure 5.12 and 5.13 than in Figure 5.6 because the SNR of real spectra is between 200 and 500 instead of 1000, and because of the smoothing effect of the off-diagonal elements of the a priori covariance used in this section. The off-diagonal elements of the a priori covariance introduce inter-layer correlations that reduce large differences between levels over a given length scale (see Sect. 5.2.2). Retrievals on real spectra after applying a +5°C offset to the radiosonde temperature profile below 5 km lead to a +100 ppm offset at ~0.9 atm. The CO_2 profiles in Figure 5.13(c) differ less with those in Figure 5.13(a) than do the profiles in Figure 5.12(a) and 5.12(c). Figure 5.14, the difference between the GGG2020 and radiosonde temperature profile on April 11th, 2017 is ~3°C for the first two levels above the surface, but the average difference between 0.85 and 0.6 atm is -0.15°C compared to -1.05°C on 14 January 2012.

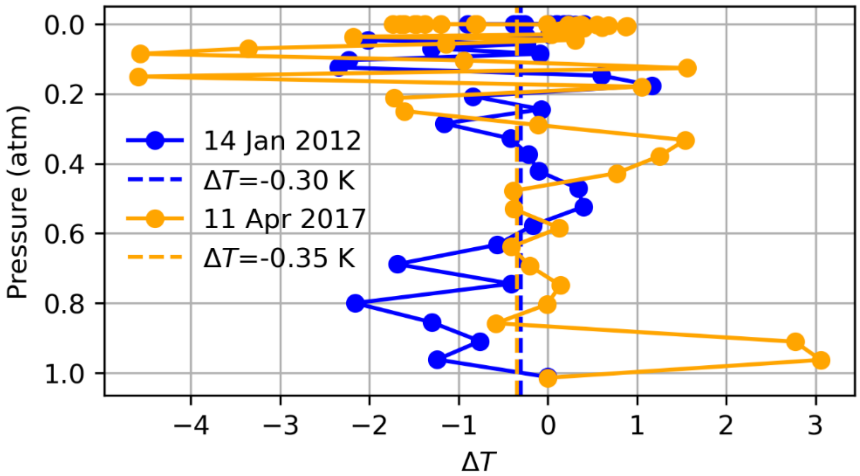

Figure 5.14: Temperature profile difference for the GGG2020 a priori temperature minus measured radiosonde temperature on January 14th, 2012 and April 11th, 2017. The radiosonde temperature profile is included in the a priori used in panel (a) of Figs. 5.12 and 5.13, and the GGG2020 a priori temperature profile is used in panel (b) of Figs. 9 and 10. In situ temperature measurements are used for both cases at the surface. The dashed line marks the average difference, with the value indicated in the legend.

In aircraft profiles over Lamont between 2008 and 2018 from NOAA's ObsPack, the steepest vertical gradients in CO_2 profiles are ~5 ppm/km between the surface and ~3 km. In its current state, CO_2 profile retrieval with GFIT2 cannot distinguish these vertical variations from CO_2 deviations caused by errors in the forward model, even with very accurate a priori meteorology. Typical errors in the a priori temperature profiles will prevent operational use of CO_2 profile retrieval without a scheme for retrieving or correcting the temperature profiles.

5.3.2.2 Information Content and Error Analysis

Table 5.4 presents the average values of the Shannon information content, *H*, and of the CO_2 profile DOFS, from all profile retrievals performed on Lamont spectra when using the GGG2020 a priori profiles. It also includes the Ratio of Residuals (RR) of the spectral fits (defined as Eq. 3.54 but with σ_y replaced by the RMS of the fit residuals from the scaling retrieval), which represents the residuals of the profile retrievals as a fraction of the residuals of the scaling retrievals. The same quantities are plotted in Figure 5.15 for each spectrum. The RR is always smaller than 1 because the profile retrieval has more freedom to adjust the calculated spectrum and so can never produce larger residuals than scaling retrievals. Figure 5.15 also shows XCO_2 obtained from the scaling retrievals subtracted from XCO_2 obtained from profile retrievals for each window.

Table 5.4: Shannon information content (H), degrees of freedom for signal (DOFS) for the CO_2 profile, and Ratio of Residuals (RR) averaged over all 492 profile retrievals from near-infrared TCCON spectra measured at Lamont and coincident within ±1 h of the AirCore last sampling time. The standard deviation is also shown.

Window name	H	DOFS	RR
TCCON1	5.4±0.6	2.7±0.2	0.988±0.014
TCCON2	5.4±0.6	2.7±0.2	0.992±0.009
Weak1	2.3±0.7	1.7±0.3	0.996±0.002
Weak2	2.5±0.9	1.8±0.4	0.994±0.008
Strong	6.8±1.0	3.0±0.4	0.957±0.038

Figure 5.16 shows the sums of the rows of the partial column averaging kernel matrix over different altitude ranges. The sum from 0 to 70 km is the total column averaging kernel (see Sect. 3.5). The total column averaging kernel is close to 1 at all levels in all windows, indicating good sensitivity to changes in the CO_2 total column. The partial column kernels show that most of this sensitivity comes from altitudes below 15 km. That the total column averaging kernel is close to 1 at all levels is not inconsistent with the large deviations we observe in the retrieved CO_2 profiles. If the total column averaging kernel is exactly one at each level, adding *N* molecules of CO_2 anywhere in the atmosphere will lead to *N* more molecules in the retrieved total column. However, in the presence of a priori temperature errors, for example, the retrieved value can be biased. The averaging kernel indicates that without the effect of these errors, the CO_2 profile

retrieval would have excellent sensitivity to CO_2 and would be able to provide information about CO_2 in two distinct layers.

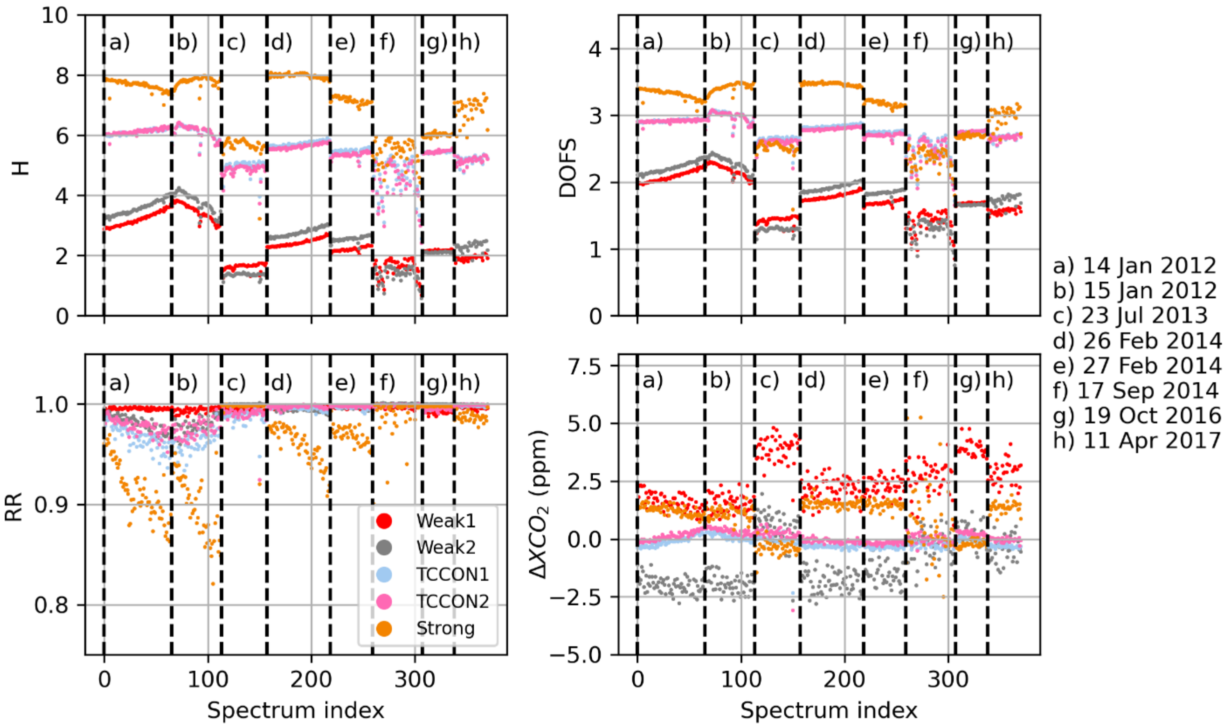

Figure 5.15: Shannon information content (top left), degrees of freedom for signal for the CO_2 profile (top right), ratio of residuals (bottom left), and profile minus scaling retrieval XCO_2 (bottom right) for all Lamont spectra coincident within ±1 h of the AirCore last sampling time for AirCores launched on the dates indicated on the right. Each new date is marked by a vertical dashed line.

Here, the vertical representation is not a concern. Using 51 vertical levels only affects the speed of the retrieval. The retrieved profiles can then be reduced to a number of partial columns corresponding to the DOFS. This was not done here because it is evident that large deviations due to temperature errors could easily bias the resulting partial columns. The reduction into a subset of layers also requires an arbitrary choice: in Figure 5.16 the altitude ranges were set such that the DOFS of the first two partial columns would be roughly close to 1 in each window. We could also have chosen two regions with approximately equal DOFS from 0–7 km and 7–70 km. The partial column averaging kernels overlap with each other, so the partial columns are not completely uncorrelated even if their respective DOFS are higher than 1. The DOFS are not exactly independent pieces of information, as it is impossible to obtain independent partial column amounts from direct sun measurements on the ground (see Sect. 3.5), but an arbitrary criterion can be defined to identify distinct layers, for example if the peaks in their partial column averaging kernels are separated by a given fraction of their widths in altitude.

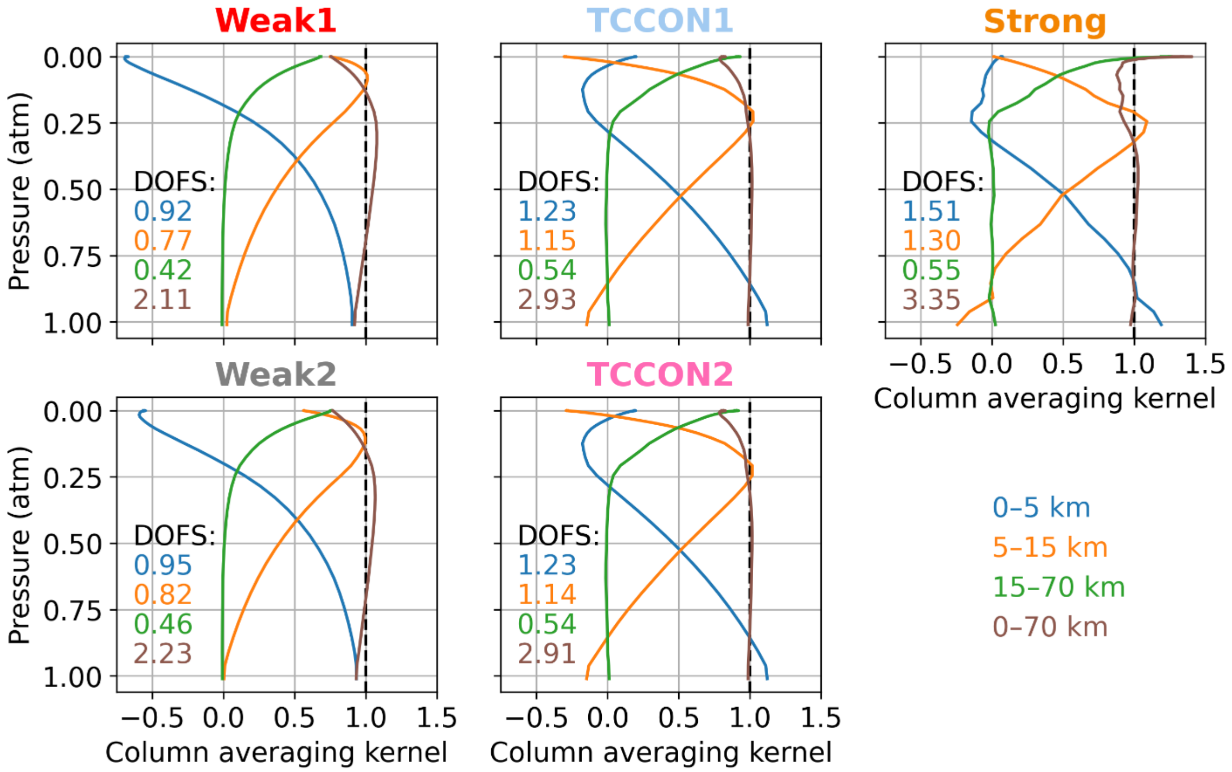

Figure 5.16: Sum of the rows of the partial column averaging kernel matrix over different altitude ranges as indicated by the legend, for each of the five CO_2 windows. The sum between 0–70 km is the total column averaging kernel. The numbers in each panel are the DOFS corresponding to each of the altitude ranges.

The singular value decomposition of the CO_2 Jacobian matrix can provide information on the relative precision with which different vertical patterns are measured. The Jacobian matrix **K** is decomposed into:

$$\mathbf{K}(nmp, nlev) = \mathbf{U}(nmp, nlev)\mathbf{L}(nlev, nlev)\mathbf{V}^T(nlev, nlev) \tag{5.7}$$

where *nmp* is the number of measured spectral points, *nlev* is the number of atmospheric levels, **U** is the matrix of left singular vectors, **L** is the diagonal matrix of singular values, and $\mathbf{V}^T$ is the transpose of the matrix of right singular vectors. The right singular vectors of **K** associated with the eight largest singular values are shown in Figure 5.17 to 5.21 for each CO_2 band on 14 January

2012. The right singular vectors represent independently measured vertical patterns with a precision indicated by their corresponding singular values shown above each panel. The singular values are also shown as a fraction of the largest singular value in parenthesis. The singular vectors all show an increasing number of oscillations with decreasing singular value. In each window, the first singular vector is close to a uniform weighting at all altitudes and has 3 to 10 times more sensitivity than the second pattern. The singular vector in panel (d) has a structure like that of the CO_2 profile deviations observed in the sensitivity tests of Sect. 5.3.1.

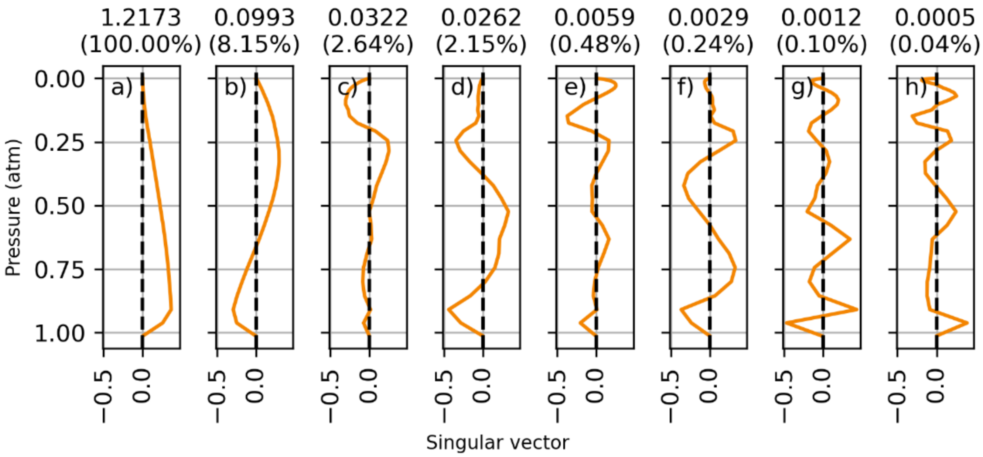

Figure 5.17: Right singular vector of the Jacobian associated with the eight largest singular values for profile retrievals from the Strong CO_2 window on 14 January 2012. The singular values are shown above each panel, and the singular value normalized to the largest singular value is shown in parenthesis.

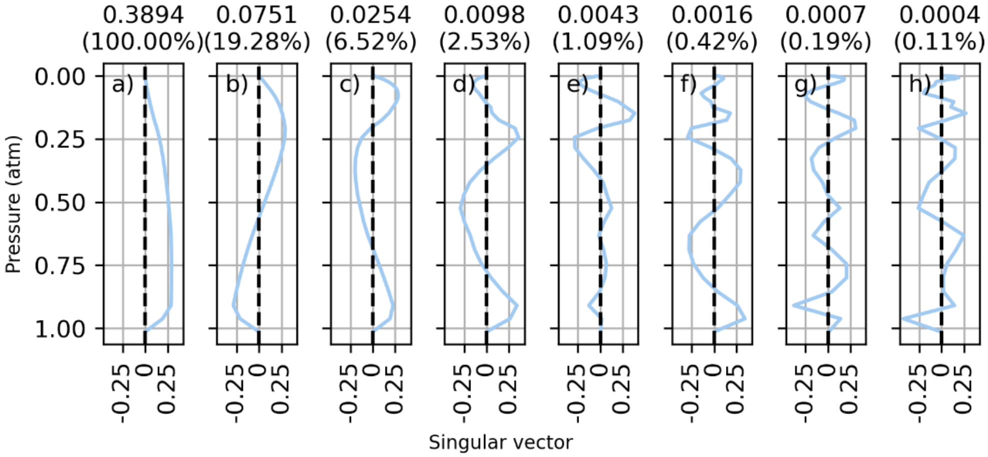

Figure 5.18: Same as Figure 5.17 but for the TCCON1 window

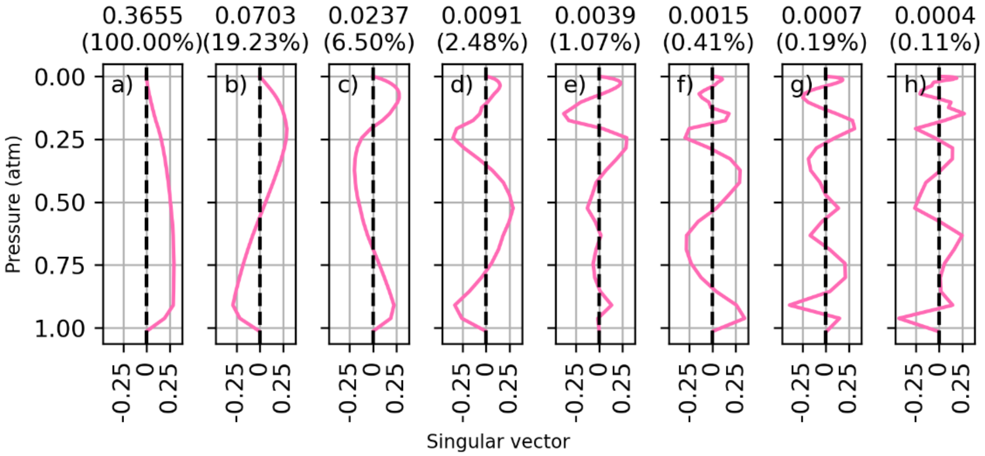

Figure 5.19: Same as Figure 5.17 but for the TCCON2 window

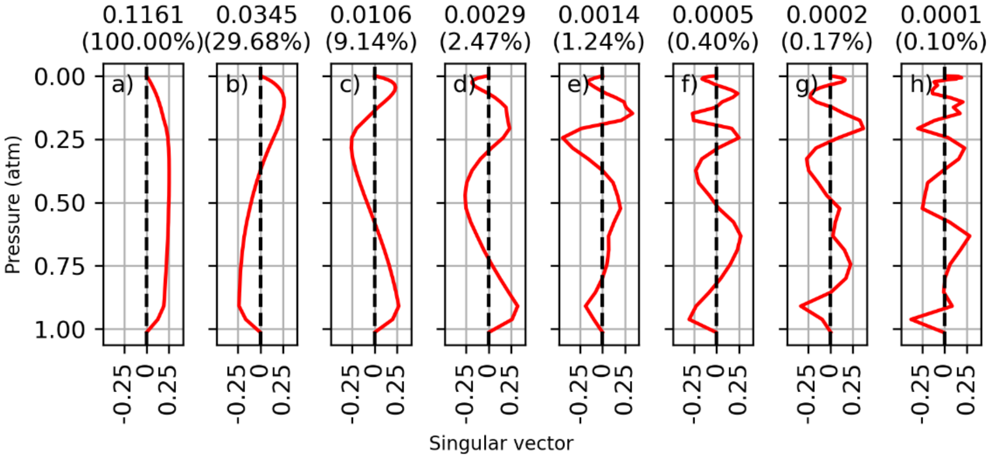

Figure 5.20: Same as Figure 5.17 but for the Weak1 window.

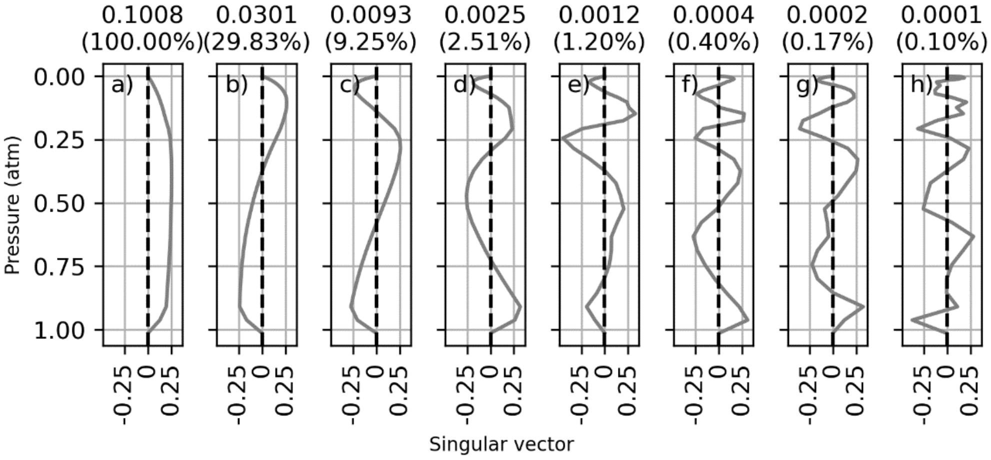

Figure 5.21: Same as Figure 5.17 but for the Weak2 window.

The retrieval covariance matrix $\hat{\mathbf{S}}$ can be expressed as a sum of the null space covariance $\mathbf{S}_{\mathrm{N}}$ and the measurement noise covariance $\mathbf{S}_{\mathbf{m}}$ (Rodgers, 1990):

$$\mathbf{S}_N = \left(\boldsymbol{S}_a^{-1} + \mathbf{K}^T \boldsymbol{S}_y^{-1} \mathbf{K}\right)^{-1} \mathbf{S}_a^{-1} \left(\boldsymbol{S}_a^{-1} + \mathbf{K}^T \mathbf{S}_y^{-1} \mathbf{K}\right)^{-1} \tag{5.8}$$

$$\mathbf{S}_m = \left(\boldsymbol{S}_a^{-1} + \boldsymbol{K}^T \boldsymbol{S}_y^{-1} \mathbf{K}\right)^{-1} \boldsymbol{K}^T \mathbf{S}_y^{-1} \mathbf{K} \left(\mathbf{S}_a^{-1} + \mathbf{K}^T \boldsymbol{S}_y^{-1} \mathbf{K}\right)^{-1} \tag{5.9}$$

The error patterns of these matrices hold information on vertical structures in the CO_2 profiles that the retrieval cannot resolve, due to the smoothing effect of the a priori covariance matrix $\mathbf{S}_{\mathrm{a}}$ in the case of $\mathbf{S}_{\mathrm{N}}$, and due to the effect of measurement noise in the case of $\mathbf{S}_{\mathrm{m}}$, as the measurement error covariance matrix $\mathbf{S}_y$ only represents random errors in the measured radiances. The error patterns of a matrix are defined as its eigenvectors multiplied by the square root of their corresponding eigenvalue. The error patterns of $\mathbf{S}_N$ associated with the four largest eigenvalues are shown in Figure 5.22, and those of $\mathbf{S}_m$ are shown in Figure 5.23. In both cases, the largest error pattern peaks at the surface and falls to 0 at ~0.9 atm; these peaks in the error patterns correspond to a minimum in the singular vectors of the CO_2 Jacobian. The large errors in the retrieved CO_2 profiles are explained by the larger a priori uncertainty in the lower troposphere, and by the relatively larger effect of errors at wavenumbers strongly weighted at low altitudes. This is because “sensitivity” is determined by the Jacobian; the retrieval will simply preferentially adjust CO_2 at levels where a given change in CO_2 causes a larger change in radiance. At pressures larger than ~0.9 atm, the error patterns of $\mathbf{S}_{\mathrm{N}}$ represent vertical scales that cannot be resolved in the retrieval, with a vertical scale of 0.3 atm or less.

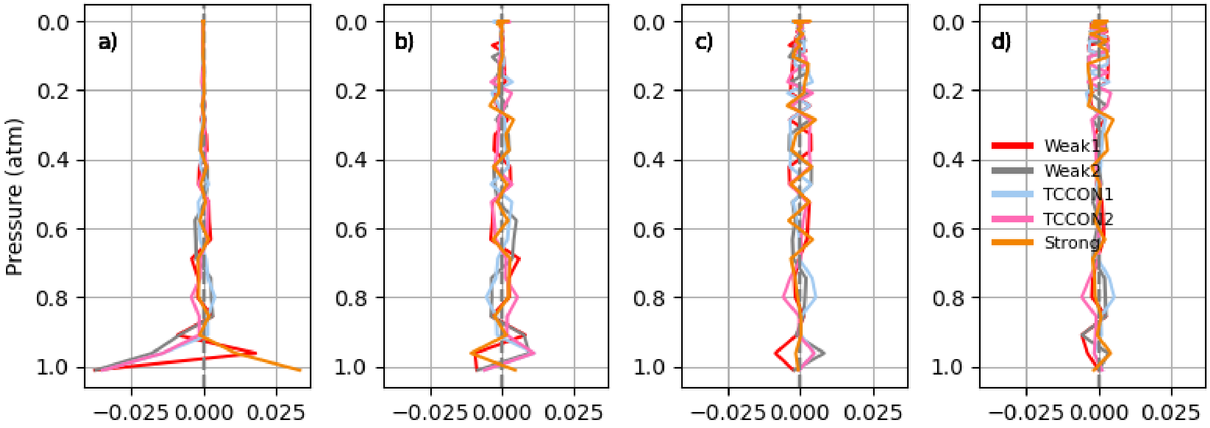

Figure 5.22: The four largest error patterns of the null space covariance matrix for a Lamont spectrum measured on 14 January 2012.

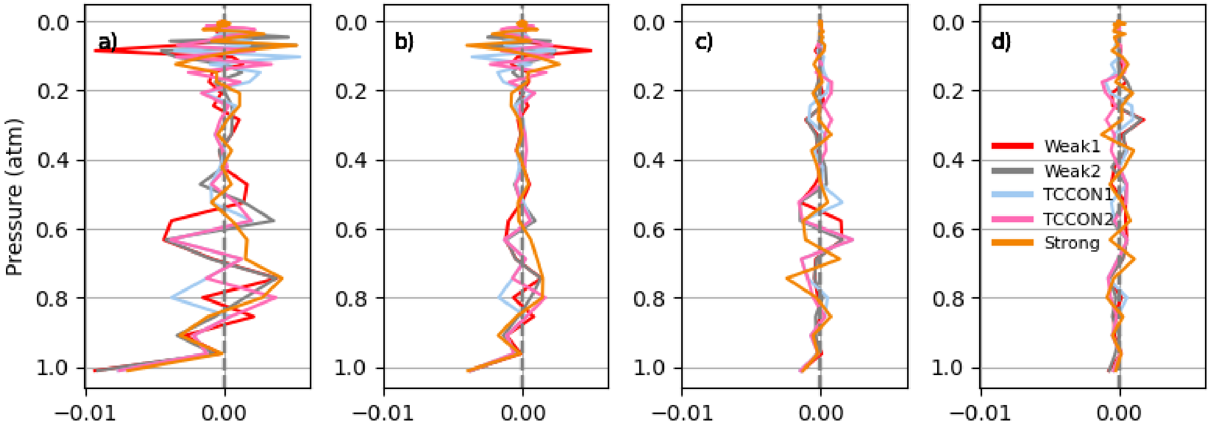

Figure 5.23: Same as Figure 5.22 but for the measurement noise covariance matrix.

The uncertainty on the retrieved CO_2 profile is taken to be the square root of the diagonal elements of $\hat{\mathbf{S}}$ even though the retrieval covariance is not diagonal. It is presented in Figure 5.24 as a percentage of the a priori uncertainties. The retrieval error is always smaller than the a priori covariance by construction in optimal estimation, so this alone gives no indication of a successful retrieval. But the retrieval is more sensitive to altitudes where the retrieval uncertainty is a smaller fraction of the a priori uncertainty. The error from the diagonal of $\mathbf{S}_N$ and $\mathbf{S}_\mathrm{m}$ is also shown. Note that the uncertainty profiles in Figure 5.24 are the square roots of the diagonal elements of the matrices considered; since $\hat{\mathbf{S}} = \mathbf{S}_\mathrm{N} + \mathbf{S}_\mathrm{m}$, the uncertainty profile from $\widehat{\boldsymbol{S}}$ is the root sum squared of the uncertainty profiles from $\mathbf{S}_\mathrm{N}$ and $\mathbf{S}_\mathrm{m}$. In addition to $\mathbf{S}_\mathrm{N}$, the smoothing contribution from state vector elements other than CO2 scale factors is shown as $\mathbf{S}_\mathrm{i}$, the interference error covariance (Rodgers and Connor, 2003):

$$\mathbf{S}_i = \mathbf{A}_\mathrm{xe}\mathbf{S}_\mathrm{a,e}\mathbf{A}_\mathrm{xe}^\mathrm{T} \tag{5.10}$$

where $\mathbf{S}_\mathrm{a,e}$ is the part of the a priori covariance matrix that corresponds to "extra" state vector elements other than CO2 scale factors. With *N* total state vector elements and *nlev* atmospheric levels, $\mathbf{S}_\mathrm{a,e}$ has dimensions (*N*-*nlev*,*N*-*nlev*). $\mathbf{A}_\mathrm{xe}$ is the subset of the averaging kernel matrix that characterizes the smoothing effect of the extra state vector elements on the CO2 profiles, with dimensions (*nlev*,*N*-*nlev*). The interference error is the smallest contribution to the total error and most of the error comes from the smoothing effect of the a priori CO2 covariance, followed by the contribution of measurement noise which oscillates between ~10–25% of the a priori CO2 uncertainty. If temperature were retrieved, for example with a temperature offset or with a scale factor added to the extra state vector elements, we would expect the interference error to increase.

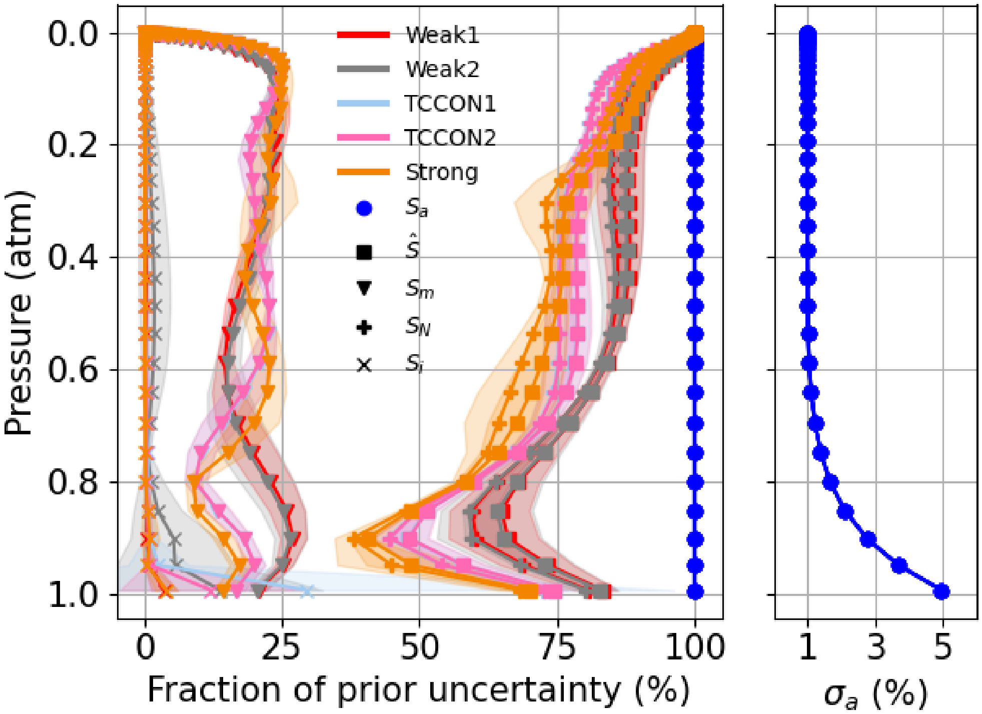

Figure 5.24: The left panel shows the square root of the diagonal elements of the retrieval total error covariance matrix $\hat{\mathbf{S}}$, the null space covariance matrix $\mathbf{S}_\mathrm{N}$, the interference error covariance matrix $\mathbf{S}_i$, and the measurement noise error covariance matrix $\mathbf{S}_\mathrm{m}$ expressed as a fraction of the a priori uncertainty σ_a. Each line is the average from the set of eight days with AirCore measurements over Lamont, and the bands indicate the standard deviation. The right panel shows the a priori uncertainty.

5.3.2.3 XCO_2

The XCO_2 derived from profile and scaling retrievals using the GGG2020 a priori information profiles was compared to XCO_2 derived from the CO_2 profile built from the AirCore CO_2 profile, in situ surface measurements of CO_2, and the GGG2020 a priori CO_2 above the maximum altitude sampled by the AirCore. The results are shown in Figure 5.25 for the eight days for which we have AirCore profiles that are coincident with measurements at the Lamont TCCON station. Despite the large deviations observed in retrieved profiles, XCO_2 derived from profile retrievals compares well to the AirCore XCO_2, but it does not present a clear improvement over XCO_2 derived from the scaling retrievals. The effect of temperature errors on XCO_2 derived from scaling and profile retrievals is relatively small because the spectral windows utilize the entire (fundamental) band. Across a wide window, the residuals due to temperature errors show alternating positive and negative residuals, because of the different temperature sensitivities of absorption lines. Collectively, these lines have a small net temperature sensitivity. The scaling retrieval, which can only add or remove CO_2 at all levels simultaneously, is limited in its ability to fit out such residuals across a wide window by adjusting the CO_2 scale factor. For profile retrievals, although large deviations are observed in the retrieved profile, they compensate each other when deriving the total column. These deviations compensate due to the wide windows including a range of spectral lines with different temperature sensitivities. If a narrow window over only a few lines were used instead, we would expect more localized errors in the retrieved CO_2 profiles, and total columns sensitive to temperature errors.

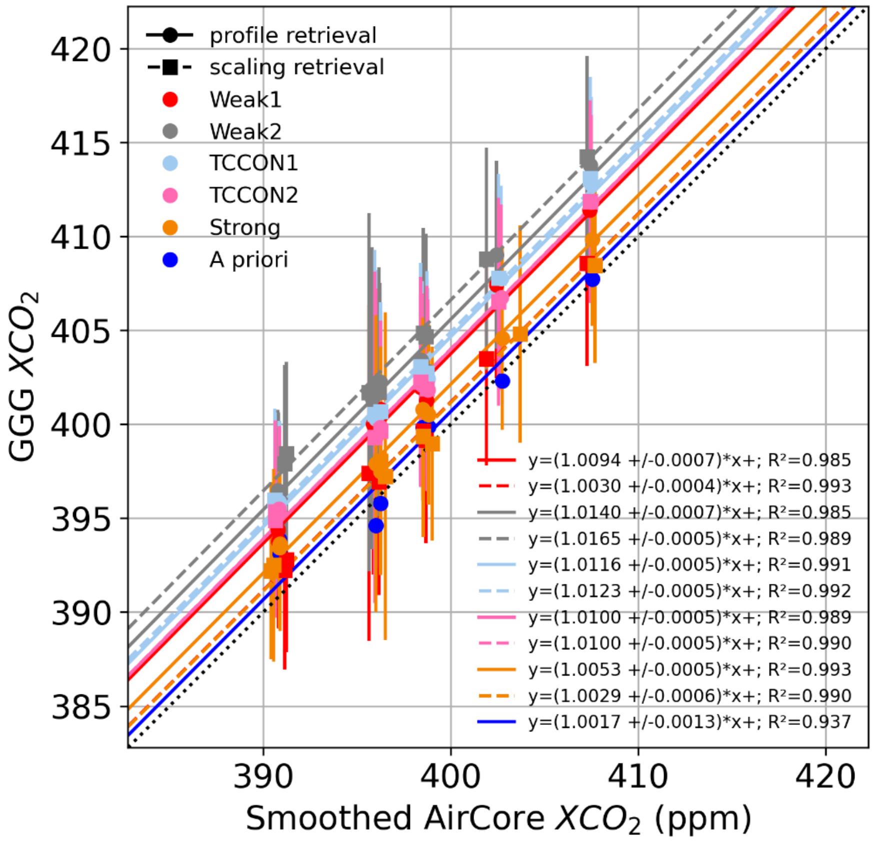

Figure 5.25: XCO_2 derived from scaling (dashed lines and squares) and profile (solid lines and circles) retrievals for each CO_2 window when using the GGG2020 a priori profiles, compared to XCO_2 derived from smoothed AirCore profiles (see Appendix C). The black dotted line marks the 1-to-1 line. When comparing with scaling retrievals, the AirCore profile is smoothed using the total column averaging kernel of the scaling retrieval, and when comparing to profile retrievals the AirCore profile is smoothed using the averaging kernel matrix of the profile retrieval. The legend indicates the slopes and squared Pearson correlation coefficients of fits to lines passing through the origin, assuming that in the absence of CO_2 the retrieval would return a CO_2 value of zero.

5.3.2.4 Real Spectra: Discussion

Profile retrievals that use real spectra and an a priori profile built from coincident in situ measurements show CO_2 profile deviations up to 40–50 ppm. Even when the errors due to the a priori meteorology are minimized, deviations from the truth due to instrument misalignment, radiative transfer, suntracker pointing, or uncertainties in line parameters are larger than the steepest vertical CO_2 gradients (~5 ppm/km) observed in the ensemble of aircraft profiles from NOAA's ObsPack.

When performing retrievals on the same spectra but replacing the AirCore a priori profile with a standard a priori profile, small errors in the a priori temperature profile cause large deviations in the retrieved CO_2 profile. Despite the large deviations in the retrieved profiles, the retrieval still shows high sensitivity to XCO_2 but does not present a clear improvement over XCO_2 obtained from scaling retrievals. Introducing a temperature retrieval or correction, as well as the ability to model an imperfect instrument line shape, is the best avenue to improve the CO_2 profile retrieval results. Section 5.4 presents an attempt at applying empirical corrections to reduce the effect of systematic imperfections in the forward model.

5.4 Empirical Corrections

In Sect. 5.3.1, we saw that CO_2 profile retrievals have high sensitivity to CO_2 in the absence of errors in the a priori meteorology and systematic errors in instrument line shape. In Sect. 5.3.2, we saw that even with minimizing the effect of a priori errors, deviations from the truth in retrieved CO_2 profiles caused by remaining forward model errors are larger than typical vertical variations of CO_2. Here we investigate the possibility of empirically removing the effect of those errors by de-weighting systematic spectral fitting residuals using empirical orthogonal functions (EOFs). EOFs have been used, for example, with retrievals from GOSAT and OCO-2 measurements (O'Dell et al., 2018). Section 5.4.1 will present how EOFs are derived and used in the retrieval. Results of the application of these EOFs will then be discussed in Sect. 5.4.2.

5.4.1 Empirical Orthogonal Functions

To reduce the effect of systematic residuals on retrieved profiles, empirical orthogonal functions of the spectral fitting residuals were derived to find and remove systematic patterns in the residuals related to temperature errors, instrument line shape, and other effects. The residuals divided by airmass, from a set of retrievals covering a wide range of observational conditions, are stored in a matrix $\mathbf{M}(m,n)$ with n the number of spectra and m the number of spectral points. Then a singular value decomposition is performed on this matrix. The columns of the matrix of left singular vectors are orthogonal basis vectors of the residuals and those associated with the largest singular values represent the main patterns in the residuals, while the corresponding right singular vectors can provide information on the temporal frequency of these patterns.

We use a linear combination of left singular vectors. Each singular vector is associated with a scaling factor. The scaling factor is part of the state vector and adjusted during the retrieval using 100% uncertainty. Before each inversion step, the spectrum “c” calculated with the forward model becomes:

$$c = c + \sum_{i=1}^{N} a_i u_i \tag{5.11}$$

where N is the number of EOFs to use, ordered with decreasing singular value. The first EOF, associated with the highest singular value, is like the scaled average residual from all the spectral residuals in the matrix **M**. Our implementation differs from that described by O’Dell et al. (2018) in that here the EOFs are derived from a set of residuals obtained using scaling retrievals, and not using profile retrievals. Since they are meant to remove systematic errors in the calculated spectra before the retrieval adjusts the CO_2 scaling factors, the EOFs should be derived from a large set of residuals obtained with scaling retrievals to have a significant effect on the profile retrieval. If they are derived from residuals obtained with profile retrievals, these mainly include systematic error patterns corresponding to interfering species, which are not the main source of deviations in retrieved CO_2 profiles. When using scaling retrieval residuals, each EOF includes different error patterns corresponding to CO_2 absorption lines. These error patterns may be attributed to systematic errors for the first EOF, such as errors in spectroscopy, or in the instrument line shape, or a persistent bias in meteorology. The error patterns can also correspond to errors in the a priori meteorology. The temporal frequency of each error pattern is contained in the corresponding right singular vector. The right singular vectors could help diagnose, for example, biases in a priori temperature profiles on different time scales. The right singular vectors can also be used to find correlations between each spectral residual patterns and other quantities measured in time, such as differences between a priori and measured meteorology.

If the residual patterns corresponding to CO_2 lines have the same shape as residuals caused by errors in the a priori CO_2 profile shape, adjustments to the CO_2 scaling factors will compete with adjustments to the EOF scaling factors in the retrieval. Because higher-order EOFs are associated with residuals with different time periodicity, they can also introduce errors that do not exist in calculated spectra. We chose to only include the first EOF, which represents residual patterns common to most spectra. The leading EOF can explain 40 to 52% of the variability in the residuals, depending on the window, as shown in Figure 5.26. The fraction of variability is obtained as the singular value of a given EOF divided by the sum of all singular values. The first ten EOFs in each window are above the noise level of singular values and account for over 90% of the variability in the residuals.

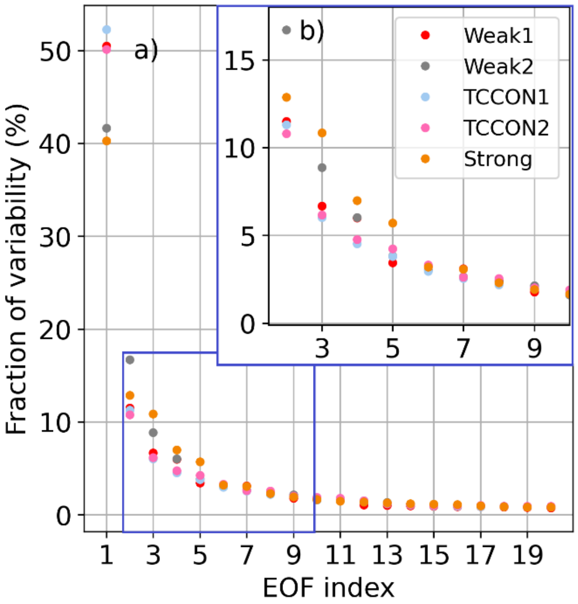

Figure 5.26: Fraction of the variability in the spectral residuals accounted for by each empirical orthogonal function in each CO_2 window. The EOF numbers are shown in decreasing order of singular value. Panel (b) highlights the blue rectangle inside panel (a).

5.4.2 Retrievals with Empirical Orthogonal Functions

One year of measurements from the East Trout Lake (SK, Canada) TCCON station were processed in three ways: with scaling retrievals, with profile retrievals, and with profile retrievals including the first EOF derived from residuals obtained with the scaling retrievals. The residuals used to derive the EOFs are filtered such that spectra that would not pass the TCCON quality checks are not included. To avoid isolated spectra with large residuals having a disproportionate impact on the singular value decomposition of the matrix of residuals, all the spectra are ordered by increasing solar zenith angle and filtered based on the root mean square of the residuals: the 500-point rolling median is computed, and the median of the 500-point rolling standard deviation is used as an estimate of the standard deviation σ, then only spectra within 1σ of the rolling median for all windows are used to derive the EOFs. The matrix of residuals resulting from this filtering includes 42037 out of 64245 total spectra. XCO_2 was retrieved from each window separately. The statistics on the retrieved XCO_2 error are shown in Table 5.5 for each retrieval type and for each window. In all windows but the Strong window, the changes in XCO_2 error between the different retrieval methods are small, less than 0.05 ppm. This is eight times smaller than the reported TCCON 1σ single-measurement precision of 0.4 ppm. However, the mean XCO_2 error is ~55% larger in the Strong window with profile retrievals compared to scaling retrievals. Figure 5.27 to 5.31 show quantities derived from each type of retrieval for an example day and for each window. In each window, the profile retrieval with the first EOF appears as an intermediate case between the profile retrieval and the scaling retrieval. In each case, the root mean square of the residuals is smaller for profile retrievals with the first EOF, but the XCO_2 error is not necessarily smaller.

Table 5.5: Statistics on the retrieved XCO_2 error for one year of measurements at the East Trout Lake TCCON station. σ indicates the standard deviation.

XCO_2 error (ppm)	Scaling retrieval error			Profile retrieval error			Profile retrieval error with the first EOF		
Window	**Mean**	**Median**	**σ**	**Mean**	**Median**	**σ**	**Mean**	**Median**	**σ**
Strong	0.51	0.38	0.37	0.79	0.63	0.60	0.78	0.61	0.59
Weak1	0.89	0.64	0.68	0.91	0.67	0.66	0.90	0.66	0.66
Weak2	0.80	0.56	0.64	0.81	0.61	0.56	0.80	0.61	0.56
TCCON1	0.74	0.48	0.66	0.79	0.51	0.70	0.79	0.51	0.70
TCCON2	0.69	0.45	0.61	0.74	0.47	0.66	0.74	0.47	0.66

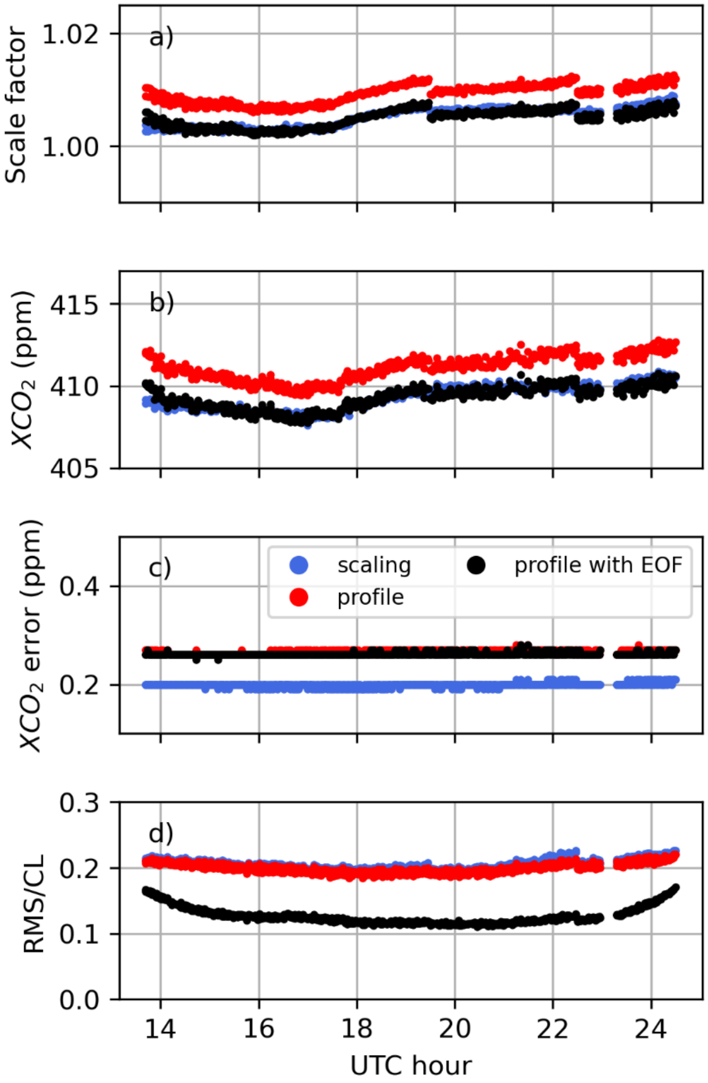

Figure 5.27: Quantities derived from retrievals on East Trout Lake measurements on 29 March 2018 for the Strong window. The retrieval type is indicated by the legend: (a) the column-integrated CO_2 scale factor, (b) XCO_2, (c) the XCO_2 error, (d) the root mean square of the residuals as a fraction of the continuum level.

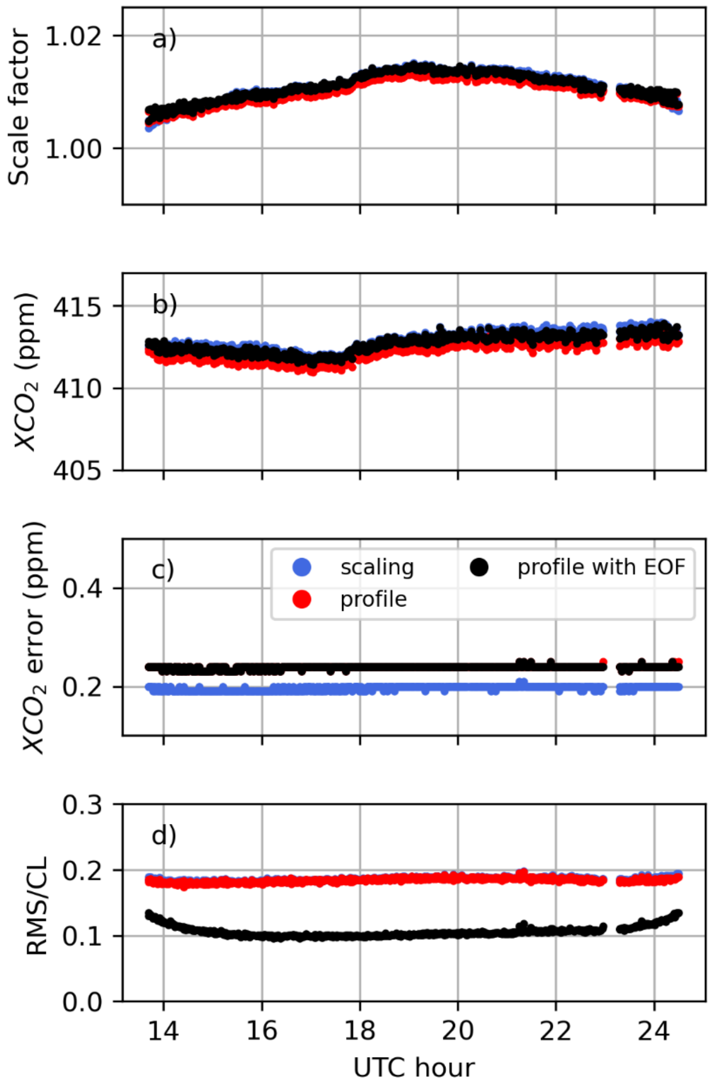

Figure 5.28: Same as Figure 5.27 but for the TCCON1 window.

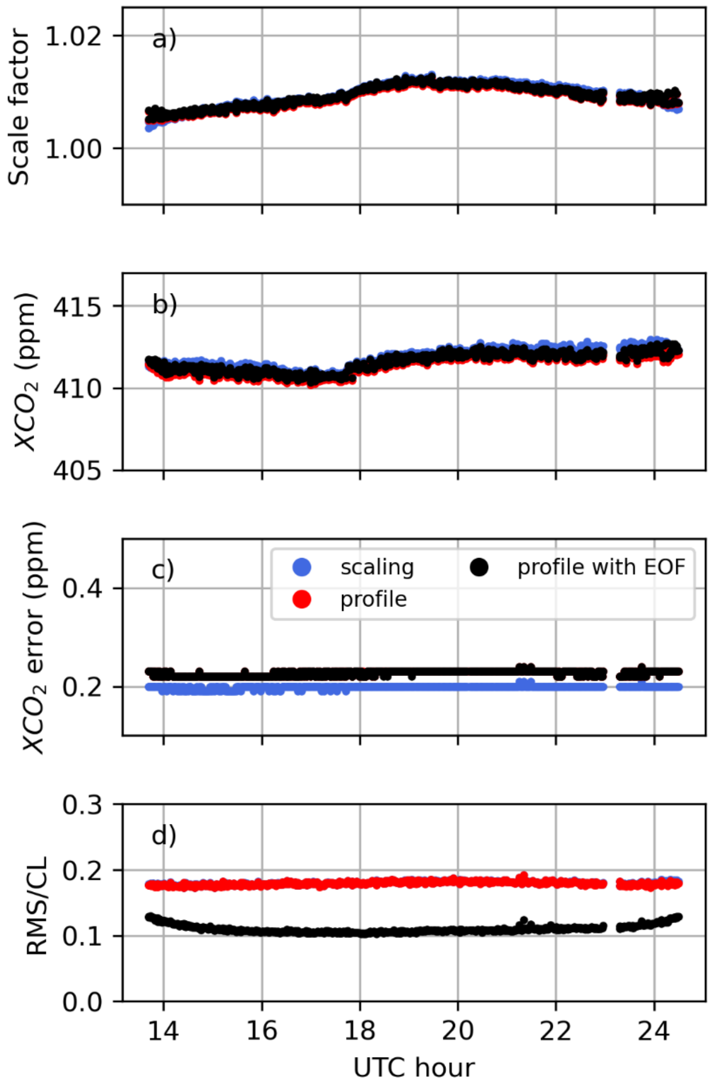

Figure 5.29: Same as Figure 5.27 but for the TCCON2 window.

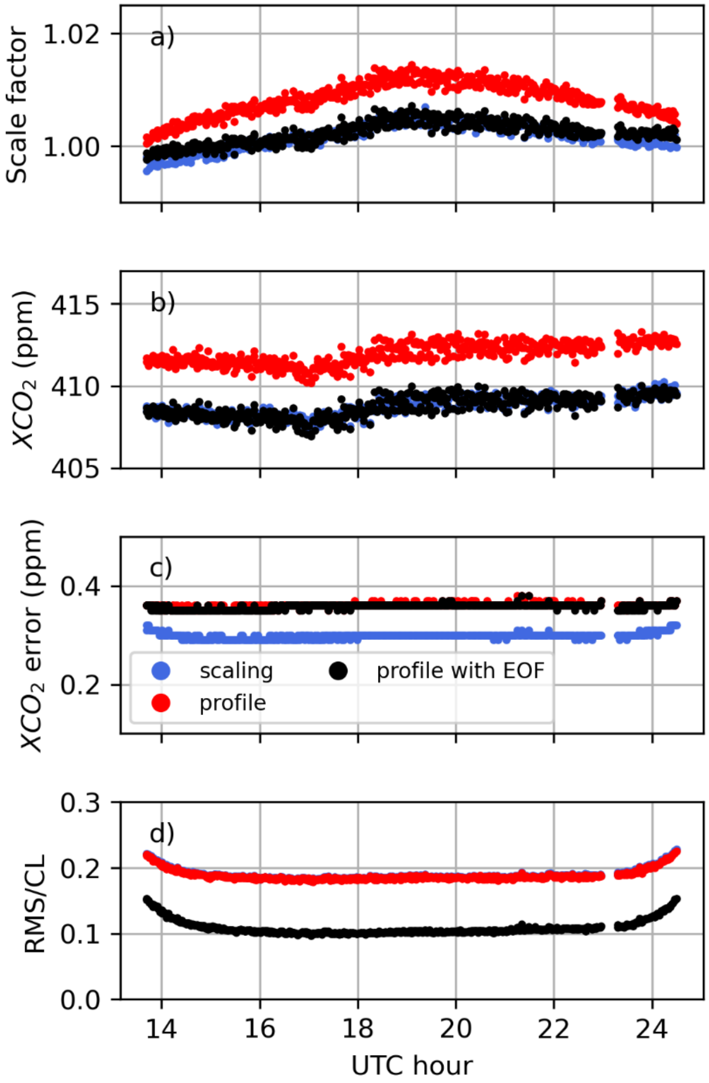

Figure 5.30: Same as Figure 5.27 but for the Weak1 window.

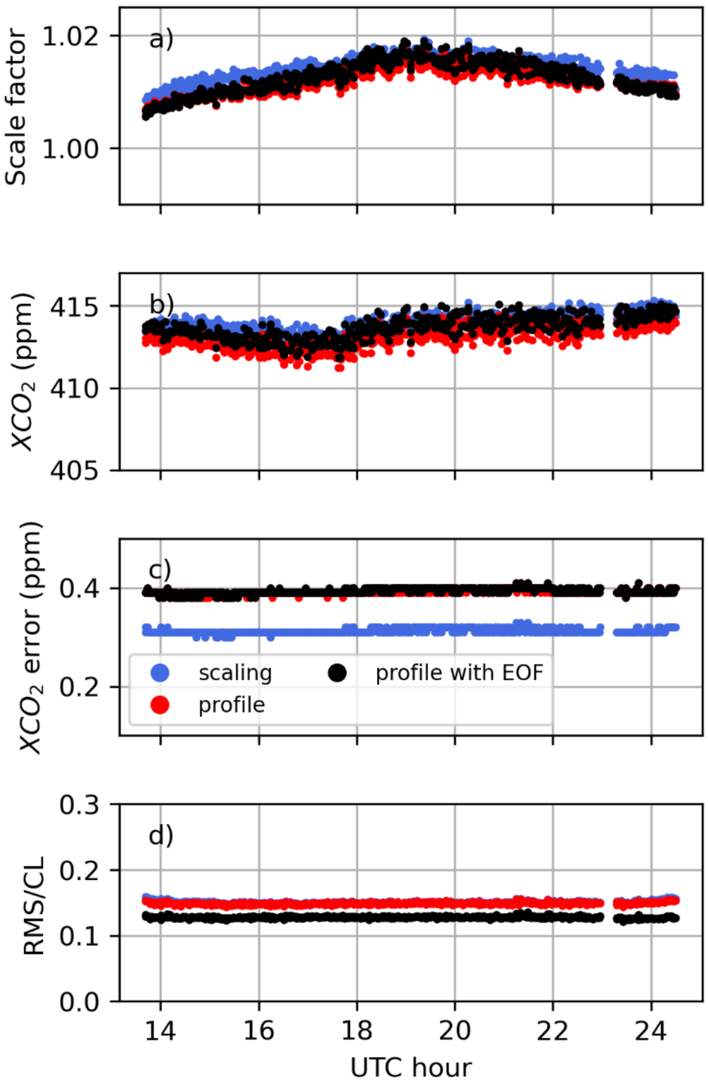

Figure 5.31: Same as Figure 5.27 but for the Weak2 window.

In Figure 5.32(a) and (b), XCO_2 differences are shown between profile and scaling retrievals, and between profile retrievals including the first EOF and scaling retrievals, respectively. We have seen that differences in XCO_2 error between the different retrieval types are within 0.05 ppm. However, differences in XCO_2 between profile and scaling retrievals can be several times larger than the XCO_2 error, indicating different sources of bias between profile and scaling retrievals. In the Weak1 window, the median of the XCO_2 absolute differences is ~4 times larger than the median XCO_2 error, and ~3 times larger in the Strong window. In the TCCON1, TCCON2, and Weak2 windows, the median of the XCO_2 absolute difference is smaller than the median XCO_2

error. In all but the Weak1 window, the XCO_2 differences are 25 to 35% smaller between August and November than for the rest of the year. In Figure 5.32(b), the XCO_2 differences between the profile retrievals with EOF and the scaling retrievals are smaller and more consistent between windows than in Figure 5.32(a). And the median of the XCO_2 absolute differences is smaller than the median XCO_2 error in all windows. Including the leading EOF in a profile retrieval reduces the XCO_2 differences between the scaling and profile retrievals, but the XCO_2 of the profile retrieval with EOF is more strongly correlated with the XCO_2 of the profile retrieval than that of the scaling retrieval as shown in Table 5.6.

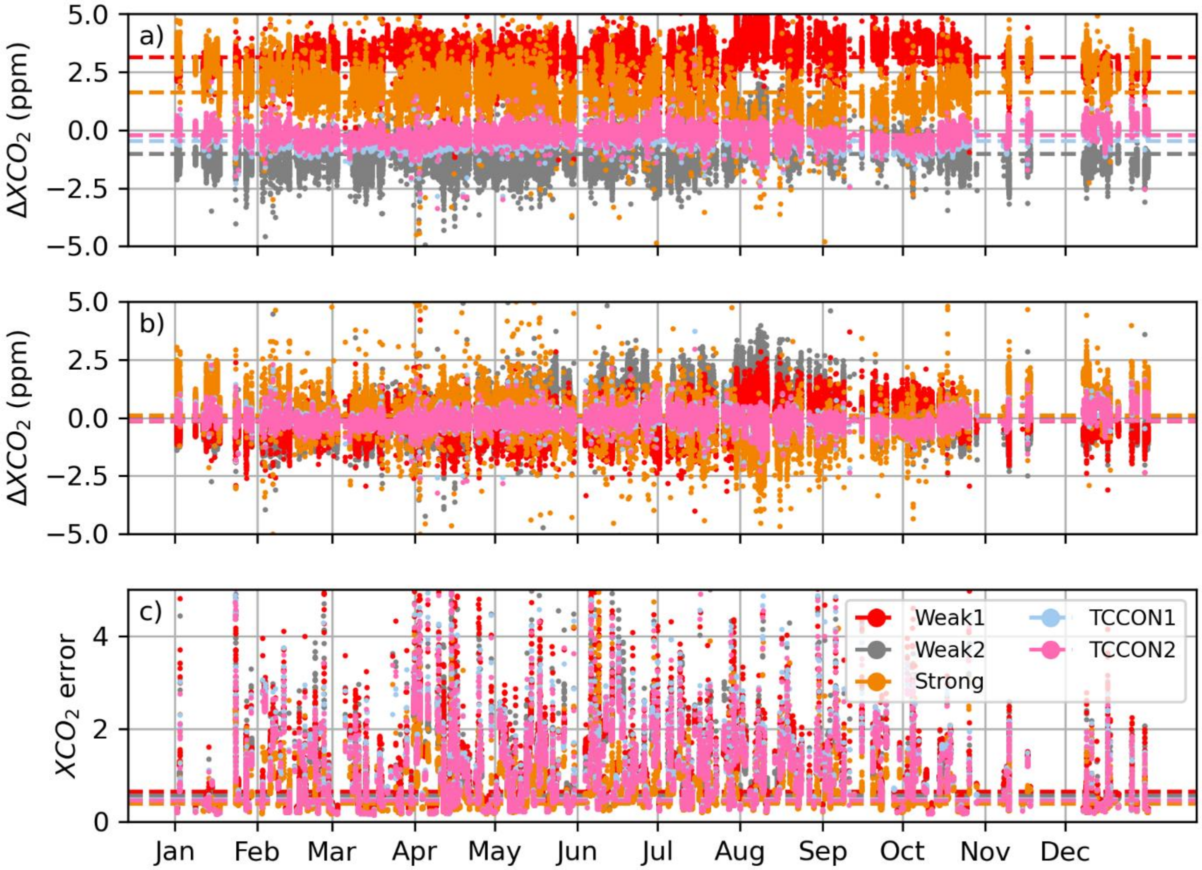

Figure 5.32: In panel (a), the XCO_2 obtained from the scaling retrieval is subtracted from the XCO_2 obtained from the profile retrieval. In panel (b), the XCO_2 obtained from the scaling retrieval is subtracted from the XCO_2 obtained from the profile retrieval with EOF. In panel (c), the XCO_2 error from the scaling retrieval is shown, with the median values as dashed lines. In the top two panels, the horizontal dashed lines show the median values of absolute differences in XCO_2.

Figure 5.33 and 5.34 presents the averaged retrieved profiles without and with the inclusion of the leading EOF, respectively, coincident within ±1 hour of the average sampling time of aircraft profiles measured over East Trout Lake. The aircraft profiles were obtained from CarbonTracker data (Jacobson et al., 2020). The deviations in the CO_2 profiles obtained with profile retrievals are larger than the vertical variations in the aircraft measurements. When the retrieved profiles present large deviations typical of temperature errors like that in Figure 5.12(b), the CO_2 profile obtained from profile retrieval with the first EOF reduces the amplitude of the deviations, but the shape persists. This is expected because the first EOF represents the average residuals, which should not include residual features caused by temperature errors, unless the temperature errors were always biased in the same way. We would expect the first EOF to reduce deviations like that in Figure 5.12(a). In such cases, the CO_2 profiles obtained from profile retrieval with the first EOF are smoother than profile retrievals but present no clear advantage over scaling retrievals.

Table 5.6: Squared Pearson correlation coefficient for XCO_2 between the scaling and profile retrievals (SCL–PRF), and between the profile retrieval with the first EOF and the profile retrieval (EOF–PRF).

R^2	SCL–PRF	EOF–PRF
Strong	0.9368	0.9929
Weak1	0.9633	0.9951
Weak2	0.9586	0.9814
TCCON1	0.9922	0.9995
TCCON2	0.9931	0.9999

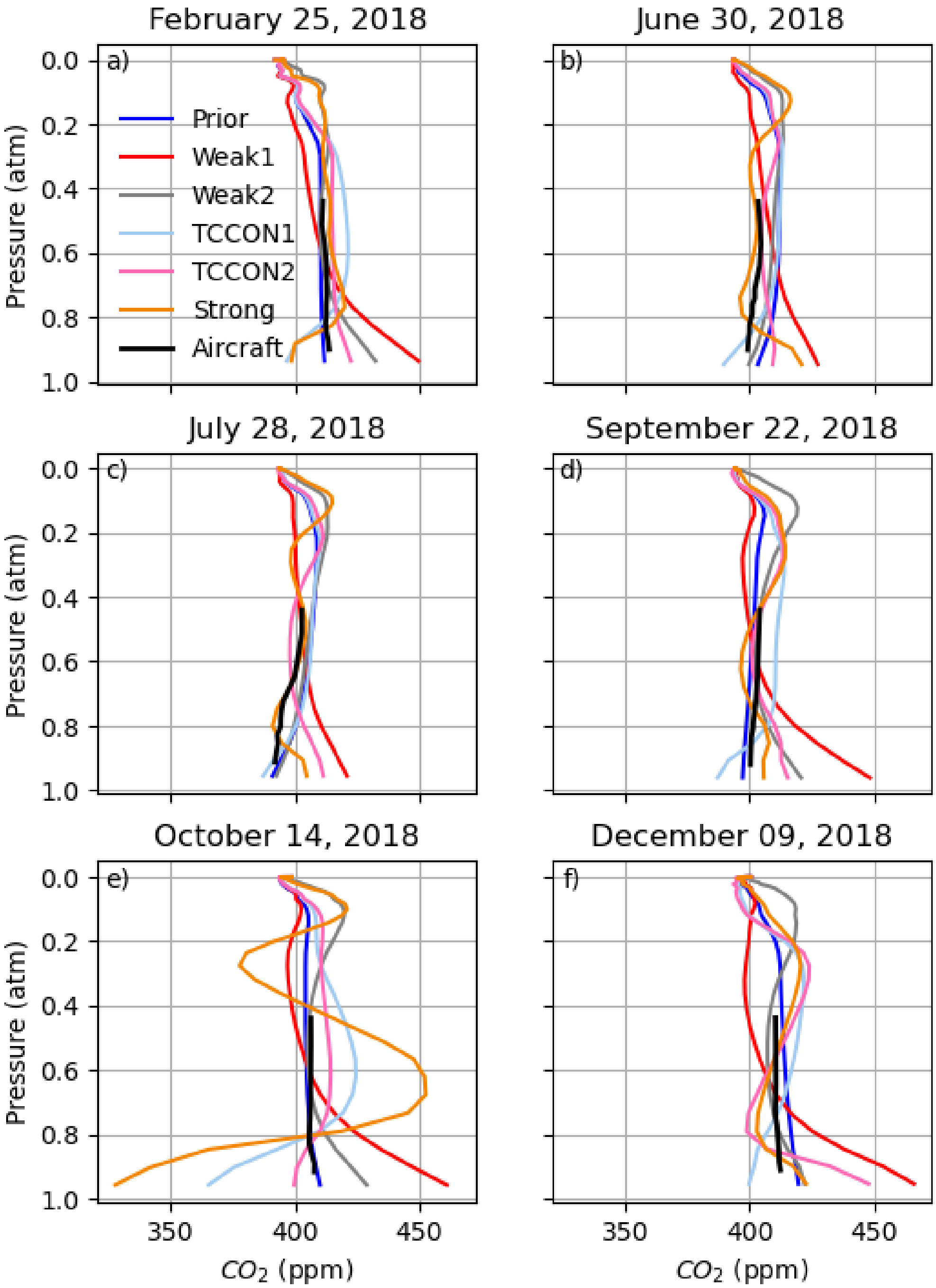

Figure 5.33: Aircraft profiles measured over East Trout Lake and average profile retrieved from spectra coincident within ±1 hour of the average sampling times of the aircraft flight and without using the leading EOF. Retrieved profiles are shown for each window as indicated by the legend. Each panel presents data from different dates.

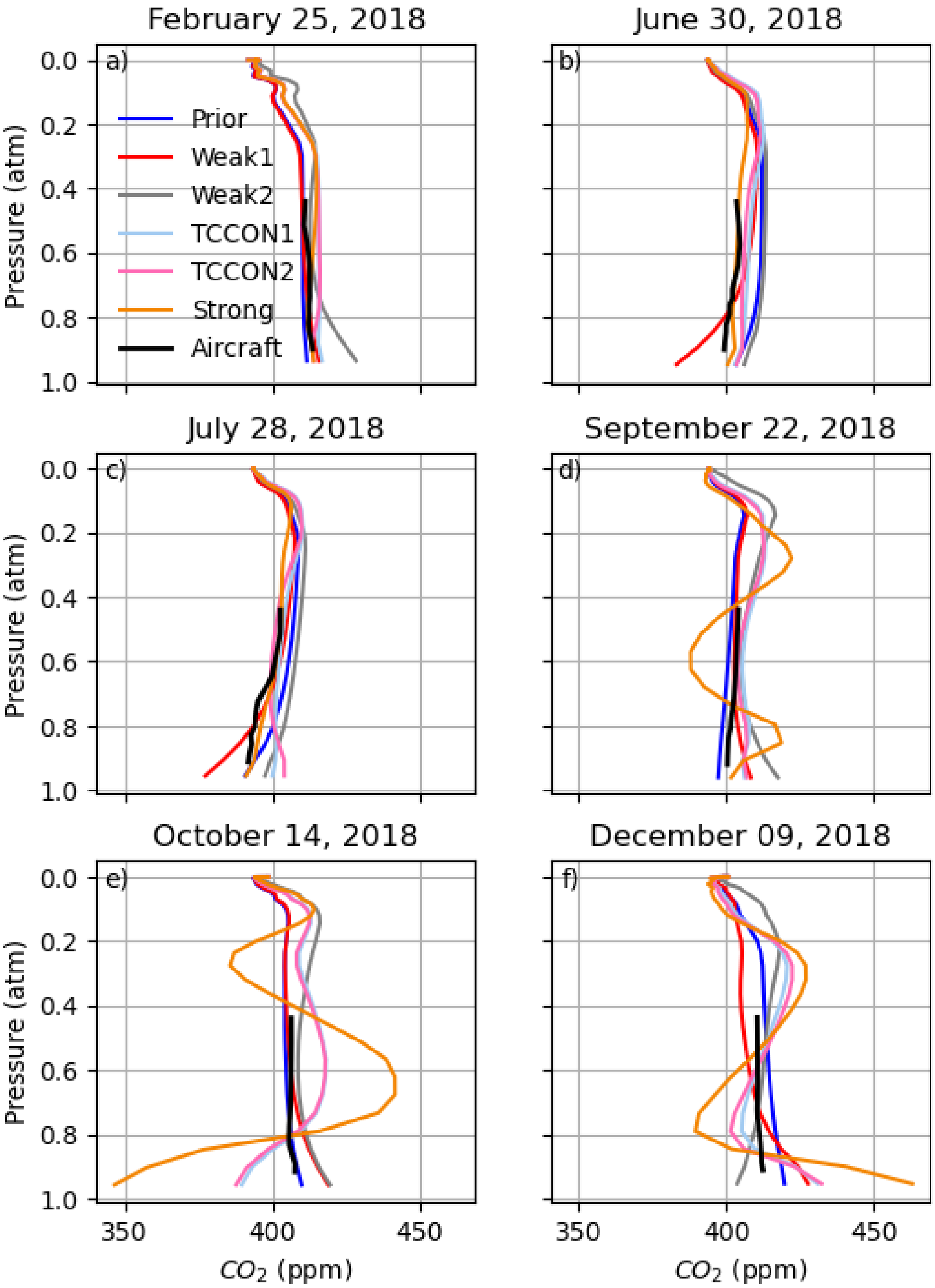

Figure 5.34: Same as Fig. 5.33 but for retrievals that include the leading EOF.

5.5 Summary and Conclusions

In this study, we investigated the use of CO_2 profile retrievals from near-infrared solar absorption spectra measured by TCCON. The performance of the CO_2 profile retrieval was reassessed after improvements were implemented in the forward model of GGG. Retrievals were performed using five CO_2 windows with significantly different optical opacities.

We first used retrievals on synthetic spectra to check the self-consistency. Typical errors in the a priori H_2O profile, which is retrieved with a scaling retrieval, caused limited deviations from the truth in the CO_2 profile, within 5–10 ppm in the Strong window, and within 2 ppm in the other windows. Perturbing the CO_2 air- and self-broadened Lorentz half-width coefficients and their temperature dependence to within their estimated uncertainties led to CO_2 deviations from the truth of less than 5 ppm. The implementation of a non-Voigt line shape is a significant improvement to CO_2 profile retrievals; errors in spectroscopic parameters are no longer the leading source of uncertainty in retrieved profiles. We observed deviations from the truth of up to 100 ppm in profiles retrieved with typical temperature errors. The temperature profile is an important retrieval input, but is not retrieved, thus spectral residuals caused by errors in the a priori temperature profile are free to be suppressed by adjustments to the CO_2 scale factors. The implementation of a temperature profile retrieval, or correction, is critical to improve CO_2 profile retrieval results. In GGG2020, 3-hourly a priori temperature profiles are used, but temperatures can still vary by several degrees between 3-hourly profiles and can still be wrong even without any time mismatch. Temperature could be retrieved from CO_2 windows and from windows with temperature-sensitive water vapour absorption lines.

We then performed retrievals with atmospheric TCCON spectra collected at the Lamont site, which were coincident with AirCore profiles, including radiosonde profiles of temperature and relative humidity; these were considered as the true state of the atmosphere. When running retrievals with the truth as the a priori information, the deviations due to errors in the a priori meteorology are minimized and the resulting deviations are caused by instrument misalignment, errors in spectroscopy, or suntracker pointing. We observed CO_2 deviations of up to 40 ppm in that case. Even with ideal knowledge of the a priori meteorology, the CO_2 deviations are larger than the largest expected vertical CO_2 variations and no useful profile information can be inferred from the profile retrieval. Stricter alignment requirements, which can be challenging to achieve in practice, or the ability to model an imperfect instrument line shape are needed to improve profile retrieval results. The sensitivity study of Sect. 5.3.1 could then be extended to assess the effect of specific misalignments on the retrieved profiles.

In these retrievals, we used a full a priori covariance matrix, with off-diagonal elements, based on comparisons between the GGG2020 a priori and aircraft vertical profiles from NOAA's ObsPack over the Lamont TCCON site. Before tuning the a priori covariance and considering stronger regularizations, it must be shown that CO_2 deviations caused by typical errors in the a priori meteorology are smaller than typical variability in real CO_2 profiles. Because it is more computationally expensive, and because it requires stronger constraints on the a priori statistics than scaling retrievals, a profile retrieval must present clear advantages over a scaling retrieval to justify its operational use. And with each new improvement to the CO_2 a priori profiles, requirements for profile retrieval to be better than scaling retrieval become more stringent.

An attempt at empirically correcting for systematic errors was presented, using the leading EOF from a large set of residuals from measured spectra at the East Trout Lake TCCON site. Although using the EOF results in smoother retrieved profiles, it still is not successful in limiting profile deviations from the truth enough to derive useful vertical information. However, we have only presented one approach using the EOFs, by including only the leading singular vector. There are several possibilities for further development of empirical corrections based on the use of EOFs that will be discussed in Chapter 7.

Chapter 6

Simulated Retrieval of XCO_2, XCH_4, and XCO in Support of AIM-North Phase 0

In Sect. 1.2 and Sect. 1.3, we saw that trace gas measurements in the Arctic are sparse despite the region's stronger sensitivity to climate change than lower latitudes. Although the Arctic tundra and boreal forests currently act as land carbon sinks, and the Arctic ocean is a more effective sink than oceans at lower latitudes, the Arctic region also holds vast amounts of carbon stored in the permafrost. In a warming climate, those carbon stocks are susceptible to become carbon sources and further accelerate global warming (Hugelius et al., 2020). In a permafrost carbon feedback, release of greenhouse gases from thawing permafrost would contribute to warming, leading to more permafrost thaw (Schuur et al., 2015). Based on incubation studies, the release of CO_2 from aerobic environments would be the main driver of that feedback, rather than CH_4 (Schädel et al., 2016, 2018). It is difficult to predict to what extent such emissions from soils might be mitigated by changes in vegetation and the northward expansion of the boreal forest (Abbott et al., 2016).

The Atmospheric Imaging Mission for Northern Regions (AIM-North) proposes to address the lack of observational coverage in the Arctic by using a pair of satellites in a Highly Elliptical Orbit (HEO). AIM-North proposes to provide a high density of measurements of greenhouse gases, air quality, clouds, and vegetation productivity between ~40°N and 80°N. In the HEO configuration, a satellite spends most of the time around the apogee, where it moves the slowest, and a pair of satellites in HEO can achieve a temporal coverage close to that of a geostationary satellite. The instrument dedicated to greenhouse gas observations would be a grating spectrometer or a FTS imaging in the NIR and SWIR to measure CO_2, CH_4, and CO. The satellite would also carry an ultraviolet-visible spectrometer to measure air quality: O_3, NO_2, BrO, HCHO, SO_2, OClO, CHOCHO, aerosols and other species (Nassar et al., 2019). The coverage that AIM-North would achieve is illustrated in Figure 6.1.

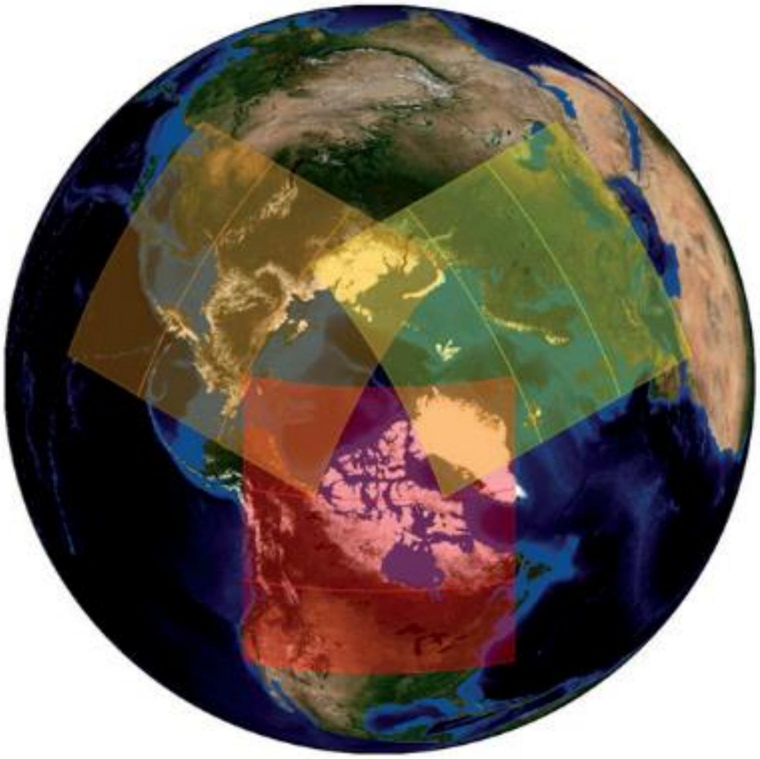

Figure 6.1: A simplified scanning pattern for AIM-North assuming the satellite reaches apogee around midday with a three-apogee orbit. Figure taken from Nassar et al. (2019).

The goal of the work presented in this chapter is to determine how well the AIM-North mission could measure XCH_4, XCO, and XCO_2 under different conditions and for two instrument designs provided by industrial partner ABB Inc. It aims to inform possible changes required to the instrument design to meet the mission target thresholds and goals for precision and accuracy. The results of this study were submitted as a report to the CSA (Strong et al., 2020b). The two instruments considered are an imaging Fourier transform spectrometer and a grating spectrometer. The spectral window ranges and resolutions for the grating instrument are the same as for the GeoCarb instrument (O'Brien et al., 2016; Moore III et al., 2018).

Section 6.1 presents the different parameters considered for the sensitivity study of the retrieval error and accuracy. Section 6.1.1 describes the implementation of the FTS noise model, and Sect. 6.1.2 describes that of the grating spectrometer.

In Sect. 6.2, the results from the sensitivity study are presented. The sensitivity to the observation geometry and surface parameters is described in Sect. 6.2.1, to a multiplicative offset in the radiance in Sect. 6.2.2, and to surface pressure errors resulting from pointing errors in Sect. 6.2.3. Finally, Sect. 6.3 summarizes the results and conclusions.

6.1 Methods

To conduct this study, we used NASA's Reusable Framework for Atmospheric Composition (ReFRACtor, McDuffie et al., 2018) code, available at https://github.com/ReFRACtor/framework and https://github.com/ReFRACtor/oco (last accessed : July 10th 2021). The ReFRACtor code was developed as a software framework for atmospheric radiative transfer and retrievals for multiple instruments, to facilitate software reuse and the fusion of different datasets. It uses the ACOS/OCO-2 retrieval algorithm (O'Dell et al., 2012; documented at https://docserver.gesdisc.eosdis.nasa.gov/public/project/OCO/OCO_L2_ATBD.pdf, last accessed: July 10th 2021) but with a different code implementation that includes Python modules as wrappers to the C++ and Fortran codebase. The code had to be adapted to use the spectral regions and instrument characteristics considered for the AIM-North greenhouse gas instrument. NASA's ABSCO (https://github.com/ReFRACtor/ABSCO; last accessed: July 10th, 2021) codes were used to generate absorption coefficient tables for the spectral windows presented in Table 6.1. The goals and thresholds are based on requirements set by the Global Climate Observing System (GCOS) which suggests a precision of 1 ppm for CO_2, with biases less than 0.2 ppm, and 10 ppb for CH_4, with biases less than 2 ppb (WMO, 2011).

Table 6.1: The AIM-North mission target goal (G) and threshold (T) for accuracy and for single observation precision for XCH_4, XCO, and XCO_2, along with the spectral windows and resolutions used in this study.

	Precision (%)	Accuracy (%)	Window		Resolution	
			FTS (cm^{-1})	Grating (nm)	FTS (cm^{-1})	Grating (nm)
XCH_4	0.5 (G) 1.5 (T)	0.1 (G) 0.3 (T)	4200-4345	2300.6-2345.6	0.25 (maximum OPD=2 cm)	0.1531
XCO	5 (G) 15 (T)	5 (G) 15 (T)				
XCO_2	0.25 (G) 0.75 (T)	0.05 G) 0.15 (T)	6180.47-6257.82	1591.6-1621.2		0.1018
			4810.0-4897.16	2045-2085		0.1361
O_2	-	-	13118.19-13192.61	757.9-772		0.0475

A set of a priori profiles was generated in the same way as the GGG2014 a priori profiles (Wunch et al., 2015): a reference profile for each gas at 35°N on January 1st 2005 is empirically adjusted to generate profiles appropriate for the latitude and date of each measurement.

The forward model computes absorption spectra from a given state vector describing surface properties (pressure, albedo) and the atmosphere (meteorology and trace gas concentration profiles, and aerosol optical depth). A set of 432 spectra was generated for all combinations of variables shown in Table 6.2 and 6.3 and saved in Level 1 (L1) files. The values of these parameters were chosen in consultation with AIM-North colleagues at ECCC to give representative ranges of observation conditions over latitudes from 40 to 80°N. The surface albedo was classified in eight surface types by Joseph Mendonca using MODTRAN (Berk et al., 2014), and ASTER for snow-covered surfaces (Abrams, 2000). Even as far north as Eureka (80.05°N), the ground is not always snow-covered and only the crop and forest surface types are not encountered.

Table 6.2: Parameters used to generate the database of 432 synthetic spectra, with 216 scenes and two instruments.

Input Parameter	Values
Instrument	FTS, grating
Solar zenith angle (SZA, degrees)	30, 60, 80
Viewing zenith angle (VZA, degrees)	0.1, 30, 60
Surface albedo (unitless)	8 surface types (see Table 6.3)
Aerosol optical depth (AOD, unitless)	0.01, 0.1, 0.25

Table 6.3: Albedo in each window for eight surface types.

	Crop	Wetland	Tundra	Shrub	Forest	Grass	New snow	Old snow
CH_4/CO	0.07	0.05	0.08	0.075	0.15	0.1	0.16	0.01
Strong CO_2	0.05	0.07	0.09	0.09	0.165	0.09	0.05	0.005
Weak CO_2	0.145	0.135	0.17	0.178	0.17	0.25	0.22	0.03
O_2	0.3	0.25	0.22	0.2	0.23	0.38	0.97	0.85

Sample spectra are shown in Figure 6.2 for each band and both instruments. A code was developed that iterates through these variables, reads the corresponding L1 spectrum from the L1 file, applies to it an instrument specific noise model (see Sect. 6.1.1 and Sect. 6.1.2), and runs the retrieval. The retrieval outputs are saved in Level 2 (L2) files, which include the L1 spectrum with added noise, the spectrum calculated with the best estimate of the state vector, the prior and retrieved state vectors, the averaging kernel, the prior and posterior covariance matrices, the prior and retrieved profiles and column-averaged dry-air mole fractions of CO_2, CH_4, and CO, and their degrees of freedom for signal.

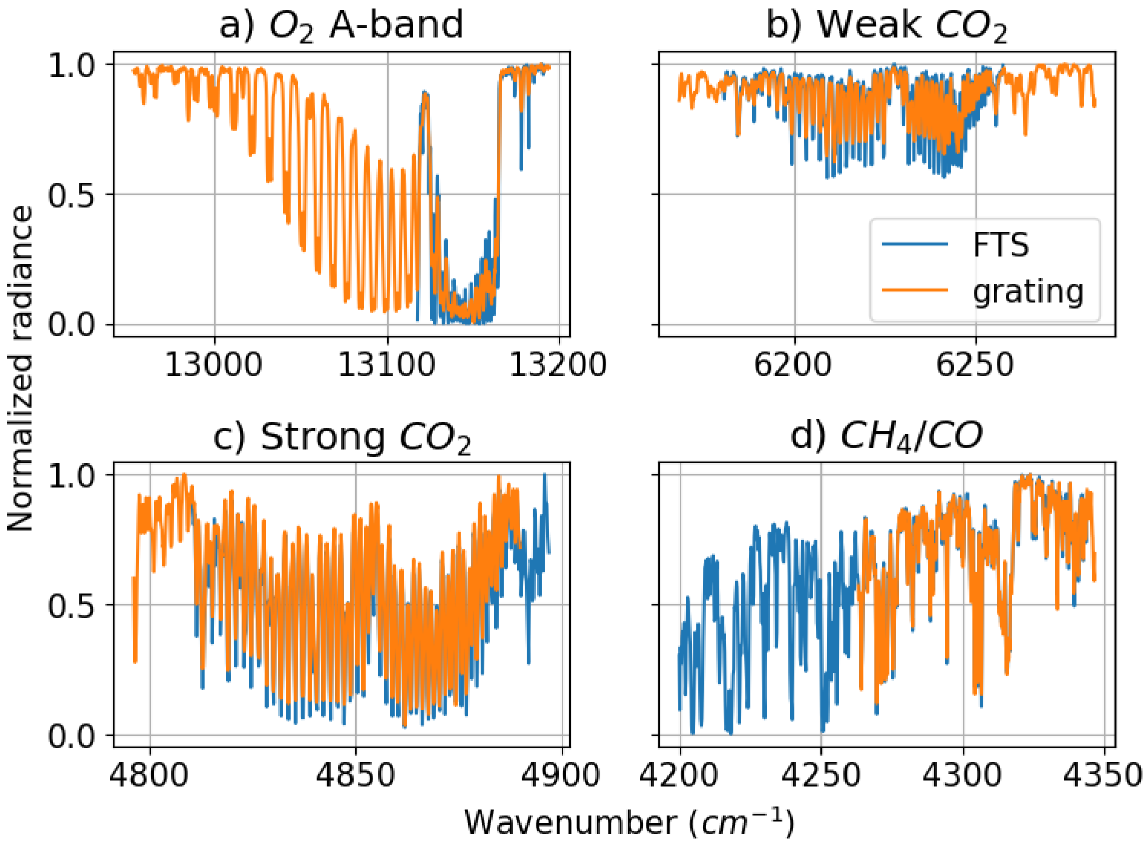

Figure 6.2: Example spectra for both instruments and for (a) the O_2 window, (b) the weak CO_2 window, (c) the strong CO_2 window, and (d) the CH_4/CO window. These were generated for a given scene with SZA=30°, VZA=0.1°, albedo=forest, and AOD=0.01.

The forward model first computes a spectrum independently from the instrument model with a small spectral spacing of 0.01 cm^{-1}, and then convolves it with an instrument line shape. Before running retrievals, a noise model can be applied, which adds noise based on instrument characteristics provided by ABB.

6.1.1 FTS

For the FTS, the ILS is a sinc function completely determined by the instrument's internal field of view and the maximum optical path difference. The same routine that computes the ILS in GFIT was implemented. In each spectral window, the ILS is derived using the window's center wavenumber and is used to convolve the spectrum in that window.

The noise model of the FTS computes a noise-equivalent spectral radiance (NESR) (Hearn, 1999; Davis et al., 2001a):

$$\mathrm{NESR} = \sqrt{\frac{\left(\sqrt{2qI}\right)^2 + (I_{det})^2}{\left(\eta\tau A_{apt}\Omega\Delta\sigma R\sqrt{T}\right)^2}} \qquad with\, I = A_{apt}\Omega \int LR\tau\, d\sigma \tag{6.1}$$

where each term is defined as:
NESR: noise-equivalent spectral radiance ($W.m^{-2}.sr^{-1}.(cm^{-1})^{-1}$)
R: detector responsivity ($A.W^{-1}$)
L: scene radiance ($W.m^{-2}.sr^{-1}.(cm^{-1})^{-1}$), this is the output of the ReFRaCtor forward model.
I: signal from scene radiance (A)
q: electron charge ($A.s$)
η: total modulation efficiency (unitless)
τ: total transmission (unitless)
A_{apt}: aperture area (m^2), 20 cm aperture diameter
Ω: solid angle of a ground sample subtended at the aperture (sr)
$A_{apt}\,\Omega = 3.14 \times 10^{-10}$: étendue ($m^2.sr$)
$T = 59.4$: scan time (s)
$\Delta\sigma = 0.25$: resolution (cm^{-1})
$I_{det} = 1.03 \times 10^{-15}$; 7.87×10^{-16} for the CO_2 strong window: detector noise current density ($A.s^{0.5}$).

The only parameter that is not an intrinsic, observation-independent instrument characteristic in Eq. 6.1 is the scene radiance *L* (and the signal *I* which is derived from it). The instrument specific parameters were provided by ABB. The NESR in this model is the root sum square of two noise contributions: the first term represents the scene shot noise contribution while the second term is the contribution from detector noise. At each spectral point, the noise is then randomly generated from a Gaussian distribution with zero mean and NESR standard deviation as illustrated in Figure 6.3. The modulation efficiency (η), transmission (τ), and detector responsivity (*R)* of the CH_4/CO window are shown in Figure 6.4.

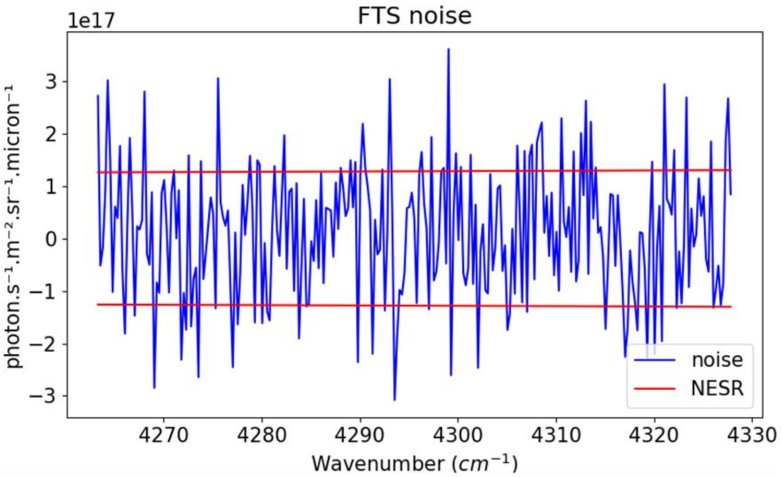

Figure 6.3: Example of FTS noise (blue) generated from a given NESR (red) for part of the CH_4/CO window and calculated for a standard scene (SZA=45°; VZA=0°; AOD=0.01; albedo=0.15).

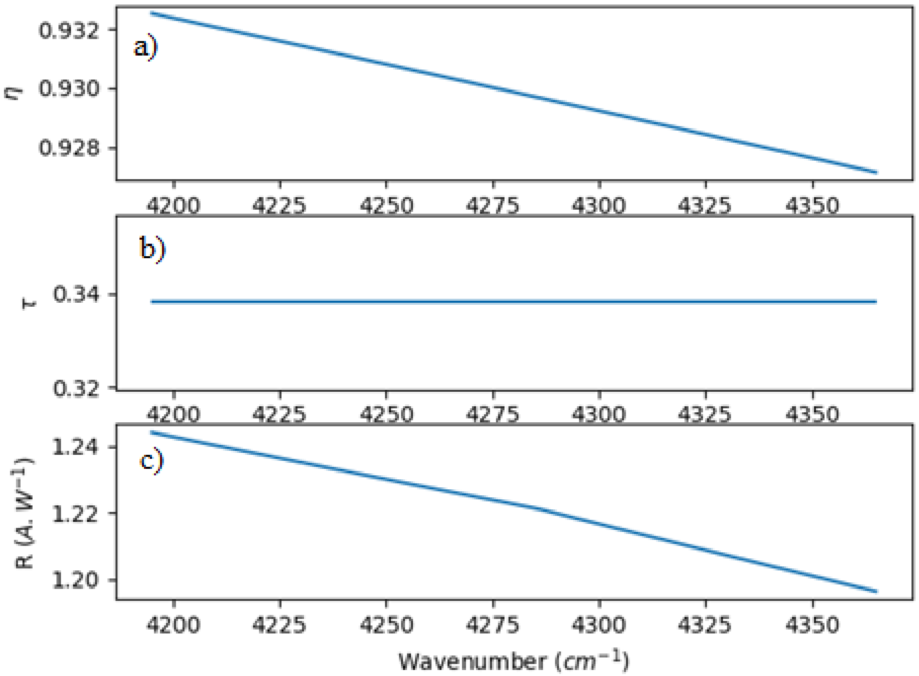

Figure 6.4: FTS instrument characteristics: (a) modulation efficiency, (b) transmission, and (c) detector responsivity in the CH_4/CO window. These parameters are independent of observations and were provided by ABB.

6.1.2 Grating Spectrometer

For the grating instrument, the ILS is assumed to be Gaussian with its standard deviation equal to the resolution. As each pixel of the detector array acts as an independent detector, the radiance in each pixel is convolved separately with the ILS.

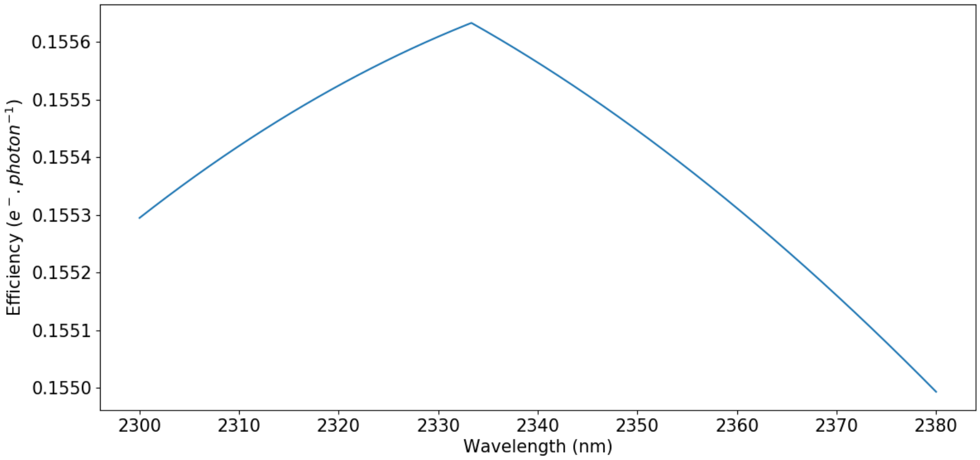

Figure 6.5: Grating instrument efficiency in the CH$_4$/CO window. This parameter was provided by ABB.

The noise model of the grating instrument is defined as:

$$S(\lambda) = A\,\Omega\,E(\lambda)\,L(\lambda)\,\Delta\lambda\,\Delta t \tag{6.2}$$

where each term is defined as:
S: number of electrons collected by a pixel with bandwidth $\Delta\lambda$ during the time interval Δt (e)
$A\,\Omega = 7.85398 \times 10^{-11}$: Etendue (m^2.$sr$)
E : efficiency ($\mathrm{e.photons}^{-1}$), shown in Figure 6.5 for the CH$_4$/CO window.
L: spectral photance ($photons.s^{-1}.m^{-2}.sr^{-1}.nm^{-1}$), the output of the ReFRActor forward model.
$\Delta\lambda = 0.0476$: spectral sampling interval (nm)
$\Delta t = 1.2$: integration time (s)
$\sqrt{S}$: Scene shot noise (e).

As with the FTS noise model, the only parameter in Eq. 6.2 that is not an intrinsic, observation-independent instrument parameter, is the spectral photance (expressed with photons instead of Watts for radiance) L. The other parameters were provided by ABB.

The total noise (e) is:

$$n(\lambda) = \sqrt{S + N^2} \tag{6.3}$$

where N = 270 was provided by ABB. N is the root-sum-square of dark current shot noise, thermal emission shot noise, quantization noise, and read-out noise (e).

The signal-to-noise ratio is defined as:

$$SNR(\lambda) = \frac{S\sqrt{m}}{n} \tag{6.4}$$

where $m = 3$ is the spectral binning provided by ABB.

6.2 Results

In this section, we present results of the sensitivity studies in the form of plots of accuracy and precision as a function of SNR. The SNR shown in the figures is computed as the scalar:

$$SNR = RMS\left(\frac{\boldsymbol{radiance}}{\sqrt{\boldsymbol{S_y}}}\right) \tag{6.5}$$

where $\boldsymbol{S_y}$ is the diagonal of the measurement covariance matrix and "$\boldsymbol{radiance}$" is the radiance vector for a given spectral window (for example, one of the spectra illustrated in Figure 6.2). This produces smaller SNR values than using the continuum of the spectrum (using only the maximum values of the signal in the window).

In the figures presented here, unless specified otherwise, the SNRs reported with XCO_2 accuracies are from the CO_2 strong window only, rather than a combination of SNRs from the two CO_2 windows. However, XCO_2 is always retrieved simultaneously from both the strong and weak CO_2 windows.

Accuracy is defined as:

$$accuracy\,\% = 100 \times \frac{X_G - X_G^{true}}{X_G^{true}} \tag{6.6}$$

where X_G is the retrieved column-averaged dry-air mole fraction of gas G, and X_G^{true} is the true value of that quantity (which was used to generate the synthetic spectrum).

Precision is defined as:

$$precision\,\% = 100 \times \frac{\Delta X_G}{X_G^{true}} \tag{6.7}$$

where ΔX_G is the retrieval error. The retrieval code produces a gradient vector $\boldsymbol{g}$ representing the change in the column-averaged dry-air mole fraction of a target gas with respect to a change of each element i of the state vector:

$$\boldsymbol{g}_i = \frac{\delta X_G}{\delta(\boldsymbol{state - vector})_i} \tag{6.8}$$

from which ΔX_G is derived as:

$$\Delta X_G = \sqrt{\boldsymbol{g}^T \boldsymbol{S} \boldsymbol{g}} \tag{6.9}$$

where **S** is the a posteriori covariance matrix.

6.2.1 Sensitivity to the Scene

6.2.1.1 Standard Scene

A “standard scene” was defined with a given set of inputs: SZA=45°, VZA=0.1°, albedo=forest, AOD=0.01. The prior covariance matrix was constructed such that the retrieval precision for XCH_4 and XCO at the lowest SNRs be greater than the mission precision threshold.

The prior covariance for CO_2 is from the diagonal of the OCO-2 prior covariance. The prior covariance for CO and CH_4 is diagonal with:

$$(\boldsymbol{S_a})_{i,i} = \left(\frac{\boldsymbol{c_i}}{c_{surf}} \times \sigma_{surf}\right)^2 \tag{6.10}$$

where c_i is the mole fraction in the i^{th} atmospheric layer, c_{surf} is the mole fraction at the surface, and σ_{surf} is the corresponding uncertainty.

Vertical profiles of the prior uncertainties are shown in Figure 6.6, with 200 ppb surface uncertainty for XCH_4 and 80 ppb for CO. Figure 6.7 shows precision vs. SNR for this standard scene; the continuous lines are obtained using a "prescribed noise model" where the SNR is given as an input instead of being derived from the instrument characteristics as described in Sect. 6.1.1 and 6.1.2. In this case, the grating SNR is just replaced by the prescribed SNR and the FTS NESR becomes:

$$\boldsymbol{NESR} = 100 \times hc\boldsymbol{\lambda} \times SNR_{prescribed} \tag{6.11}$$

where h is the Planck constant, c is the speed of light, and $\boldsymbol{\lambda}$ is the wavenumber grid.

When the prescribed noise model is used, the prescribed SNR value is given for the CH_4/CO window ($SNR^{CH_4}_{prescribed}$), and the SNR in other windows is scaled to match the relative difference of SNR between the windows when using the instrument characteristics:

$$SNR_{window} = SNR^{CH_4}_{prescribed} \frac{SNR^{window}_{REAL}}{SNR^{CH4}_{REAL}}. \tag{6.12}$$

In Figure 6.7, the black markers show the precision for the SNR derived from the current instrument characteristics. Figure 6.7 shows that we can expect the precision threshold to be met for all target gases with the current instrument design over "standard scenes", but not the goal. Table 6.4 shows the SNR required in each window to meet the precision goal for the standard scene. The CO_2 goal seems especially difficult to meet and would require more than a doubling of the current instrument SNR. In Sect. 6.2.1.2, only the realistic noise model is used (not the prescribed SNR) for all the scenes generated from Table 6.2 and 6.3.

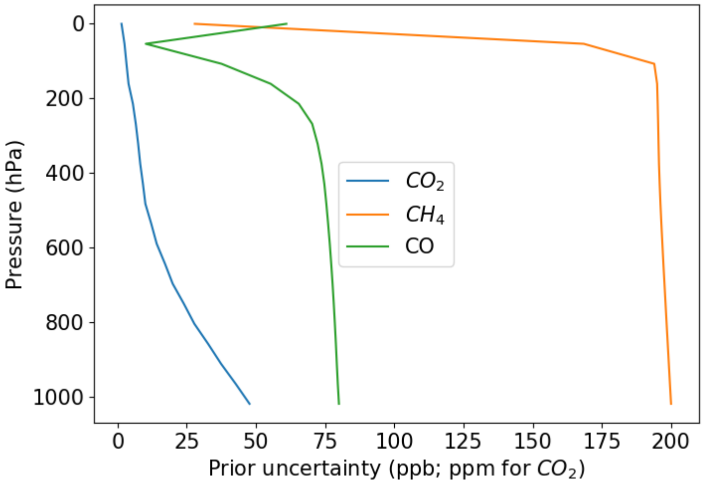

Figure 6.6: Square root of the diagonal elements of the prior covariance of each species.

Table 6.4: SNR required to meet the single observation precision goal for each gas over the standard scene. The SNR value for CO_2 is given for the strong window.

	CH_4	**CO**	**CO_2**
Grating	100	125	>250
FTS	110	140	>250

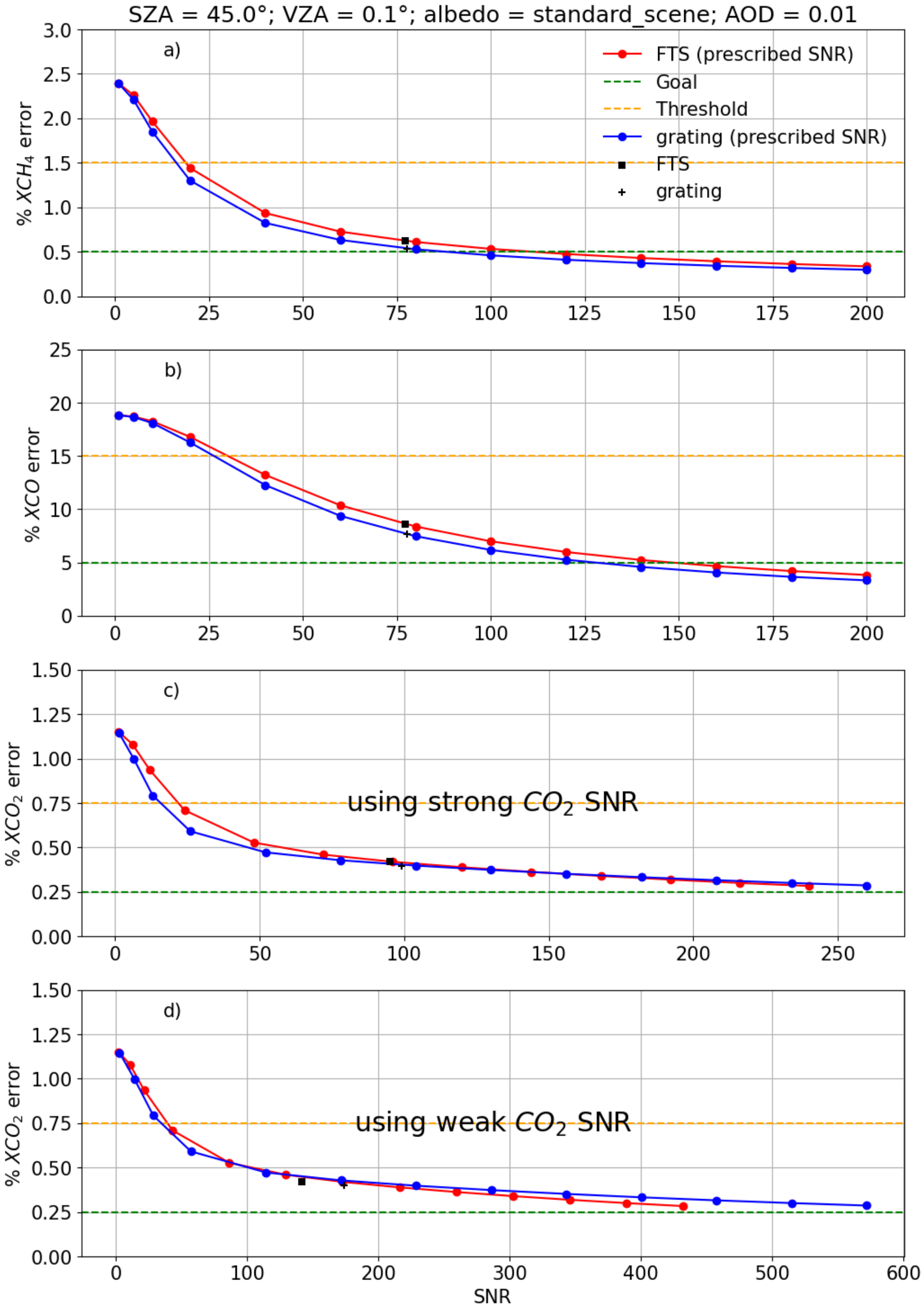

Figure 6.7: Precision vs. SNR for the standard scene described in the text for (a) XCH_4, (b) XCO, (c) XCO_2 using the strong window SNR, and (d) XCO_2 using the weak window SNR. Continuous curves use a prescribed SNR model, and black markers use the actual instrument characteristics.

6.2.1.2 All scenes

In this section, we investigate how the instrument precision and accuracy would vary above different scenes.

Figure 6.8 to 6.19 present results from retrievals using the real noise models, such that each point corresponds to the black markers from Figure 6.7. For each of the 216 scenes obtained from Table 6.2 and 6.3 and for both instruments, an ensemble of 20 retrievals is run. The difference between retrievals in each ensemble (for a given scene) only comes from a newly generated random noise. In all the figures of Sect. 6.2.1.2, each point shows the average accuracy or precision from one of these ensembles of retrievals.

The results shown in Figure 6.8 to 6.19 come from retrievals using the exact same a priori state vector that was used to generate the pseudo-observation spectra. Thus, the variability only comes from the added noise. The accuracy shown in Figure 6.8 to 6.13 is centered on zero and highlights the spread on accuracy in an ideal case, which would be superimposed on any accuracy relationship with SNR following a prior offset in concentration. For XCH_4 and XCO_2 and for both the FTS and grating instrument, it happens that this spread is coincidentally close to the mission target goal for accuracy. For CO, the spread is close to 1%, five times smaller than the goal. What cannot be inferred from Figure 6.8 to 6.13 is how that accuracy would evolve with SNR because it is not possible to distinguish between a well-behaved retrieval extracting information from the measurement and a retrieval that relies more on prior information, such as at the lower SNRs or for CO which only presents weak absorption lines. But these show that XCH_4 and XCO_2 would barely meet the accuracy goal, even in the best scenes, simply due to the spread. And prior offsets are likely to be larger than the goal accuracies.

Figure 6.14 to 6.19 present the results for precision. For each gas, the precision at SNR=0 starts above the precision threshold by the design of the a priori covariance matrices as explained in Sect. 6.2.1.1. The precision depends strongly on SZA as SNR is higher at lower SZA. A summary of the number of scenes that match the target threshold and goal precision is shown in Table 6.5.

For XCH_4, all the scenes meet the precision threshold except scenes with old snow albedo, and all scenes at 80° SZA except over forest, grass, or new snow albedo. Only 18/216 scenes meet the precision goal for the FTS, and 27/216 for the grating, at 30° SZA and for the highest albedos. Most scenes below 30° SZA could meet the goal precision.

For XCO, none of the scenes meet the goal precision for both instruments. None of the scenes over old snow meet the threshold, and for the FTS more scenes meet the threshold at 80° SZA than for the grating.

For XCO_2, no scenes meet the goal precision for the FTS, while only scenes at 30° SZA and at the highest albedos meet the goal for the grating. If the goal were 0.5%, all scenes at and below 60° SZA would meet the goal, except over old snow albedo.

Both accuracy and precision results depend strongly on the choice of a priori covariances. Reducing the prior covariance leads to improved precision but reduced accuracy. But unlike precision, the accuracy also depends strongly on the a priori profile offset from the truth. At zero SNR, the accuracy is equal to the offset as all the information comes from the a priori. This can be seen in Figure 6.21 to 6.26 in Sect. 6.2.2 for which noiseless retrievals were run with a priori concentration profiles of CO_2 and CH_4 increased by 2%, and CO by 15%, before running the retrievals. In Figure 6.21 to 6.26, none of the scenes with no radiance scaling meet the goal accuracy for any of the target gases and instruments. And for CO, all the scenes meet the threshold accuracy only because the prior offset is equal to the threshold and accuracy decreases with SNR. It can be argued that a constant offset to the prior profiles is unrealistic, for example for CO_2 a more realistic offset might be 2-5% near the surface, decreasing to ~1% above 5 km, or simply use the true a priori profile plus one or two a priori standard deviations. We could expect the accuracy curves to decrease faster with SNR in that case.

Table 6.5: Number of scenes that meet the threshold and goal precision, out of 216 total scenes.

	Meet threshold		**Meet goal**	
	FTS	**Grating**	**FTS**	**Grating**
XCH_4	153	144	18	27
XCO	173	138	0	0
XCO_2	189	189	0	45

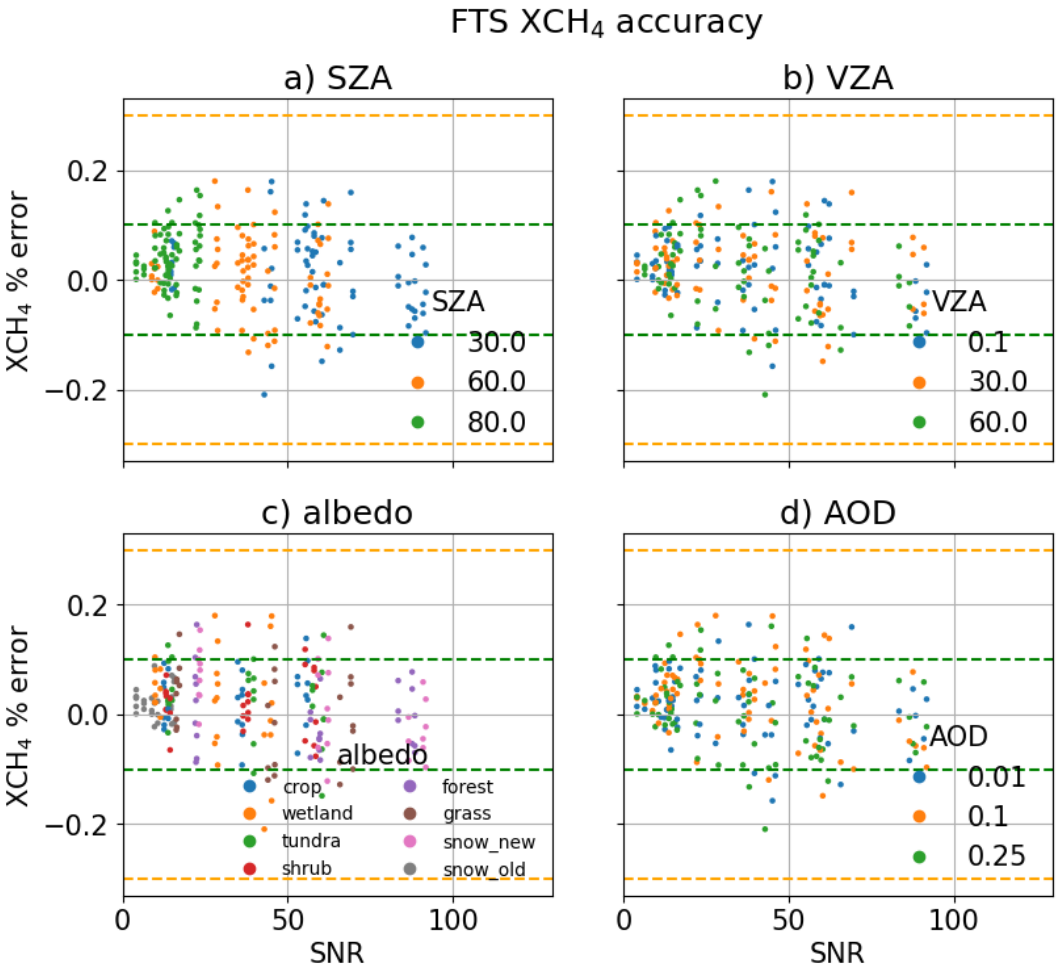

Figure 6.8: XCH$_4$ accuracy vs. SNR for the FTS. Each point is the average accuracy from an ensemble of 20 retrievals. Each panel shows the same points highlighted by a different variable with values indicated by the legends: (a) SZA, (b) VZA, (c) albedo, and (d) AOD. The green lines indicate the mission goal accuracy and the orange lines indicate the threshold.

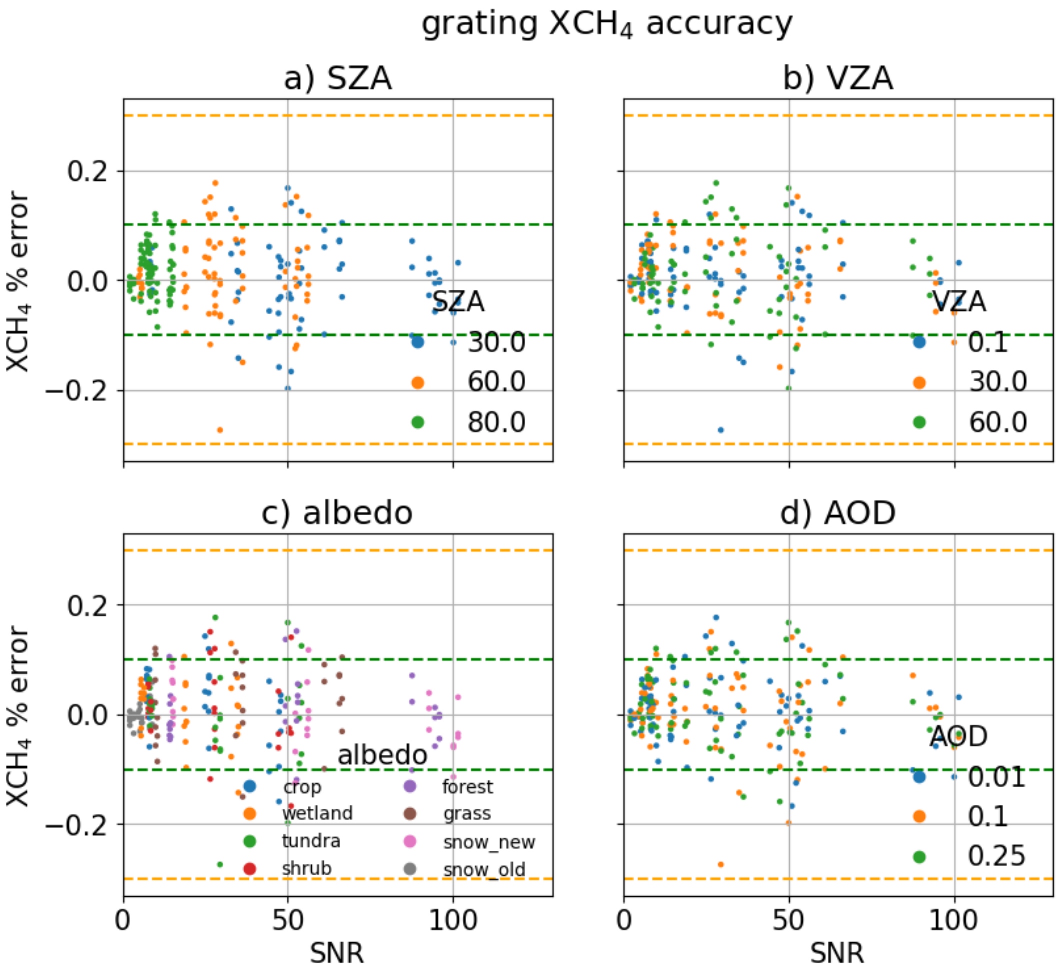

Figure 6.9: Same as Figure 6.8 but for the grating instrument.

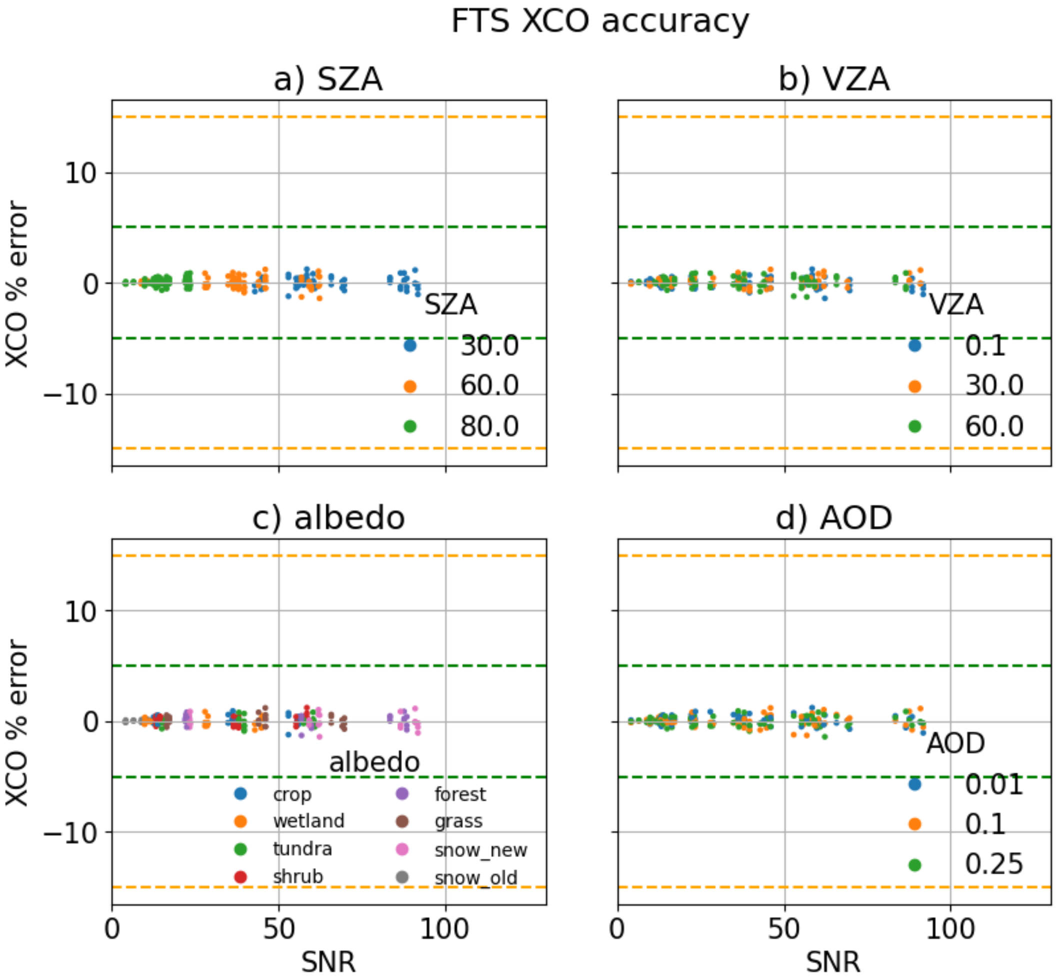

Figure 6.10: Same as Figure 6.8 but for XCO.

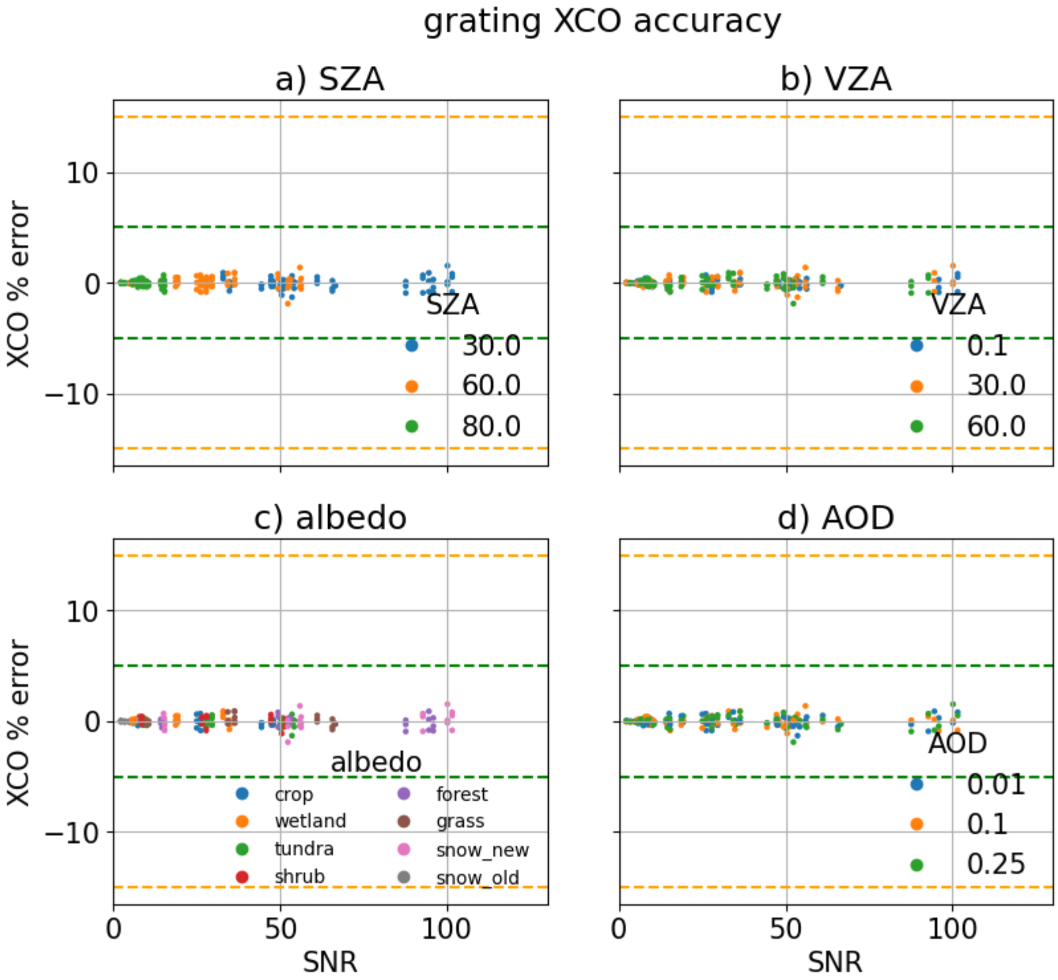

Figure 6.11: Same as Figure 6.8 but for XCO and the grating instrument.

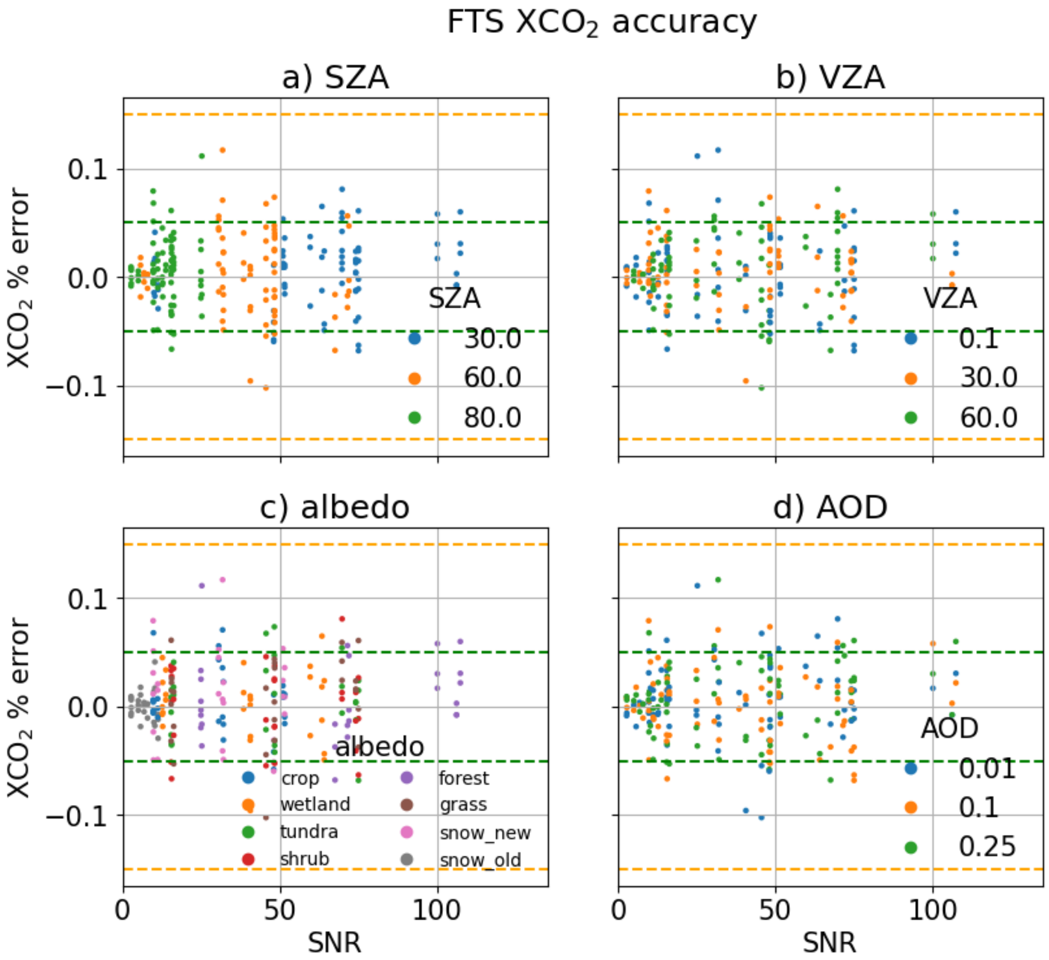

Figure 6.12: Same as Figure 6.8 but for XCO_2.

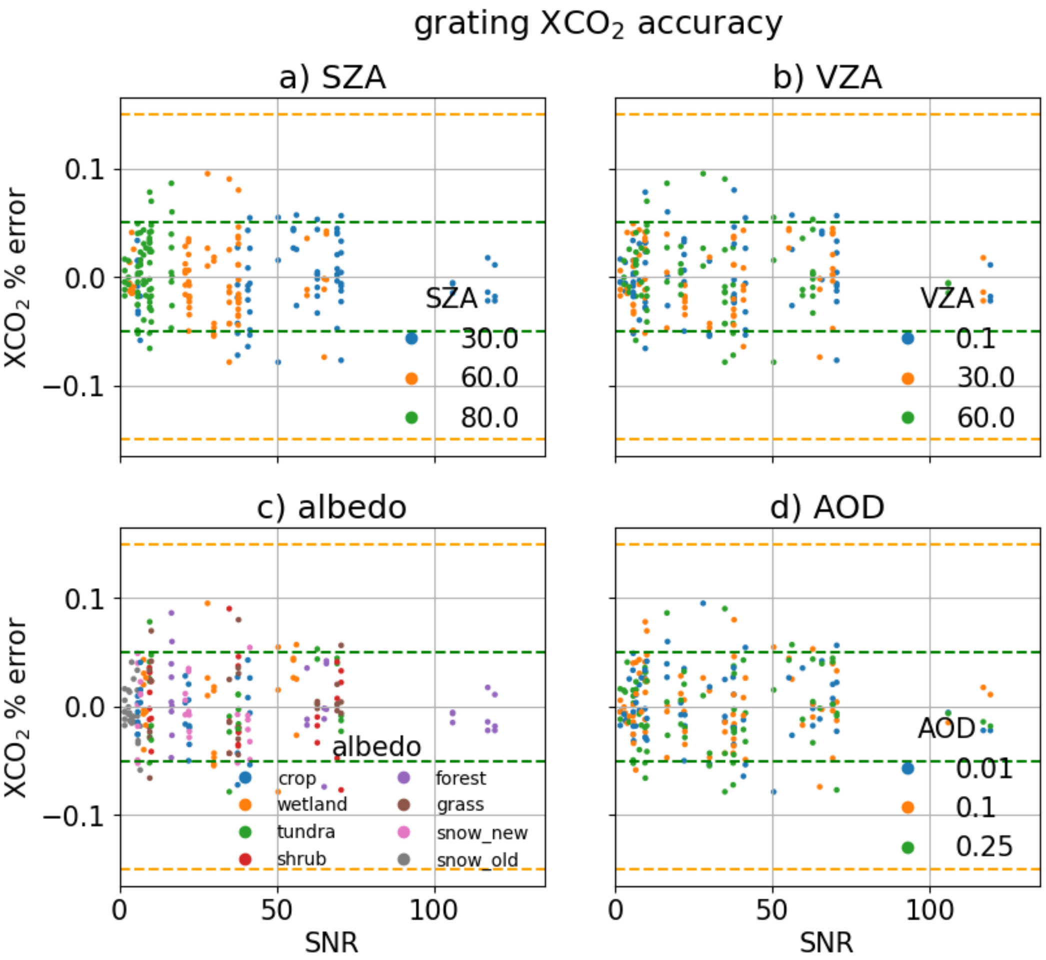

Figure 6.13: Same as Figure 6.8 but for XCO_2 and the grating instrument.

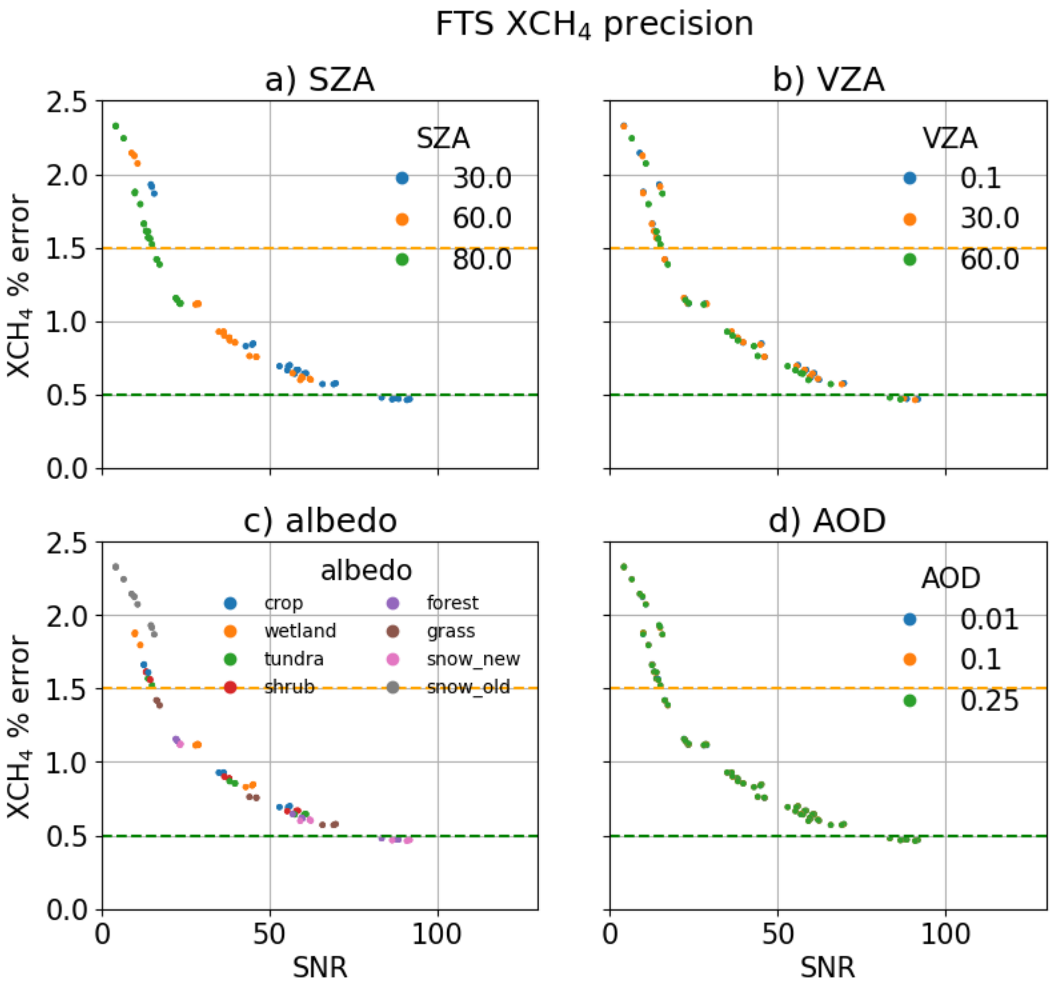

Figure 6.14: XCH$_4$ precision vs. SNR for the FTS. Each point is the average precision from an ensemble of 20 retrievals. Each panel shows the same points highlighted by a different variable with values indicated by the legends: (a) SZA, (b) VZA, (c) albedo, and (d) AOD.

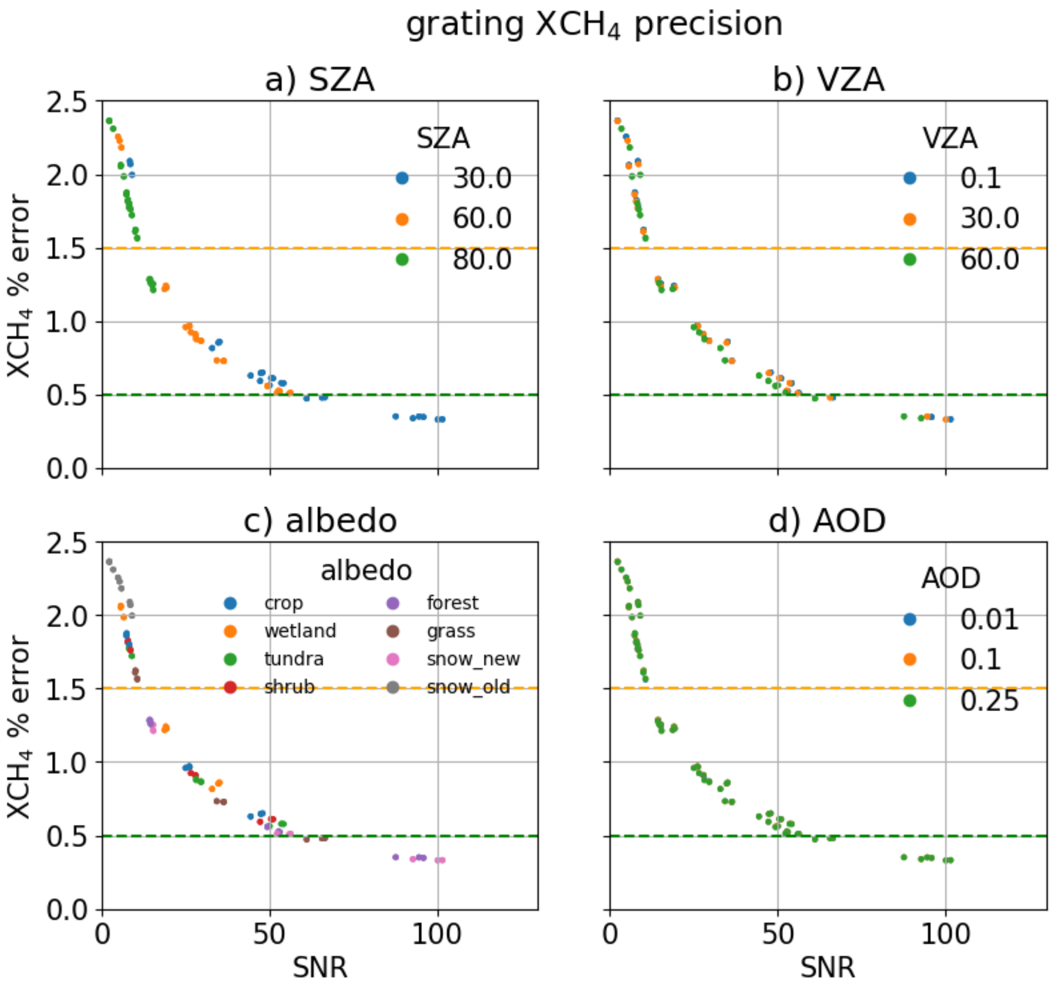

Figure 6.15: Same as Figure 6.14 but for the grating instrument.

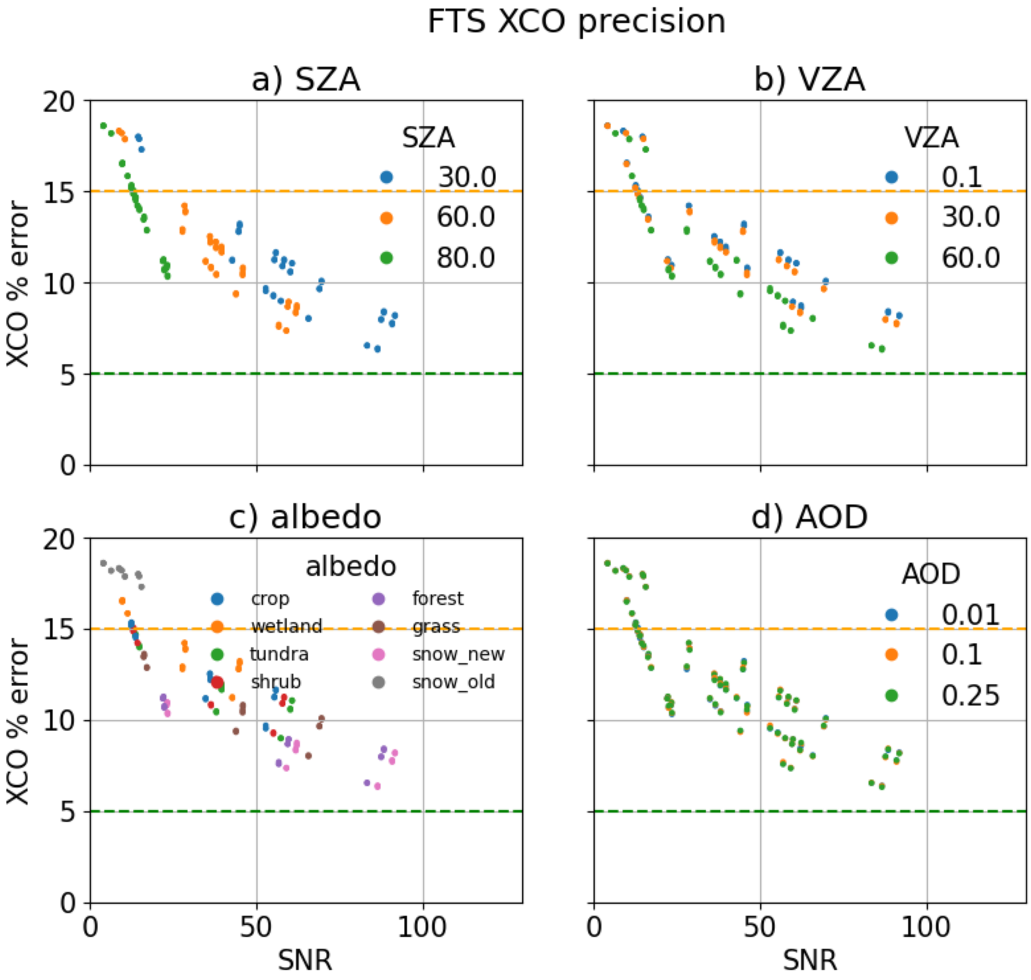

Figure 6.16: Same as Figure 6.14 but for XCO.

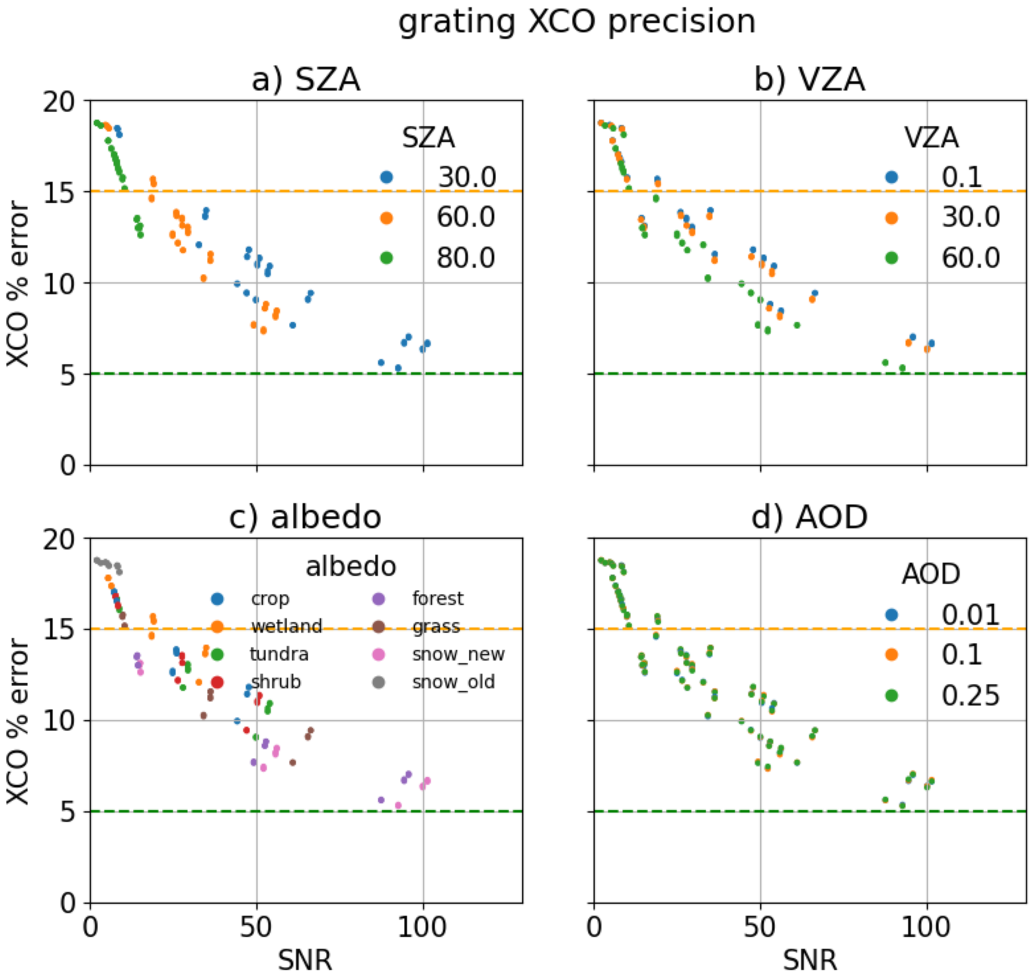

Figure 6.17: Same as Figure 6.14 but for XCO and the grating instrument.

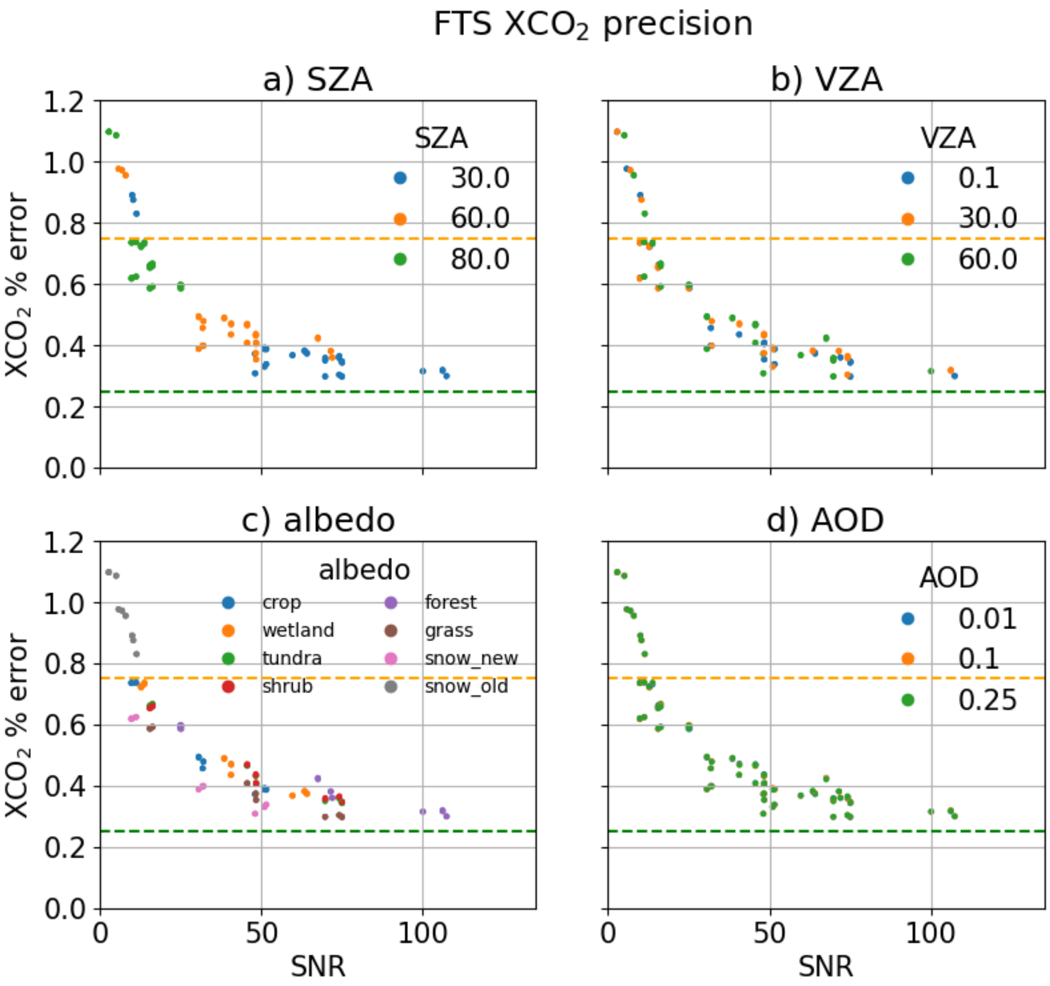

Figure 6.18: Same as Figure 6.14 but for XCO_2.

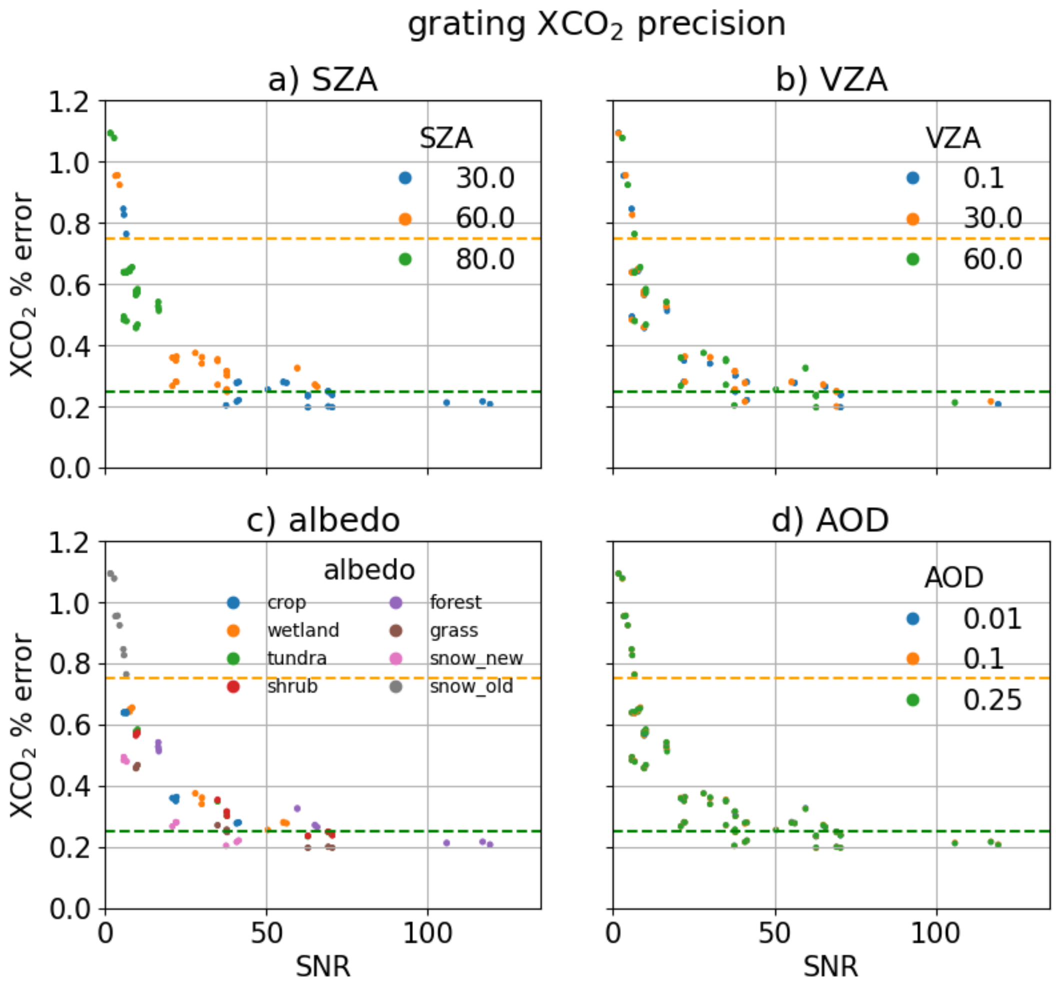

Figure 6.19: Same as Figure 6.14 but for XCO$_2$ and the grating instrument.

6.2.2 Sensitivity to Radiance Scaling

In this section, we investigate the effect of a radiance scaling offset on XCH$_4$, XCO, and XCO$_2$ retrievals. Radiance offsets could arise from errors in the instrument calibration. A new "radiance scaling" parameter was added that scales the radiance of the pseudo-observations by 0.1, 0.3, 1, 3, and 10%.

For each instrument, 1296 pseudo-observation spectra were generated with all combinations of radiance scaling and parameters from Table 6.2. For each scene, the noise model computes the noise variance and uses it to set the diagonal of the measurement covariance matrix, but no noise is added to the pseudo-observation spectra before running the retrievals. In the figures presented here, only one retrieval was run for each scene instead of an ensemble of retrievals. The SNR is always computed using the unscaled radiance, so the relative weight of the measurement and the prior is the same for all radiance scaling values.

Before the retrieval is performed, the a priori CO_2 and CH_4 profiles are increased by 2%, and the a priori CO profile is increased by 15% compared to the profiles used to generate the pseudo-observation spectra.

Figure 6.21 to 6.26 show the accuracy vs. the SNR for all scenes and both instruments. For a given set of inputs, the accuracy does not always increase monotonically with radiance scaling for XCH_4 and XCO_2, and for XCO the errors become smaller for higher radiance scaling. Here the smaller errors for scaled pseudo-observations do not indicate an improvement from the reference case (scaling=1), instead they should be considered as a bias to the reference accuracy. A subset of 30 retrievals did not converge (true for both instruments) for new snow albedo and for radiance scaling values of 3% and 10%, as they reached the maximum number of iterations even after this was raised from 7 to 20, with only one iteration reducing the cost function. In these noiseless retrievals there is no variability caused by changing AOD, so the figures do not include an AOD panel.

Figure 6.27 to 6.32 correspond to Figure 6.21 to 6.26, but without increasing the prior concentration profiles before the retrievals. From these we can see that the scatter in accuracy depends strongly on the radiance scaling, with all scenes within the goal accuracies with radiance scaling smaller than 1%. These figures also show the larger spread in accuracy for retrievals with the grating instrument compared to the FTS. The variability in accuracy for all the scenes considered is relatively small for XCO, with a target goal of 5% and accuracies within 0.1% when using the true profiles (that generated the pseudo-observation) as a priori, except for a radiance scaling of 10%. When using the truth as prior, it is not possible to distinguish a well-behaved retrieval from a retrieval that heavily weights the prior, such as at the lowest SNRs. Panel d) of Figure 6.27 to 6.32 show that accuracy increases monotonically with radiance scaling, except for new snow albedo with 10% radiance scaling.

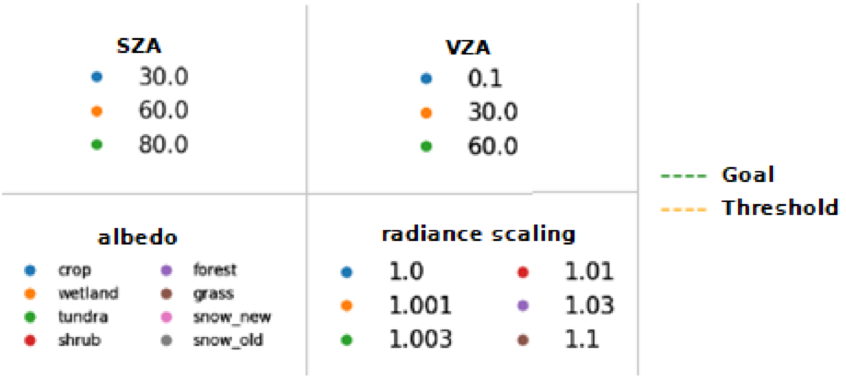

Figure 6.20: Legend for Figures 6.21 to 6.32.

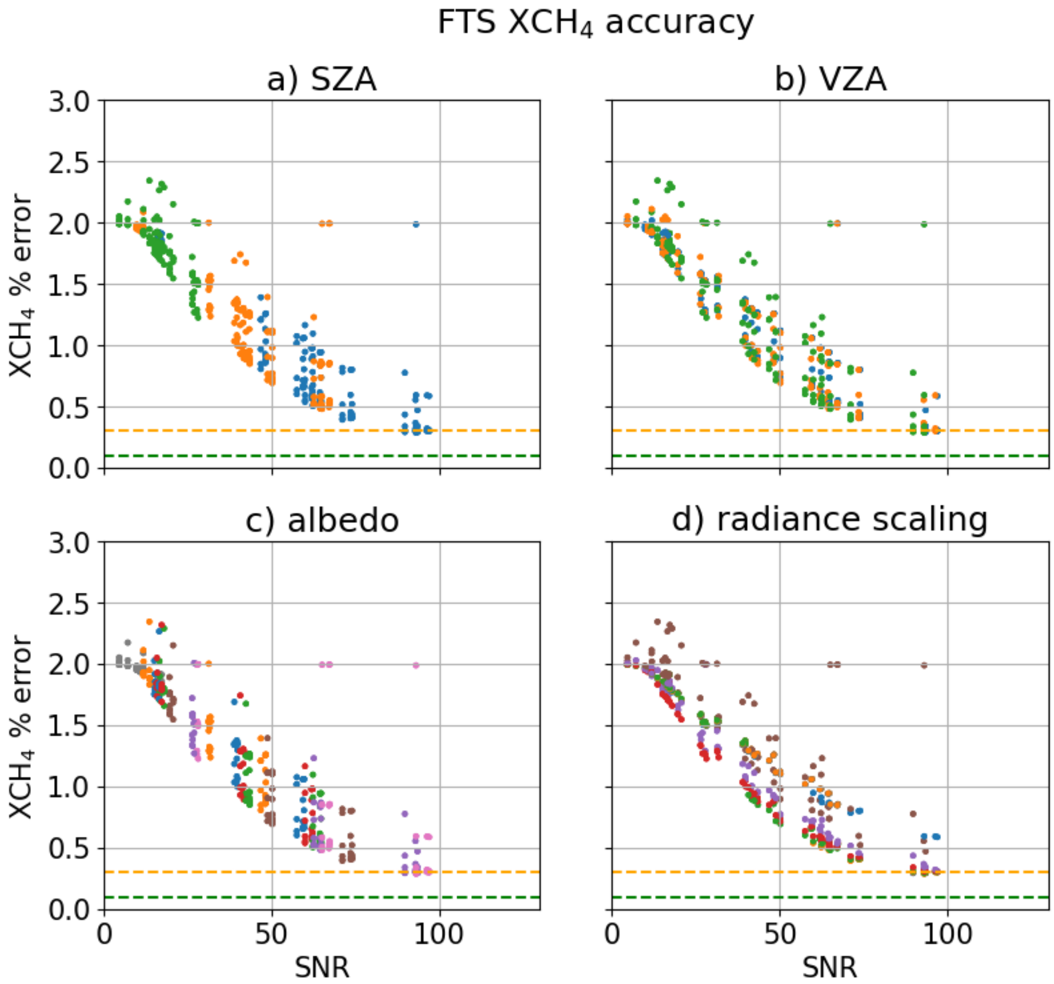

Figure 6.21: XCH_4 accuracy vs. SNR for the FTS, with prior concentration offset. Each panel shows the same points but highlighted by a different input from Table 6.2: (a) SZA, (b) VZA, (c) albedo, and (d) radiance scaling. The legend is presented in Figure 6.20.

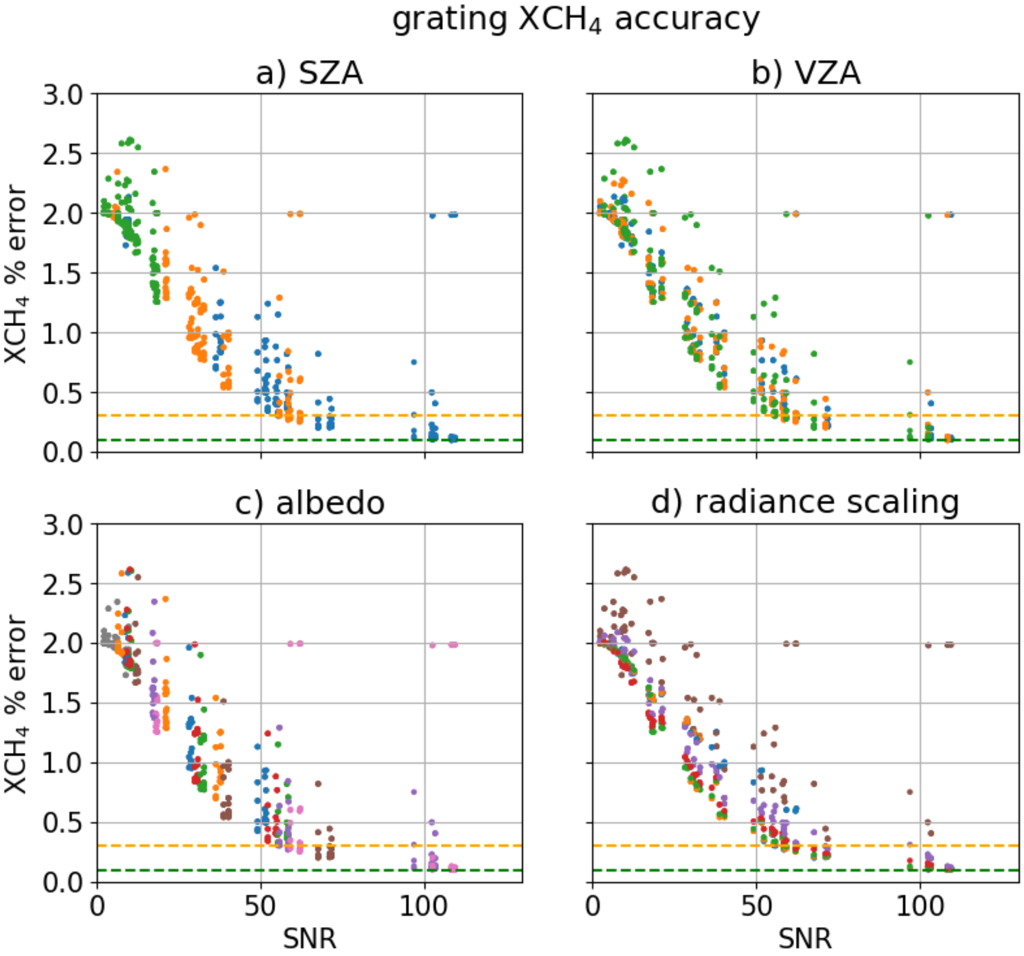

Figure 6.22: Same as Figure 6.21 but for the grating instrument.

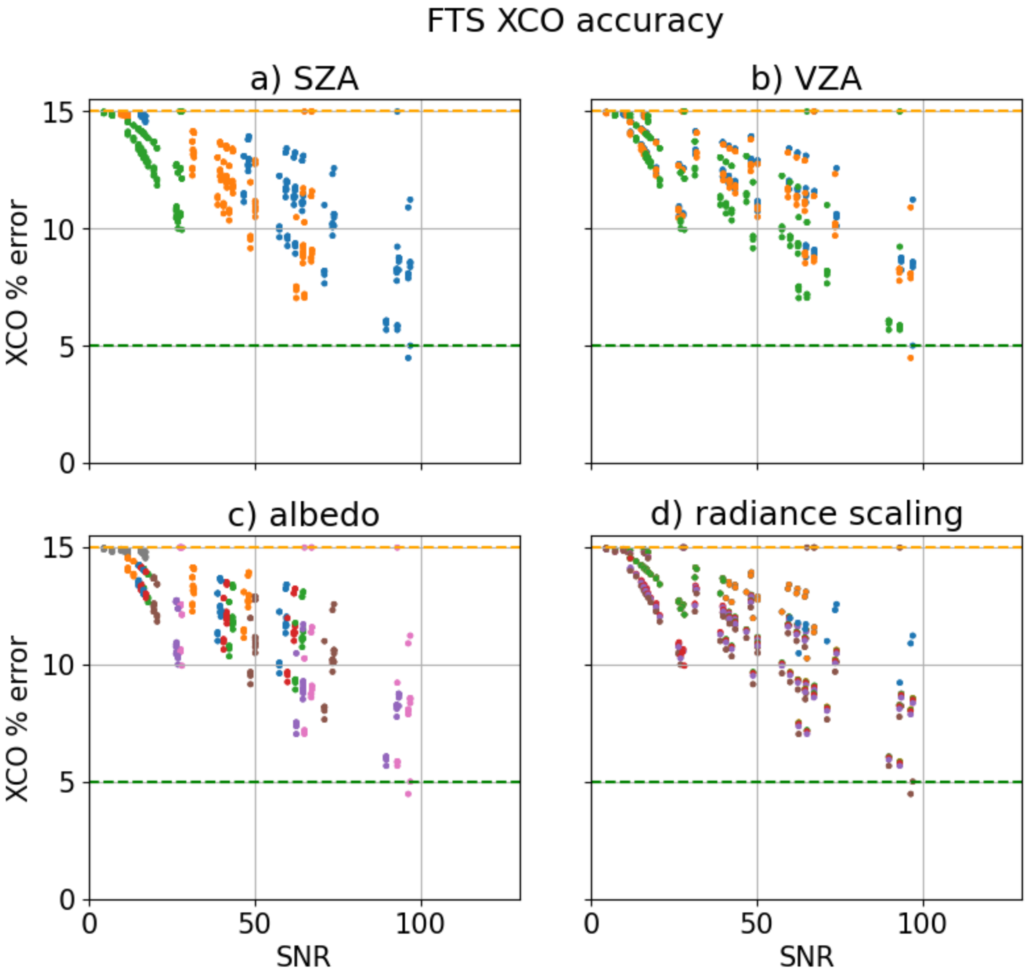

Figure 6.23: Same as Figure 6.21 but for XCO.

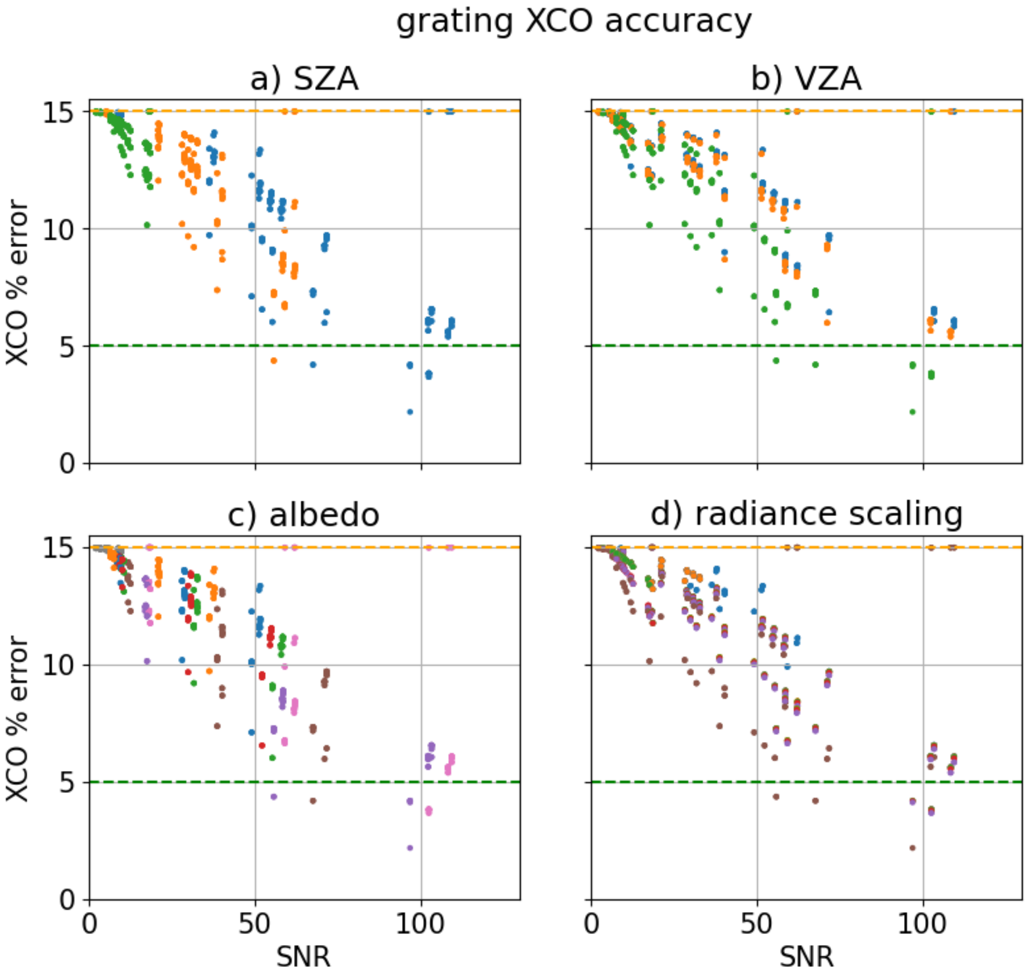

Figure 6.24: Same as Figure 6.21 but for XCO and the grating instrument.

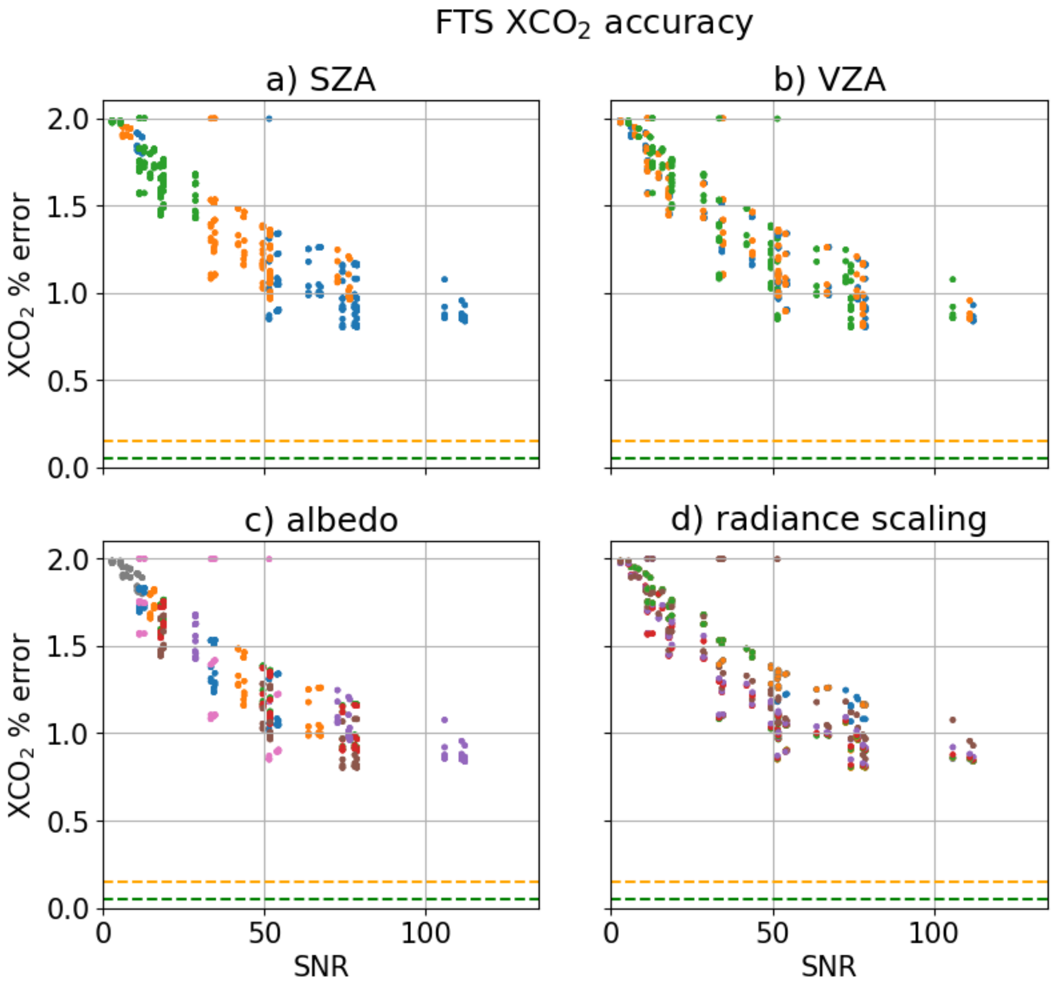

Figure 6.25: Same as Figure 6.21 but for XCO$_2$.

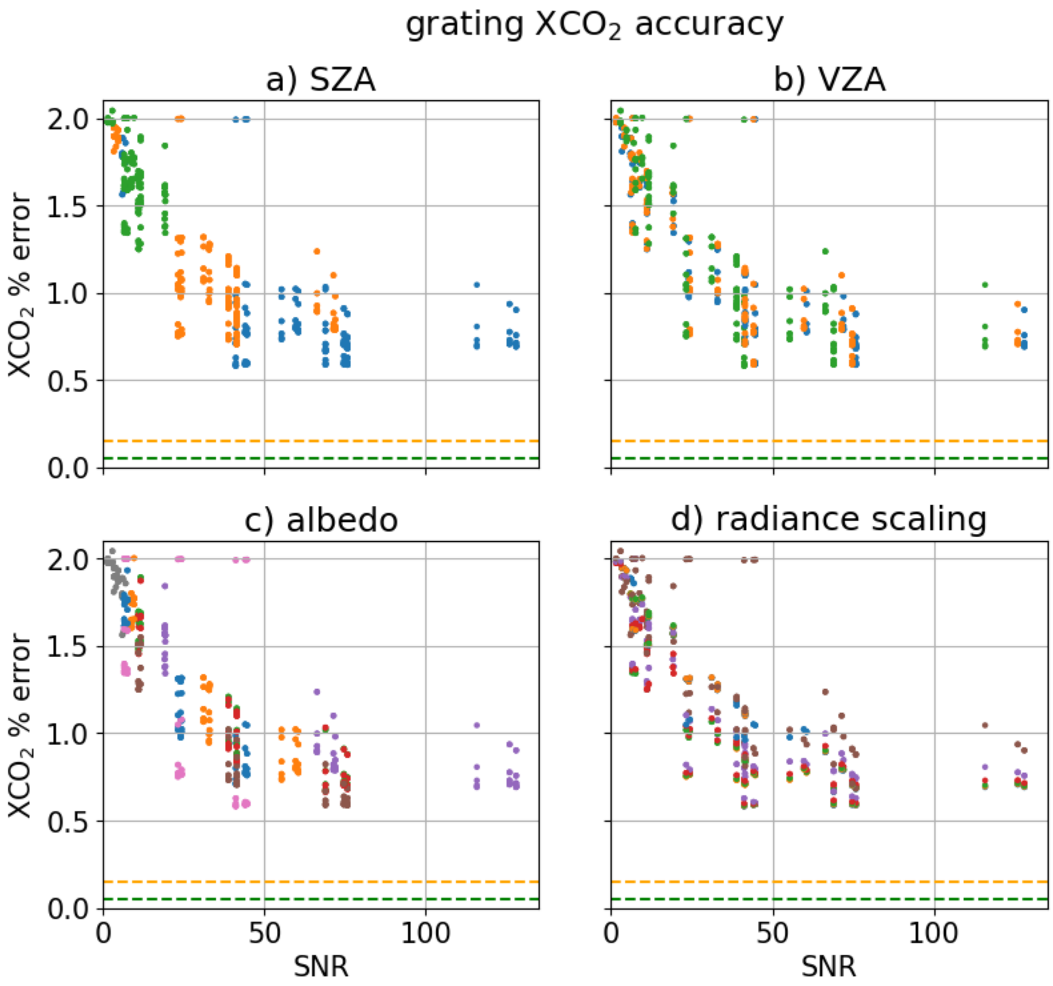

Figure 6.26: Same as Figure 6.21 but for XCO$_2$ and the grating instrument.

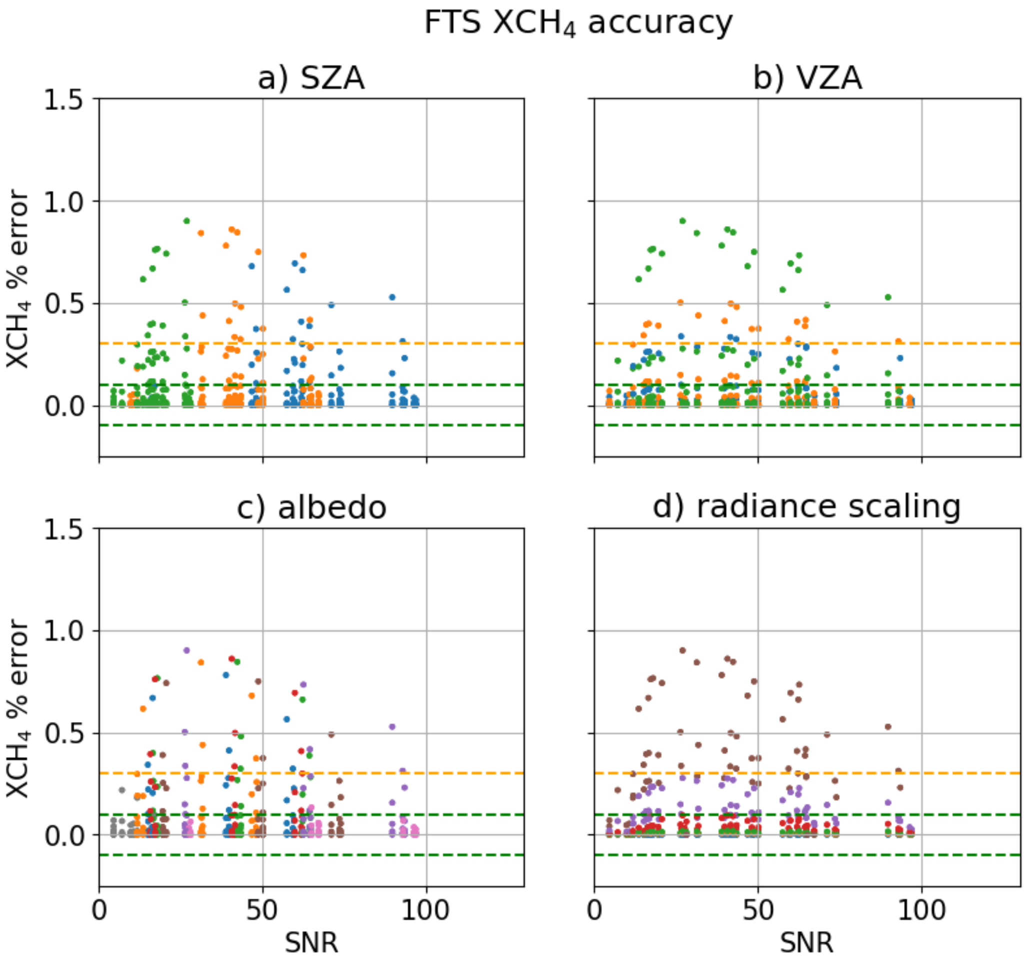

Figure 6.27: XCH$_4$ accuracy vs. SNR for the FTS, without prior concentration offset. Each panel shows the same points but highlighted by a different input from Table 6.2: (a) SZA, (b) VZA, (c) albedo, and (d) radiance scaling. The legend is presented in Figure 6.20.

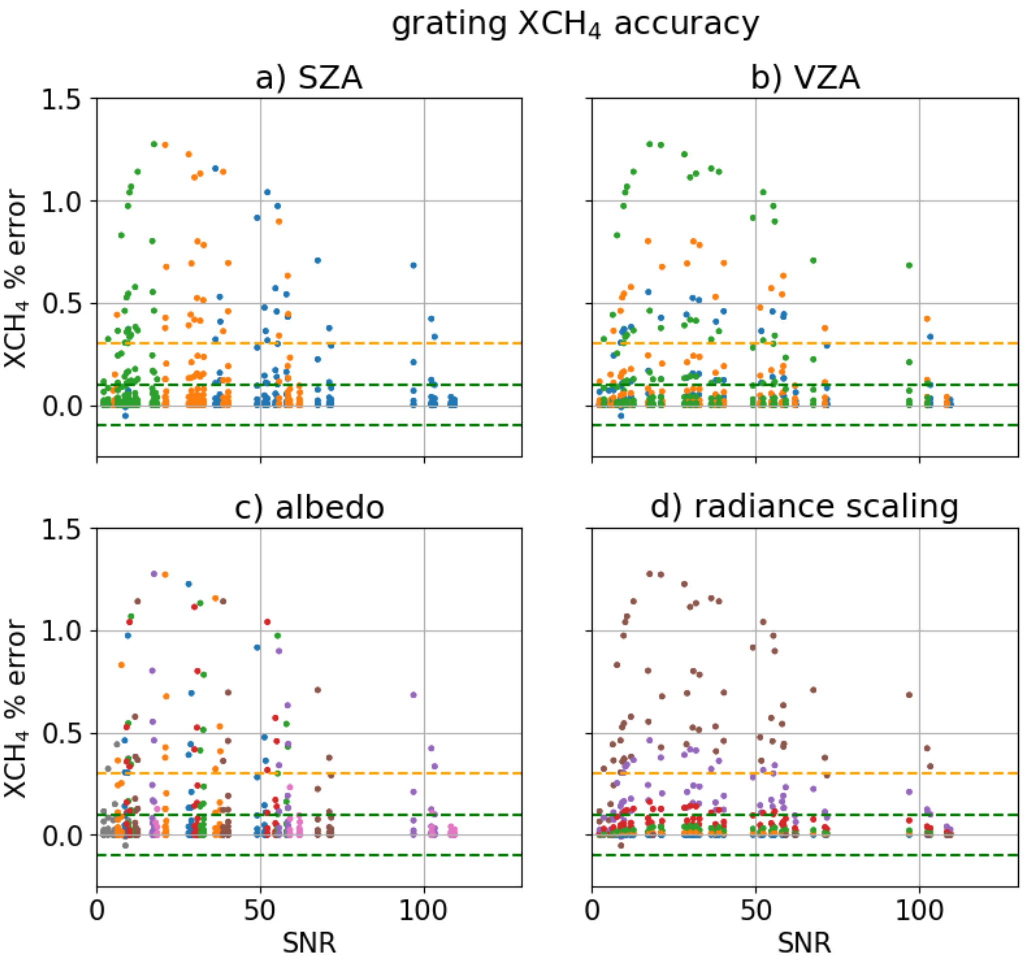

Figure 6.28: Same as Figure 6.27 but for the grating instrument.

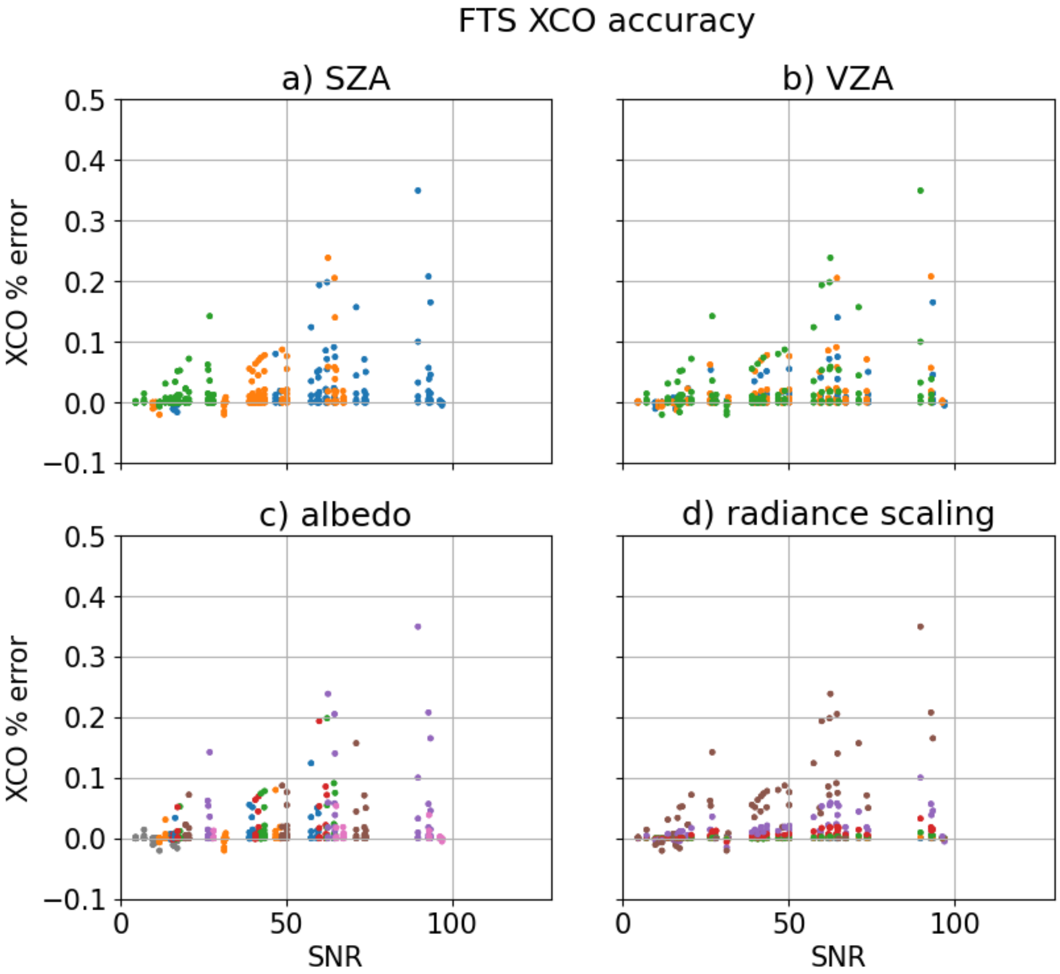

Figure 6.29: Same as Figure 6.27 but for XCO.

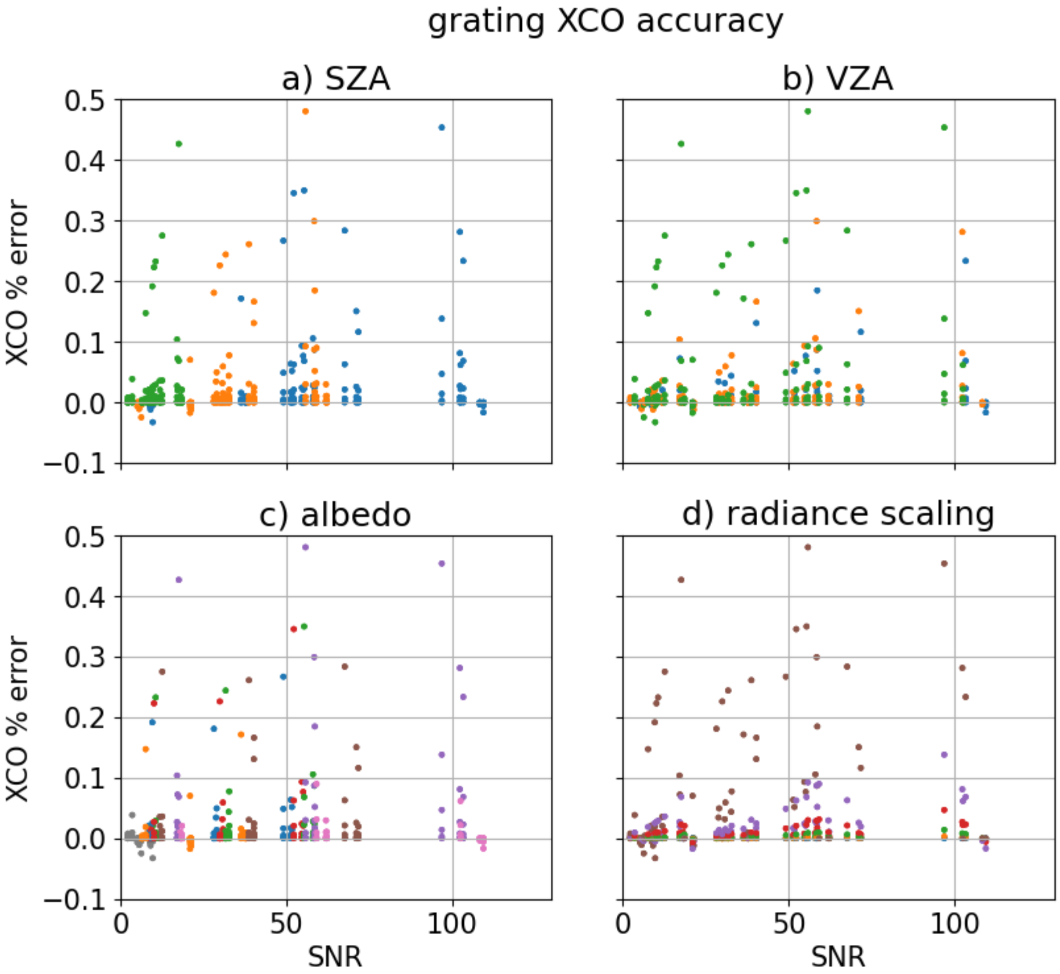

Figure 6.30: Same as Figure 6.27 but for XCO and the grating instrument.

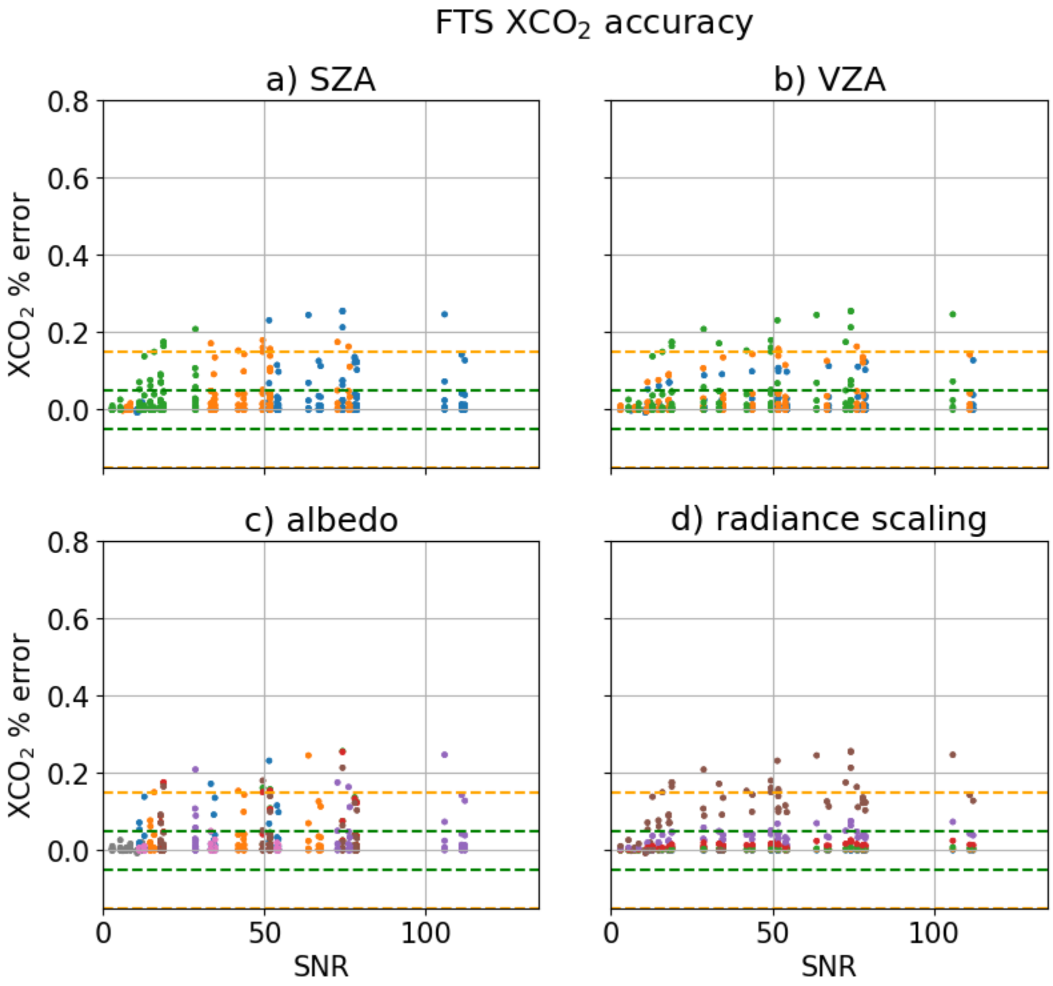

Figure 6.31: Same as Figure 6.27 but for XCO_2.

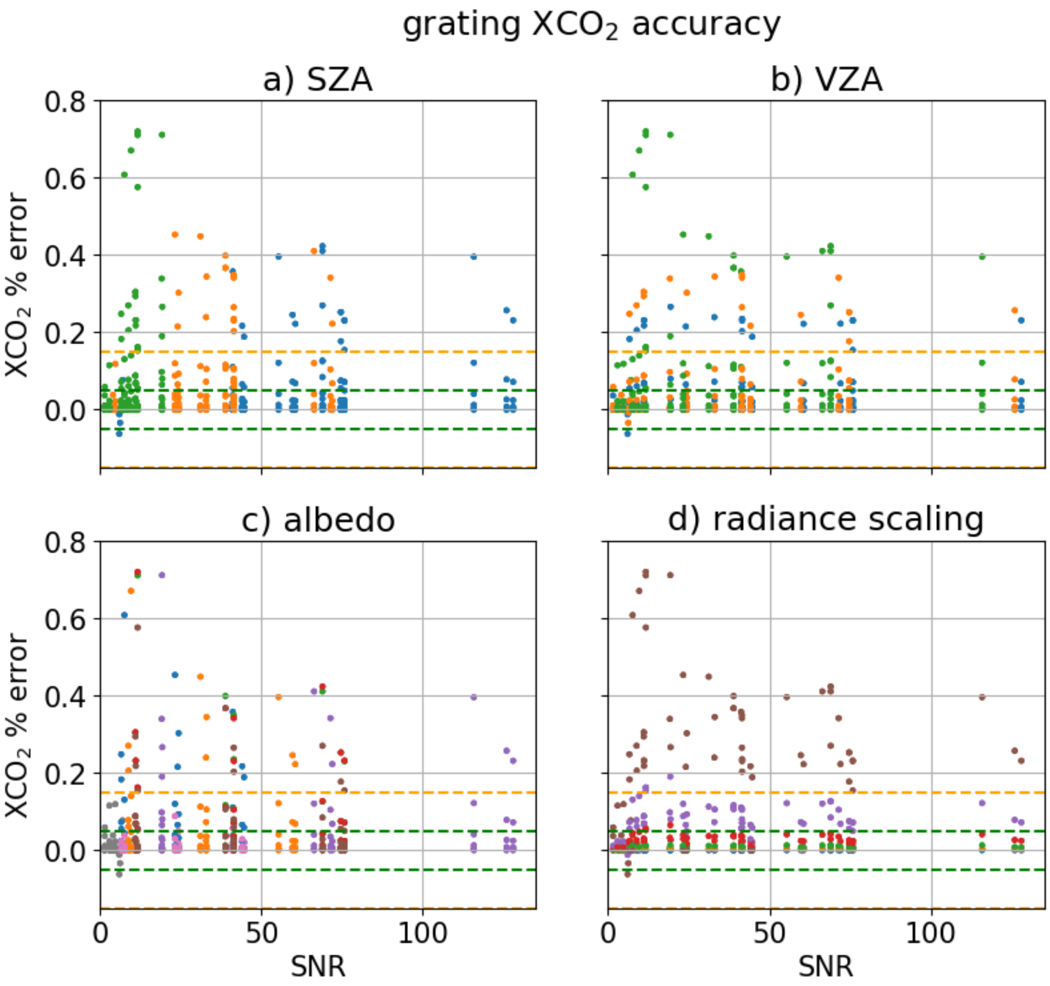

Figure 6.32: Same as Figure 6.27 but for XCO_2 and the grating instrument.

6.2.3 Sensitivity to Surface Pressure

In this section, we investigate the effect of surface pressure offsets on retrievals of XCH_4, XCO, and XCO_2. Kiel et al. (2019) showed that pointing errors of up to 130 arcseconds could cause XCO_2 biases over topography for OCO-2 measurements. A surface pressure error of 1 hPa, which corresponds to an altitude difference of ~8 m at sea level, could cause XCO_2 biases of 0.4 ppm. It is the steepness rather than the actual elevation that is relevant for the pointing offsets to translate to prior surface pressure errors. A mis-pointing of a few arcseconds over topography with steep slopes can lead to large surface pressure errors. The origin of pointing errors will be different for AIM-North's highly elliptical orbit, which is further from Earth and slower compared to a low-Earth orbit like that of OCO-2.

ECCC derived a set of 36 surface pressure offsets over hilly and mountainous terrain and for two pointing errors of 0.72 and 20.6 arcseconds using a digital elevation model over the St. Elias Mountains (Yukon, the tallest mountain in Canada) for the mountains and over the La Cloche Mountains (Ontario) for the hills. 0.72 arcseconds (3.5 microradians) was chosen as an optimistic estimate of the pointing knowledge accuracy that we would hope to achieve from AIM-North over a period of 60 s (after geolocation correction), while 20.6 arcseconds (100 microradians) was arbitrarily chosen. Each pressure offset is associated with a given viewing angle. 288 synthetic spectra were generated for each set of VZA and true surface pressure from Table 6.6 and 6.7 and for four SZAs (30°, 45°, 60°, and 80°). The pressure offsets are defined for three different positions of the satellite on its orbit, and for each of these positions three pressure offsets are considered using the median difference with the true pressure plus one, two, and three standard deviations. The other input parameters are AOD=0.01, and forest albedo (see Table 6.2). Before running retrievals on these spectra, the erroneous surface pressure is used as a priori surface pressure, and the same offset as with the radiance scaling test (Sect. 6.2.2) is applied to the prior concentration profiles: +2% for CH_4 and CO_2, and +15% for CO. Surface pressure is one of the retrieved quantities and its prior uncertainty is set to 4 hPa, the same as used for OCO-2 retrievals. With this prior uncertainty, retrievals will typically not adjust the a priori pressure by more than 10 hPa. When the pressure offset is close to 0 hPa we do not expect an accuracy close to 0, instead we expect the accuracy to be the same as presented in Figure 6.21 to 6.26, with a radiance scaling value of 1.0 and forest albedo. Even though the retrievals are noiseless, the measurement covariance is still set the same way as if noise was added, and so is the relative weight of the measurement to the prior.

The results are shown in Figure 6.33 to 6.38 for each retrieved gas and both instruments. Both XCO_2 and XCH_4 errors decrease as the pressure offset decreases, but there is no clear effect on XCO accuracy. This could be due to the CO absorption lines being much weaker than the XCH_4 lines and thus less affected by a pressure offset, or because most of the differences caused by the pressure offsets are compensated by adjustments to the CH_4 lines rather than CO.

Figure 6.39 to 6.42 show the results for retrievals without applying an offset to the prior concentration profiles for pressure offsets smaller than 10 hPa. Note the accuracy as defined by Eq. 6.6 has a negative value when the retrieved Xgas is smaller than the truth (used to generate the synthetic spectrum). The errors are smaller for the grating instrument compared to the FTS. In both cases, the XCO errors are below the target goal for accuracy (0.5%) even for the largest surface pressure errors. Figure 6.45 to 6.50 correspond to Figure 6.39 to 6.44 but include the full range of surface pressure errors. Table 6.8 shows the surface pressure error below which the goal and threshold accuracies are met for XCH_4 and XCO_2 at SZA=45°. The grating instrument presents a better tolerance to surface pressure error because the retrieval recovers more of the surface pressure offset as shown in Figure 6.51. This could be due to the different SNR in the O_2 window in which the grating SNR is ~1.8 times greater than the FTS SNR. Meeting the target threshold for XCO_2 accuracy requires surface pressure errors smaller than 2.5 hPa for the FTS and less than 7.5 hPa for the grating (at SZA=45°). Such a requirement will make it difficult to obtain good observations over topography without bias correction, even with a 0.72 arcsecond pointing error.

Table 6.6: Viewing zenith angle, true surface pressure ("Truth"), and erroneous surface pressure ("Err") due to a 0.72 arcsecond pointing error over mountains and hills. ΔP is the pressure difference between "Truth" and "Err", and σ is standard deviation.

Terrain	Orbital Location	Case	VZA (degrees)	Truth (Pa)	Err (Pa)	ΔP (Pa)
Mountain	Beginning	Median	21	92592.6	92525.16	-67.44
		Median + 1σ	19.78	90500.96	90385.49	-115.47
		Median + 3σ	21.28	93808.73	93254.15	-554.58
	Middle	Median	18.62	90252.47	90190.86	-61.61
		Median + 1σ	18.19	91698.25	91471.63	-226.62
		Median + 3σ	19.35	92592.85	92232.38	-360.47
	Apogee	Median	39.25	99396.06	99347.78	-48.28
		Median + 1σ	38.73	85989.7	85943.85	-45.85
		Median + 3σ	40.14	89552.37	89272.1	-280.27
Hills	Beginning	Median	23.68	98249.96	98246.56	-3.4
		Median + 1σ	23.72	97757.43	97751.31	-6.12
		Median + 3σ	23.7	98041.71	98025.39	-16.32
	Middle	Median	22.54	97422.85	97419.46	-3.39
		Median + 1σ	22.57	97390.27	97396.01	5.74
		Median + 3σ	22.49	97453.27	97450.42	-2.85
	Apogee	Median	18.18	97661.51	97658.9	-2.61
		Median + 1σ	18.61	96515.29	96516.5	1.21
		Median + 3σ	18.57	96452.5	96459.62	7.12

Table 6.7: Same as Table 6.6 but for a pointing error of 20.6 arcsecond.

Terrain	Orbital Location	Case	VZA (degrees)	Truth (Pa)	Err (Pa)	ΔP (Pa)
Mountain	Beginning	Median	20.81	86557.9	84937.56	-1620.34
		Median + 1σ	20.53	90109.52	86452.09	-3657.43
		Median + 3σ	22.19	96318.75	85344.06	-10974.7
	Middle	Median	19.33	88602.45	87052.48	-1549.97
		Median + 1σ	20.54	93474.12	89803.55	-3670.57
		Median + 3σ	21.13	92255.43	81784.2	-10471.2
	Apogee	Median	41.26	72527.4	70488.33	-2039.07
		Median + 1σ	40.7	97875.91	95172.55	-2703.36
		Median + 3σ	39.63	94928.07	87032.51	-7895.56
Hills	Beginning	Median	23.62	98546.9	98460.31	-86.59
		Median + 1σ	23.73	97721.4	97549.63	-171.77
		Median + 3σ	23.1	97692.26	96988.84	-703.42
	Middle	Median	20.88	98395.51	98310.84	-84.67
		Median + 1σ	22.59	97496.33	97296.28	-200.05
		Median + 3σ	21.45	97898.23	97180.76	-717.47
	Apogee	Median	17.71	98500.17	98432.36	-67.81
		Median + 1σ	18.3	97209.19	96940.6	-268.59
		Median + 3σ	18.47	97066.08	96526.64	-539.44

Table 6.8: Surface pressure errors below which the target goal and threshold accuracies are met for SZA=45°.

(hPa)	XCH_4		XCO_2	
	FTS	**Grating**	**FTS**	**Grating**
Goal	2.5	20	1.25	2
Threshold	7.5	30	2.5	7.5

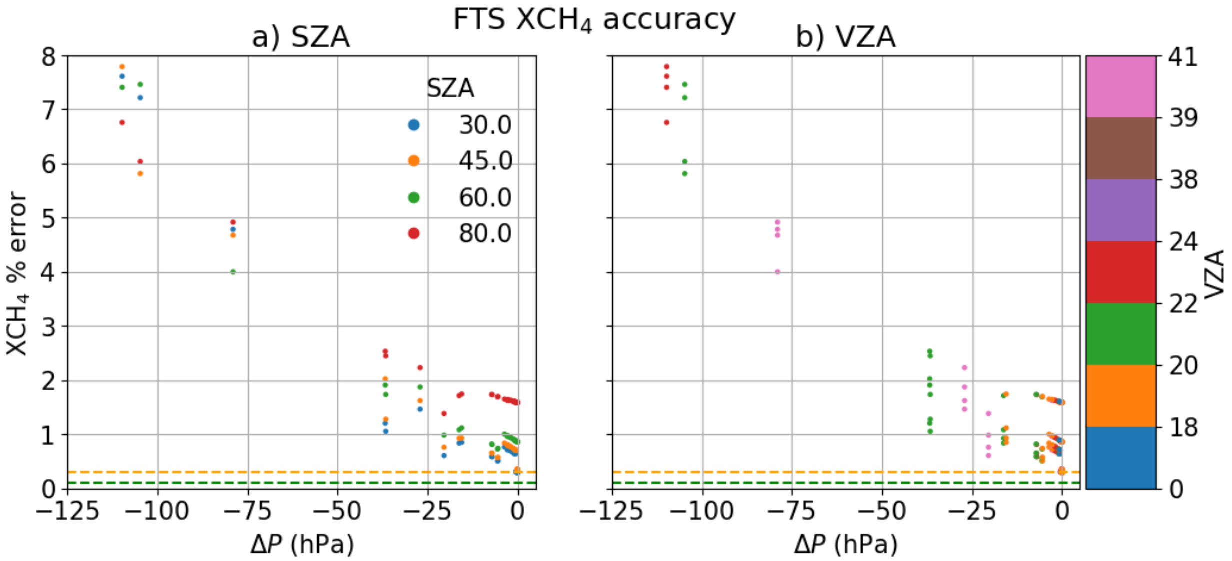

Figure 6.33: XCH$_4$ accuracy vs. surface pressure error for the FTS, highlighted by (a) SZA, and (b) VZA.

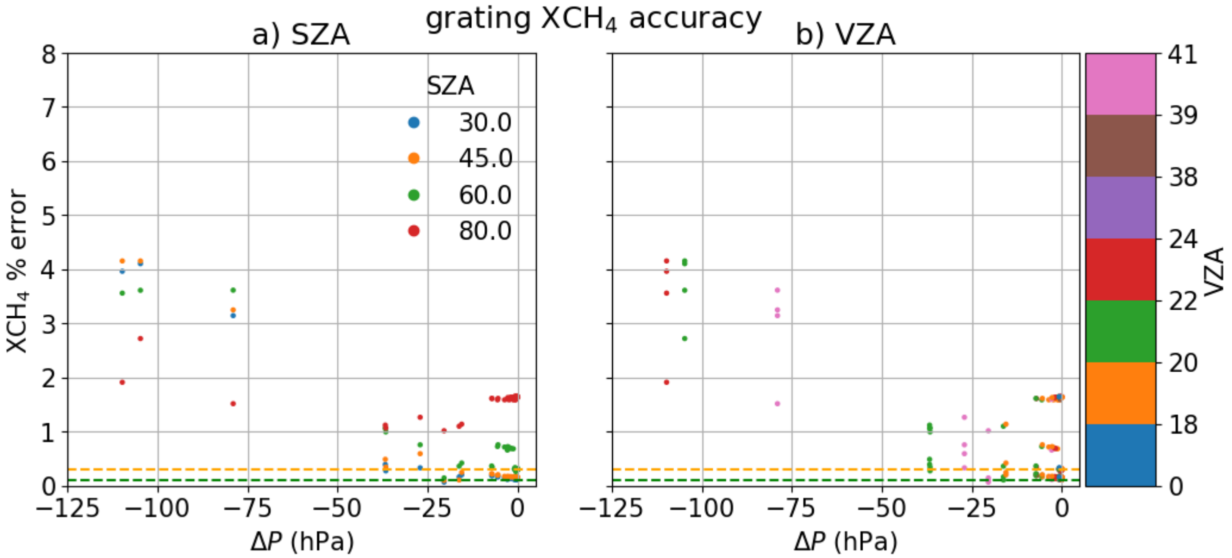

Figure 6.34: Same as Figure 6.33 but for the grating instrument.

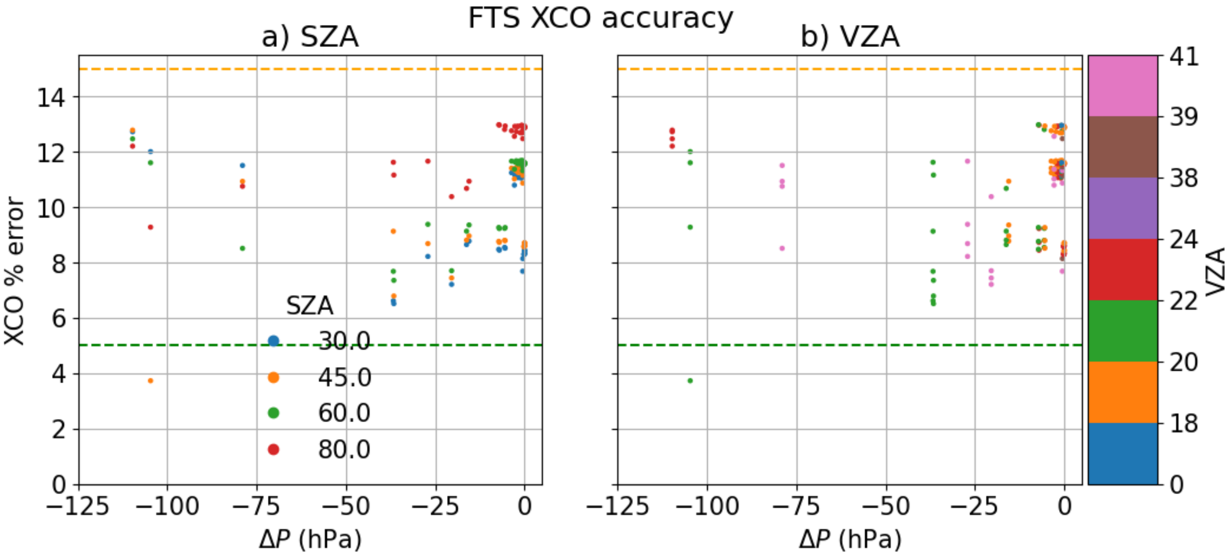

Figure 6.35: Same as Figure 6.33 but for XCO.

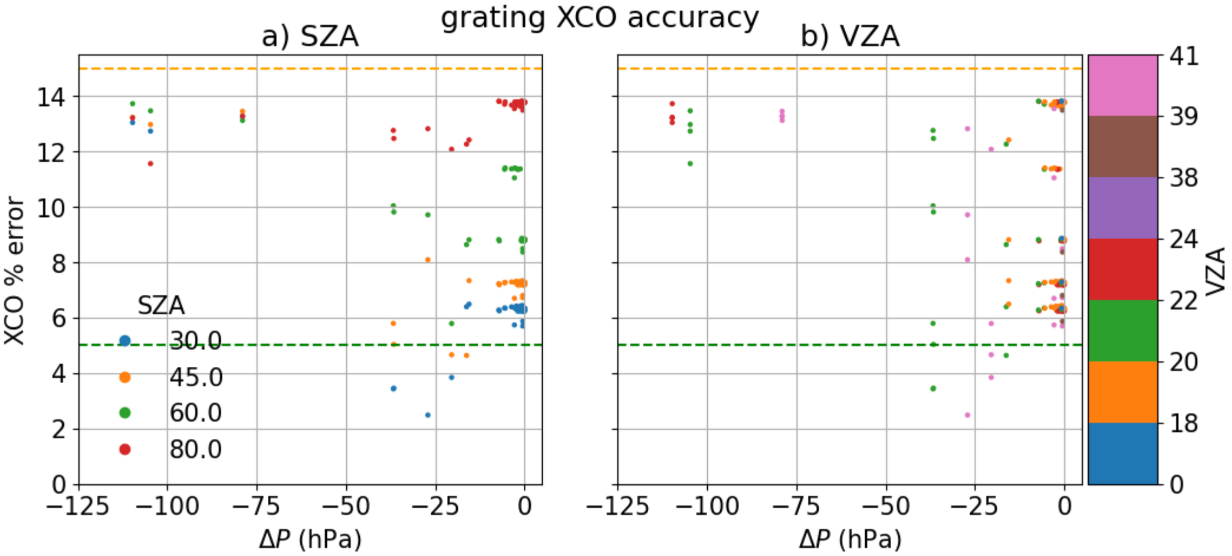

Figure 6.36: Same as Figure 6.33 but for XCO and the grating instrument.

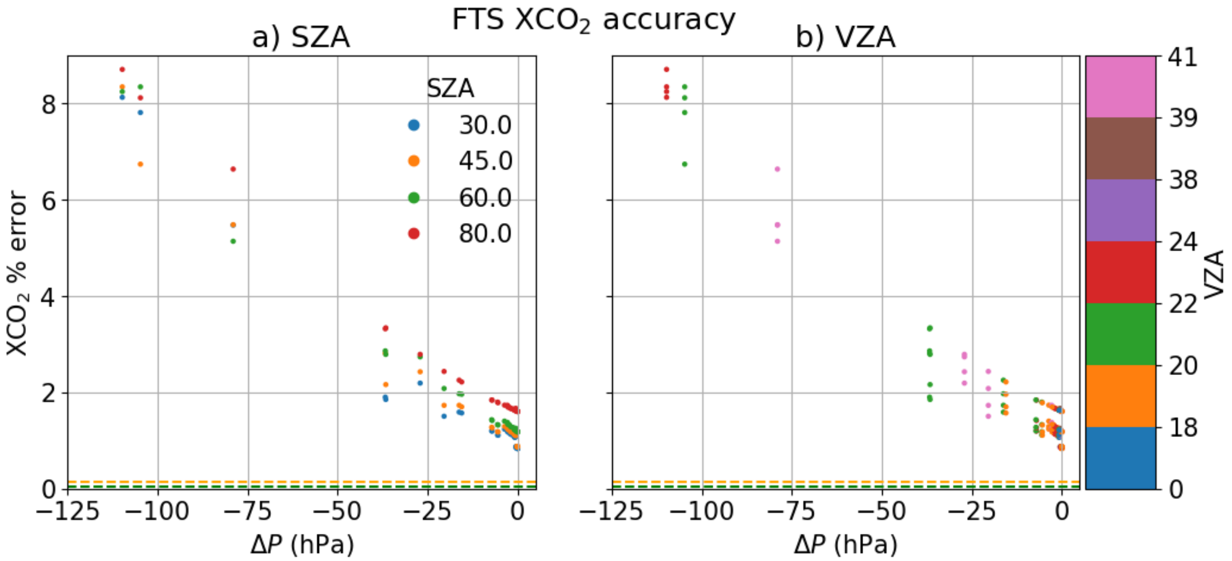

Figure 6.37: Same as Figure 6.33 but for XCO$_2$.

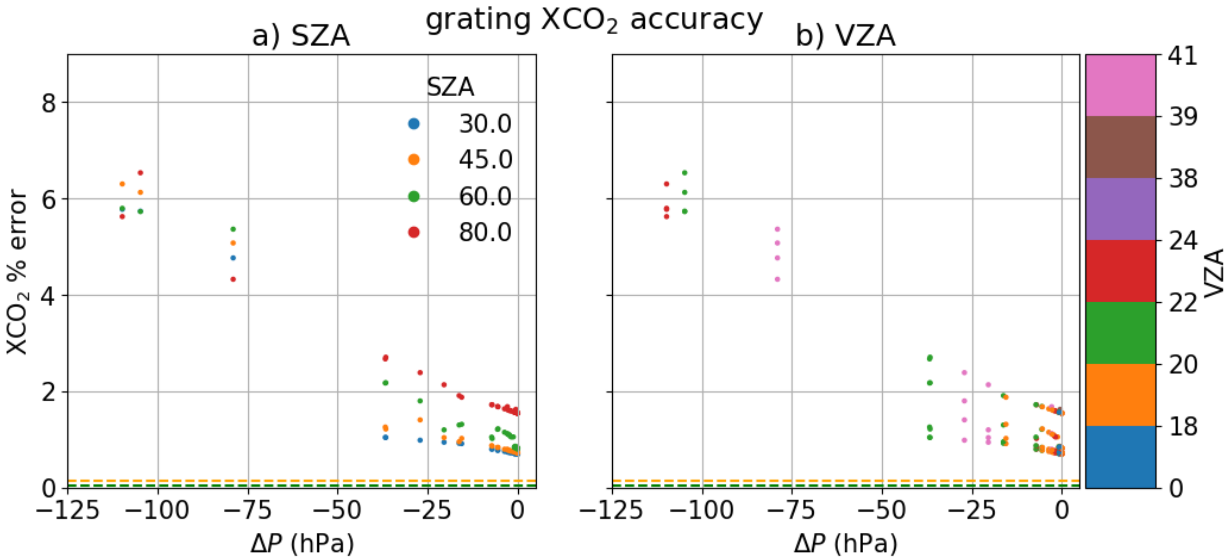

Figure 6.38: Same as Figure 6.33 but for XCO$_2$ and the grating instrument.

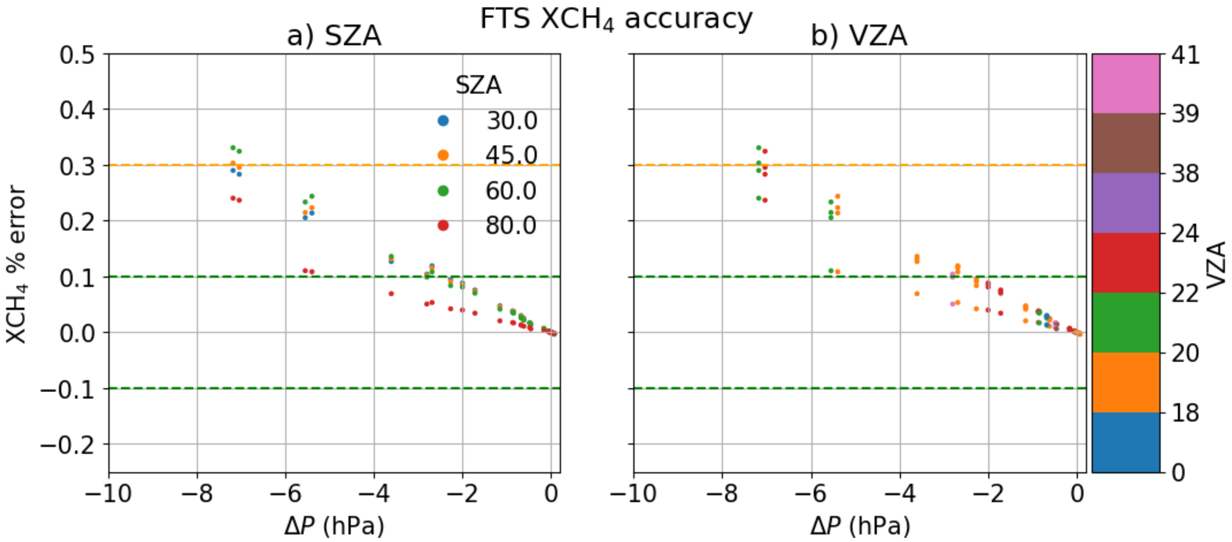

Figure 6.39: XCH4 accuracy vs. surface pressure error for the FTS, highlighted by (a) SZA, and (b) VZA. The a priori concentration profiles were not offset before the retrievals.

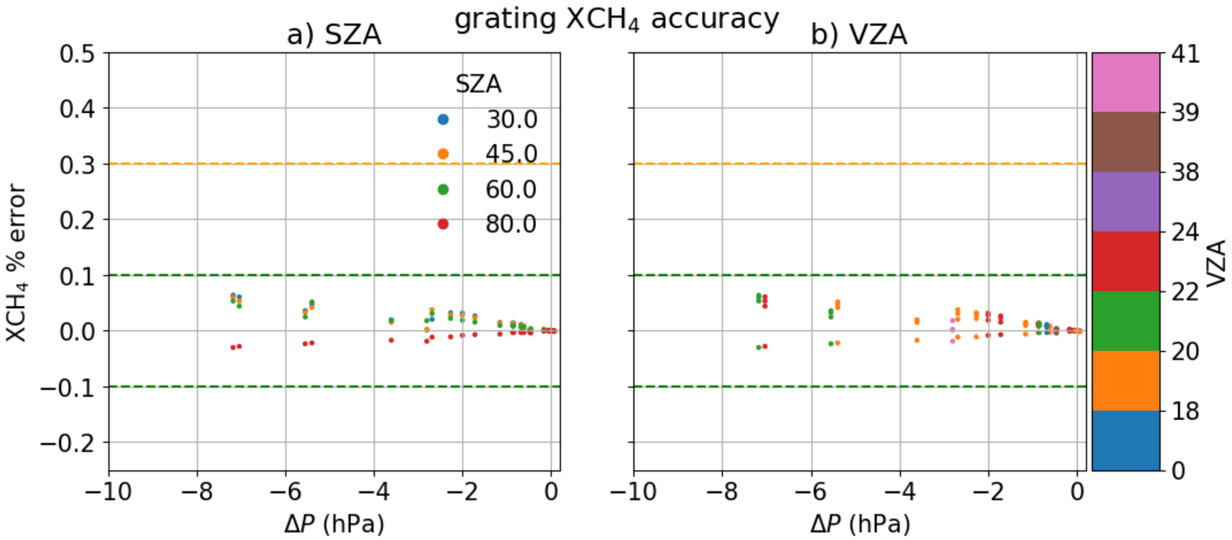

Figure 6.40: Sane as Figure 6.39 but for the grating instrument.

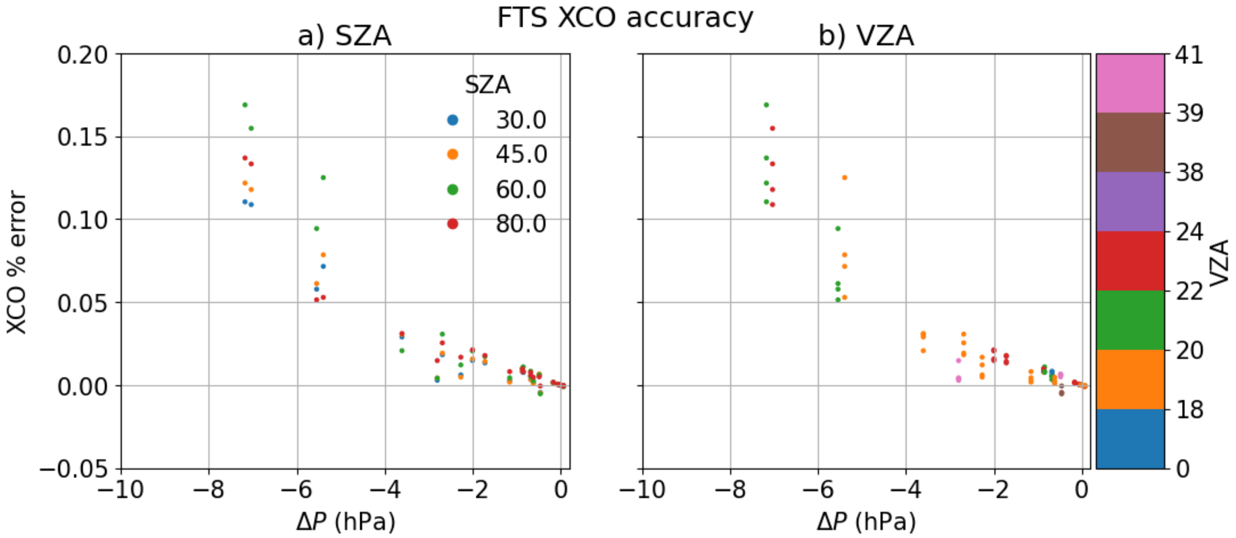

Figure 6.41: Sane as Figure 6.39 but for XCO.

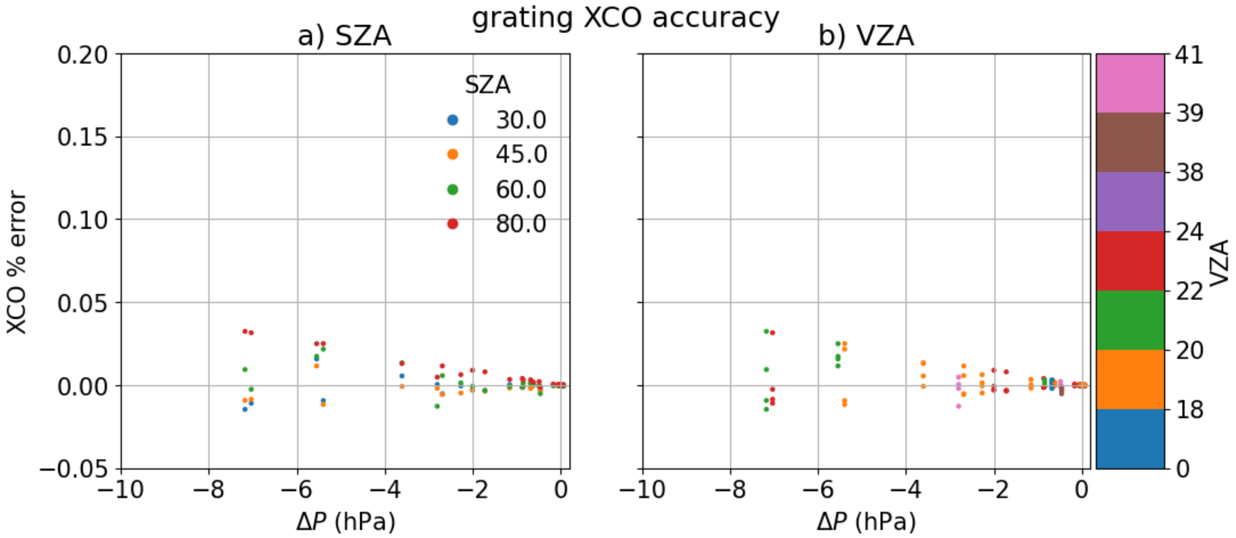

Figure 6.42: Same as Figure 6.39 but for XCO and the grating instrument.

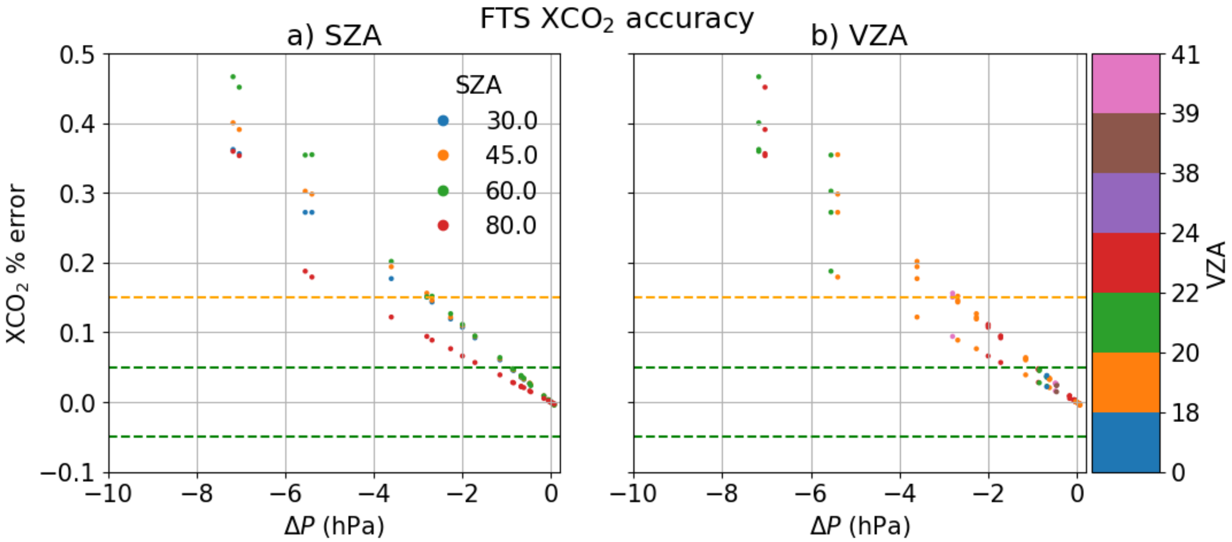

Figure 6.43: Same as Figure 6.39 but for XCO_2.

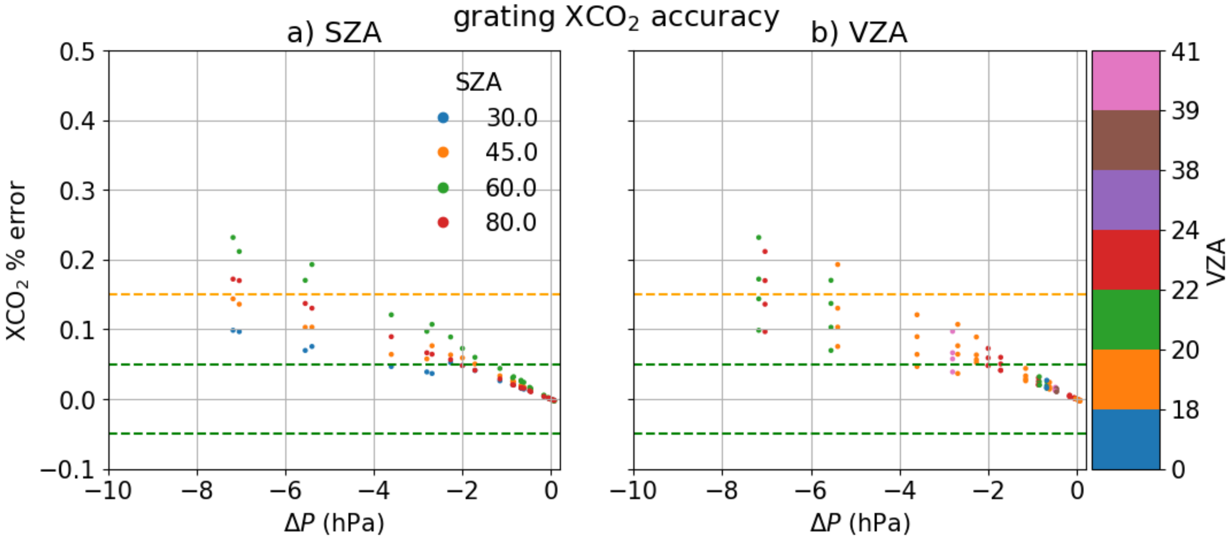

Figure 6.44: Same as Figure 6.39 but for XCO_2 and the grating instrument.

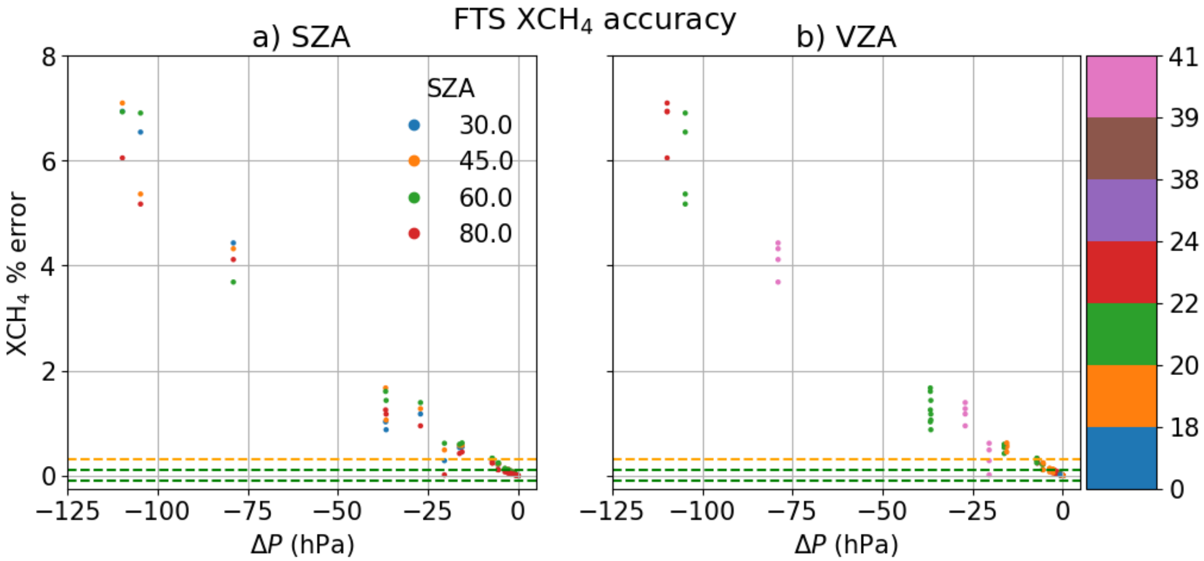

Figure 6.45: Same as Figure 6.39 but including the full range of surface pressure errors.

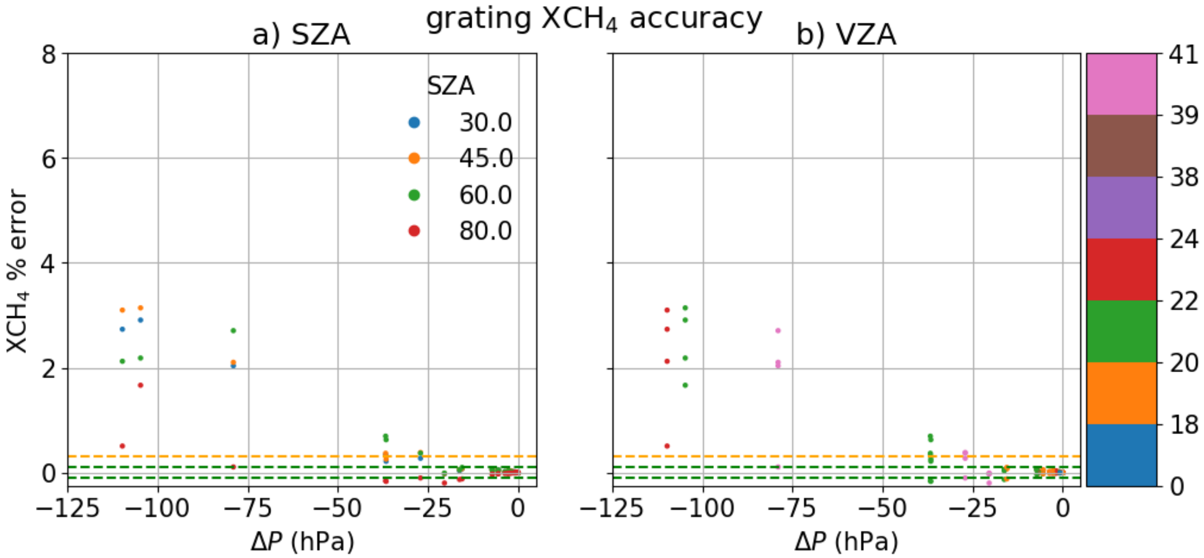

Figure 6.46: Same as Figure 6.45 but for the grating instrument.

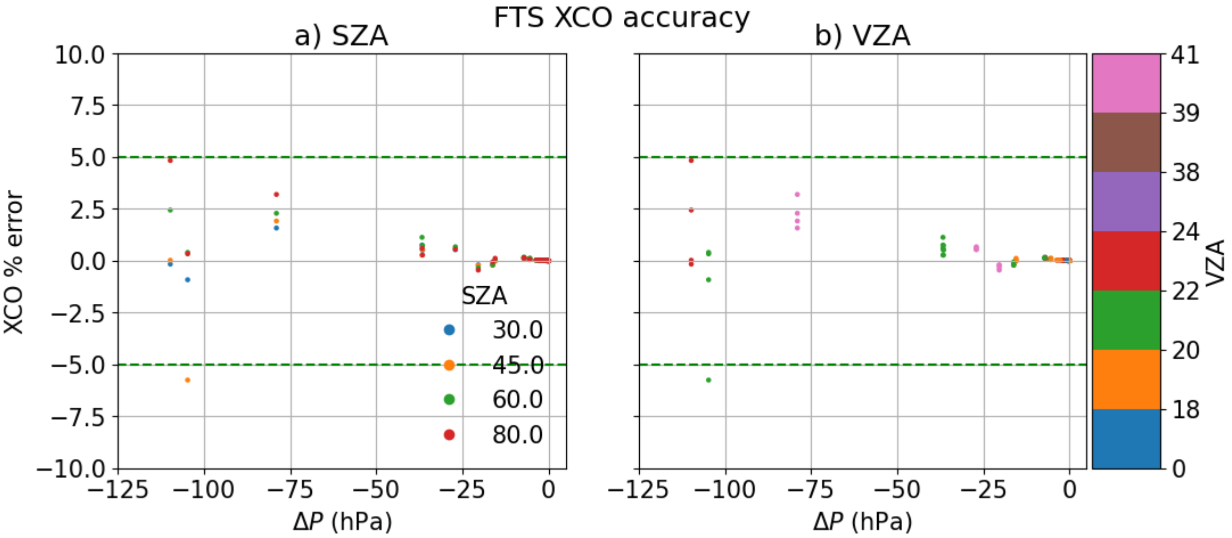

Figure 6.47: Same as Figure 6.45 but for XCO.

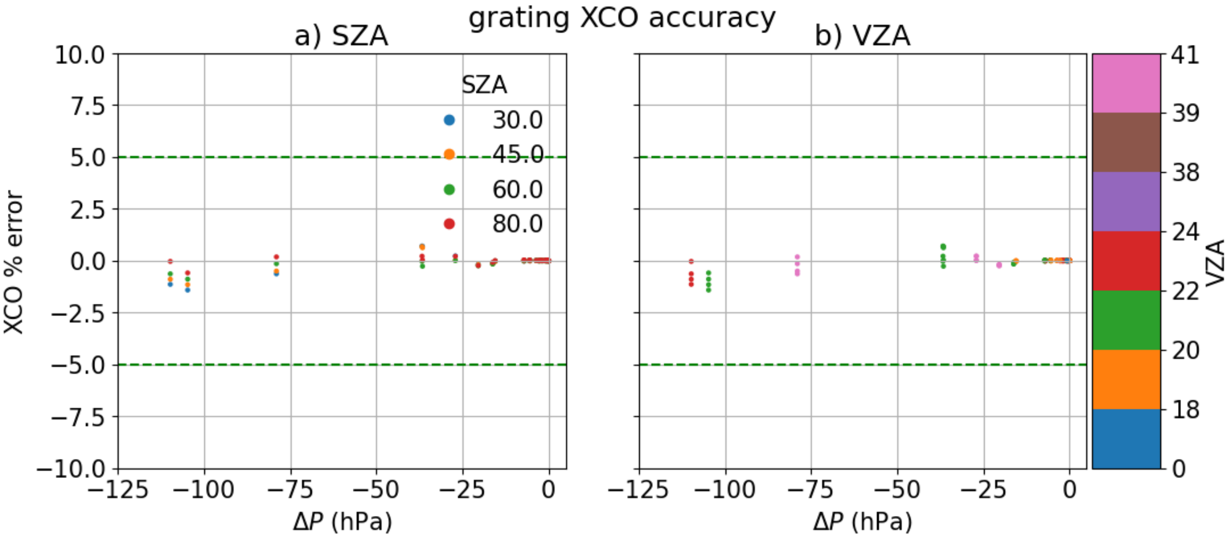

Figure 6.48: Same as Figure 6.45 but for XCO and the grating instrument.

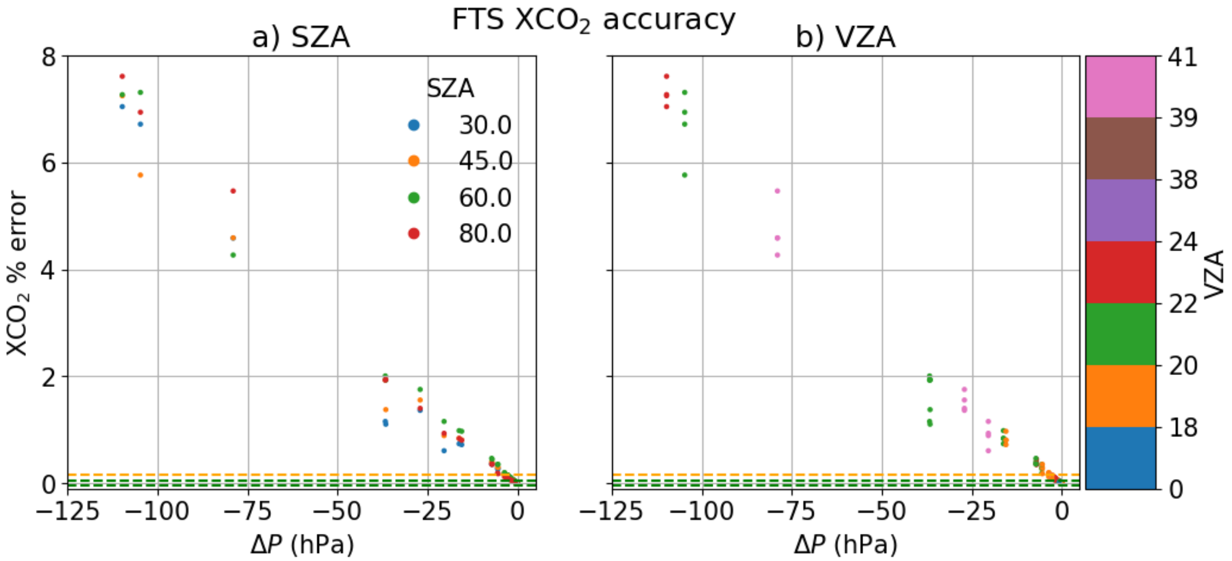

Figure 6.49: Same as Figure 6.45 but for XCO₂.

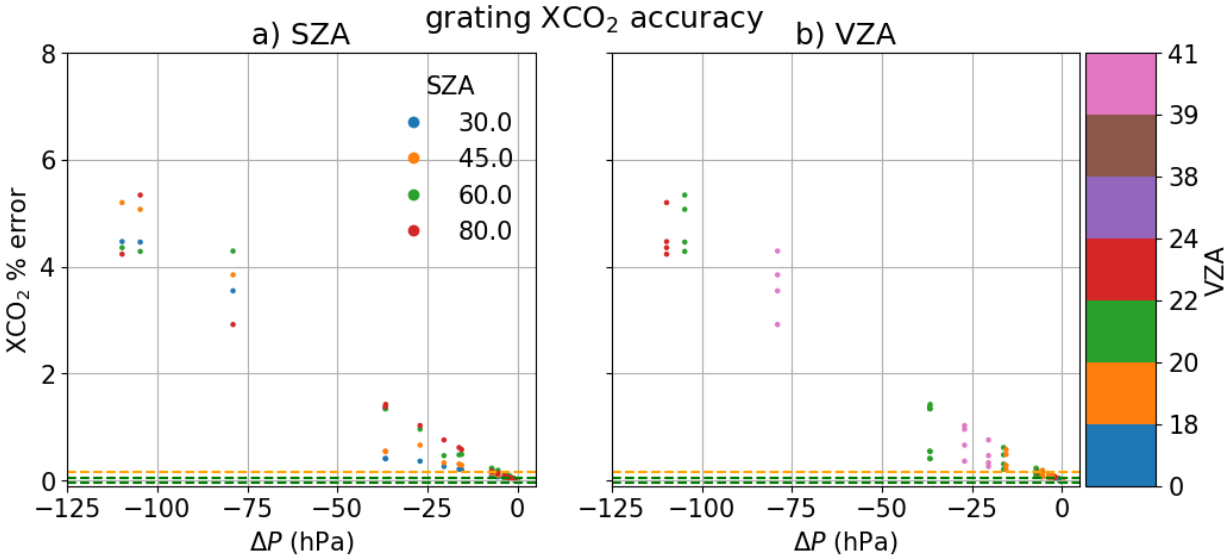

Figure 6.50: Same as Figure 6.45 but for XCO₂ and the grating instrument.

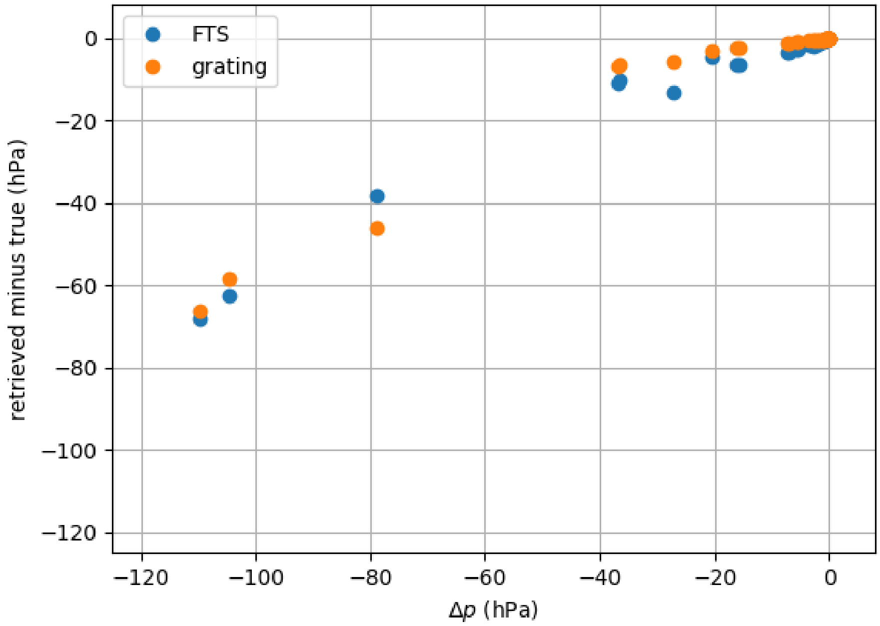

Figure 6.51: Retrieved minus true pressure as a function of the surface pressure offset, at 30° SZA.

6.3 Summary and Conclusions

This work explored the predicted behaviour of the precision and accuracy of the two instruments considered by AIM-North for measuring greenhouse gases. The ReFRACtor retrieval code was adapted to match the instrument design of the AIM-North mission. Sets of synthetic spectra were generated for 216 scenes with varying albedo, solar zenith angle, observation zenith angle, and aerosol optical depth.

For both the FTS and grating instruments, most scenes at SZA<30° should meet the precision goal for XCH_4 and XCO_2, and most scenes at SZA<80° should meet the precision threshold, except over surfaces with old snow albedo. None of the scenes met the precision goal for XCO, and all scenes except over old snow or over low albedo surfaces at 80° SZA met the precision threshold for XCO. For XCH_4, all scenes at SZA<60° have a precision better than 1% except over old snow and wetland albedo. For XCO_2 all scenes at SZA<60° have a precision better than 0.5% (0.4% for the grating), and all scenes at SZA<30° have a precision better than 0.4% (0.3% for the grating).

When performing retrievals with the same state used to generate the noisy pseudo-observations, the spread in the retrieved accuracy is of the order of the accuracy goal for XCH_4 and XCO_2, indicating that even in an ideal case, the goal would be difficult to meet. When applying a constant +2% offset to the a priori concentration profiles, none of the scenes meet the threshold accuracy for XCO_2 and XCH_4. Since the retrieval accuracy strongly depends on the a priori profile errors, it could be useful to run simulations with more realistic a priori profiles.

For both XCO_2 and XCH_4, radiance scaling errors should be less than 1% to meet the goal accuracy and less than 3% to meet the threshold accuracy in an ideal case with exact a priori concentration profiles. For XCO, the retrieval accuracy was better than 0.5% even for a +10% radiance scaling.

The retrievals with erroneous surface pressures lead to more stringent requirements for the FTS than for the grating, possibly due to the higher SNR in the O_2 window for the grating compared to the FTS, allowing the retrieval to recover more of the applied pressure offsets. Meeting the goal accuracy would require surface pressure errors smaller than 1.25 hPa for the FTS and 2.5 hPa for the grating at SZA=45°.

Chapter 7
Summary, Conclusions, and Future Work

7.1 Summary and Conclusions

This thesis first highlighted the importance of studying the carbon cycle and of improving measurements of greenhouse gases. The Arctic region is of particular interest because of its higher sensitivity to climate change and because it holds large reservoirs of carbon that may become new carbon sources during this century. Measurements of total column CO_2 can help improve our understanding of the carbon cycle and monitor the distribution and evolution of carbon sources and sinks. Such measurements can be made with a high spatial coverage from space and rely on more accurate ground-based measurements for their validation. The use of atmospheric measurements of CO_2 to characterize surface sources and sinks in inversion studies requires highly precise and accurate measurements to be reliable, to better than 1 ppm for XCO_2. And ground-based measurements need to be even better to be used as validation tools for space-based measurements.

A total of 57865 NIR solar spectra were collected at PEARL since 2015 over 413 measurements days, extending the previous 2010-2014 record. The processing of these measurements was improved by applying solar zenith angle corrections to mitigate the effect of pointing errors of the solar tracker; these corrections reduce the diurnal variations in XAir and the resulting change in XCO_2 is up to 0.05 ppm. The importance of accurate surface pressure measurements was highlighted and errors in the record of surface pressure were addressed, initially as high as ~1.2 hPa in the original R0 data revision, leading to XCO_2 errors of ~0.1 ppm. These improvements led to new TCCON data revisions R1, R2, and R3. This work fulfilled the first objective of this thesis as outlined in Sect. 1.4 to maintain and improve the record of NIR measurements at Eureka. TCCON measurements were used to validate results of CO_2 and CH_4 simulations by the GEM-MACH-GHG model in development at ECCC (Polavarapu et al., 2016). The data collected also contributed to validation studies of OCO-2 XCO_2 (Wunch et al., 2017; Kulawik et al., 2019; Kiel et al., 2019), TROPOMI XCH_4 and XCO (Schneising et al., 2019; Sha et al., 2021), and MOPITT XCO (Hedelius et al., 2019).

The GFIT2 profile retrieval algorithm was implemented in GGG2020, which is a new version of the TCCON retrieval algorithm that includes improvements to the forward model and spectroscopic linelist. A method was developed to determine the leading sources of variability in retrieved CO_2 profiles using synthetic spectra. It was shown that the retrieved profiles are most sensitive to realistic errors in the a priori temperature profiles, as a 2°C error between 0.8-0.65 atm would cause CO_2 profile artifacts too large to detect even the steepest vertical gradients of CO_2 (~ 5 ppm/km from the surface to 3 km). This work addressed the second objective of the thesis and showed that a temperature retrieval, or correction, would be the best avenue to improve CO_2 profile retrievals. Another method was developed to estimate how well CO_2 profiles can be retrieved when the errors in the a priori state of the atmosphere are minimized. Composite profiles using AirCore and surface measurements were built and used in retrievals with real spectra coincident with the measurements. This work showed that even with ideal a priori knowledge of the atmospheric state, further improvements to the forward model would be needed to retrieve CO_2 profiles accurately enough to detect changes in the vertical distribution of CO_2. Despite the large variability observed in retrieved profiles, XCO_2 compares well to that obtained with scaling retrievals but presents no clear advantage. The option to use empirical orthogonal functions was implemented in GFIT2 and first tested using only the leading EOF. Possible next steps to improve GFIT2 profile retrievals are discussed in Sect. 7.2.2.

To address the lack of observational coverage in the Arctic region, ECCC and the CSA are proposing the AIM-North satellite mission. Work was done to support Phase 0 of this proposal to inform the future instrument design, fulfilling the third objective of this thesis. The satellites would carry, amongst other instruments, a spectrometer to measure XCO_2, XCH_4, and XCO. NASA's ReFRACtor algorithm was adapted to generate synthetic spectra based on given instrument characteristics. Retrievals were run on these spectra to evaluate with what precision and accuracy the target gases could be retrieved over different scenes and in the presence of errors in the measured radiance or in the pointing of the instrument. Over a standard scene (forest albedo; SZA=45°; VZA=0.1°; AOD=0.01) the retrieval precision for the given instrument characteristics were ~0.6% for XCH_4, ~8% for XCO, and ~0.4% for XCO_2. Results showed that meeting the mission goal accuracy would require the instrument to measure radiances with an accuracy better than 1% and to use an a priori surface pressure with an accuracy better than 1.25 hPa for the FTS and 2.5 hPa for the grating at SZA=45. GEOS5-FPIT assimilates surface pressure observations with errors of ~1 hPa, but OCO-2 retrieved surface pressure presents a mean bias of +2 hPa (up to ~5 hPa at high latitudes) that could be attributed to errors in the parametrization of the temperature dependence of O_2 absorption lines (O'Dell et al., 2018). Thus, accurate surface pressure retrievals may prove challenging and require improvements to the O_2 A-Band spectroscopy. These results can be used by the AIM-North team to decide if they should adapt the instrument design for the instrument to meet their precision and accuracy goals and thresholds over specific scenes and given expected pointing accuracies.

7.2 Future Work

Direct follow-up work from this thesis should include further improvements to the measurements at Eureka and further improvements to the GFIT2 profile retrieval algorithm.

7.2.1 Measurements at Eureka

There are several ways the measurements at Eureka with the PEARL Bruker 125HR FTS could be improved. The instrument could benefit from improved automation to take full advantage of periods with permanent daylight, and the data processing could be improved by making the derivation of solar zenith angle corrections more systematic. Finally, the surface pressure measurements could be improved by more frequent calibrations.

7.2.1.1 Automation

The 125HR measurements at Eureka are currently not fully automated. The solar tracker needs to be started manually, and the detectors need to be filled with liquid nitrogen for MIR measurements. The tracker can shut down by itself when there is not enough sunlight, but not when the wind speed is too high nor when there is precipitation. The tracker computer could be set up to read wind and precipitation measurements from the PEARL weather station and use that information to determine when to open or close the dome. To complete the automation of measurements, an automated liquid nitrogen filler could be installed. However, even with these improvements, the operation of the PEARL 125HR would still require operator intervention to change the beamsplitter between

MIR measurements for NDACC and NIR measurements for TCCON. But the automation of the tracker would result in at least a doubling of the measurements made when Eureka is under permanent daylight from mid-April to late August; this might also require modifying the suntracker program to avoid cable wrapping by avoiding to rotating more than 360° degrees in azimuth. If there is such an issue with the azimuth angle range, the tracker could be sent in the opposite azimuth direction past a fixed threshold. Currently and despite the permanent daylight, measurements are stopped when operators return to the Eureka Weather Station at the end of the day, or before they go to sleep if they are willing to keep monitoring the measurements remotely until then.

7.2.1.2 NIR Data Processing

Section 4.4 described a solar zenith angle correction applied during the processing of Eureka NIR spectra for TCCON to correct for small pointing errors of the solar tracker. Although this method is reproducible, it requires filtering the data in a way that may seem arbitrary, and two users applying the method independently to new data may identify different time periods for deriving the SZA corrections. Unless the derivation of the SZA corrections can be made completely automated, the application of the SZA corrections may need to be reconsidered. The application of the SZA corrections may not be necessary if the camera could be placed inside the source compartment of the FTS in order to observe the image of the sun on the entrance field stop rather than its current placement on the side of the instrument looking directly at the sunbeam. The camera would also be less vulnerable to accidents inside the instrument.

7.2.1.3 Pressure Measurements

Section 4.5 presented issues with surface pressure measurements that were found since 2014. It highlights the importance of regularly monitoring the quality of the surface pressure measurements. These should be compared to a Paroscientific Digiquartz pressure standard once a year. The processing of the Eureka data could benefit from installing a new complete weather station dedicated for the 125HR measurements.

7.2.2 Profile Retrieval

Based on results presented in Chapter 5, the best avenue to improve profile retrievals with GFIT2 is to implement a temperature retrieval. Different methods to retrieve temperature or correct for temperature errors are presented in Sect. 7.2.2.1. The use of Empirical Othogonal Functions could be further explored as suggested in Sect. 7.2.2.2. Finally, a method to combine profiles retrieved from different windows is introduced in Sect. 7.2.2.3 and could be re-evaluated after the implementation of a temperature retrieval.

7.2.2.1 Temperature Retrieval

A direct follow-up of the profile retrieval study presented in Chapter 5 would be the implementation of a temperature retrieval in GFIT2. There are several ways temperature can be retrieved, for example using a scaling retrieval with the whole a priori temperature profile scaled by a single scale factor, or using a profile retrieval with a scaling factor at each level. We saw that the CO_2 profile retrieval is particularly sensitive to temperature errors between 0.8-0.65 atm. When comparing a priori temperature profiles to coincident radiosonde profiles, the differences are typically within 2 K above 5 km and can grow to >5 K close to the surface. Thus, a scaling factor could also be retrieved for the troposphere only. First, the derivative of the forward model with respect to temperature must be implemented in GFIT/2 when computing the Jacobian matrix (the derivative of Eq. 3.38 with respect to temperature). In GFIT/2, the absorption coefficients are pre-computed and do not change between iterations, even though they are a function of temperature and gas amounts. For a temperature retrieval, it may be necessary to recompute absorption coefficients at each iteration, which is very time consuming. The OCO-2 retrieval algorithm does this, which is why it uses lookup tables for absorption coefficients to optimize the time taken to recompute them at each iteration.

A temperature retrieval could also be attempted with a method similar to the empirical orthogonal functions described in Sect. 5.4.1. Instead of using error patterns derived from the SVD of a large set of spectra, we could try using the residual vector from a scaling retrieval on a synthetic spectrum, but with a known temperature perturbation applied. A retrieved scale factor applied to that residual vector could be converted to a temperature offset.

Finally, instead of being adjusted during the retrieval, temperature can be corrected in post-processing. This was tested for GFIT by Sabrina Arnold at Caltech, A detailed description of this method was presented by Geoff Toon at the 2016 NDACC-IRWG and TCCON meeting (Toon et al., 2016b). It relies on a sensitivity analysis to estimate the change in the volume scale factor (VSF) of as a given trace gas for a change in temperature, and then expressing the VSF with a given temperature error with a linear expansion:

$$VSF(T+\Delta T) = VSF(T) + \sum_{i=1}^{N} \Delta T_i \frac{d(VSF)}{dT_i} \tag{7.1}$$

where N is the number of atmospheric levels, $VSF(T)$ is the VSF retrieved by GFIT with the a priori temperature profile T, ΔT is the temperature error (or temperature correction) derived from fits to H_2O windows with different temperature sensitivities, and the term $\frac{d(VSF)}{dT_i}$ is derived for each retrieval window from a set of retrievals using synthetic spectra and specific temperature and H_2O offsets at various airmasses. A regression is performed on the results of these retrievals on synthetic spectra to derive coefficients that best fit the retrieved VSF for each spectrum following the assumed expression:

$$\frac{d(VSF)}{dT} \approx c_1 + c_2 AM + c_3 H_2O + c_4 T \tag{7.2}$$

where AM is the airmass, H_2O is the column of water, and T is the surface temperature. An issue with this method of applying temperature corrections is that a temperature correction can be obtained even in the absence of temperature error, for example when applied with retrievals on synthetic spectra where only the H_2O profiles are perturbed. Such a drawback would likely be present in all of the temperature retrieval methods proposed, with errors in other parameters resulting in spurious temperature errors.

The different methods of temperature retrieval and correction summarized here could be tested with GFIT2 and the results compared with each other. These methods could be evaluated using real spectra with coincident radiosonde profiles of temperature, such that a good estimate of the true temperature error would be known.

7.2.2.2 Empirical Orthogonal Functions

In Sect. 5.4, the use of EOFs was presented but only included the leading EOF. However, the leading EOF corresponds to systematic biases common to most spectra and should not include residual patterns caused by temperature errors, which are the errors that should cause the most variability in retrieved profiles. The use of EOFs could be extended by identifying and including the EOF that most closely corresponds to residuals caused by temperature errors.

7.2.2.3 Combined Windows

During this thesis, a method to combine profiles retrieved from different spectral windows was tested. However, it still requires more work and results were not included in the study presented in Chapter 5. The principle is to obtain the combined profile $\boldsymbol{x_r}$ from the profiles retrieved in N windows as:

$$\boldsymbol{x_r} = \mathbf{S}_{\boldsymbol{r}} \left(\left[\sum_{i=1}^{N} \hat{\mathbf{S}}_i^{-1} \hat{\boldsymbol{x}}_{\boldsymbol{i}} \right] - (N-1) \boldsymbol{S_a^{-1} x_a} \right) \tag{7.3}$$

Where $\hat{\mathbf{S}}_{\mathrm{i}}$ is the a posteriori error covariance matrix for the ith window and $\mathbf{S}_{\boldsymbol{r}}$ is the combined a posteriori covariance matrix:

$$\mathbf{S}_{\boldsymbol{r}} = \left(\sum_{i=1}^{N} \mathbf{S}_{\boldsymbol{a}}^{\mathbf{-1}} + \mathbf{K}_{\boldsymbol{i}}^{\boldsymbol{T}} \mathbf{S}_{\boldsymbol{y,i}}^{\mathbf{-1}} \mathbf{K}_{\boldsymbol{i}} \right) - (N-1) \mathbf{S}_{\boldsymbol{a}}^{\mathbf{-1}}. \tag{7.4}$$

The combined averaging kernel can be defined as:

$$\mathbf{A}_{\boldsymbol{r}} = \left(\mathbf{S}_{\boldsymbol{a}}^{\mathbf{-1}} + \sum_{i=1}^{N} \mathbf{K}_{\boldsymbol{i}}^{\boldsymbol{T}} \mathbf{S}_{\boldsymbol{y,i}} \mathbf{K}_{\boldsymbol{i}} \right)^{-1} \sum_{i=1}^{N} \mathbf{K}_{\boldsymbol{i}}^{\boldsymbol{T}} \mathbf{S}_{\boldsymbol{y,i}}^{\mathbf{-1}} \mathbf{K}_{\boldsymbol{i}}. \tag{7.5}$$

In these equations $(N-1)$ contributions of the a priori profile or covariance matrix are empirically subtracted to obtain expressions equivalent to a joint-band retrieval. These combined profiles tend to be strongly weighted towards the profile retrieved from the Strong window and can amplify deviations from the truth caused by systematic errors. The removal of window-dependent biases as done for total columns in the TCCON post-processing was not straightforwardly applicable to retrieved profiles and could be the subject of future work.

7.2.3 AIM-North

The study presented in Chapter 6 could be extended by investigating the effect of changing the FTS instrument resolution on retrieval precision and accuracy. More sensitivity experiments could be explored, like the effect of perturbing the aerosol optical depth. Not taking aerosols into account can lead to ~1% (~4 ppm) errors in XCO_2 for OCO-2 retrievals (Nelson and O'Dell, 2019). Further sensitivity studies could examine polarization, scene inhomogeneity, optimization of the spectral resolution of the FTS, and improvements to the quality of O_2 and surface pressure retrieval perhaps using the 1.27 micron band, with or without the A band.

Validation is crucial to the success of every satellite mission. The accuracy requirements of greenhouse gases like CO_2 and CH_4 are stringent as we need to detect changes in emissions that are small compared to their natural fluxes and interannual variability. Global persistent biases are most easily removed by applying an additive or scaling factor to match ground-based observations like that of TCCON, which are tied to the WMO scale. However, more complex bias correction schemes are necessary to identify and remove biases that depend on time or retrieval parameters (e.g., solar zenith angle, surface pressure, surface albedo, topography). The OCO-2 bias-correction algorithm improves the XCO_2 precision from 3.11 ppm to 0.83 ppm when using a multi-model median approach (O'Dell et al., 2018); this allows the OCO-2 XCO_2 products to meet the demanding 0.25% (~1 ppm) XCO_2 precision requirements for improving our understanding of the carbon cycle (Rayner and O'Brien, 2001; Miller et al., 2007). To ensure its success, the AIM-North mission should develop a validation plan that includes support for the maintenance or expansion of existing ground-based networks in the Arctic and boreal regions. AIM-North will need a bias-correction team and a validation team.

Bibliography

Abbott, B. W., Jones, J. B., Schuur, E. A. G., Chapin, F. S., Bowden, W. B., Bret-Harte, M. S., Epstein, H. E., Flannigan, M. D., Harms, T. K., Hollingsworth, T. N., Mack, M. C., McGuire, A. D., Natali, S. M., Rocha, A. V., Tank, S. E., Turetsky, M. R., Vonk, J. E., Wickland, K. P., Aiken, G. R., Alexander, H. D., Amon, R. M. W., Benscoter, B. W., Bergeron, Y., Bishop, K., Blarquez, O., Bond-Lamberty, B., Breen, A. L., Buffam, I., Cai, Y., Carcaillet, C., Carey, S. K., Chen, J. M., Chen, H. Y. H., Christensen, T. R., Cooper, L. W., Cornelissen, J. H. C., De Groot, W. J., Deluca, T. H., Dorrepaal, E., Fetcher, N., Finlay, J. C., Forbes, B. C., French, N. H. F., Gauthier, S., Girardin, M. P., Goetz, S. J., Goldammer, J. G., Gough, L., Grogan, P., Guo, L., Higuera, P. E., Hinzman, L., Hu, F. S., Hugelius, G., Jafarov, E. E., Jandt, R., Johnstone, J. F., Karlsson, J., Kasischke, E. S., Kattner, G., Kelly, R., Keuper, F., Kling, G. W., Kortelainen, P., Kouki, J., Kuhry, P., Laudon, H., Laurion, I., MacDonald, R. W., Mann, P. J., Martikainen, P. J., McClelland, J. W., Molau, U., Oberbauer, S. F., Olefeldt, D., Paré, D., Parisien, M. A., Payette, S., Peng, C., Pokrovsky, O. S., Rastetter, E. B., Raymond, P. A., Raynolds, M. K., Rein, G., Reynolds, J. F., Robards, M., Rogers, B. M., Schdel, C., Schaefer, K., Schmidt, I. K., Shvidenko, A., Sky, J., Spencer, R. G. M., Starr, G., Striegl, R. G., Teisserenc, R., Tranvik, L. J., Virtanen, T., Welker, J. M., et al.: Biomass offsets little or none of permafrost carbon release from soils, streams, and wildfire: An expert assessment, Environ. Res. Lett., 11, 034014, https://doi.org/10.1088/1748-9326/11/3/034014, 2016.

Abrams, M.: The Advanced Spaceborne Thermal Emission and Reflection Radiometer (ASTER): Data products for the high spatial resolution imager on NASA's Terra platform, Int. J. Remote Sens., 21, 847–859, https://doi.org/10.1080/014311600210326, 2000.

Abrams, M. C., Toon, G. C., and Schindler, R. A.: Practical example of the correction of Fourier-transform spectra for detector nonlinearity, Appl. Opt., 33, 6307–6314, https://doi.org/10.1364/AO.33.006307, 1994.

Adams, C. L. F.: Measurements of atmospheric ozone, NO_2, OClO, and BrO at 80 degrees N using UV-visible spectroscopy (PhD thesis), University of Toronto, Toronto, 298 pp., 2012.

Amat, G. and Pimbert, M.: On Fermi resonance in carbon dioxide, J. Mol. Spectrosc., 16, 278–290, https://doi.org/10.1016/0022-2852(65)90123-2, 1965.

Andrews, A. E., Boering, K. A., Daube, B. C., Wofsy, S. C., Loewenstein, M., Jost, H., Podolske, J. R., Webster, C. R., Herman, R. L., Scott, D. C., Flesch, G. J., Moyer, E. J., Elkins, J. W., Dutton, G. S., Hurst, D. F., Moore, F. L., Ray, E. A., Romashkin, P. A., and Strahan, S. E.: Mean ages of stratospheric air derived from in situ observations of CO_2, CH_4, and N_2O, J. Geophys. Res. Atmos., 106, 32295–32314, https://doi.org/10.1029/2001JD000465, 2001.

Aumann, H. H., Chahine, M. T., Gautier, C., Goldberg, M. D., Kalnay, E., McMillin, L. M., Revercomb, H., Rosenkranz, P. W., Smith, W. L., Staelin, D. H., Strow, L. L., and Susskind, J.: AIRS/AMSU/HSB on the aqua mission: design, science objectives, data products, and processing systems, IEEE Trans. Geosci. Remote Sens., 41, 253–264, https://doi.org/10.1109/TGRS.2002.808356, 2003.

Basu, S., Houweling, S., Peters, W., Sweeney, C., Machida, T., Maksyutov, S., Patra, P. K., Saito, R., Chevallier, F., Niwa, Y., Matsueda, H., and Sawa, Y.: The seasonal cycle amplitude of total column CO_2 : Factors behind the model-observation mismatch, J. Geophys. Res. Atmos., 116, D23306, https://doi.org/10.1029/2011JD016124, 2011.

Basu, S., Baker, D. F., Chevallier, F., Patra, P. K., Liu, J., and Miller, J. B.: The impact of transport model differences on CO_2 surface flux estimates from OCO-2 retrievals of column average CO_2, Atmos. Chem. Phys., 18, 7189–7215, https://doi.org/10.5194/acp-18-7189-2018, 2018.

Batchelor, R. L., Strong, K., Lindenmaier, R., Mittermeier, R. L., Fast, H., Drummond, J. R., and Fogal, P. F.: A New Bruker IFS 125HR FTIR Spectrometer for the Polar Environment Atmospheric Research Laboratory at Eureka, Nunavut, Canada: Measurements and Comparison with the Existing Bomem DA8 Spectrometer, J. Atmos. Ocean. Technol., 26, 1328–1340, https://doi.org/10.1175/2009JTECHA1215.1, 2009.

Beer, R.: TES on the aura mission: scientific objectives, measurements, and analysis overview, IEEE Trans. Geosci. Remote Sens., 44, 1102–1105, https://doi.org/10.1109/TGRS.2005.863716, 2006.

Belshe, E. F., Schuur, E. A. G., and Bolker, B. M.: Tundra ecosystems observed to be CO_2 sources due to differential amplification of the carbon cycle, Ecol. Lett., 16, 1307–1315, https://doi.org/10.1111/ele.12164, 2013.

Benner, D. C., Rinsland, C. P., Devi, V. M., Smith, M. A. H., and Atkins, D.: A multispectrum nonlinear least squares fitting technique, J. Quant. Spectrosc. Radiat. Transf., 53, 705–721, https://doi.org/10.1016/0022-4073(95)00015-D, 1995.

Benner, D. C., Devi, V. M., Sung, K., Brown, L. R., Miller, C. E., Payne, V. H., Drouin, B. J., Yu, S., Crawford, T. J., Mantz, A. W., Smith, M. A. H., and Gamache, R. R.: Line parameters including temperature dependences of air- and self-broadened line shapes of $^{12}C^{16}O_2$: 2.06-μm region, J. Mol. Spectrosc., 326, 21–47, https://doi.org/10.1016/j.jms.2016.02.012, 2016.

Berk, A., Conforti, P., Kennett, R., Perkins, T., Hawes, F., and van den Bosch, J.: MODTRAN6: a major upgrade of the MODTRAN radiative transfer code, in: Algorithms and Technologies for Multispectral, Hyperspectral, and Ultraspectral Imagery XX, 113–119, 2014.

Bindoff, N. L., Cheung, W. W. L., Kairo, J. G., Arístegui, J., Guinder, V. A., Hallberg, R., Hilmi, N., Jiao, N., Karim, M. S., Levin, L., O'Donoghue, S., Cuicapusa, S. R. P., Rinkevich, B., Suga, T., Tagliabue, A., and Williamson, P.: Changing Ocean, Marine Ecosystems, and Dependent Communities. In: IPCC Special Report on the Ocean and Cryosphere in a Changing Climate, In Press, 2019.

Biraud, S. and Moyes, A.: Atmospheric Radiation Measurement (ARM) user facility. Updated hourly. Precision Carbon Dioxide Mixing Ratio System (PGS). 2001-04-11 to 2019-07-22, Southern Great Plains (SGP) Central Facility, Lamont, OK (C1). ARM Data Center., https://doi.org/dx.doi.org/10.5439/1025262, 2001.

Biraud, S., Moyes, A., and Ermold, B.: Atmospheric Radiation Measurement (ARM) user facility. Updated hourly. Flask Samplers for Carbon Cycle Gases and Isotopes (GHGFLASK). 2002-04-02 to 2019-05-23, Southern Great Plains (SGP) Central Facility, Lamont, OK (C1). ARM Data Center., https://doi.org/dx.doi.org/10.5439/1482660, 2002.

Biraud, S. C., Torn, M. S., Smith, J. R., Sweeney, C., Riley, W. J., and Tans, P. P.: A multi-year record of airborne CO_2 observations in the US Southern Great Plains, Atmos. Meas. Tech., 6, 751–763, https://doi.org/10.5194/amt-6-751-2013, 2013.

Blumenstock, T., Hase, F., Schneider, M., García, O. E., and Sepúlveda, E.: TCCON data from Izana (ES), Release GGG2014.R1, https://doi.org/10.14291/TCCON.GGG2014.IZANA01.R1, 2017.

Boisvert, L. N. and Stroeve, J. C.: The Arctic is becoming warmer and wetter as revealed by the Atmospheric Infrared Sounder, Geophys. Res. Lett., 42, 4439–4446, https://doi.org/10.1002/2015GL063775, 2015.

Boone, C. D., Walker, K. A., and Bernath, P. F.: An efficient analytical approach for calculating line mixing in atmospheric remote sensing applications, J. Quant. Spectrosc. Radiat. Transf., 112, 980–989, https://doi.org/10.1016/j.jqsrt.2010.11.013, 2011.

Bovensmann, H., Burrows, J. P., Buchwitz, M., Frerick, J., Noël, S., Rozanov, V. V., Chance, K. V., and Goede, A. P. H.: SCIAMACHY: Mission Objectives and Measurement Modes, J. Atmos. Sci., 56, 127–150, https://doi.org/10.1175/1520-0469(1999)056<0127:SMOAMM>2.0.CO;2, 1999.

van den Broek, M. M. P., van Aalst, M. K., Bregman, A., Krol, M., Lelieveld, J., Toon, G. C., Garcelon, S., Hansford, G. M., Jones, R. L., and Gardiner, T. D.: The impact of model grid zooming on tracer transport in the 1999/2000 Arctic polar vortex, Atmos. Chem. Phys., 3, 1833–1847, https://doi.org/10.5194/acp-3-1833-2003, 2003.

Brown, J. M., Hougen, J. T., Huber, K.-P., Johns, J. W. C., Kopp, I., Lefebvre-Brion, H., Merer, A. J., Ramsay, D. A., Rostas, J., and Zare, R. N.: The labeling of parity doublet levels in linear molecules, J. Mol. Spectrosc., 55, 500–503, https://doi.org/10.1016/0022-2852(75)90291-X, 1975.

Brown, L. R., Farmer, C. B., Rinsland, C. P., and Zander, R.: Remote Sensing of the Atmosphere by High Resolution Infrared Absorption Spectroscopy, in: Spectroscopy of the Earth's Atmosphere and Interstellar Medium, edited by: Narahari Rao, K. and Weber, A., Academic Press Inc., San Diego, CA, 97–151, 1992.

Buchwitz, M., de Beek, R., Burrows, J. P., Bovensmann, H., Warneke, T., Notholt, J., Meirink, J. F., Goede, A. P. H., Bergamaschi, P., Körner, S., Heimann, M. and Schulz, A.: Atmospheric methane and carbon dioxide from SCIAMACHY satellite data: initial comparison with chemistry and transport models, Atmos. Chem. Phys., 5(4), 941–962, doi:10.5194/acp-5-941-2005, 2005a.

Buchwitz, M., de Beek, R., Noël, S., Burrows, J. P., Bovensmann, H., Bremer, H., Bergamaschi, P., Körner, S. and Heimann, M.: Carbon monoxide, methane and carbon dioxide columns retrieved from SCIAMACHY by WFM-DOAS: year 2003 initial data set, Atmos. Chem. Phys., 5(12), 3313–3329, doi:10.5194/acp-5-3313-2005, 2005b.

Chevallier, F., Engelen, R. J. and Peylin, P.: The contribution of AIRS data to the estimation of CO_2 sources and sinks, Geophys. Res. Lett., 32(23), L23801, doi:10.1029/2005GL024229, 2005.

Chevallier, F., Bréon, F.-M., and Rayner, P. J.: Contribution of the Orbiting Carbon Observatory to the estimation of CO_2 sources and sinks: Theoretical study in a variational data assimilation framework, J. Geophys. Res., 112, D09307, https://doi.org/10.1029/2006JD007375, 2007.

Chevallier, F., Remaud, M., O'Dell, C. W., Baker, D., Peylin, P., and Cozic, A.: Objective evaluation of surface- and satellite-driven carbon dioxide atmospheric inversions, Atmos. Chem. Phys., 19, 14233–14251, https://doi.org/10.5194/acp-19-14233-2019, 2019.

Ciais, P., Sabine, C., Bala, G., Bopp, L., Brovkin, V., Canadell, A., Chhabra, R., DeFries, R., Galloway, J., Heimann, C., Jones, C., Le Quéré, C., Myneni, R. B., Piao, S., and Thornton, P.: Carbon and Other Biogeochemical Cycles, in: Climate Change 2013 - The Physical Science Basis, edited by: Intergovernmental Panel on Climate Change, Cambridge University Press, Cambridge, United Kingdom and New York, NY, USA, 465–570, https://doi.org/10.1017/CBO9781107415324.015, 2013.

Ciais, P., Dolman, A. J., Bombelli, A., Duren, R., Peregon, A., Rayner, P. J., Miller, C., Gobron, N., Kinderman, G., Marland, G., Gruber, N., Chevallier, F., Andres, R. J., Balsamo, G., Bopp, L., Bréon, F.-M., Broquet, G., Dargaville, R., Battin, T. J., Borges, A., Bovensmann, H., Buchwitz, M., Butler, J., Canadell, J. G., Cook, R. B., DeFries, R., Engelen, R., Gurney, K. R., Heinze, C., Heimann, M., Held, A., Henry, M., Law, B., Luyssaert, S., Miller, J., Moriyama, T., Moulin, C., Myneni, R. B., Nussli, C., Obersteiner, M., Ojima, D., Pan, Y., Paris, J.-D., Piao, S. L., Poulter, B., Plummer, S., Quegan, S., Raymond, P., Reichstein, M., Rivier, L., Sabine, C., Schimel, D., Tarasova, O., Valentini, R., Wang, R., van der Werf, G., Wickland, D., Williams, M., and Zehner, C.: Current systematic carbon-cycle observations and the need for implementing a policy-relevant carbon observing system, 11, 3547–3602, https://doi.org/10.5194/bg-11-3547-2014, 2014.

Cohen, J., Screen, J. A., Furtado, J. C., Barlow, M., Whittleston, D., Coumou, D., Francis, J., Dethloff, K., Entekhabi, D., Overland, J., and Jones, J.: Recent Arctic amplification and extreme mid-latitude weather, Nat. Geosci., 7, 627–637, https://doi.org/10.1038/ngeo2234, 2014.

Colbourn, G., Ridgwell, A., and Lenton, T. M.: The time scale of the silicate weathering negative feedback on atmospheric CO_2, Global Biogeochem. Cycles, 29, 583–596, https://doi.org/10.1002/2014GB005054, 2015.

Collins, M., Knutti, R., Arblaster, J., Dufresne, J., Fichefet, T., Friedlingstein, P., Gao, X., Gutowski, W., Johns, T., Krinner, G., Shongwe, M., Tebaldi, C., Weaver, A., Wehner, M., Qin, D., Plattner, G., Tignor, M., Allen, S., Boschung, J., Nauels, A., Xia, Y., Bex, V., Midgley, P., Collins, M., Knutti, R., Arblaster, J., Dufresne, J.-L., Fichefet, T., Friedlingstein, P. U., Gao, X., Gutowski Jr, W. J., Johns, T., and Allen, M. R.: Long-term Climate Change: Projections, Commitments and Irreversibility Pages 1029 to 1076, in: Climate Change 2013 - The Physical Science Basis, edited by: Intergovernmental Panel on Climate Change, Cambridge University Press, Cambridge, United Kingdom and New York, NY, USA, 1029–1136, https://doi.org/10.1017/CBO9781107415324.024, 2013.

Connor, B. J., Sherlock, V., Toon, G., Wunch, D., and Wennberg, P. O.: GFIT2: an experimental algorithm for vertical profile retrieval from near-IR spectra, Atmos. Meas. Tech., 9, 3513–3525, https://doi.org/10.5194/amt-9-3513-2016, 2016.

Cooley, J. W. and Tukey, J. W.: An algorithm for the machine calculation of complex Fourier series, Math. Comput., 19, 297–297, https://doi.org/10.1090/S0025-5718-1965-0178586-1, 1965.

Cooperative Global Atmospheric Data Integration Project: Multi-laboratory compilation of atmospheric carbon dioxide data for the period 1957-2018; obspack_co2_1_GLOBALVIEWplus_v5.0_2019_08_12, https://doi.org/10.25925/20190812, 2019.

Cooperative Global Atmospheric Data Integration Project: Multi-laboratory compilation of atmospheric carbon dioxide data for the period 1957-2018; obspack_ch4_1_GLOBALVIEWplus_v2.0_2020_04_24, https://doi.org/10.25925/20200424, 2020.

Corredera, P., Hernanz, M. L., González-Herráez, M., and Campos, J.: Anomalous non-linear behaviour of InGaAs photodiodes with overfilled illumination, 40, S150–S153, https://doi.org/10.1088/0026-1394/40/1/334, 2003.

Côté, J., Gravel, S., Méthot, A., Patoine, A., Roch, M., and Staniforth, A.: The Operational CMC–MRB Global Environmental Multiscale (GEM) Model. Part I: Design Considerations and Formulation, Mon. Weather Rev., 126, 1373–1395, https://doi.org/10.1175/1520-0493(1998)126<1373:TOCMGE>2.0.CO;2, 1998.

Crisp, D.: NASA Orbiting Carbon Observatory: measuring the column averaged carbon dioxide mole fraction from space, J. Appl. Remote Sens., 2, 1–14, https://doi.org/10.1117/1.2898457, 2008.

Crisp, D.: Measuring atmospheric carbon dioxide from space with the Orbiting Carbon Observatory-2 (OCO-2), in: Earth Observing Systems XX, 1–7, https://doi.org/10.1117/12.2187291, 2015.

Crowell, S., Baker, D., Schuh, A., Basu, S., Jacobson, A. R., Chevallier, F., Liu, J., Deng, F., Feng, L., McKain, K., Chatterjee, A., Miller, J. B., Stephens, B. B., Eldering, A., Crisp, D., Schimel, D., Nassar, R., O'Dell, C. W., Oda, T., Sweeney, C., Palmer, P. I., and Jones, D. B. A.: The 2015--2016 carbon cycle as seen from OCO-2 and the global in situ network, Atmos. Chem. Phys., 19, 9797–9831, https://doi.org/10.5194/acp-19-9797-2019, 2019.

Davis, S. P., Abrams, M. C., and Brault, J. W.: Effects of noise in its various forms, in: Fourier Transform Spectrometry, Elsevier, 119–141, https://doi.org/10.1016/B978-012042510-5/50008-1, 2001a.

Davis, S. P., Abrams, M. C., and Brault, J. W.: Nonideal (real-world) interferograms, in: Fourier Transform Spectrometry, Elsevier, 67–80, https://doi.org/10.1016/B978-012042510-5/50005-6, 2001b.

Davis, S. P., Abrams, M. C., and Brault, J. W.: Phase corrections and their significance, in: Fourier Transform Spectrometry, Elsevier, 101–117, https://doi.org/10.1016/B978-012042510-5/50007-X, 2001c.

Davis, S. P., Abrams, M. C., and Brault, J. W.: Theory of the ideal instrument, in: Fourier Transform Spectrometry, Elsevier, 29–39, https://doi.org/10.1016/B978-012042510-5/50003-2, 2001d.

Deutscher, N. M., Notholt, J., Messerschmidt, J., Weinzierl, C., Warneke, T., Petri, C., and Grupe, P.: TCCON data from Bialystok (PL), Release GGG2014.R2, https://doi.org/10.14291/TCCON.GGG2014.BIALYSTOK01.R2, 2019.

Devi, V. M., Benner, D. C., Brown, L. R., Miller, C. E., and Toth, R. A.: Line mixing and speed dependence in CO$_2$ at 6227.9 cm^{-1}: Constrained multispectrum analysis of intensities and line shapes in the 30013←00001 band, J. Mol. Spectrosc., 245, 52–80, https://doi.org/10.1016/j.jms.2007.05.015, 2007.

Devi, V. M., Benner, D. C., Sung, K., Brown, L. R., Crawford, T. J., Miller, C. E., Drouin, B. J., Payne, V. H., Yu, S., Smith, M. A. H., Mantz, A. W., and Gamache, R. R.: Line parameters including temperature dependences of self- and air-broadened line shapes of ^{12}C^{16}O$_2$: 1.6-μm region, J.

Quant. Spectrosc. Radiat. Transf., 177, 117–144, https://doi.org/10.1016/j.jqsrt.2015.12.020, 2016.

Dlugokencky, E. J., Nisbet, E. G., Fisher, R., and Lowry, D.: Global atmospheric methane: budget, changes and dangers, Philos. Trans. R. Soc. A Math. Phys. Eng. Sci., 369, 2058–2072, https://doi.org/10.1098/rsta.2010.0341, 2011.

Dlugokencky, E. J., Mund, J. W., Crotwell, A. M., Crotwell, M. J., and Thoning, K. W.: Atmospheric Carbon Dioxide Dry Air Mole Fractions from the NOAA ESRL Carbon Cycle Cooperative Global Air Sampling Network, 1968-2018, Version: 2019-07, https://doi.org/https://doi.org/10.15138/wkgj-f215, 2019.

Dohe, S.: Measurements of atmospheric CO_2 columns using ground-based FTIR spectra (PhD thesis), Karlsruhe Institute of Technology, Karlsruhe, 161 pp., 2013.

Doney, S. C., Fabry, V. J., Feely, R. A., and Kleypas, J. A.: Ocean Acidification: The Other CO_2 Problem, Ann. Rev. Mar. Sci., 1, 169–192, https://doi.org/10.1146/annurev.marine.010908.163834, 2009.

Drummond, J. R., Zou, J., Nichitiu, F., Kar, J., Deschambaut, R., and Hackett, J.: A review of 9-year performance and operation of the MOPITT instrument, Adv. Sp. Res., 45, 760–774, https://doi.org/10.1016/j.asr.2009.11.019, 2010.

Dusenge, M. E., Duarte, A. G., and Way, D. A.: Plant carbon metabolism and climate change: elevated CO_2 and temperature impacts on photosynthesis, photorespiration and respiration, New Phytol., 221, 32–49, https://doi.org/10.1111/nph.15283, 2019.

Eldering, A., Taylor, T. E., O'Dell, C. W., and Pavlick, R.: The OCO-3 mission: measurement objectives and expected performance based on 1 year of simulated data, Atmos. Meas. Tech., 12, 2341–2370, https://doi.org/10.5194/amt-12-2341-2019, 2019.

Farahani, E., Fast, H., Mittermeier, R. L., Makino, Y., Strong, K., McLandress, C., Shepherd, T. G., Chipperfield, M. P., Hannigan, J. W., Coffey, M. T., Mikuteit, S., Hase, F., Blumenstock, T., and Raffalski, U.: Nitric acid measurements at Eureka obtained in winter 2001–2002 using solar and lunar Fourier transform infrared absorption spectroscopy: Comparisons with observations at Thule and Kiruna and with results from three-dimensional models, J. Geophys. Res., 112, D01305, https://doi.org/10.1029/2006JD007096, 2007.

Fast, H., Mittermeier, R. L., and Makino, Y.: A Ten-Year Record of Arctic Trace Gas Total Column Measurements at Eureka, Canada, from 1997 to 2006, 49, 67–94, https://doi.org/10.1080/07055900.2011.562470, 2011.

Fehr, T.: Sentinel-5 Precursor: Scientific Validation Implementation Plan, 280 pp., https://doi.org/10.5281/ZENODO.165739, 2016.

Fletcher, R.: A modified Marquardt subroutine for non-linear least squares, Report R67., Atomic Energy Research Establishment, Harwell, Berkshire, 1971.

FLUXNET: FLUXNET Canada Research Network - Canadian Carbon Program Data Collection, 1993-2014, https://doi.org/10.3334/ORNLDAAC/1335, 2016.

Foken, T., Aubinet, M., and Leuning, R.: The Eddy Covariance Method, in: Eddy Covariance, Springer Netherlands, Dordrecht, 1–19, https://doi.org/10.1007/978-94-007-2351-1_1, 2012.

Franklin, J. E.: Solar Absorption Spectroscopy at the Dalhousie Atmospheric Observatory (PhD thesis), Dalhousie University, Halifax, 134 pp., 2015.

Friedlingstein, P., Jones, M. W., O'Sullivan, M., Andrew, R. M., Hauck, J., Peters, G. P., Peters, W., Pongratz, J., Sitch, S., Le Quéré, C., Bakker, D. C. E., Canadell, J. G., Ciais, P., Jackson, R. B., Anthoni, P., Barbero, L., Bastos, A., Bastrikov, V., Becker, M., Bopp, L., Buitenhuis, E., Chandra, N., Chevallier, F., Chini, L. P., Currie, K. I., Feely, R. A., Gehlen, M., Gilfillan, D., Gkritzalis, T., Goll, D. S., Gruber, N., Gutekunst, S., Harris, I., Haverd, V., Houghton, R. A., Hurtt, G., Ilyina, T., Jain, A. K., Joetzjer, E., Kaplan, J. O., Kato, E., Klein Goldewijk, K., Korsbakken, J. I., Landschützer, P., Lauvset, S. K., Lefèvre, N., Lenton, A., Lienert, S., Lombardozzi, D., Marland, G., McGuire, P. C., Melton, J. R., Metzl, N., Munro, D. R., Nabel, J. E. M. S., Nakaoka, S.-I., Neill, C., Omar, A. M., Ono, T., Peregon, A., Pierrot, D., Poulter, B., Rehder, G., Resplandy, L., Robertson, E., Rödenbeck, C., Séférian, R., Schwinger, J., Smith, N., Tans, P. P., Tian, H., Tilbrook, B., Tubiello, F. N., van der Werf, G. R., Wiltshire, A. J., and Zaehle, S.: Global Carbon Budget 2019, Earth Syst. Sci. Data, 11, 1783–1838, https://doi.org/10.5194/essd-11-1783-2019, 2019.

Gerlach, T.: Volcanic versus anthropogenic carbon dioxide, Eos, Trans. Am. Geophys. Union, 92, 201–202, https://doi.org/10.1029/2011EO240001, 2011.

Gillett, N. P., Arora, V. K., Matthews, D., and Allen, M. R.: Constraining the Ratio of Global Warming to Cumulative CO_2 Emissions Using CMIP5 Simulations, J. Clim., 26, 6844–6858, https://doi.org/10.1175/JCLI-D-12-00476.1, 2013.

Girard, C., Plante, A., Desgagné, M., McTaggart-Cowan, R., Côté, J., Charron, M., Gravel, S., Lee, V., Patoine, A., Qaddouri, A., Roch, M., Spacek, L., Tanguay, M., Vaillancourt, P. A., and Zadra, A.: Staggered Vertical Discretization of the Canadian Environmental Multiscale (GEM) Model Using a Coordinate of the Log-Hydrostatic-Pressure Type, Mon. Weather Rev., 142, 1183–1196, https://doi.org/10.1175/MWR-D-13-00255.1, 2014.

Gisi, M., Hase, F., Dohe, S., and Blumenstock, T.: Camtracker: a new camera controlled high precision solar tracker system for FTIR-spectrometers, Atmos. Meas. Tech., 4, 47–54, https://doi.org/10.5194/amt-4-47-2011, 2011.

Gordon, I. E., Rothman, L. S., Hill, C., Kochanov, R. V., Tan, Y., Bernath, P. F., Birk, M., Boudon, V., Campargue, A., Chance, K. V., Drouin, B. J., Flaud, J.-M., Gamache, R. R., Hodges, J. T., Jacquemart, D., Perevalov, V. I., Perrin, A., Shine, K. P., Smith, M.-A. H., Tennyson, J., Toon, G. C., Tran, H., Tyuterev, V. G., Barbe, A., Császár, A. G., Devi, V. M., Furtenbacher, T., Harrison, J. J., Hartmann, J.-M., Jolly, A., Johnson, T. J., Karman, T., Kleiner, I., Kyuberis, A. A., Loos, J., Lyulin, O. M., Massie, S. T., Mikhailenko, S. N., Moazzen-Ahmadi, N., Müller, H. S. P., Naumenko, O. V., Nikitin, A. V., Polyansky, O. L., Rey, M., Rotger, M., Sharpe, S. W., Sung, K., Starikova, E., Tashkun, S. A., Auwera, J. Vander, Wagner, G., Wilzewski, J., Wcisło, P., Yu, S., and Zak, E. J.: The HITRAN2016 molecular spectroscopic database, J. Quant. Spectrosc. Radiat. Transf., 203, 3–69, https://doi.org/10.1016/j.jqsrt.2017.06.038, 2017.

Griffith, D. W. T., Deutscher, N. M., Velazco, V. A., Wennberg, P. O., Yavin, Y., Keppel-Aleks, G., Washenfelder, R. A., Toon, G. C., Blavier, J.-F., Paton-Walsh, C., Jones, N. B., Kettlewell, G. C., Connor, B. J., Macatangay, R. C., Roehl, C., Ryczek, M., Glowacki, J., Culgan, T., and Bryant, G. W.: TCCON data from Darwin (AU), Release GGG2014.R0, https://doi.org/10.14291/TCCON.GGG2014.DARWIN01.R0/1149290, 2014a.

Griffith, D. W. T., Velazco, V. A., Deutscher, N. M., Paton-Walsh, C., Jones, N. B., Wilson, S. R., Macatangay, R. C., Kettlewell, G. C., Buchholz, R. R., and Riggenbach, M. O.: TCCON data from Wollongong (AU), Release GGG2014.R0, https://doi.org/10.14291/TCCON.GGG2014.WOLLONGONG01.R0/1149291, 2014b.

Grosse, G., Romanovsky, V., Jorgenson, T., Anthony, K. W., Brown, J., and Overduin, P. P.: Vulnerability and Feedbacks of Permafrost to Climate Change, Eos, Trans. Am. Geophys. Union, 92, 73–74, https://doi.org/10.1029/2011EO090001, 2011.

Hartmann, D. L., Klein Tank, A., Rusticucci, M., Alexander, L., Brönnimann, S., Charabi, Y., Dentener, F., Dlugo-kencky, E., Easterling, D., Kaplan, A., Soden, B., Thorne, P., Wild, M., Zhai, P., Qin, D., Plattner, G., Tignor, M., Allen, S., Boschung, J., Nauels, A., Xia, Y., Bex, V., Midgley, P., Hartmann, D. L., Klein Tank, A. M., Rusticucci, M., Alexander, L. V, Brönnimann, S., Abdul-Rahman Charabi, Y., Dentener, F. J., Adler, R., Allan, R., Allan, R., and Blake, D.: Observations: Atmosphere and Surface, in: Climate Change 2013 - The Physical Science Basis, edited by: Intergovernmental Panel on Climate Change, Cambridge University Press, Cambridge, United Kingdom and New York, NY, USA, 159–254, https://doi.org/10.1017/CBO9781107415324.008, 2013.

Hartmann, J.-M., Boulet, C., and Robert, D.: Collisional Line Mixing (Within Clusters of Lines), in: Collisional Effects on Molecular Spectra, Elsevier, 147–240, https://doi.org/10.1016/B978-0-444-52017-3.00004-2, 2008a.

Hartmann, J.-M., Boulet, C., and Robert, D.: Isolated Lines, in: Collisional Effects on Molecular Spectra, Elsevier, 63–145, https://doi.org/10.1016/B978-0-444-52017-3.00003-0, 2008b.

Hartmann, J. M., Boulet, C., and Robert, D.: Collisional Effects on Molecular Spectra, Elsevier, https://doi.org/10.1016/B978-0-444-52017-3.X0001-5, 2008c.

Hase, F., Blumenstock, T., and Paton-Walsh, C.: Analysis of the instrumental line shape of high-resolution Fourier transform IR spectrometers with gas cell measurements and new retrieval software, Appl. Opt., 38, 3417, https://doi.org/10.1364/AO.38.003417, 1999.

Hase, F., Hannigan, J. W., Coffey, M. T., Goldman, A., Höpfner, M., Jones, N. B., Rinsland, C. P., and Wood, S. W.: Intercomparison of retrieval codes used for the analysis of high-resolution, ground-based FTIR measurements, J. Quant. Spectrosc. Radiat. Transf., 87, 25–52, https://doi.org/10.1016/j.jqsrt.2003.12.008, 2004.

Hase, F., Blumenstock, T., Dohe, S., Groß, J., and Kiel, M.: TCCON data from Karlsruhe (DE), Release GGG2014.R1, https://doi.org/10.14291/TCCON.GGG2014.KARLSRUHE01.R1/1182416, 2015.

Hausmann, P., Sussmann, R., and Smale, D.: Contribution of oil and natural gas production to renewed increase in atmospheric methane (2007–2014): top–down estimate from ethane and methane column observations, Atmos. Chem. Phys., 16, 3227–3244, https://doi.org/10.5194/acp-16-3227-2016, 2016.

Hearn, D. R.: Fourier Transform Interferometry, Tech. Rep. 1053, Lexington, MA, 1999.

Hedelius, J. K., He, T.-L., Jones, D. B. A., Baier, B. C., Buchholz, R. R., De Mazière, M., Deutscher, N. M., Dubey, M. K., Feist, D. G., Griffith, D. W. T., Hase, F., Iraci, L. T., Jeseck, P., Kiel, M., Kivi, R., Liu, C., Morino, I., Notholt, J., Oh, Y.-S., Ohyama, H., Pollard, D. F., Rettinger, M., Roche, S., Roehl, C. M., Schneider, M., Shiomi, K., Strong, K., Sussmann, R., Sweeney, C., Té, Y., Uchino, O., Velazco, V. A., Wang, W., Warneke, T., Wennberg, P. O., Worden, H. M., and Wunch, D.: Evaluation of MOPITT Version 7 joint TIR–NIR XCO retrievals with TCCON, Atmos. Meas. Tech., 12, 5547–5572, https://doi.org/10.5194/amt-12-5547-2019, 2019.

Heymann, J., Reuter, M., Hilker, M., Buchwitz, M., Schneising, O., Bovensmann, H., Burrows, J. P., Kuze, A., Suto, H., Deutscher, N. M., Dubey, M. K., Griffith, D. W. T., Hase, F., Kawakami, S., Kivi, R., Morino, I., Petri, C., Roehl, C., Schneider, M., Sherlock, V., Sussmann, R., Velazco, V. A., Warneke, T. and Wunch, D.: Consistent satellite XCO_2 retrievals from SCIAMACHY and GOSAT using the BESD algorithm, Atmos. Meas. Tech., 8(7), 2961–2980, doi:10.5194/amt-8-2961-2015, 2015.

Hollas, J. M.: Vibrational spectroscopy, in: Basic Atomic and Molecular Spectroscopy, edited by: Hollas, J. M., Royal Society of Chemistry, Cambridge, 126–145, https://doi.org/10.1039/9781847550194-00126, 2002.

Hollas, J. M.: Molecular rotation, in: Basic Atomic and Molecular Spectroscopy, edited by: Hollas, J. M., Royal Society of Chemistry, Cambridge, 91–99, https://doi.org/10.1039/9781847550194-00091, 2007a.

Hollas, J. M.: Molecular vibrations, in: Basic Atomic and Molecular Spectroscopy, edited by: Hollas, J. M., Royal Society of Chemistry, Cambridge, 75–90, https://doi.org/10.1039/9781847550194-00075, 2007b.

Hollas, J. M.: Rotational spectroscopy, in: Basic Atomic and Molecular Spectroscopy, edited by: Hollas, J. M., Royal Society of Chemistry, Cambridge, 110–125, https://doi.org/10.1039/9781847550194-00110, 2007c.

Hugelius, G., Strauss, J., Zubrzycki, S., Harden, J. W., Schuur, E. A. G., Ping, C.-L., Schirrmeister, L., Grosse, G., Michaelson, G. J., Koven, C. D., O'Donnell, J. A., Elberling, B., Mishra, U., Camill, P., Yu, Z., Palmtag, J., and Kuhry, P.: Estimated stocks of circumpolar permafrost carbon with quantified uncertainty ranges and identified data gaps, 11, 6573–6593, https://doi.org/10.5194/bg-11-6573-2014, 2014.

Hugelius, G., Loisel, J., Chadburn, S., Jackson, R. B., Jones, M., MacDonald, G., Marushchak, M., Olefeldt, D., Packalen, M., Siewert, M. B., Treat, C., Turetsky, M., Voigt, C., and Yu, Z.: Large stocks of peatland carbon and nitrogen are vulnerable to permafrost thaw, Proc. Natl. Acad. Sci., 117, 20438–20446, https://doi.org/10.1073/pnas.1916387117, 2020.

IPCC: Summary for Policymakers, in: Climate Change 2013 - The Physical Science Basis, edited by: Intergovernmental Panel on Climate Change, Cambridge University Press, Cambridge, United Kingdom and New York, NY, USA, 1–30, https://doi.org/10.1017/CBO9781107415324.004, 2013.

Jacob, D. J.: Introduction to Atmospheric Chemistry, Princeton University Press, 264 pp., 1999.

Jacobson, A. R., Schuldt, K. N., Miller, J. B., Oda, T., Tans, P., Arlyn Andrews, Mund, J., Ott, L., Collatz, G. J., Aalto, T., Afshar, S., Aikin, K., Aoki, S., Apadula, F., Baier, B., Bergamaschi, P., Beyersdorf, A., Biraud, S. C., Bollenbacher, A., Bowling, D., Brailsford, G., Abshire, J. B., Chen, G., Huilin Chen, Lukasz Chmura, Sites Climadat, Colomb, A., Conil, S., Cox, A., Cristofanelli, P., Cuevas, E., Curcoll, R., Sloop, C. D., Davis, K., Wekker, S. De, Delmotte, M., DiGangi, J. P., Dlugokencky, E., Ehleringer, J., Elkins, J. W., Emmenegger, L., Fischer, M. L., Forster, G., Frumau, A., Galkowski, M., Gatti, L. V, Gloor, E., Griffis, T., Hammer, S., Haszpra, L., Hatakka, J., Heliasz, M., Hensen, A., Hermanssen, O., Hintsa, E., Holst, J., Jaffe, D., Karion, A., Kawa, S. R., Keeling, R., Keronen, P., Kolari, P., Kominkova, K., Kort, E., Krummel, P., Kubistin, D., Labuschagne, C., Langenfelds, R., Laurent, O., Laurila, T., Lauvaux, T., Law, B., Lee, J., Lehner, I., Leuenberger, M., Levin, I., Levula, J., Lin, J., Lindauer, M., Loh, Z., Lopez, M., Luijkx, I. T., Myhre, C. L., Machida, T., Mammarella, I., Manca, G., Manning, A., Manning, A., Marek, M. V, Marklund, P., Martin, M. Y., Matsueda, H., McKain, K., Meijer, H., Meinhardt, F., Miles, N., Miller, C. E., Mölder, M., Montzka, S., et al.: CarbonTracker CT2019B, https://doi.org/10.25925/20201008, 2020.

Janssens-Maenhout, G., Crippa, M., Guizzardi, D., Dentener, F., Muntean, M., Pouliot, G., Keating, T., Zhang, Q., Kurokawa, J., Wankmüller, R., Denier van der Gon, H., Kuenen, J. J. P., Klimont, Z., Frost, G., Darras, S., Koffi, B., and Li, M.: HTAP_v2.2: a mosaic of regional and global emission grid maps for 2008 and 2010 to study hemispheric transport of air pollution, Atmos. Chem. Phys., 15, 11411–11432, https://doi.org/10.5194/acp-15-11411-2015, 2015.

Karion, A., Sweeney, C., Tans, P., and Newberger, T.: AirCore: An Innovative Atmospheric Sampling System, J. Atmos. Ocean. Technol., 27, 1839–1853, https://doi.org/10.1175/2010JTECHA1448.1, 2010.

Keeling, C. D., Piper, S. C., Bacastow, R. B., Wahlen, M., Whorf, T. P., Heimann, M., and Meijer, H. A.: Exchanges of Atmospheric CO_2 and $^{13}CO_2$ with the Terrestrial Biosphere and Oceans from 1978 to 2000. I. Global Aspects, SIO Reference Series, No. 01-06, Scripps Institution of Oceanography, San Diego, 88 pp., 2001.

Keppel-Aleks, G., Wennberg, P. O., and Schneider, T.: Sources of variations in total column carbon dioxide, Atmos. Chem. Phys., 11, 3581–3593, https://doi.org/10.5194/acp-11-3581-2011, 2011.

Kiel, M., O'Dell, C. W., Fisher, B., Eldering, A., Nassar, R., MacDonald, C. G., and Wennberg, P. O.: How bias correction goes wrong: measurement of XCO_2 affected by erroneous surface pressure estimates, Atmos. Meas. Tech., 12, 2241–2259, https://doi.org/10.5194/amt-12-2241-2019, 2019.

Kiel, M., Eldering, A., Roten, D. D., Lin, J. C., Feng, S., Lei, R., Lauvaux, T., Oda, T., Roehl, C. M., Blavier, J.-F. and Iraci, L. T.: Urban-focused satellite CO_2 observations from the Orbiting Carbon Observatory-3: A first look at the Los Angeles megacity, Remote Sens. Environ., 258, 112314, doi:10.1016/j.rse.2021.112314, 2021.

Kim, J., Polavarapu, S. M., Chan, D., and Neish, M.: The Canadian atmospheric transport model for simulating greenhouse gas evolution on regional scales: GEM–MACH–GHG v.137-reg, Geosci. Model Dev., 13, 269–295, https://doi.org/10.5194/gmd-13-269-2020, 2020.

Kirschke, S., Bousquet, P., Ciais, P., Saunois, M., Canadell, J. G., Dlugokencky, E. J., Bergamaschi, P., Bergmann, D., Blake, D. R., Bruhwiler, L., Cameron-Smith, P., Castaldi, S., Chevallier, F., Feng, L., Fraser, A., Heimann, M., Hodson, E. L., Houweling, S., Josse, B., Fraser, P. J., Krummel, P. B., Lamarque, J.-F., Langenfelds, R. L., Le Quéré, C., Naik, V., O'Doherty, S., Palmer, P. I., Pison, I., Plummer, D., Poulter, B., Prinn, R. G., Rigby, M., Ringeval, B., Santini, M., Schmidt, M., Shindell, D. T., Simpson, I. J., Spahni, R., Steele, L. P., Strode, S. A., Sudo, K., Szopa, S., van der Werf, G. R., Voulgarakis, A., van Weele, M., Weiss, R. F., Williams, J. E., and Zeng, G.: Three decades of global methane sources and sinks, Nat. Geosci., 6, 813–823, https://doi.org/10.1038/ngeo1955, 2013.

Kivi, R., Heikkinen, P., and Kyrö, E.: TCCON data from Sodankylä (FI), Release GGG2014.R0, https://doi.org/10.14291/TCCON.GGG2014.SODANKYLA01.R0/1149280, 2014.

Kuai, L., Wunch, D., Shia, R.-L., Connor, B., Miller, C., and Yung, Y.: Vertically constrained CO_2 retrievals from TCCON measurements, J. Quant. Spectrosc. Radiat. Transf., 113, 1753–1761, https://doi.org/10.1016/j.jqsrt.2012.04.024, 2012.

Kulawik, S. S., Jones, D. B. A., Nassar, R., Irion, F. W., Worden, J. R., Bowman, K. W., Machida, T., Matsueda, H., Sawa, Y., Biraud, S. C., Fischer, M. L. and Jacobson, A. R.: Characterization of Tropospheric Emission Spectrometer (TES) CO_2 for carbon cycle science, Atmos. Chem. Phys., 10(12), 5601–5623, doi:10.5194/acp-10-5601-2010, 2010.

Kulawik, S. S., Worden, J. R., Wofsy, S. C., Biraud, S. C., Nassar, R., Jones, D. B. A., Olsen, E. T., Jimenez, R., Park, S., Santoni, G. W., Daube, B. C., Pittman, J. V., Stephens, B. B., Kort, E. A. and Osterman, G. B.: Comparison of improved Aura Tropospheric Emission Spectrometer CO_2 with HIPPO and SGP aircraft profile measurements, Atmos. Chem. Phys., 13(6), 3205–3225, doi:10.5194/acp-13-3205-2013, 2013.

Kulawik, S. S., Crowell, S., Baker, D., Liu, J., McKain, K., Sweeney, C., Biraud, S. C., Wofsy, S., O'Dell, C. W., Wennberg, P. O., Wunch, D., Roehl, C. M., Deutscher, N. M., Kiel, M., Griffith, D. W. T., Velazco, V. A., Notholt, J., Warneke, T., Petri, C., De Mazière, M., Sha, M. K., Sussmann, R., Rettinger, M., Pollard, D. F., Morino, I., Uchino, O., Hase, F., Feist, D. G., Roche, S., Strong, K., Kivi, R., Iraci, L., Shiomi, K., Dubey, M. K., Sepulveda, E., Rodriguez, O. E. G., Té, Y., Jeseck, P., Heikkinen, P., Dlugokencky, E. J., Gunson, M. R., Eldering, A., Crisp, D., Fisher, B., and Osterman, G. B.: Characterization of OCO-2 and ACOS-GOSAT biases and errors for CO_2 flux estimates, Atmos. Meas. Tech. Discuss., 2019, 1–61, https://doi.org/10.5194/amt-2019-257, 2019.

Kuze, A., Suto, H., Nakajima, M., and Hamazaki, T.: Thermal and near infrared sensor for carbon observation Fourier-transform spectrometer on the Greenhouse Gases Observing Satellite for greenhouse gases monitoring, Appl. Opt., 48, 6716, https://doi.org/10.1364/AO.48.006716, 2009.

Kuze, A., Suto, H., Shiomi, K., Kawakami, S., Tanaka, M., Ueda, Y., Deguchi, A., Yoshida, J., Yamamoto, Y., Kataoka, F., Taylor, T. E., and Buijs, H. L.: Update on GOSAT TANSO-FTS performance, operations, and data products after more than 6 years in space, Atmos. Meas. Tech., 9, 2445–2461, https://doi.org/10.5194/amt-9-2445-2016, 2016.

Lamouroux, J., Régalia, L., Thomas, X., Vander Auwera, J., Gamache, R. R., and Hartmann, J.-M.: CO_2 line-mixing database and software update and its tests in the 2.1 μm and 4.3 μm regions, J. Quant. Spectrosc. Radiat. Transf., 151, 88–96, https://doi.org/10.1016/j.jqsrt.2014.09.017, 2015.

Laughner, J., Andrews, A., Wunch, D., Roche, S., Kiel, M., Toon, G. C., ACE-FTS, ATom, AirCore, and Wennberg, P. O.: Revised formulation of the TCCON priors in GGG2020, (in prep), n.d.

di Lauro, C.: Nuclear Spin Statistical Weights, in: Rotational Structure in Molecular Infrared Spectra, Elsevier, 83–96, https://doi.org/10.1016/B978-0-12-821336-0.00005-5, 2020a.

di Lauro, C.: Rotational Structure in Molecular Infrared Spectra, Elsevier, https://doi.org/10.1016/c2019-0-00629-2, 2020b.

Lévy, A., Lacome, N., and Chackerian, C.: Collisional Line Mixing, in: Spectroscopy of the Earth's

Atmosphere and Interstellar Medium, edited by: Narahari Rao, K. and Weber, A., Academic Press Inc., San Diego, CA, 261–337, 1992.

Lindqvist, H., O'Dell, C. W., Basu, S., Boesch, H., Chevallier, F., Deutscher, N., Feng, L., Fisher, B., Hase, F., Inoue, M., Kivi, R., Morino, I., Palmer, P. I., Parker, R., Schneider, M., Sussmann, R. and Yoshida, Y.: Does GOSAT capture the true seasonal cycle of carbon dioxide?, Atmos. Chem. Phys., 15(22), 13023–13040, doi:10.5194/acp-15-13023-2015, 2015.

Liu, P. R. and Raftery, A. E.: Country-based rate of emissions reductions should increase by 80% beyond nationally determined contributions to meet the 2 °C target, Commun. Earth Environ., 2, 29, https://doi.org/10.1038/s43247-021-00097-8, 2021.

Liu, Y., Yang, D., and Cai, Z.: A retrieval algorithm for TanSat XCO_2 observation: Retrieval experiments using GOSAT data, Chinese Sci. Bull., 58, 1520–1523, https://doi.org/10.1007/s11434-013-5680-y, 2013.

López, M., Molina, J. C., Hofer, H., Sperling, A., and Kück, S.: Measurement of the nonlinearity of Ge- and InGaAs-photodiodes at high irradiance levels, 25, 47–52, https://doi.org/10.1007/s12647-010-0008-8, 2010.

Lucchesi, R.: File Specification for GEOS-5 FP-IT. GMAO Office Note No. 2 (Version 1.4), available from http://gmao.gsfc.nasa.gov/pubs/office_notes., 2015.

Lüthi, D., Le Floch, M., Bereiter, B., Blunier, T., Barnola, J.-M., Siegenthaler, U., Raynaud, D., Jouzel, J., Fischer, H., Kawamura, K., and Stocker, T. F.: High-resolution carbon dioxide concentration record 650,000–800,000 years before present, Nature, 453, 379–382, https://doi.org/10.1038/nature06949, 2008.

MacGilchrist, G. A., Naveira Garabato, A. C., Tsubouchi, T., Bacon, S., Torres-Valdés, S., and Azetsu-Scott, K.: The Arctic Ocean carbon sink, Deep Sea Res. Part I Oceanogr. Res. Pap., 86, 39–55, https://doi.org/10.1016/j.dsr.2014.01.002, 2014.

Maddy, E. S., Barnet, C. D., Goldberg, M., Sweeney, C. and Liu, X.: CO_2 retrievals from the Atmospheric Infrared Sounder: Methodology and validation, J. Geophys. Res., 113(D11), D11301, doi:10.1029/2007JD009402, 2008.

Malathy Devi, V., Benner, D. C., Brown, L. R., Miller, C. E., and Toth, R. A.: Line mixing and speed dependence in CO_2 at 6348 cm_{-1}: Positions, intensities, and air- and self-broadening derived with constrained multispectrum analysis, J. Mol. Spectrosc., 242, 90–117, https://doi.org/10.1016/j.jms.2007.02.018, 2007.

Manney, G. L., Zurek, R. W., O'Neill, A., and Swinbank, R.: On the Motion of Air through the Stratospheric Polar Vortex, J. Atmos. Sci., 51, 2973–2994, https://doi.org/10.1175/1520-0469(1994)051<2973:OTMOAT>2.0.CO;2, 1994.

Masson-Delmotte, V., Schulz, M., Abe-Ouchi, A., Beer, J., Ganopolski, A., González Rouco, J. F., Jansen, E., Lambeck, K., Luterbacher, J., Naish, T., Osborn, T., Otto-Bliesner, B., Quinn, T., Ramesh, R., Rojas, M., Shao, X., and Timmermann, A.: Information from Paleoclimate Archives, in: Climate Change 2013 - The Physical Science Basis, edited by: Intergovernmental Panel on Climate Change, Cambridge University Press, Cambridge, United Kingdom and New York, NY, USA, 383–464, https://doi.org/10.1017/CBO9781107415324.013, 2013.

McDuffie, J., Bowman, K. ~W., Hobbs, J., Natraj, V., Val, S., Sarkissian, E., and Thill, M. ~D.:

ReFRACtor: Reusable Software Framework for Retrieval of Satellite Atmospheric Composition, in: AGU Fall Meeting Abstracts, A11F-2282, 2018.

McGuire, A. D., Anderson, L. G., Christensen, T. R., Dallimore, S., Guo, L., Hayes, D. J., Heimann, M., Lorenson, T. D., Macdonald, R. W., and Roulet, N.: Sensitivity of the carbon cycle in the Arctic to climate change, Ecol. Monogr., 79, 523–555, https://doi.org/10.1890/08-2025.1, 2009.

McGuire, A. D., Christensen, T. R., Hayes, D., Heroult, A., Euskirchen, E., Kimball, J. S., Koven, C., Lafleur, P., Miller, P. A., Oechel, W., Peylin, P., Williams, M., and Yi, Y.: An assessment of the carbon balance of Arctic tundra: comparisons among observations, process models, and atmospheric inversions, 9, 3185–3204, https://doi.org/10.5194/bg-9-3185-2012, 2012.

McKenna, D. S.: A new Chemical Lagrangian Model of the Stratosphere (CLaMS) 1. Formulation of advection and mixing, J. Geophys. Res., 107, 4309, https://doi.org/10.1029/2000JD000114, 2002.

Mendonca, J., Strong, K., Toon, G. C., Wunch, D., Sung, K., Deutscher, N. M., Griffith, D. W. T., and Franklin, J. E.: Improving atmospheric CO_2 retrievals using line mixing and speed-dependence when fitting high-resolution ground-based solar spectra, J. Mol. Spectrosc., 323, 15–27, https://doi.org/10.1016/j.jms.2016.01.007, 2016.

Mendonca, J., Strong, K., Sung, K., Devi, V. M., Toon, G. C., Wunch, D., and Franklin, J. E.: Using high-resolution laboratory and ground-based solar spectra to assess CH_4 absorption coefficient calculations, J. Quant. Spectrosc. Radiat. Transf., 190, 48–59, https://doi.org/10.1016/j.jqsrt.2016.12.013, 2017.

Mendonca, J., Strong, K., Wunch, D., Toon, G. C., Long, D. A., Hodges, J. T., Sironneau, V. T., and Franklin, J. E.: Using a speed-dependent Voigt line shape to retrieve O_2 from Total Carbon Column Observing Network solar spectra to improve measurements of XCO&lt;sub&gt;2&lt;/sub&gt;, Atmos. Meas. Tech., 12, 35–50, https://doi.org/10.5194/amt-12-35-2019, 2019.

Merrelli, A., Bennartz, R., O’Dell, C. W., and Taylor, T. E.: Estimating bias in the OCO-2 retrieval algorithm caused by 3-D radiation scattering from unresolved boundary layer clouds, Atmos. Meas. Tech., 8, 1641–1656, https://doi.org/10.5194/amt-8-1641-2015, 2015.

Michelson, A. A. and Morley, E. W.: On the relative motion of the Earth and the luminiferous ether, Am. J. Sci., s3-34, 333–345, https://doi.org/10.2475/ajs.s3-34.203.333, 1887.

Miller, C. E., Crisp, D., DeCola, P. L., Olsen, S. C., Randerson, J. T., Michalak, A. M., Alkhaled, A., Rayner, P., Jacob, D. J., Suntharalingam, P., Jones, D. B. A., Denning, A. S., Nicholls, M. E., Doney, S. C., Pawson, S., Boesch, H., Connor, B. J., Fung, I. Y., O’Brien, D., Salawitch, R. J., Sander, S. P., Sen, B., Tans, P., Toon, G. C., Wennberg, P. O., Wofsy, S. C., Yung, Y. L., and Law, R. M.: Precision requirements for space-based data, J. Geophys. Res. Atmos., 112, https://doi.org/10.1029/2006JD007659, 2007.

Montzka, S. A., Dutton, G. S., Yu, P., Ray, E., Portmann, R. W., Daniel, J. S., Kuijpers, L., Hall, B. D., Mondeel, D., Siso, C., Nance, J. D., Rigby, M., Manning, A. J., Hu, L., Moore, F., Miller, B. R., and Elkins, J. W.: An unexpected and persistent increase in global emissions of ozone-depleting CFC-11, Nature, 557, 413–417, https://doi.org/10.1038/s41586-018-0106-2, 2018.

Montzka, S. A., Dutton, G. S., Portmann, R. W., Chipperfield, M. P., Davis, S., Feng, W., Manning, A.

J., Ray, E., Rigby, M., Hall, B. D., Siso, C., Nance, J. D., Krummel, P. B., Mühle, J., Young, D., O’Doherty, S., Salameh, P. K., Harth, C. M., Prinn, R. G., Weiss, R. F., Elkins, J. W., Walter-Terrinoni, H., and Theodoridi, C.: A decline in global CFC-11 emissions during 2018−2019, Nature, 590, 428–432, https://doi.org/10.1038/s41586-021-03260-5, 2021.

Moore III, B., Crowell, S. M. R., Rayner, P. J., Kumer, J., O’Dell, C. W., O’Brien, D., Utembe, S., Polonsky, I., Schimel, D., and Lemen, J.: The Potential of the Geostationary Carbon Cycle Observatory (GeoCarb) to Provide Multi-scale Constraints on the Carbon Cycle in the Americas, Front. Environ. Sci., 6, 109, https://doi.org/10.3389/fenvs.2018.00109, 2018.

Moran, M., Ménard, S., Talbot, D., Huang, P., Makar, P., Gong, wf, Landry, H., Gravel, S., Gong, S., Crevier, L.-P., Kallaur, A., and Sassi, M.: Particulate-matter forecasting with GEM-MACH15, a new Canadian air-quality forecast model, Air Pollut. Model. Its Appl. XX, 289-292M, 2010.

Myhre, G. D., Shindell, D., Bréon, F., Collins, W., Fuglestvedt, J., Huang, J., Koch, D., Lamarque, J., Lee, D., Mendoza, B., Nakajima, T., Robock, A., Stephens, G., Takemura, T., Zhang, H., Qin, D., Plattner, G., Tignor, M., Allen, S., Boschung, J., Nauels, A., Xia, Y., Bex, V., and Midgley, P.: Anthropogenic and Natural Radiative Forcing, in: Climate Change 2013 - The Physical Science Basis, edited by: Intergovernmental Panel on Climate Change, Cambridge University Press, Cambridge, United Kingdom and New York, NY, USA, 659–740, https://doi.org/10.1017/CBO9781107415324.018, 2013.

Nakajima, M., Kuze, A., and Suto, H.: The current status of GOSAT and the concept of GOSAT-2, in: Sensors, Systems, and Next-Generation Satellites XVI, 853306, https://doi.org/10.1117/12.974954, 2012.

Nassar, R., McLinden, C., Sioris, C. E., McElroy, C. T., Mendonca, J., Tamminen, J., MacDonald, C. G., Adams, C., Boisvenue, C., Bourassa, A., Cooney, R., Degenstein, D., Drolet, G., Garand, L., Girard, R., Johnson, M., Jones, D. B. A., Kolonjari, F., Kuwahara, B., Martin, R. V., Miller, C. E., O’Neill, N., Riihelä, A., Roche, S., Sander, S. P., Simpson, W. R., Singh, G., Strong, K., Trishchenko, A. P., van Mierlo, H., Zanjani, Z. V., Walker, K. A., and Wunch, D.: The Atmospheric Imaging Mission for Northern Regions: AIM-North, Can. J. Remote Sens., 45, 423–442, https://doi.org/10.1080/07038992.2019.1643707, 2019.

Naylor, D. A. and Tahic, M. K.: Apodizing functions for Fourier transform spectroscopy, J. Opt. Soc. Am. A, 24, 3644–3648, https://doi.org/10.1364/JOSAA.24.003644, 2007.

Nelson, R. R. and O’Dell, C. W.: The impact of improved aerosol priors on near-infrared measurements of carbon dioxide, Atmos. Meas. Tech., 12, 1495–1512, https://doi.org/10.5194/AMT-12-1495-2019, 2019.

Neuman, C. P. and Schonbach, D. I.: Discrete (Legendre) orthogonal polynomials-a survey, Int. J. Numer. Methods Eng., 8, 743–770, https://doi.org/10.1002/nme.1620080406, 1974.

Ngo, N. H., Lisak, D., Tran, H., and Hartmann, J.-M.: An isolated line-shape model to go beyond the Voigt profile in spectroscopic databases and radiative transfer codes, J. Quant. Spectrosc. Radiat. Transf., 129, 89–100, https://doi.org/10.1016/j.jqsrt.2013.05.034, 2013.

Nisbet, E. G., Dlugokencky, E. J., Manning, M. R., Lowry, D., Fisher, R. E., France, J. L., Michel, S. E., Miller, J. B., White, J. W. C., Vaughn, B., Bousquet, P., Pyle, J. A., Warwick, N. J., Cain, M., Brownlow, R., Zazzeri, G., Lanoisellé, M., Manning, A. C., Gloor, E., Worthy, D. E. J., Brunke, E.-G., Labuschagne, C., Wolff, E. W., and Ganesan, A. L.: Rising atmospheric methane: 2007-

2014 growth and isotopic shift, Global Biogeochem. Cycles, 30, 1356–1370, https://doi.org/10.1002/2016GB005406, 2016.

Notholt, J., Petri, C., Warneke, T., Deutscher, N. M., Palm, M., Buschmann, M., Weinzierl, C., Macatangay, R. C., and Grupe, P.: TCCON data from Bremen (DE), Release GGG2014.R1, https://doi.org/10.14291/TCCON.GGG2014.BREMEN01.R1, 2019.

O'Brien, D. M., Polonsky, I. N., Utembe, S. R., and Rayner, P. J.: Potential of a geostationary geoCARB mission to estimate surface emissions of CO_2, CH_4 and CO in a polluted urban environment: case study Shanghai, Atmos. Meas. Tech., 9, 4633–4654, https://doi.org/10.5194/amt-9-4633-2016, 2016.

O'Dell, C. W., Connor, B., Bösch, H., O'Brien, D., Frankenberg, C., Castano, R., Christi, M., Eldering, D., Fisher, B., Gunson, M., McDuffie, J., Miller, C. E., Natraj, V., Oyafuso, F., Polonsky, I., Smyth, M., Taylor, T., Toon, G. C., Wennberg, P. O., and Wunch, D.: The ACOS CO_2 retrieval algorithm – Part 1: Description and validation against synthetic observations, Atmos. Meas. Tech., 5, 99–121, https://doi.org/10.5194/amt-5-99-2012, 2012.

O'Dell, C. W., Eldering, A., Wennberg, P. O., Crisp, D., Gunson, M. R., Fisher, B., Frankenberg, C., Kiel, M., Lindqvist, H., Mandrake, L., Merrelli, A., Natraj, V., Nelson, R. R., Osterman, G. B., Payne, V. H., Taylor, T. E., Wunch, D., Drouin, B. J., Oyafuso, F., Chang, A., McDuffie, J., Smyth, M., Baker, D. F., Basu, S., Chevallier, F., Crowell, S. M. R., Feng, L., Palmer, P. I., Dubey, M., García, O. E., Griffith, D. W. T., Hase, F., Iraci, L. T., Kivi, R., Morino, I., Notholt, J., Ohyama, H., Petri, C., Roehl, C. M., Sha, M. K., Strong, K., Sussmann, R., Te, Y., Uchino, O., and Velazco, V. A.: Improved retrievals of carbon dioxide from Orbiting Carbon Observatory-2 with the version 8 ACOS algorithm, Atmos. Meas. Tech., 11, 6539–6576, https://doi.org/10.5194/amt-11-6539-2018, 2018.

Parazoo, N. C., Denning, A. S., Kawa, S. R., Pawson, S., and Lokupitiya, R.: CO_2 flux estimation errors associated with moist atmospheric processes, Atmos. Chem. Phys., 12, 6405–6416, https://doi.org/10.5194/acp-12-6405-2012, 2012.

Peters, G. P., Andrew, R. M., Boden, T., Canadell, J. G., Ciais, P., Le Quéré, C., Marland, G., Raupach, M. R., and Wilson, C.: The challenge to keep global warming below 2 °C, Nat. Clim. Chang., 3, 4–6, https://doi.org/10.1038/nclimate1783, 2013.

Peters, W., Jacobson, A. R., Sweeney, C., Andrews, A. E., Conway, T. J., Masarie, K., Miller, J. B., Bruhwiler, L. M. P., Petron, G., Hirsch, A. I., Worthy, D. E. J., van der Werf, G. R., Randerson, J. T., Wennberg, P. O., Krol, M. C., and Tans, P. P.: An atmospheric perspective on North American carbon dioxide exchange: CarbonTracker, Proc. Natl. Acad. Sci., 104, 18925–18930, https://doi.org/10.1073/pnas.0708986104, 2007.

Peylin, P., Law, R. M., Gurney, K. R., Chevallier, F., Jacobson, A. R., Maki, T., Niwa, Y., Patra, P. K., Peters, W., Rayner, P. J., Rödenbeck, C., van der Laan-Luijkx, I. T., and Zhang, X.: Global atmospheric carbon budget: results from an ensemble of atmospheric CO_2 inversions, 10, 6699–6720, https://doi.org/10.5194/bg-10-6699-2013, 2013.

Pistone, K., Eisenman, I., and Ramanathan, V.: Observational determination of albedo decrease caused by vanishing Arctic sea ice, Proc. Natl. Acad. Sci., 111, 3322–3326, https://doi.org/10.1073/pnas.1318201111, 2014.

Polavarapu, S. M., Neish, M., Tanguay, M., Girard, C., de Grandpré, J., Semeniuk, K., Gravel, S., Ren, S., Roche, S., Chan, D., and Strong, K.: Greenhouse gas simulations with a coupled meteorological and transport model: the predictability of CO_2, Atmos. Chem. Phys., 16, 12005–12038, https://doi.org/10.5194/acp-16-12005-2016, 2016.

Prather, M. J., Holmes, C. D., and Hsu, J.: Reactive greenhouse gas scenarios: Systematic exploration of uncertainties and the role of atmospheric chemistry, Geophys. Res. Lett., 39, https://doi.org/10.1029/2012GL051440, 2012.

Predoi-Cross, A., McKellar, A. R. W., Benner, D. C., Devi, V. M., Gamache, R. R., Miller, C. E., Toth, R. A., and Brown, L. R.: Temperature dependences for air-broadened Lorentz half-width and pressure shift coefficients in the 30013←00001 and 30012←00001 bands of CO_2 near 1600 nm This article is part of a Special Issue on Spectroscopy at the University of New Brunswick, Can. J. Phys., 87, 517–535, https://doi.org/10.1139/P08-137, 2009.

Le Quéré, C., Andres, R. J., Boden, T., Conway, T., Houghton, R. A., House, J. I., Marland, G., Peters, G. P., van der Werf, G. R., Ahlström, A., Andrew, R. M., Bopp, L., Canadell, J. G., Ciais, P., Doney, S. C., Enright, C., Friedlingstein, P., Huntingford, C., Jain, A. K., Jourdain, C., Kato, E., Keeling, R. F., Klein Goldewijk, K., Levis, S., Levy, P., Lomas, M., Poulter, B., Raupach, M. R., Schwinger, J., Sitch, S., Stocker, B. D., Viovy, N., Zaehle, S., and Zeng, N.: The global carbon budget 1959–2011, Earth Syst. Sci. Data, 5, 165–185, https://doi.org/10.5194/essd-5-165-2013, 2013.

Le Quéré, C., Peters, G. P., Andres, R. J., Andrew, R. M., Boden, T. A., Ciais, P., Friedlingstein, P., Houghton, R. A., Marland, G., Moriarty, R., Sitch, S., Tans, P., Arneth, A., Arvanitis, A., Bakker, D. C. E., Bopp, L., Canadell, J. G., Chini, L. P., Doney, S. C., Harper, A., Harris, I., House, J. I., Jain, A. K., Jones, S. D., Kato, E., Keeling, R. F., Klein Goldewijk, K., Körtzinger, A., Koven, C., Lefèvre, N., Maignan, F., Omar, A., Ono, T., Park, G.-H., Pfeil, B., Poulter, B., Raupach, M. R., Regnier, P., Rödenbeck, C., Saito, S., Schwinger, J., Segschneider, J., Stocker, B. D., Takahashi, T., Tilbrook, B., van Heuven, S., Viovy, N., Wanninkhof, R., Wiltshire, A., and Zaehle, S.: Global carbon budget 2013, Earth Syst. Sci. Data, 6, 235–263, https://doi.org/10.5194/essd-6-235-2014, 2014.

Le Quéré, C., Moriarty, R., Andrew, R. M., Peters, G. P., Ciais, P., Friedlingstein, P., Jones, S. D., Sitch, S., Tans, P., Arneth, A., Boden, T. A., Bopp, L., Bozec, Y., Canadell, J. G., Chini, L. P., Chevallier, F., Cosca, C. E., Harris, I., Hoppema, M., Houghton, R. A., House, J. I., Jain, A. K., Johannessen, T., Kato, E., Keeling, R. F., Kitidis, V., Klein Goldewijk, K., Koven, C., Landa, C. S., Landschützer, P., Lenton, A., Lima, I. D., Marland, G., Mathis, J. T., Metzl, N., Nojiri, Y., Olsen, A., Ono, T., Peng, S., Peters, W., Pfeil, B., Poulter, B., Raupach, M. R., Regnier, P., Rödenbeck, C., Saito, S., Salisbury, J. E., Schuster, U., Schwinger, J., Séférian, R., Segschneider, J., Steinhoff, T., Stocker, B. D., Sutton, A. J., Takahashi, T., Tilbrook, B., van der Werf, G. R., Viovy, N., Wang, Y.-P., Wanninkhof, R., Wiltshire, A., and Zeng, N.: Global carbon budget 2014, Earth Syst. Sci. Data, 7, 47–85, https://doi.org/10.5194/essd-7-47-2015, 2015a.

Le Quéré, C., Moriarty, R., Andrew, R. M., Canadell, J. G., Sitch, S., Korsbakken, J. I., Friedlingstein, P., Peters, G. P., Andres, R. J., Boden, T. A., Houghton, R. A., House, J. I., Keeling, R. F., Tans, P., Arneth, A., Bakker, D. C. E., Barbero, L., Bopp, L., Chang, J., Chevallier, F., Chini, L. P., Ciais, P., Fader, M., Feely, R. A., Gkritzalis, T., Harris, I., Hauck, J., Ilyina, T., Jain, A. K., Kato, E., Kitidis, V., Klein Goldewijk, K., Koven, C., Landschützer, P., Lauvset, S. K., Lefèvre, N., Lenton, A., Lima, I. D., Metzl, N., Millero, F., Munro, D. R., Murata, A., Nabel, J. E. M. S., Nakaoka, S., Nojiri, Y., O'Brien, K., Olsen, A., Ono, T., Pérez, F. F., Pfeil, B., Pierrot, D., Poulter, B., Rehder, G., Rödenbeck, C., Saito, S., Schuster, U., Schwinger, J., Séférian, R., Steinhoff, T., Stocker, B. D., Sutton, A. J., Takahashi, T., Tilbrook, B., van der Laan-Luijkx, I. T., van der Werf, G. R., van Heuven, S., Vandemark, D., Viovy, N., Wiltshire, A., Zaehle, S., and Zeng, N.: Global Carbon Budget 2015, Earth Syst. Sci. Data, 7, 349–396, https://doi.org/10.5194/essd-7-349-2015, 2015b.

Le Quéré, C., Andrew, R. M., Canadell, J. G., Sitch, S., Korsbakken, J. I., Peters, G. P., Manning, A. C., Boden, T. A., Tans, P. P., Houghton, R. A., Keeling, R. F., Alin, S., Andrews, O. D., Anthoni, P., Barbero, L., Bopp, L., Chevallier, F., Chini, L. P., Ciais, P., Currie, K., Delire, C., Doney, S. C., Friedlingstein, P., Gkritzalis, T., Harris, I., Hauck, J., Haverd, V., Hoppema, M., Klein Goldewijk, K., Jain, A. K., Kato, E., Körtzinger, A., Landschützer, P., Lefèvre, N., Lenton, A., Lienert, S., Lombardozzi, D., Melton, J. R., Metzl, N., Millero, F., Monteiro, P. M. S., Munro, D. R., Nabel, J. E. M. S., Nakaoka, S., O’Brien, K., Olsen, A., Omar, A. M., Ono, T., Pierrot, D., Poulter, B., Rödenbeck, C., Salisbury, J., Schuster, U., Schwinger, J., Séférian, R., Skjelvan, I., Stocker, B. D., Sutton, A. J., Takahashi, T., Tian, H., Tilbrook, B., van der Laan-Luijkx, I. T., van der Werf, G. R., Viovy, N., Walker, A. P., Wiltshire, A. J., and Zaehle, S.: Global Carbon Budget 2016, Earth Syst. Sci. Data, 8, 605–649, https://doi.org/10.5194/essd-8-605-2016, 2016.

Le Quéré, C., Andrew, R. M., Friedlingstein, P., Sitch, S., Pongratz, J., Manning, A. C., Korsbakken, J. I., Peters, G. P., Canadell, J. G., Jackson, R. B., Boden, T. A., Tans, P. P., Andrews, O. D., Arora, V. K., Bakker, D. C. E., Barbero, L., Becker, M., Betts, R. A., Bopp, L., Chevallier, F., Chini, L. P., Ciais, P., Cosca, C. E., Cross, J., Currie, K., Gasser, T., Harris, I., Hauck, J., Haverd, V., Houghton, R. A., Hunt, C. W., Hurtt, G., Ilyina, T., Jain, A. K., Kato, E., Kautz, M., Keeling, R. F., Klein Goldewijk, K., Körtzinger, A., Landschützer, P., Lefèvre, N., Lenton, A., Lienert, S., Lima, I., Lombardozzi, D., Metzl, N., Millero, F., Monteiro, P. M. S., Munro, D. R., Nabel, J. E. M. S., Nakaoka, S., Nojiri, Y., Padin, X. A., Peregon, A., Pfeil, B., Pierrot, D., Poulter, B., Rehder, G., Reimer, J., Rödenbeck, C., Schwinger, J., Séférian, R., Skjelvan, I., Stocker, B. D., Tian, H., Tilbrook, B., Tubiello, F. N., van der Laan-Luijkx, I. T., van der Werf, G. R., van Heuven, S., Viovy, N., Vuichard, N., Walker, A. P., Watson, A. J., Wiltshire, A. J., Zaehle, S., and Zhu, D.: Global Carbon Budget 2017, Earth Syst. Sci. Data, 10, 405–448, https://doi.org/10.5194/essd-10-405-2018, 2018a.

Le Quéré, C., Andrew, R. M., Friedlingstein, P., Sitch, S., Hauck, J., Pongratz, J., Pickers, P. A., Korsbakken, J. I., Peters, G. P., Canadell, J. G., Arneth, A., Arora, V. K., Barbero, L., Bastos, A., Bopp, L., Chevallier, F., Chini, L. P., Ciais, P., Doney, S. C., Gkritzalis, T., Goll, D. S., Harris, I., Haverd, V., Hoffman, F. M., Hoppema, M., Houghton, R. A., Hurtt, G., Ilyina, T., Jain, A. K., Johannessen, T., Jones, C. D., Kato, E., Keeling, R. F., Goldewijk, K. K., Landschützer, P., Lefèvre, N., Lienert, S., Liu, Z., Lombardozzi, D., Metzl, N., Munro, D. R., Nabel, J. E. M. S., Nakaoka, S., Neill, C., Olsen, A., Ono, T., Patra, P., Peregon, A., Peters, W., Peylin, P., Pfeil, B., Pierrot, D., Poulter, B., Rehder, G., Resplandy, L., Robertson, E., Rocher, M., Rödenbeck, C., Schuster, U., Schwinger, J., Séférian, R., Skjelvan, I., Steinhoff, T., Sutton, A., Tans, P. P., Tian, H., Tilbrook, B., Tubiello, F. N., van der Laan-Luijkx, I. T., van der Werf, G. R., Viovy, N., Walker, A. P., Wiltshire, A. J., Wright, R., Zaehle, S., and Zheng, B.: Global Carbon Budget 2018, Earth Syst. Sci. Data, 10, 2141–2194, https://doi.org/10.5194/essd-10-2141-2018, 2018b.

Ravishankara, A. R., Daniel, J. S., and Portmann, R. W.: Nitrous Oxide (N_2O): The Dominant Ozone-Depleting Substance Emitted in the 21st Century, Science, 326, 123–125, https://doi.org/10.1126/science.1176985, 2009.

Rayner, P. J. and O'Brien, D. M.: The utility of remotely sensed CO_2 concentration data in surface source inversions, Geophys. Res. Lett., 28, 175–178, https://doi.org/10.1029/2000GL011912, 2001.

Reuter, M., Bösch, H., Bovensmann, H., Bril, A., Buchwitz, M., Butz, A., Burrows, J. P., O'Dell, C. W., Guerlet, S., Hasekamp, O., Heymann, J., Kikuchi, N., Oshchepkov, S., Parker, R., Pfeifer, S., Schneising, O., Yokota, T., and Yoshida, Y.: A joint effort to deliver satellite retrieved atmospheric CO_2 concentrations for surface flux inversions: the ensemble median algorithm EMMA, Atmos. Chem. Phys., 13, 1771–1780, https://doi.org/10.5194/acp-13-1771-2013, 2013.

Reuter, M., Buchwitz, M., Schneising, O., Noël, S., Bovensmann, H., Burrows, J. P., Boesch, H., Di Noia, A., Anand, J., Parker, R. J., Somkuti, P., Wu, L., Hasekamp, O. P., Aben, I., Kuze, A., Suto, H., Shiomi, K., Yoshida, Y., Morino, I., Crisp, D., O'Dell, C. W., Notholt, J., Petri, C., Warneke, T., Velazco, V. A., Deutscher, N. M., Griffith, D. W. T., Kivi, R., Pollard, D. F., Hase, F., Sussmann, R., Té, Y. V., Strong, K., Roche, S., Sha, M. K., De Mazière, M., Feist, D. G., Iraci, L. T., Roehl, C. M., Retscher, C., and Schepers, D.: Ensemble-based satellite-derived carbon dioxide and methane column-averaged dry-air mole fraction data sets (2003–2018) for carbon and climate applications, Atmos. Meas. Tech., 13, 789–819, https://doi.org/10.5194/amt-13-789-2020, 2020.

Rigby, M., Montzka, S. A., Prinn, R. G., White, J. W. C., Young, D., O'Doherty, S., Lunt, M. F., Ganesan, A. L., Manning, A. J., Simmonds, P. G., Salameh, P. K., Harth, C. M., Mühle, J., Weiss, R. F., Fraser, P. J., Steele, L. P., Krummel, P. B., McCulloch, A., and Park, S.: Role of atmospheric oxidation in recent methane growth, Proc. Natl. Acad. Sci., 114, 5373–5377, https://doi.org/10.1073/pnas.1616426114, 2017.

Roche, S., Strong, K., Wunch, D., Mendonca, J., Sweeney, C., Baier, B., Biraud, S. C., Laughner, J. L., Toon, G. C., and Connor, B. J.: Retrieval of atmospheric CO_2 vertical profiles from ground-based near-infrared spectra, Atmos. Meas. Tech., 14, 3087–3118, https://doi.org/10.5194/amt-14-3087-2021, 2021.

Rodgers, C. D.: Characterization and error analysis of profiles retrieved from remote sounding measurements, J. Geophys. Res., 95, 5587, https://doi.org/10.1029/JD095iD05p05587, 1990.

Rodgers, C. D.: Inverse Methods for Atmospheric Sounding, world scientific, https://doi.org/10.1142/3171, 2000.

Rodgers, C. D. and Connor, B. J.: Intercomparison of remote sounding instruments, J. Geophys. Res. Atmos., 108, https://doi.org/10.1029/2002JD002299, 2003.

Rosenkranz, P.: Shape of the 5 mm oxygen band in the atmosphere, IEEE Trans. Antennas Propag., 23, 498–506, https://doi.org/10.1109/TAP.1975.1141119, 1975.

Rothman, L. S., Rinsland, C. P., Goldman, A., Massie, S. T., Edwards, D. P., Flaud, J. M., Perrin, A., Camy-Peyret, C., Dana, V., Mandin, J. Y., Schroeder, J., McCann, A., Gamache, R. R., Wattson, R. B., Yoshino, K., Chance, K. V., Jucks, K. W., Brown, L. R., Nemtchinov, V., and Varanasi, P.: The HITRAN molecular spectroscopic database and HAWKS (HITRAN Atmospheric Workstation): 1996 edition, J. Quant. Spectrosc. Radiat. Transf., 60, 665–710, https://doi.org/10.1016/S0022-4073(98)00078-8, 1998.

Rothman, L. S., Jacquemart, D., Barbe, A., Chris Benner, D., Birk, M., Brown, L. R., Carleer, M. R., Chackerian, C., Chance, K., Coudert, L. H., Dana, V., Devi, V. M., Flaud, J.-M., Gamache, R.

R., Goldman, A., Hartmann, J.-M., Jucks, K. W., Maki, A. G., Mandin, J.-Y., Massie, S. T., Orphal, J., Perrin, A., Rinsland, C. P., Smith, M. A. H., Tennyson, J., Tolchenov, R. N., Toth, R. A., Vander Auwera, J., Varanasi, P., and Wagner, G.: The HITRAN 2004 molecular spectroscopic database, J. Quant. Spectrosc. Radiat. Transf., 96, 139–204, https://doi.org/10.1016/j.jqsrt.2004.10.008, 2005.

Rothman, L. S., Gordon, I. E., Barbe, A., Benner, D. C., Bernath, P. F., Birk, M., Boudon, V., Brown, L. R., Campargue, A., Champion, J.-P., Chance, K., Coudert, L. H., Dana, V., Devi, V. M., Fally, S., Flaud, J.-M., Gamache, R. R., Goldman, A., Jacquemart, D., Kleiner, I., Lacome, N., Lafferty, W. J., Mandin, J.-Y., Massie, S. T., Mikhailenko, S. N., Miller, C. E., Moazzen-Ahmadi, N., Naumenko, O. V., Nikitin, A. V., Orphal, J., Perevalov, V. I., Perrin, A., Predoi-Cross, A., Rinsland, C. P., Rotger, M., Šimečková, M., Smith, M. A. H., Sung, K., Tashkun, S. A., Tennyson, J., Toth, R. A., Vandaele, A. C., and Vander Auwera, J.: The HITRAN 2008 molecular spectroscopic database, J. Quant. Spectrosc. Radiat. Transf., 110, 533–572, https://doi.org/10.1016/j.jqsrt.2009.02.013, 2009.

Rothman, L. S., Gordon, I. E., Babikov, Y., Barbe, A., Chris Benner, D., Bernath, P. F., Birk, M., Bizzocchi, L., Boudon, V., Brown, L. R., Campargue, A., Chance, K., Cohen, E. A., Coudert, L. H., Devi, V. M., Drouin, B. J., Fayt, A., Flaud, J.-M., Gamache, R. R., Harrison, J. J., Hartmann, J.-M., Hill, C., Hodges, J. T., Jacquemart, D., Jolly, A., Lamouroux, J., Le Roy, R. J., Li, G., Long, D. A., Lyulin, O. M., Mackie, C. J., Massie, S. T., Mikhailenko, S., Müller, H. S. P., Naumenko, O. V., Nikitin, A. V., Orphal, J., Perevalov, V., Perrin, A., Polovtseva, E. R., Richard, C., Smith, M. A. H., Starikova, E., Sung, K., Tashkun, S., Tennyson, J., Toon, G. C., Tyuterev, V. G., and Wagner, G.: The HITRAN2012 molecular spectroscopic database, J. Quant. Spectrosc. Radiat. Transf., 130, 4–50, https://doi.org/10.1016/j.jqsrt.2013.07.002, 2013.

Sabine, C. L.: The Oceanic Sink for Anthropogenic CO_2, Science, 305, 367–371, https://doi.org/10.1126/science.1097403, 2004.

Schädel, C., Bader, M. K. F., Schuur, E. A. G., Biasi, C., Bracho, R., Čapek, P., De Baets, S., Diáková, K., Ernakovich, J., Estop-Aragones, C., Graham, D. E., Hartley, I. P., Iversen, C. M., Kane, E., Knoblauch, C., Lupascu, M., Martikainen, P. J., Natali, S. M., Norby, R. J., O'Donnell, J. A., Chowdhury, T. R., Šantrůčková, H., Shaver, G., Sloan, V. L., Treat, C. C., Turetsky, M. R., Waldrop, M. P., and Wickland, K. P.: Potential carbon emissions dominated by carbon dioxide from thawed permafrost soils, Nat. Clim. Chang., 6, 950–953, https://doi.org/10.1038/nclimate3054, 2016.

Schädel, C., Koven, C. D., Lawrence, D. M., Celis, G., Garnello, A. J., Hutchings, J., Mauritz, M., Natali, S. M., Pegoraro, E., Rodenhizer, H., Salmon, V. G., Taylor, M. A., Webb, E. E., Wieder, W. R., and Schuur, E. A. G.: Divergent patterns of experimental and model-derived permafrost ecosystem carbon dynamics in response to Arctic warming, Environ. Res. Lett., 13, 105002, https://doi.org/10.1088/1748-9326/aae0ff, 2018.

Schimel, D., Pavlick, R., Fisher, J. B., Asner, G. P., Saatchi, S., Townsend, P., Miller, C., Frankenberg, C., Hibbard, K., and Cox, P.: Observing terrestrial ecosystems and the carbon cycle from space, Glob. Chang. Biol., 21, 1762–1776, https://doi.org/10.1111/gcb.12822, 2015.

Schneising, O., Buchwitz, M., Reuter, M., Heymann, J., Bovensmann, H. and Burrows, J. P.: Long-term analysis of carbon dioxide and methane column-averaged mole fractions retrieved from SCIAMACHY, Atmos. Chem. Phys., 11(6), 2863–2880, doi:10.5194/acp-11-2863-2011, 2011.

Schneising, O., Buchwitz, M., Reuter, M., Bovensmann, H., Burrows, J. P., Borsdorff, T., Deutscher, N. M., Feist, D. G., Griffith, D. W. T., Hase, F., Hermans, C., Iraci, L. T., Kivi, R., Landgraf, J., Morino, I., Notholt, J., Petri, C., Pollard, D. F., Roche, S., Shiomi, K., Strong, K., Sussmann, R., Velazco, V. A., Warneke, T., and Wunch, D.: A scientific algorithm to simultaneously retrieve carbon monoxide and methane from TROPOMI onboard Sentinel-5 Precursor, Atmos. Meas. Tech., 12, 6771–6802, https://doi.org/10.5194/amt-12-6771-2019, 2019.

Schoolmeester, T., Gjerdi, H. L., Crump, J., Alfthan, B., Fabres, J., Johnsen, K., Puikkonen, L., Kurvits, T., and Baker, E.: Global Linkages: A Graphic Look at the Changing Arctic (rev.1). Nairobi and Arendal: UN Environment and GRID-Arendal, https://www.grida.no/publications/431, 2019.

Schuur, E. A. G., Bockheim, J., Canadell, J. G., Euskirchen, E., Field, C. B., Goryachkin, S. V., Hagemann, S., Kuhry, P., Lafleur, P. M., Lee, H., Mazhitova, G., Nelson, F. E., Rinke, A., Romanovsky, V. E., Shiklomanov, N., Tarnocai, C., Venevsky, S., Vogel, J. G., and Zimov, S. A.: Vulnerability of Permafrost Carbon to Climate Change: Implications for the Global Carbon Cycle, Bioscience, 58, 701–714, https://doi.org/10.1641/B580807, 2008.

Schuur, E. A. G., McGuire, A. D., Schädel, C., Grosse, G., Harden, J. W., Hayes, D. J., Hugelius, G., Koven, C. D., Kuhry, P., Lawrence, D. M., Natali, S. M., Olefeldt, D., Romanovsky, V. E., Schaefer, K., Turetsky, M. R., Treat, C. C., and Vonk, J. E.: Climate change and the permafrost carbon feedback, Nature, 520, 171–179, https://doi.org/10.1038/nature14338, 2015.

Sevanto, S., Suni, T., Pumpanen, J., Gronholm, T., Kolari, P., Nikinmaa, E., Hari, P., and Vesala, T.: Wintertime photosynthesis and water uptake in a boreal forest, Tree Physiol., 26, 749–757, https://doi.org/10.1093/treephys/26.6.749, 2006.

Sha, M. K., Langerock, B., Blavier, J.-F. L., Blumenstock, T., Borsdorff, T., Buschmann, M., Dehn, A., De Mazière, M., Deutscher, N. M., Feist, D. G., Garc\'\ia, O. E., Griffith, D. W. T., Grutter, M., Hannigan, J. W., Hase, F., Heikkinen, P., Hermans, C., Iraci, L. T., Jeseck, P., Jones, N., Kivi, R., Kumps, N., Landgraf, J., Lorente, A., Mahieu, E., Makarova, M. V, Mellqvist, J., Metzger, J.-M., Morino, I., Nagahama, T., Notholt, J., Ohyama, H., Ortega, I., Palm, M., Petri, C., Pollard, D. F., Rettinger, M., Robinson, J., Roche, S., Roehl, C. M., Röhling, A. N., Rousogenous, C., Schneider, M., Shiomi, K., Smale, D., Stremme, W., Strong, K., Sussmann, R., Té, Y., Uchino, O., Velazco, V. A., Vrekoussis, M., Wang, P., Warneke, T., Wizenberg, T., Wunch, D., Yamanouchi, S., Yang, Y., and Zhou, M.: Validation of Methane and Carbon Monoxide from Sentinel-5 Precursor using TCCON and NDACC-IRWG stations, Atmos. Meas. Tech. Discuss., 1–84, https://doi.org/10.5194/amt-2021-36, 2021.

Sherlock, V., Connor, B., Robinson, J., Shiona, H., Smale, D., and Pollard, D. F.: TCCON data from Lauder (NZ), 120HR, Release GGG2014.R0, https://doi.org/10.14291/TCCON.GGG2014.LAUDER01.R0/1149293, 2014a.

Sherlock, V., Connor, B., Robinson, J., Shiona, H., Smale, D., and Pollard, D. F.: TCCON data from Lauder (NZ), 125HR, Release GGG2014.R0, https://doi.org/10.14291/TCCON.GGG2014.LAUDER02.R0/1149298, 2014b.

Sierk, B., Bézy, J.-L., Löscher, A., and Meijer, Y.: The European CO_2 Monitoring Mission: observing anthropogenic greenhouse gas emissions from space, in: International Conference on Space Optics — ICSO 2018, 237–250, 2019.

Steck, T.: Methods for determining regularization for atmospheric retrieval problems, Appl. Opt., 41, 1788–1797, https://doi.org/10.1364/AO.41.001788, 2002.

Stephens, B. B., Gurney, K. R., Tans, P. P., Sweeney, C., Peters, W., Bruhwiler, L., Ciais, P., Ramonet, M., Bousquet, P., Nakazawa, T., Aoki, S., Machida, T., Inoue, G., Vinnichenko, N., Lloyd, J., Jordan, A., Heimann, M., Shibistova, O., Langenfelds, R. L., Steele, L. P., Francey, R. J., and Denning, A. S.: Weak Northern and Strong Tropical Land Carbon Uptake from Vertical Profiles of Atmospheric CO_2, Science, 316, 1732–1735, https://doi.org/10.1126/science.1137004, 2007.

Strong, K., Bailak, G., Barton, D., Bassford, M.R., Blatherwick, R.D., Brown, S., Chartrand, D., Davies, J., Drummond, J.R., Fogal, P.F., Forsberg, E., Hall, R., Jofre, A., Kaminski, J., Kosters, J., Laurin, C., McConnell, J.C., McElroy, C.T., McLinden, C.A., Melo, S.M.L., Menzies, K., Midwinter, C., Murcray, F.J., Nowlan, C., Olson, R.J., Quine, B.M., Rochon, Y., Savastiouk, V, Solheim, B., Sommerfeldt, D., Ullberg, A., Werchohlad, S., Wu, H., and Wunch, D.: MANTRA – A Balloon Mission to Study the Odd-Nitrogen Budget of the Stratosphere, Atmos.-Ocean, 43 (4), 283–299, 2005.

Strong, K., Mendonca, J., Weaver, D., Fogal, P., Drummond, J. R., Batchelor, R., and Lindenmaier, R.: TCCON data from Eureka (CA), Release GGG2014.R0, https://doi.org/10.14291/TCCON.GGG2014.EUREKA01.R0/1149271, 2014.

Strong, K., Roche, S., Franklin, J. E., Mendonca, J., Lutsch, E., Weaver, D., Fogal, P. F., Drummond, J. R., Batchelor, R., and Lindenmaier, R.: TCCON data from Eureka (CA), Release GGG2014.R1, https://doi.org/10.14291/TCCON.GGG2014.EUREKA01.R1/1325515, 2016.

Strong, K., Roche, S., Franklin, J. E., Mendonca, J., Lutsch, E., Weaver, D., Fogal, P. F., Drummond, J. R., Batchelor, R., and Lindenmaier, R.: TCCON data from Eureka (CA), Release GGG2014.R2, https://doi.org/10.14291/TCCON.GGG2014.EUREKA01.R2, 2017.

Strong, K., Roche, S., Franklin, J. E., Mendonca, J., Lutsch, E., Weaver, D., Fogal, P. F., Drummond, J. R., Batchelor, R., and Lindenmaier, R.: TCCON data from Eureka (CA), Release GGG2014.R3, https://doi.org/10.14291/TCCON.GGG2014.EUREKA01.R3, 2019.

Strong, K., Simpson, W. R., Bognar, K., Lindenmaier, R., and Roche, S.: Trace Gases in the Arctic Atmosphere, in: Physics and Chemistry of the Arctic Atmosphere, edited by: Kokhanovsky, A. and Tomasi, C., Springer International Publishing, 153–207, https://doi.org/10.1007/978-3-030-33566-3_3, 2020a.

Strong, K., Wunch, D., and Roche, S.: CH_4 and CO Retrievals In Support of the AIM-North Phase 0 study, University of Toronto, CSA Contract No. 45-7014551, 58 pp., 2020b.

Sussmann, R. and Rettinger, M.: TCCON data from Garmisch (DE), Release GGG2014.R2, https://doi.org/10.14291/TCCON.GGG2014.GARMISCH01.R2, 2018.

Suto, H., Kataoka, F., Kikuchi, N., Knuteson, R. O., Butz, A., Haun, M., Buijs, H., Shiomi, K., Imai, H. and Kuze, A.: Thermal and near-infrared sensor for carbon observation Fourier transform spectrometer-2 (TANSO-FTS-2) on the Greenhouse gases Observing SATellite-2 (GOSAT-2) during its first year in orbit, Atmos. Meas. Tech., 14(3), 2013–2039, doi:10.5194/amt-14-2013-2021, 2021.

Suzuki, I.: General anharmonic force constants of carbon dioxide, J. Mol. Spectrosc., 25, 479–500, https://doi.org/10.1016/S0022-2852(68)80018-9, 1968.

Sweeney, C., Higgs, J., Wolter, S., Crotwell, A., Neff, D., Dlugokencky, E., Lang, P., Novelli, P., Mund, J., Moglia, E., and Crotwell, M.: Earth System Research Laboratory Carbon Cycle and Greenhouse Gases Group Flask-Air Sample Measurements of CO_2, CH_4, CO, N_2O, H_2, and SF_6 from the Aircraft Program, 1992-Present, Version 1, https://doi.org/https://doi.org/10.7289/V5N58JMF, 2017.

Tarnocai, C., Canadell, J. G., Schuur, E. A. G., Kuhry, P., Mazhitova, G., and Zimov, S.: Soil organic carbon pools in the northern circumpolar permafrost region, Global Biogeochem. Cycles, 23, https://doi.org/10.1029/2008GB003327, 2009.

Taylor, T. E., Eldering, A., Merrelli, A., Kiel, M., Somkuti, P., Cheng, C., Rosenberg, R., Fisher, B., Crisp, D., Basilio, R., Bennett, M., Cervantes, D., Chang, A., Dang, L., Frankenberg, C., Haemmerle, V. R., Keller, G. R., Kurosu, T., Laughner, J. L., Lee, R., Marchetti, Y., Nelson, R. R., O'Dell, C. W., Osterman, G., Pavlick, R., Roehl, C., Schneider, R., Spiers, G., To, C., Wells, C., Wennberg, P. O., Yelamanchili, A. and Yu, S.: OCO-3 early mission operations and initial (vEarly) XCO_2 and SIF retrievals, Remote Sens. Environ., 251, 112032, doi:10.1016/j.rse.2020.112032, 2020.

Tennyson, J., Bernath, P. F., Campargue, A., Császár, A. G., Daumont, L., Gamache, R. R., Hodges, J. T., Lisak, D., Naumenko, O. V., Rothman, L. S., Tran, H., Zobov, N. F., Buldyreva, J., Boone, C. D., De Vizia, M. D., Gianfrani, L., Hartmann, J.-M., McPheat, R., Weidmann, D., Murray, J., Ngo, N. H., and Polyansky, O. L.: Recommended isolated-line profile for representing high-resolution spectroscopic transitions (IUPAC Technical Report), Pure Appl. Chem., 86, 1931–1943, https://doi.org/10.1515/pac-2014-0208, 2014.

Tian, H., Xu, R., Canadell, J. G., Thompson, R. L., Winiwarter, W., Suntharalingam, P., Davidson, E. A., Ciais, P., Jackson, R. B., Janssens-Maenhout, G., Prather, M. J., Regnier, P., Pan, N., Pan, S., Peters, G. P., Shi, H., Tubiello, F. N., Zaehle, S., Zhou, F., Arneth, A., Battaglia, G., Berthet, S., Bopp, L., Bouwman, A. F., Buitenhuis, E. T., Chang, J., Chipperfield, M. P., Dangal, S. R. S., Dlugokencky, E., Elkins, J. W., Eyre, B. D., Fu, B., Hall, B., Ito, A., Joos, F., Krummel, P. B., Landolfi, A., Laruelle, G. G., Lauerwald, R., Li, W., Lienert, S., Maavara, T., MacLeod, M., Millet, D. B., Olin, S., Patra, P. K., Prinn, R. G., Raymond, P. A., Ruiz, D. J., van der Werf, G. R., Vuichard, N., Wang, J., Weiss, R. F., Wells, K. C., Wilson, C., Yang, J., and Yao, Y.: A comprehensive quantification of global nitrous oxide sources and sinks, Nature, 586, 248–256, https://doi.org/10.1038/s41586-020-2780-0, 2020.

Tikhonov, A. N.: On the solution of ill-posed problems and the method of regularization, Dokl. Akad. Nauk SSSR, 151, 501–504, 1963.

Toon, G. C.: Atmospheric Line List for the 2014 TCCON Data Release (Version GGG2014.R0) [Data set], https://doi.org/https://doi.org/10.14291/tccon.ggg2014.atm.r0/1221656, 2015.

Toon, G. C., Blavier, J.-F., Sung, K., Rothman, L. S., and E. Gordon, I.: HITRAN spectroscopy evaluation using solar occultation FTIR spectra, J. Quant. Spectrosc. Radiat. Transf., 182, 324–336, https://doi.org/10.1016/j.jqsrt.2016.05.021, 2016a.

Toon, G. C., Wunch, D., Wennberg, P. O., and Arnold, S. G.: Post-Facto Temperature Correction, in: NDACC-IRWG and TCCON meeting, 46, 2016b.

Toth, R. A., Brown, L. R., Miller, C. E., Malathy Devi, V., and Benner, D. C.: Spectroscopic database of CO_2 line parameters: 4300–7000 cm^{-1}, J. Quant. Spectrosc. Radiat. Transf., 109, 906–921, https://doi.org/10.1016/j.jqsrt.2007.12.004, 2008.

Tran, H., Ngo, N. H., and Hartmann, J.-M.: Efficient computation of some speed-dependent isolated line profiles, J. Quant. Spectrosc. Radiat. Transf., 129, 199–203, https://doi.org/10.1016/j.jqsrt.2013.06.015, 2013.

Turner, A. J., Frankenberg, C., Wennberg, P. O., and Jacob, D. J.: Ambiguity in the causes for decadal trends in atmospheric methane and hydroxyl, Proc. Natl. Acad. Sci., 114, 5367–5372, https://doi.org/10.1073/pnas.1616020114, 2017.

UNFCCC: Report of the Conference of the Parties on its twenty-first session, held in Paris from 30 November to 11 December 2015, 42 pp., https://doi.org/https://unfccc.int/resource/docs/2015/cop21/eng/10.pdf, 2015.

Veefkind, J. P., Aben, I., McMullan, K., Förster, H., de Vries, J., Otter, G., Claas, J., Eskes, H. J., de Haan, J. F., Kleipool, Q., van Weele, M., Hasekamp, O., Hoogeveen, R., Landgraf, J., Snel, R., Tol, P., Ingmann, P., Voors, R., Kruizinga, B., Vink, R., Visser, H., and Levelt, P. F.: TROPOMI on the ESA Sentinel-5 Precursor: A GMES mission for global observations of the atmospheric composition for climate, air quality and ozone layer applications, Remote Sens. Environ., 120, 70–83, https://doi.org/10.1016/j.rse.2011.09.027, 2012.

Victor, D. G., Zhou, D., Hassan Mohamed Ahmed, E., Kumar Dadhich, P., Olivier, J., Rogner, H.-H., Sheikho, K., Yamaguchi, M., Baiocchi, G. U., Mulugetta Ethiopia, Y., Wong, L., G, V. D., Zhou, D., M Ahmed, E. H., Dadhich, P. K., J Olivier, J. G., Rogner, H., Sheikho, K., Yamaguchi, M., Pichs-Madruga, R., Sokona, Y., Farahani, E., Kadner, S., Seyboth, K., Adler, A., Baum, I., Brunner, S., Eickemeier, P., Kriemann, B., Savolainen, J., Schlömer, S., von Stechow, C., Zwickel, T., and Minx, J.: Introductory Chapter. In: Climate Change 2014: Mitigation of Climate Change. Contribution of Working Group III to the Fifth Assessment Report of the Intergovernmental Panel on Climate Change, Mitigation of Climate Change, Cambridge, United Kingdom and New York, USA, 2014.

Wallace, J. M. and Hobbs, P. V: Atmospheric Science: An Introductory Survey, Elsevier Academic Press, 2006.

Warneke, T., Messerschmidt, J., Notholt, J., Weinzierl, C., Deutscher, N. M., Petri, C., and Grupe, P.: TCCON data from Orléans (FR), Release GGG2014.R1, https://doi.org/10.14291/TCCON.GGG2014.ORLEANS01.R1, 2019.

Wennberg, P. O., Wunch, D., Roehl, C. M., Blavier, J.-F., Toon, G. C., and Allen, N. T.: TCCON data from Lamont (US), Release GGG2014.R1 [Data set]., https://doi.org/https://doi.org/10.14291/tccon.ggg2014.lamont01.r1/1255070, 2016.

Wennberg, P. O., Roehl, C. M., Wunch, D., Toon, G. C., Blavier, J.-F., Washenfelder, R., Keppel-Aleks, G., Allen, N. T., and Ayers, J.: TCCON data from Park Falls (US), Release GGG2014.R1, https://doi.org/10.14291/TCCON.GGG2014.PARKFALLS01.R1, 2017.

Whitmarsh, J. and Govindjee: The Photosynthetic Process, in: Concepts in Photobiology, Springer Netherlands, Dordrecht, 11–51, https://doi.org/10.1007/978-94-011-4832-0_2, 1999.

Witteman, W. J.: Rotational-Vibrational Structure of CO2, in: The CO2 Laser, Springer Series in Optical Sciences, vol. 53. Springer, Berlin, Heidelberg, 8–52, https://doi.org/10.1007/978-3-540-47744-0_2, 1987.

WMO: WMO WDCGG Data Summary (WDCGG no. 41). GAW data, Volume IV-Greenhouse Gases and Other Atmospheric Gases, https://doi.org/https://gaw.kishou.go.jp/static/publications/summary/sum41/sum41.pdf, 2017.

WMO: WMO Statement on the State of the Global Climate in 2017 (WMO-no. 1212), Geneva, https://doi.org/https://library.wmo.int/doc_num.php?explnum_id=4453, 2018.

WMO, UNESCO, UNEP, and ICSU: Systematic Observation Requirements for Satellite-based Products for Climate, Supplemental details to the satellite-based component of the "Implementation Plan for the Global Observing System for Climate in Support of the UNFCCC (2010 Update)," WMO, Geneva, 138 pp., 2011.

Wofsy, S. C.: HIAPER Pole-to-Pole Observations (HIPPO): fine-grained, global-scale measurements of climatically important atmospheric gases and aerosols, Philos. Trans. R. Soc. A, 369, 2073–2086, https://doi.org/10.1098/rsta.2010.0313, 2011.

Wofsy, S. C., Afshar, S., Allen, H. M., Apel, E., Asher, E. C., Barletta, B., Bent, J., Bian, H., Biggs, B. C., Blake, D. R., Blake, N., Bourgeois, I., Brock, C. A., Brune, W. H., Budney, J. W., Bui, T. P., Butler, A., Campuzano-Jost, P., Chang, C. S., Chin, M., Commane, R., Correa, G., Crounse, J. D., Cullis, P. D., Daube, B. C., Day, D. A., Dean-Day, J. M., Dibb, J. E., Digangi, J. P., Diskin, G. S., Dollner, M., Elkins, J. W., Erdesz, F., Fiore, A. M., Flynn, C. M., Froyd, K., Gesler, D. W., Hall, S. R., Hanisco, T. F., Hannun, R. A., Hills, A. J., Hintsa, E. J., Hoffman, A., Hornbrook, R. S., Huey, L. G., Hughes, S., Jimenez, J. L., Johnson, B. J., Katich, J. M., Keeling, R., Kim, M. J., Kupc, A., Lait, L. R., Lamarque, J.-F., Liu, J., McKain, K., McLaughlin, R. J., Meinardi, S., Miller, D. O., Montzka, S. A., Moore, F. L., Morgan, E. J., Murphy, D. M., Murray, L. T., Nault, B. A., Neuman, J. A., Newman, P. A., Nicely, J. M., Pan, X., Paplawsky, W., Peischl, J., Prather, M. J., Price, D. J., Ray, E., Reeves, J. M., Richardson, M., Rollins, A. W., Rosenlof, K. H., Ryerson, T. B., Scheuer, E., Schill, G. P., Schroder, J. C., Schwarz, J. P., St.Clair, J. M., Steenrod, S. D., Stephens, B. B., Strode, S. A., Sweeney, C., Tanner, D., Teng, A. P., Thames, A. B., Thompson, C. R., Ullmann, K., Veres, P. R., Vizenor, N., Wagner, N. L., Watt, A., Weber, R., Weinzierl, B., et al.: ATom: Merged Atmospheric Chemistry, Trace Gases, and Aerosols, https://doi.org/10.3334/ORNLDAAC/1581, 2018.

Wunch, D., Toon, G. C., Wennberg, P. O., Wofsy, S. C., Stephens, B. B., Fischer, M. L., Uchino, O., Abshire, J. B., Bernath, P., Biraud, S. C., Blavier, J.-F. L., Boone, C., Bowman, K. P., Browell, E. V, Campos, T., Connor, B. J., Daube, B. C., Deutscher, N. M., Diao, M., Elkins, J. W., Gerbig, C., Gottlieb, E., Griffith, D. W. T., Hurst, D. F., Jiménez, R., Keppel-Aleks, G., Kort, E. A., Macatangay, R., Machida, T., Matsueda, H., Moore, F., Morino, I., Park, S., Robinson, J., Roehl, C. M., Sawa, Y., Sherlock, V., Sweeney, C., Tanaka, T., and Zondlo, M. A.: Calibration of the Total Carbon Column Observing Network using aircraft profile data, Atmos. Meas. Tech., 3, 1351–1362, https://doi.org/10.5194/amt-3-1351-2010, 2010.

Wunch, D., Toon, G. C., Blavier, J.-F. L., Washenfelder, R. A., Notholt, J., Connor, B. J., Griffith, D. W. T., Sherlock, V., and Wennberg, P. O.: The Total Carbon Column Observing Network, Philos. Trans. R. Soc. A, 369, 2087–2112, https://doi.org/10.1098/rsta.2010.0240, 2011.

Wunch, D., Toon, G. C., Sherlock, V., Deutscher, N. M., Liu, C., Feist, D. G., and Wennberg, P. O.: Documentation for the 2014 TCCON Data Release (Version GGG2014.R0). CaltechDATA., https://doi.org/https://doi.org/10.14291/tccon.ggg2014.documentation.r0/1221662, 2015.

Wunch, D., Wennberg, P. O., Osterman, G., Fisher, B., Naylor, B., Roehl, M. C., O'Dell, C., Mandrake, L., Viatte, C., Kiel, M., Griffith, D. W. T., Deutscher, N. M., Velazco, V. A., Notholt, J., Warneke, T., Petri, C., De Maziere, M., Sha, M. K., Sussmann, R., Rettinger, M., Pollard, D., Robinson, J., Morino, I., Uchino, O., Hase, F., Blumenstock, T., Feist, D. G., Arnold, S. G., Strong, K., Mendonca, J., Kivi, R., Heikkinen, P., Iraci, L., Podolske, J., Hillyard, P., Kawakami, S., Dubey, M. K., Parker, H. A., Sepulveda, E., García, O. E., Te, Y., Jeseck, P., Gunson, M. R., Crisp, D., and Eldering, A.: Comparisons of the Orbiting Carbon Observatory-2 (OCO-2) XCO_2 measurements with TCCON, https://doi.org/10.5194/amt-10-2209-2017, 13 June 2017.

Yang, D., Liu, Y., Cai, Z., Chen, X., Yao, L., and Lu, D.: First Global Carbon Dioxide Maps Produced from TanSat Measurements, Adv. Atmos. Sci., 35, 621–623, https://doi.org/10.1007/s00376-018-7312-6, 2018.